

673A

Amstrong
Oct 10 1968
216
676157

TECHNICAL REPORT NO. 10022 (Final)

THE EFFECT OF LEAD ON MICRO-CRACK
INITIATION AND PROPAGATION IN ALLOY STEELS

FINAL REPORT PHASE I

PART A: EMBRITTLEMENT OF LEADED STEELS AT
INTERMEDIATE TEMPERATURES



TECHNICAL LIBRARY
REFERENCE COPY

CATALOGED

Distribution of this document is unlimited

by Sheldon Mostovy and Norman N. Breyer
ILLINOIS INSTITUTE OF TECHNOLOGY

Date: July 1968

Contract No. DA-20-113-AMC-10820(T)

TACOM

VEHICULAR COMPONENTS & MATERIALS LABORATORY

U.S. ARMY TANK AUTOMOTIVE COMMAND Warren, Michigan

20040113035

AN 30534

THE EFFECT OF LEAD ON MICRO-CRACK
INITIATION AND PROPAGATION IN ALLOY STEELS

Final Report - Phase I

Part A

EMBRITTLEMENT OF LEADED STEEL
AT INTERMEDIATE TEMPERATURES

by

Sheldon Mostovoy and Norman N. Breyer

July 1968

Distribution of this document is unlimited

Contract No. DA-20-113-AMC-10820(T)
U.S. Army Tank-Automotive Command
Warren, Michigan 48090

Department of Metallurgical Engineering
Illinois Institute of Technology
Chicago, Illinois 60616

ABSTRACT

A detailed investigation was made of the influence of 0.30 per cent lead on the room and elevated temperature mechanical properties of a 4145 steel. Leaded and non-leaded versions of this identical steel were quenched and tempered to room temperature strength levels ranging from 120 to 240 ksi. The properties measured included both complete tensile data and impact energies for all strength levels. Macrofractographs detailing differences in fracture morphology at specific test temperatures were also included.

A comparison of tensile ductility between the non-leaded and leaded steel showed small differences in reduction of area below 400 or above 900°F. However, between 400 and 621°F, the melting point of lead, RA decreased rapidly at all strength levels. Maximum embrittlement occurred at or somewhat above 621°F and its severity was directly related to strength level. Variations of RA in the temperature range between 621 and 890°F was relatively minor but at room temperature strengths at and about 200 ksi leaded steels showed no measurable ductility.

Most of the observations made regarding embrittlement of leaded steel were similar to those reported for surface wetted liquid-metal-embrittlement experiments. The major difference was that substantial embrittlement occurred well below the melting point of lead in the leaded steel. The explanation of this effect is based on the Stoloff and Johnston theory of liquid-metal embrittlement which states that a reduction of the binding forces producing cohesion takes place when the embrittling metal atoms are chemisorbed at the crack tip. Thus, the embrittlement observed below the melting point suggests that the transport of these atoms to the crack tip occurs through the vapor phase. The substantial loss in strength and ductility at the melting point of lead is attributed to the mobility of the liquid metal which by following the growing crack can expedite atom transport. The restoration of mechanical properties above 890°F, independent of strength level, is proposed to result from the decrease in sticking coefficient with increasing temperature.

Ductility losses in low strength leaded steels tested in the embrittlement trough suggest that this hypothesis is more acceptable than the dislocation-flow-stress theory proposed for liquid-metal-embrittlement recovery.

ACKNOWLEDGEMENT

—FOREWORD—

The report which summarizes the findings of the first phase of the program has been broken into two parts. The portion included in this bound report is Part A and defines the embrittlement of a leaded 4145 steel at intermediate temperatures (400-900°F). Part B which is a separately bound report examines the nature of the fractures encountered utilizing both macrofractography and electron microscope fractography. The work to which these two reports is addressed is the understanding of catastrophic fractures which have all too frequently been encountered during the heat treatment, processing and subsequent service of leaded high strength alloy steels.

The program was authorized by the U.S. Army Tank Automotive Command (TACOM), Warren, Michigan under Contract No. ~~DA-20-113-AMC-10820(T)~~. Technical administration of the contract was the responsibility of V. H. Pagano, Chief, Metals Branch, Materials Laboratory, VCML, TACOM. The TACOM project engineer was C. J. Kropf.

Test Director was
MR PAUL KELPS, PROJECT
ENGINEER OF THE TRAILER
BRANCH, DEVELOPMENT &
ENGINEERING DIRECTORATE

TABLE OF CONTENTS

	Page No.
1. INTRODUCTION	1
1.1 The Problem	1
1.2 Background	2
2. OBJECTIVE	5
3. SUMMARY	5
4. CONCLUSIONS	6
5. RECOMMENDATIONS	7
6. EXPERIMENTS AND RESULTS	8
6.1 Materials used and Their Processing and Testing . . .	8
6.2 Mechanical Properties	12
6.2.1 Tensile Tests on Longitudinal Specimens . .	12
6.2.2 Impact Tests	14
6.2.3 Tensile Tests on Transverse Specimens . . .	15
6.2.4 Thermal Expansion	16
6.2.5 Static Fatigue	16
6.3 Fractography	17
6.3.1 Macro-Fractography	17
6.3.2 Electron Fractography	19
7. DISCUSSION	20
7.1 Similarities of Lead Steel Data to Liquid-Metal-Wetted Observations	21
7.2 Dissimilarities of Lead Steel Data to Liquid-Metal-Wetted Observations	23
7.3 Mechanisms of Liquid-Metal Embrittlement	25
7.4 Atom Transport to the Crack Tip	27

TABLE OF CONTENTS (Cont.)

		Page No.
APPENDIX A	VAPOR PRESSURE OF LEAD AS A FUNCTION OF TEMPERATURE	33
BIBLIOGRAPHY	35
DISTRIBUTION LIST	171
DD FORM 1473	175

LIST OF TABLES

Table	Page No.
1. Materials List, Heat Treatment and Code for Use on Figures	38
2. Influence of Tensile Specimen Orientation and Specimen Configuration on the Mechanical Properties of Leaded and Non-Leaded Steels Heat Treated to Two Strength Levels and Tested at Room Temperature and in the Embrittlement Trough	39

LIST OF FIGURES

Figure		Page No.
1	Photomicrographs of Leaded Cold Drawn AISI 4145 Steel Taken Parallel to Bar Axis. Unetched to Show Inclusion Morphology. 500X. Note Manganese Sulfide (Grey) and Iron or Manganese Oxides (Black) in Rounded Inclusion Surrounded by Strung Out Lead (Whitish).	41
2	Photomicrographs of Non-leaded Cold Drawn AISI 4145 Steel Taken Parallel to Bar Axis. Unetched to Show Inclusion Morphology. 500X. Note Manganese Sulfide as Round Black Inclusions with Strung Out Iron and Manganese Oxides Which Appear as Greyish Surroundings. .	42
3	Electron Microprobe Scan Across a Leaded Steel Inclusion Using Back Scattered Electron, BSE, and Characteristic X-ray Counters. a) BSE, b) Pb-Ma, c) Mn-Ka, d) S-Ka. 800X.	43
4	Electron Microprobe Scan Across a Leaded Steel Inclusion Using Back Scattered Electron, BSE, and Characteristic X-ray Counters. a) BSE, b) Pb-Ma, c) Mn-Ka, d) S-Ka. 800X.	44
5	(A) Tensile Specimen Engineering Drawing. (B) As-received Leaded and Non-leaded AISI 4140 Steel Bar Cross-Section Showing Specimen Location. Note: Specimen Dimensions in Inches.	45
6	Radiused Transverse Tensile Specimen (Initial Bar Stock Diameter 1-9/16 in.) Note: Specimen Dimensions in Inches.	46

LIST OF FIGURES (Cont.)

Figure		Page No.
7	Room and Elevated Temperature Tensile Test Equipment: a) Baldwin 60,000 lb. cap. Tensile Machine with Autographic Recorder. b) Load Frame Equipped with Furnace: Controller and Specimen Temperature Recorder (Shown at Side). d) Load Train with Extensometer in Place Prior to Insertion in Furnace. Note Thermocouples Tied on to Specimen.	47
8	Room and Elevated Temperature Impact Test Equipment. Note Fitted Tongs Shown in Insert	48
9	Apparatus for Measurement of the Thermal Coefficient of Expansion, α	49
10	Static Fatigue Radiused Longitudinal Tensile Specimen Engineering Drawing. Note: Specimen Dimensions in Inches.	50
11	Engineering Tensile Properties of Cold Drawn Non-leaded AISI 4145 Steel as a Function of Test Temperature. Crosshead Rate .01 to .1 in./min. (NO Series)	51
12	Effect of Test Temperature on True Fracture Stress, $\bar{\sigma}_F$, and Proportional Limit, σ_{PL} , for Cold Drawn Non-leaded AISI 4145 Steel. (NO Series)	52
13	Effect of Test Temperature on Elastic Modulus, E , for Cold Drawn Non-leaded AISI 4145 Steel. (NO Series)	53

LIST OF FIGURES (Cont.)

Figure		Page No.
14	Engineering Tensile Properties of Cold Drawn Leaded AISI 4145 Steel as a Function of Test Temperature. Crosshead Rate .01 to .1 in./min. Note that Between 700 and 850°F σ_{YS} Cannot be Measured Due to the Small Elongation in this Region. (LO Series)	54
15	Effect of Test Temperature on True Fracture Stress, $\bar{\sigma}_F$, and Proportional Limit, σ_{PL} , for Cold Drawn Leaded AISI 4145 Steel. (LO Series)	55
16	Effect of Test Temperature on Elastic Modulus, E, for Cold Drawn Leaded AISI 4145 Steel. (LO Series)	56
17	Effect of Test Temperature on Fracture Appearance of Leaded and Non-leaded Cold-drawn AISI 4145 Steel Broken at Indicated Temperatures. LO are leaded; NO are not leaded.	57
18	Engineering Tensile Properties of Non-leaded N24 Material.	58
19	Effect of Test Temperature on $\bar{\sigma}_F$ and σ_{PL} for Non-leaded N24 Material	59
20	Engineering Tensile Properties of Leaded L24 Material. . .	60
21	Effect of Test Temperature on $\bar{\sigma}_F$ and σ_{PL} for Leaded L24 Material.	61
22	Tensile Fracture Surfaces of Leaded and Non-leaded N24 and L24 Material Below 620°F.	62
23	Tensile Fracture Surfaces of Leaded and Non-leaded N24 and L24 Material Above 620°F.	63
24	Engineering Tensile Properties of Non-leaded N22 Material.	64

LIST OF FIGURES (Cont.)

Figure		Page No.
25	Effect of Test Temperature on $\bar{\sigma}_F$ and σ_{PL} for Non-leaded N22 Material.	65
26	Engineering Tensile Properties of Leaded L22 Material. . .	66
27	Effect of Test Temperature on $\bar{\sigma}_F$ and σ_{PL} for Leaded L22 Material.	67
28	Tensile Fracture Surfaces of Leaded and Non-leaded L22 and N22 Material Below 600°F.	68
29	Tensile Fracture Surfaces of Leaded and Non-leaded L22 and N22 Material Above 600°F.	69
30	Engineering Tensile Properties of Non-leaded N20 Material	70
31	Effect of Test Temperature on $\bar{\sigma}_F$ and σ_{PL} for Non-leaded N20 Material.	71
32	Engineering Tensile Properties of Leaded L20 Material. .	72
33	Effect of Test Temperature on $\bar{\sigma}_F$ and σ_{PL} for Leaded L20 Material.	73
34	Effect of Test Temperature on Fracture Appearance of Leaded and Non-leaded L20 and N20 Steel.	74
35	Effect of Test Temperature on Fracture Appearance of Leaded and Non-leaded L20 and N20 Steel.	75
36	Effect of Test Temperature on Fracture Appearance of Leaded and Non-Leaded AISI 4145 Steel Oil Quenched from 1525°F and Tempered at 940°F. L20 are Leaded; N20 are not Leaded.	76

LIST OF FIGURES (Cont.)

Figure.		Page No.
37	Engineering Tensile Properties of Non-leaded N18 Material.	77
38	Effect of Test Temperature on $\bar{\sigma}_F$ and σ_{PL} for Non-leaded N18 Material.	78
39	Engineering Tensile Properties of Leaded L18 Material. . .	79
40	Effect of Test Temperature on $\bar{\sigma}_F$ and σ_{PL} for Leaded L18 Material.	80
41	Tensile Fracture Surfaces of Leaded and Non-leaded L18 and N18 Material Below 650°F.	81
42	Tensile Fracture Surfaces of Leaded and Non-leaded L18 and N18 Material Above 650°F.	82
43	Engineering Tensile Properties of Non-leaded N16 Material.	83
44	Effect of Test Temperature on $\bar{\sigma}_F$ and σ_{PL} for Non-leaded N16 Material.	84
45	Engineering Tensile Properties of Leaded L16 Material. . .	85
46	Effect of Test Temperature on $\bar{\sigma}_F$ and σ_{PL} for Leaded L16 Material.	86
47	Tensile Fracture Surfaces of Leaded and Non-leaded L16 and N16 Material Below 650°F.	87
48	Tensile Fracture Surfaces of Leaded and Non-leaded L16 and N16 Material Above 650°F.	88
49	Engineering Tensile Properties of Non-leaded N14 Material.	89

LIST OF FIGURES (Cont.)

Figure		Page No.
50	Effect of Test Temperature on $\bar{\sigma}_F$ and σ_{PL} for Non- leaded N14 Material.	90
51	Engineering Tensile Properties of Leaded L14 Material. . .	91
52	Effect of Test Temperature on $\bar{\sigma}_F$ and σ_{PL} for Leaded L14 Material.	92
53	Tensile Fracture Surfaces of Leaded and Non-leaded L14 and N14 Material Below 620°F.	93
54	Tensile Fracture Surfaces of Leaded and Non-leaded L14 and N14 Material Above 620°F.	94
55	Engineering Tensile Properties of Non-leaded N12 Material.	95
56	Effect of Test Temperature on $\bar{\sigma}_F$ and σ_{PL} for Non- leaded N12 Material.	96
57	Engineering Tensile Properties of Leaded L12 Material.	97
58	Effect of Test Temperature on $\bar{\sigma}_F$ and σ_{PL} for Leaded L12 Material.	98
59	Tensile Fracture Surfaces of Leaded and Non-leaded L12 and N12 Material Below 620°F.	99
60	Tensile Fracture Surfaces of Leaded and Non-leaded L12 and N12 Material Above 620°F.	100
61	Hardness, R_C , vs. Tempering Temperature, T_p , for Leaded and Non-leaded AISI 4145 Steel Oil Quenched from 1525°F. . .	101

LIST OF FIGURES (Cont.)

Figure		Page No.
62	Empirical Relationship Between Hardness, R_c Scale, and Tensile Strength, σ_{UTS} , for Heat Treated Carbon and Low Alloy Steels.	102
63	Ultimate Tensile Strength, σ_{UTS} , (Converted from Hardness) vs. Tempering Temperature, T_T , for AISI 4145 Steel, Lead and Non-lead. Hardness, R_c , Added for Comparison. Note that Tempering Temperature Selected for Specific σ_{UTS} Falls on Curve.	103
64	Comparison of R.A. for Non-lead Material.	104
65	Comparison of R.A. for Lead Material.	105
66	Ratio of R.A. for Lead to Non-lead Material.	106
67	Comparison of \bar{e} for Non-lead Material.	107
68	Comparison of \bar{e} for Lead Material.	108
69	Ratio of \bar{e} for Lead to Non-lead Material.	109
70	Comparison of σ_{UTS} for Non-lead Material.	110
71	Comparison of σ_{UTS} for Lead Material.	111
72	Ratio of σ_{UTS} for Lead to Non-lead Material.	112
73	Comparison of $\bar{\sigma}_F$ for Non-lead Material.	113
74	Comparison of $\bar{\sigma}_F$ for Lead Material.	114
75	Ratio of $\bar{\sigma}_F$ for Lead to Non-lead Material.	115

LIST OF FIGURES (Cont.)

Figure		Page No.
76	Comparison of σ_{YS} for Non-leaded Material.	116
77	Comparison of σ_{YS} for Leded Material.	117
78	Comparison of σ_{PL} for Non-leaded Material.	118
79	Comparison of σ_{PL} for Leded Material.	119
80	Effect of Test Temperature on Absorbed Energy of a Charpy "V" Notch Impact Specimen for Leded and Non-leaded L20 and N20 Material.	120
81	Effect of Test Temperature on Absorbed Energy of a Charpy "V" Notch Impact Specimen for Leded and Non-leaded L24 and N24 Material.	121
82	Effect of Test Temperature on Absorbed Energy of a Charpy "V" Notch Impact Specimen for Leded and Non-leaded L14 and N14 Material.	122
83	Effect of Test Temperature on Absorbed Energy of a Charpy "V" Notch Impact Specimen for Leded and Non-leaded L18 and N18 Material.	123
84	Ratio of Charpy "V" Notch Absorbed Energy for Leded to Non-leaded Steels at Four Strength Levels as a Function of Test Temperature.	124
85	Tensile Properties of Radiused Transverse N24T Specimens as a Function of Test Temperature.	125
86	Tensile Properties of Radiused Transverse L24T Specimens as a Function of Test Temperature.	126
87	Tensile Properties of Radiused Transverse N22T Specimens as a Function of Test Temperature.	127

LIST OF FIGURES (Cont.)

Figure		Page No.
88	Tensile Properties of Radiused Transverse L22T Specimens as a Function of Test Temperature.	128
89	Tensile Properties of Radiused Transverse N20T Specimens as a Function of Test Temperature.	129
90	Tensile Properties of Radiused Transverse L20T Specimens as a Function of Test Temperature.	130
91	Tensile Properties of Radiused Transverse N18T Specimens as a Function of Test Temperature.	131
92	Tensile Properties of Radiused Transverse L18T Specimens as a Function of Test Temperature.	132
93	Tensile Properties of Radiused Transverse N16T Specimens as a Function of Test Temperature.	133
94	Tensile Properties of Radiused Transverse L16T Specimens as a Function of Test Temperature.	134
95	Tensile Properties of Radiused Transverse N14T Specimens as a Function of Test Temperature.	135
96	Tensile Properties of Radiused Transverse L14T Specimens as a Function of Test Temperature.	136
97	Tensile Properties of Radiused Transverse L12T Specimens as a Function of Test Temperature.	137
98	Engineering Stress-Strain Plots of Standard Longitudinal Specimens of N22 Material at Room and Elevated Temperatures. (Note Strain Scale Change at 1.0 per cent)	138

LIST OF TABLES (Cont.)

Figure		Page No.
99	Engineering Stress-Strain Plots of Standard Longitudinal Specimens of L22 Material at Room and Elevated Temperatures. (Note Strain Scale Change at 1.0 per cent)	139
100	Engineering Stress-Strain Plots of Standard Longitudinal Specimens of N20 Material at Room and Elevated Temperatures. (Note Strain Scale Change at 1.0 per cent)	140
101	Engineering Stress-Strain Plots of Standard Longitudinal Specimens of L20 Material at Room and Elevated Temperatures. (Note Strain Scale Change at 1.0 per cent)	141
102	Engineering Stress-Deflection Plots of Fatigue Type Longitudinal Specimens of N22 Material at 75 and 750°F. . . .	142
103	Engineering Stress-Deflection Plots of Fatigue Type Longitudinal Specimens of L22 Material at 75 and 755°F. . . .	143
104	Engineering Stress-Deflection Plots of Fatigue Type Longitudinal Specimens of N20 Material at 75 and 758°F. . . .	144
105	Engineering Stress-Deflection Plots of Fatigue Type Longitudinal Specimens of L20 Material at 75 and 750°F. . . .	145
106	Engineering Stress-Deflection Plots of Fatigue Type Transverse Specimens of N22 Material at Room and Elevated Temperature.	146
107	Engineering Stress-Deflection Plots of Fatigue Type Transverse Specimens of L22 Material at Room and Elevated Temperatures.	147
108	Engineering Stress-Deflection Plots of Fatigue Type Transverse Specimens of N20 Material at Room and Elevated Temperatures.	148

LIST OF FIGURES (Cont.)

Figure		Page No.
109	Engineering Stress-Deflection Plots of Fatigue Type Transverse Specimens of L20 Material at Room and Elevated Temperatures.	109
110	Thermal Expansion of Leaded and Non-leaded L20 and N20 Steel from 75 to 920°F. Note Scale Axis Separation to Separate Data Points.	150
111	Applied Static Fatigue Stress at 750°F Versus Time to Fracture for L20 Material.	151
112	Applied Static Fatigue Stress at 750°F Versus Time to Fracture for L22 Material.	152
113	Fracture Surface Photographs of Transverse Tensile Specimen at (Top) 4X and (Bottom) 6X Magnification. Note These Fractures Obtained on a Leaded Material Are Typical of Those Obtained on Both Leaded and Non-leaded Steel Tested in a Transverse Direction.	153
114	Impact Fracture Surface Photographs of Leaded and Non-leaded L20 and N20 Material. Test Temperatures and Related Impact Values Indicated Opposite Photograph. . .	154
115	Enlarged Oblique View of Impact Fracture Surfaces from Figure 114 in Temperature Range of Embrittlement of the Leaded L20 Material.	155
116	Fracture Surface Classification for Longitudinal Tensile Specimens.	156
117	Schematic Drawing of Type D Fracture.	157

LIST OF FIGURES (Cont.)

Figure		Page No.
118	Electron Fractographs of Lead ^{ed} Steel Showing a <u>B</u> Type Fracture Which Appears Intergranular in Nature. (3000X)	158
119	Electron Fractographs of Lead ^{ed} Steel Showing a <u>B</u> Type Fracture Which Exhibits Both Intergranular and Transgranular Fracture Modes. (3000X).	159
120	Electron Fractographs of Lead ^{ed} Steel Showing a <u>C</u> Type Fracture in the Proximity of One of the "Fish-eyes" Which Appears Intergranular in Nature. (Top, 2000X; Bottom, 4000X). . .	160
121	Electron Fractographs of Lead ^{ed} Steel Showing a <u>C</u> Type Fracture at Some Distance from a Small "Fish-eye" Which Exhibits Both Intergranular and Transgranular Fracture Modes. (3000X)	161
122	Electron Fractographs of Lead ^{ed} Steel Showing a <u>D</u> Type Fracture Near the Origin of Cracking. Note that the Fracture is Completely Intergranular. (4000X)	162
123	σ_{UTS} of Lead ^{ed} and Non-lead ^{ed} 4145 Steel as a Function of Room Temperature R_c Hardness at 700°F.	163
124	Lead ^{ed} σ_{UTS} Versus Non-lead ^{ed} σ_{UTS} at 700°F.	164
125	Lead ^{ed} σ_{UTS} Versus Non-lead ^{ed} σ_{UTS} with Temperature as a Parameter.	165
126	Ratio of R.A. for Lead ^{ed} to Non-lead ^{ed} Material as a Function of Non-lead ^{ed} σ_{UTS} with Temperature as a Parameter.	166

LIST OF FIGURES (Cont.)

Figure		Page No.
127	Vapor Pressure of Lead as a Function of the Reciprocal of Absolute Temperature. (Note Fahrenheit Scale for Reference)	167
128	Atomic Flux to an Internal Surface in Equilibrium with Lead Vapor as a Function of the Reciprocal of the Absolute Temperature. (Number of Monolayers Added for Comparison Assuming $\beta = 1$, $t_m = 100$ sec., and $C_m = 100 \text{ \AA}^2$)	168
129	Parametric Plot of the Average Surface Concentration, C_o , on a Temperature-Time Plot as Obtained from the Expression: $C_o = I_t$. (Note Units of C_o are Atoms/cm ²)	169
130	Vapor Pressure of Mercury as a Function of the Reciprocal of the Absolute Temperature. (Note Fahrenheit Scale for Reference)	170

Section I

INTRODUCTION

1.1 THE PROBLEM

In the thirty years since the beginning of quantity production of leaded, free-machining steels, their use in low strength applications has grown steadily. By switching to leaded, free-machining steels, the production machining rates for larger numbers of parts using automatic or semi-automatic screw machines have been substantially increased with an accompanying decrease in unit cost. However, a number of service failures were encountered during the developmental period for leaded steel melting practice, which were traced to a metallographically "dirty" structure. The lead segregated into long stringers which extended 1/4" or more. Often the structural effect of such a morphology on a finished part was not noticeable, although occasionally it did result in faulty service performance. In one instance, the presence of a lead inclusion near the surface of a diesel injector nozzle resulted in a failure due to the melting of the inclusion. This failure is typical of those seen for "dirty," low-strength, leaded steels produced by improper melting techniques. Current practices for adding lead have essentially eliminated the early processing difficulties caused by gross lead segregations.

The use of lead in alloy steel is relatively recent and the number of applications for this material are increasing. There has been, however, some resistance to the use of any steel not considered "clean" in high strength applications. This is true even though the room temperature tensile, fatigue, and impact properties of leaded steels are similar to those of non-leaded materials at all strength levels. In the cases where leaded steels are used in a moderate to high strength form, unexpected failures by brittle crack propagation may occasionally result. Catastrophic failures in some instances occur during heat treatment and subsequent processing. These failures are not to be confused with those resulting from poor lead morphology and ingot separation. Several examples will serve to illustrate the nature

of this unexpected behavior.

Upon switching to a leaded alloy steel, a die casting firm found extensive die cracking after short service when the moderately elevated temperatures of die casting were reached. A heat treating firm, experiencing heretofore unknown cracking in a spindle subjected to warm-punch straightening after heat treatment, determined that the only change in practice was that a leaded 4140 type had been substituted for the non-leaded alloy used previously.^{1*} Manufacturers of heat treated gears with flame or induction hardened teeth found extensive radial cracking in a leaded alloy steel grade after the hardening treatment.²

1.2 BACKGROUND

The literature is not very enlightening with regard to possible property differences which could have been introduced by the lead addition. Indeed, early investigators confirmed that differences in room temperature mechanical properties of leaded and non-leaded steels (in both carbon and alloy grades) were not statistically significant. Dolan and Price³ summarized these early studies by the producers of leaded steels in 1940 and concluded from them and their own work that the only effect of lead is to improve machinability. Swindon,⁴ however, showed in 1942 that at elevated test temperatures differences in tensile properties were noticeable. Investigating both leaded and non-leaded manganese-molybdenum steel containing 0.36 per cent carbon, heat treated to an ultimate tensile strength of 110 to 130 ksi, he found tensile elongation and reduction of area were somewhat reduced in the temperature region between 500 and 850°F. Reduction of area in non-leaded steel was about twice what it was in the leaded equivalent when specimens were taken parallel to the direction of lead stringers. The values for reduction of area of leaded transverse specimens were a third those of the non-leaded. Nevertheless, tensile and yield strengths were unaffected. Izod impact energy values for both materials decreased with increasing temperature. However, the energy values for the leaded stock were about ten foot-pounds lower than for the non-leaded material from 75 to 958°F. In a discussion of Swindon's paper, W. B. Wragge⁴ referred to the elevated temperature impact data of Nead, Sims, and Harder.⁵ The reported data also

* For all numbered references, see bibliography.

shows a general decrease in impact energy with increasing testing temperature for both the leaded and non-leaded material. As found by Swindon, the differences in impact energy between the leaded and non-leaded steel specimens were about constant over the range of testing temperatures covered. In addition, Wragge presented elevated temperature tensile data on leaded and non-leaded normalized 1020 and 1314 steels with room-temperature ultimate tensile strengths of 60 ksi. Surprisingly, both steels showed about the same ratio of leaded to non-leaded reduction of area, i.e., fifty per cent at 600 to 700°F, as was the case for Swindon's higher strength manganese-molybdenum steel. Since these early studies, a number of investigators have examined the room temperature mechanical properties of leaded and non-leaded steels. Woolman and Jacques⁶ determined many of the important machinability variables and found no significant differences between the two steel types in notched and unnotched tensile and impact tests at ultimate strength levels between 70 and 230 ksi. Fatigue endurance limits were the same for both materials at low strength levels but were seven per cent higher for the non-leaded steel at the 230 ksi strength level.

Weaver⁷ found that the fifteen foot-pound impact transition temperature was 10 to 30°F lower for leaded 1141 and 1050 material than for the non-leaded types. He proposed that this phenomenon was due to the grain refining effect of lead. Room temperature tensile properties of both leaded and non-leaded 1141 and 1050 types of steel were found to be essentially identical.

Recently, a number of comparative fatigue studies have been undertaken on the many leaded grades of commercial carbon and low alloy steels.^{8,9,10,11} All of these fatigue tests, conducted at room temperature, show little or no difference between leaded and non-leaded types in preliminary longitudinal tensile or impact properties. However, transverse tensile properties of both types are considerably lower. Fatigue endurance limits of the two types, tested longitudinally, differ by at most sixteen per cent; both show much lower fatigue limits when tested in the transverse direction.

Although the effect of lead on mechanical properties seems relatively minor, the disparity between the mechanical properties of leaded alloy steels reported in the literature on the one hand, and the service failures traced to changeover to a leaded steel type on the other, has prompted a closer look at the elevated temperature properties of a leaded and non-leaded grade of 4145 steel.

The failures seem to have a common factor: at some time during processing or service, the leaded part had been subjected to stress at an elevated temperature. While Swindon showed leaded steels do have reduced ductility at elevated temperatures, this data would not explain the extensive failure by cracking of leaded steels subjected to service stresses at levels similar to those found safe for non-leaded material. The array of lead stringers parallel to the working direction might well be among the possible causes of the elevated temperature cracking under load. Since the embrittlement is most severe at about 621°F, i.e., the melting point for lead, another possibility is that the expansion of the lead upon melting could act as a stress raiser at the site of the stringers. In addition, the coincidence of the severe embrittlement with the lead melting point strongly suggests that it is a liquid-metal embrittlement phenomenon.

Metallographically, the difference between a leaded and a non-leaded steel is the larger quantity and greater length of hot-processing-oriented stringers in the leaded steel. This detrimental morphology no doubt contributes to the observed property loss at elevated temperature; however, since mechanical properties for leaded and non-leaded materials at room temperature are similar, additional contributory mechanisms are likely.

Poorer elevated temperature properties might result from stress generated in the inclusion cavities due to differences in thermal expansion between lead and steel at temperatures below 620°F and the large expansion accompanying the melting of lead. This effect should be largely obviated, however, by the fact that the volumes containing the lead particles were at high temperatures during previous hot rolling and thus should have already been enlarged plastically by the lead expansion. In addition, subsequent austenization would have further relaxed any size discrepancies between the lead particle and its enclosing steel matrix. Cooling from the high temperature would, if anything, leave the lead particles in a state of hydrostatic tension. Thus, one would not expect that any differential expansion of lead in the steel matrix could account for ductility losses.

The cases of failure cited above suggest that in order to use leaded steels safely the effect of lead in-situ must be defined quantitatively at elevated temperatures. The experimental work in this report has been directed towards defining selected mechanical properties of a leaded and non-leaded alloy steel over an elevated temperature range which includes

the temperature region in which failures have been observed. The effect of lead is then evaluated by a comparison of the properties of leaded and non-leaded steels as a function of temperature.

Section 2

OBJECTIVE

The overall objective of the program is to provide design and materials engineers with information regarding the effect of lead upon the mechanical properties of alloy steels. This objective includes the influence of the intrinsic strength upon mechanical properties of leaded steels and is aimed at understanding unexplained catastrophic failures which have been encountered during the processing and subsequent service. Frequently contractors and sub-contractors producing tank-automotive equipment request permission to use leaded steels for their improved machinability. The design agency can now realistically consider the possibilities of part failures due to the brittleness introduced with the lead additive and make judgments as to equivalency and/or increase inspection requirements.

Section 3

SUMMARY

Leaded (0.30 per cent) and non-leaded ingot material of a 4145 steel were heat treated to room temperature strength levels ranging from 120 to 240 ksi. An extreme brittleness in the steel is encountered when the following conditions are present:

- a) The steel is leaded
- b) The strength of the matrix is high (200 ksi or above)
- c) The steel is in the temperature range of above 400° to 900°F.

Section 4

CONCLUSIONS

A detailed investigation has been made of the influence of 0.30 per cent lead on the room and elevated temperature mechanical properties of a 4145 steel. Leaded and non-leaded versions of this identical steel were quenched and tempered to room temperature strength levels ranging from 120 to 240 ksi. The properties measured included both complete tensile data and impact energies for all strength levels. Macrofractographs detailing differences in fracture morphology at specific test temperatures have also been included.

A comparison of tensile ductility between the non-leaded and leaded steel shows small differences in reduction of area below 400°F or above 900°F. However, between 400 and 621°F, the melting point of lead, R.A. decreases rapidly at all strength levels. Maximum embrittlement occurs at or somewhat above 621°F and its severity is directly related to strength level. Partial losses of R.A. in the temperature range between 621 and 890°F are encountered but at room temperature strengths at and above 200 ksi leaded steels show a complete loss of ductility.

Most of the observations made regarding embrittlement of leaded steel are similar to those reported for surface wetted liquid-metal-embrittlement experiments. The presence of the liquid-metal as a fine dispersion in the steel is believed to magnify any tendency for embrittlement and account for some contradictions in the literature regarding the embrittling effect of surface applied lead on tension or bend specimens. The major difference is that substantial embrittlement is shown to occur well below the melting point of lead in the leaded steel. The explanation of this effect is based on the Stoloff and Johnston theory of liquid-metal-embrittlement which states that a reduction of the binding forces producing cohesion takes place when the embrittling metal atoms are chemisorbed at the crack tip. Thus, the embrittlement observed below the melting point suggests that the transport of these atoms to the crack tip occurs through the vapor phase. The substantial loss in strength and ductility at the melting point of lead is attributed to the mobility of the liquid metal which, by following the growing crack, can expedite atoms transport. The restoration of mechanical properties above

890°F, independent of strength level, is proposed to result from the decrease in sticking coefficient with increasing temperature.

This hypothesis appears more acceptable than the dislocation flow stress theory because of the following: (1) an embrittlement of low yield strength leaded steels, (2) although $\bar{\sigma}_F$ for transverse and longitudinal leaded steel specimens are similar at 900°F, the transverse specimens suffer much larger losses of $\bar{\sigma}_F$ when both are tested in the trough region, and (3) a return of all mechanical properties at the same temperature independent of room temperature strength level.

The apparently anomalous failure of leaded steel parts are thus seen to be a result of thermal or mechanical stresses applied at temperatures between 500 and 900°F. For high strength leaded alloy steel, service or processing stresses in this embrittlement trough cause catastrophic failure by brittle crack propagation. While room temperature properties of these steels are not impaired, the existence of a moderately elevated temperature region where a severe loss in properties is observed should be a serious deterrent to the specification of leaded alloy steels for service much above room temperature.¹

Section 5

RECOMMENDATIONS

It is recommended that the substitution of leaded alloy steel not be made for the non-leaded variety as a routine basis. Consideration of the part and the intensive inspection procedures to insure the freedom from cracks are mandatory. Although only one steel analysis at one lead level has been tested to date in the program the continuing investigation which encompasses other steel types and lead levels as well as other testing methods will aid the materials engineer in specifying alloy steels.

Section 6

EXPERIMENTS AND RESULTS

6.1 MATERIALS USED AND THEIR PROCESSING AND TESTING

A 4145 steel was selected as the base material for the investigation. The steel was obtained in the form of leaded and non-leaded ingots teemed from the same heat and then hot rolled and warm drawn at 650°F into bars of 1-9/16 in. diameter. Chemical analysis of the ingot material was as follows:

	<u>Leaded</u>	<u>Non-Leaded</u>
Carbon	0.46	0.47
Manganese	0.87	0.88
Chromium	0.98	1.00
Nickel	0.15	0.16
Molybdenum	0.15	0.18
Phosphorus	0.014	0.015
Sulfur	0.023	0.022
Copper	0.15	0.15
Silicon	0.33	0.33
Lead	0.30	--

Note that the lead addition is ten to twenty per cent greater than the upper limit for commercial leaded alloy steel. Metallographic specimens were taken only from the "as-received" materials. The inclusion structure of leaded and non-leaded 4145 steel is shown in the photomicrographs in Figures 1 and 2. The non-leaded steel structure contains the processing oriented manganese sulfide stringers surrounding a nucleus of iron and manganese silicates. The leaded steel contains about the same volume of manganese-sulfide and silicates; however, surrounding each of these inclusions is a lead envelope. The average length of the stringer in this case is about 0.006 in. compared to 0.0015 in. for the non-leaded material.

A determination of the actual microchemical constitution was performed using an electron microprobe analyzer. This part of the investigation was carried out using the microprobe analyzer facility at Detroit Arsenal under the

direction of J. Vettraino.¹² The purpose of this investigation was to verify the metallographic analysis of the morphology and distribution of lead and to determine its impurity content. Metallographic specimens were polished in order to preserve the lead inclusions¹³ prior to examination in the probe. The techniques involved in using the probe have been described in some detail by Schreiber.¹⁴ For the leaded steel specimens an electron beam 2.0 microns (8×10^{-5} in.) in diameter was produced. The spectral scans were made using thirty kilovolts. The base line was set to read thirty volts and the channel width value was adjusted to 1.0 volts. This technique will provide an X-ray emission sensitivity of 0.1 per cent. Characteristic X-rays and back scattered-electrons (BSE) produced by the beam were analyzed separately with the aid of the appropriate sensing equipment. Both back scattered-electron scan photographs and characteristic X-ray photographs were obtained. Specific X-rays scans were taken initially for manganese, sulfur, and lead. In the second phase of the study, X-ray scans were made of other trace elements in both the steel matrix and the lead inclusions.

The inclusion morphology of non-leaded alloy steel was indeed verified by the microprobe analyzer. The results of this work are not included here. The inclusion structure of leaded steel was similarly determined by the microprobe. The photographs in Figures 3 and 4 are separate scans across two different inclusions. In each case, back scattered-electron photographs show a heavy element at the inclusion extremities. Characteristic X-ray scan photographs of manganese, sulfur, and lead positively identify the nucleus of the inclusion as predominantly manganese sulfide. The surrounding lead envelope is clearly shown in the lead- M_{α} scan on both of the figures.

In the second phase of the study, the X-ray spectrometers were used to detect differences in trace element composition between the steel matrix and lead inclusion. Analysis for copper, tin, zinc, chromium, nickel, and several other elements of lesser importance were made by this procedure. Since no significant differences were found between the matrix and the lead for any element, the lead inclusion must be considered to have an impurity content, for each element tested, either equal to or less than the amount of that element present in the matrix.

Mechanical properties over the temperature range from 75 to about 900°F were measured on longitudinal and transverse specimens in the "as-

received" condition and after heat treatment to a variety of room temperature strength levels. The heat-treated material was quenched into 140°F oil after a one hour austenitizing anneal at 1525°F. The room temperature tensile strength, σ_{UTS} , and R_c hardness values for "as-received" materials and those produced by tempering for one hour at the indicated temperatures are listed in Table I. A coding system which designates the presence or absence of lead (L and N, respectively) and σ_{UTS} in units of 10,000 psi (or 10 ksi) has been adopted and is indicated in the table; this system is used throughout the remainder of this work.

Both leaded and non-leaded materials were machined into standard longitudinal 0.252 in. diameter tensile specimens (Figure 5) and 0.394 in. Charpy "V" notch impact specimens after all processing. Additional transverse tensile specimens were made in a fatigue configuration having no uniform gage length but having a 0.252 in. diameter in the minimum section (Figure 6). Thermal expansion specimens, 1/4 in. in diameter by 3 in. long, were machined from N20 and L20 material only.

Tensile tests were performed at room and elevated temperature on a hydraulic testing machine equipped with a tube furnace and a controller (Figure 7). Crosshead rates were about 0.05 in./min. during specimen straining in the elastic range. The entire load-deflection diagram for the elastic and the plastic ranges was recorded using a high temperature micro-extensometer and a remote macro-extensometer. The micro-extensometer was attached, by high temperature metal extenders, directly to the specimen, while the macro-extensometer was fastened to the grip extenders outside the hot zone of the furnace. Using this arrangement, the following properties were measured:

1. Young's modulus, E
2. Proportional limit at no offset, σ_{PL} .
3. Yield strength at 0.2 per cent offset, σ_{YS} .
4. Ultimate tensile strength, σ_{UTS} .
5. Fracture stress, $\bar{\sigma}_F$ (fracture load divided by smallest area at fracture).
6. Reduction of area, $R.A.$
7. Elongation, \underline{e} , in a 1.85 in. gage length.

In addition, photographs were made of the tensile fracture surfaces. Impact tests at room and elevated temperature were performed in a calibrated 120 foot-pound machine using standard "V" notch Charpy bars. Specimens were heated away from the machine. When at temperature, they were placed in the anvil of the machine with the aid of fitted tongs and broken (Figure 8). In accordance with ASTM specifications, less than four seconds elapsed between specimen removal and test completion.

Measurements of thermal expansion were made on the leaded and non-leaded material heat treated to a σ_{UTS} of 200 ksi, using a quartz dilatometer (Figure 9). The dilatometer displacement, obtained as a voltage signal from a linear variable differential transformer, was recorded versus temperature on X-Y recorder.

Susceptibility to delayed failure at stresses below σ_{YS} ("static-fatigue") using standard creep rupture facilities was evaluated for standard longitudinal tensile specimens and fatigue type longitudinal (Figure 10) and transverse specimen types (Figure 6). All tests were conducted at $750^{\circ}\text{F} \pm 10^{\circ}\text{F}$ for both leaded and non-leaded materials. At this temperature, the embrittlement is a maximum, but creep flow is quite small. Accurate temperature control was maintained using a control thermocouple near the furnace heating element for a high response, and a thermocouple on the specimen for measurement purposes. Stabilization at 750°F was obtained by manually adjusting the controller in response to periodic measurements of specimen temperature. Once the specimen had reached temperature equilibrium, the desired stress level was slowly applied by lowering the weights and scale pan with a hydraulic jack.

Using the electron microscope, the fracture surfaces of leaded and non-leaded material have been examined to determine fracturing modes for both materials. This work has been carried out by R. Zipp¹⁵ under the direction of W. Warke. A standard plastic-carbon replica technique has been used on a number of tensile specimen fracture surfaces of both leaded and non-leaded material. Repetitive stripping of plastic replicas has been employed to clean the surface of dirt and oxides. A JEM electron microscope has been used for examination and photography of prepared fractography replicas.

6.2 MECHANICAL PROPERTIES

6.2.1 TENSILE TESTS ON LONGITUDINAL SPECIMENS

Longitudinal engineering properties of both the leaded and non-leaded 4145 steels have been determined for specimens in the "as-received" condition and heat treated to the strength levels listed in Table I. Tensile data for leaded and non-leaded steels are plotted in Figures 11 through 60 for the various strength levels as well as for the "as-received" materials. Macro-fractographs of leaded and non-leaded steels at magnifications less than five diameters are included for comparison following tensile data at each strength level.

Heat treatment data are included in Figures 61 through 63. For the lower strength non-leaded materials, there was a slight loss in ductility with little change in σ_{UTS} up to 500°F. Above 500°F, σ_{UTS} decreased uniformly as the ductility, measured by R.A., increased. In the higher strength non-leaded steels, i.e., 200 ksi, losses in ductility were also noted to 500°F. However, σ_{UTS} dropped slightly from its room temperature value. As with the lower strength material above 500°F, σ_{UTS} decreased as ductility increased; above 800°F little changes in ductility were evidenced. Elevated-temperature tensile property data from free machining and alloy steels, reported by Peterson,¹⁵ also showed this decrease in ductility as temperatures were increased from 75 to 400°F.

Above 400°F, 220°F below the lead melting point, ductility losses for the leaded material were evident although σ_{UTS} values were the same for both steel types. At approximately the lead melting point (621°F), or somewhat above, the lower strength leaded steels (120 ksi) showed fifty to sixty per cent less ductility than the non-leaded material. This data on 4145 steel is equivalent to that reported by Swindon for a manganese-molybdenum steel. Higher strength leaded 4145, however, loses all ductility at 621°F. At 900°F, the mechanical properties for leaded steels at every strength level return to those seen for the equivalent non-leaded steel.

The extent of the leaded steel embrittlement and its dependence on strength level is most easily demonstrated by comparing reduction of area, R.A., for the leaded and non-leaded types over the range of strength levels tested.

A plot of R.A. for each of the heat treated steel types is given in Figures 64 and 65 and a ratio plot of leaded R.A. to non-leaded R.A. as a function of test temperature is shown in Figure 66. For the temperature range from room temperature to 400°F and also the range above 900°F, the lead addition has little or no effect. The ratio plot, however, indicates an embrittlement range between 400 and 900°F, this range can be divided into two regions, one below and one above the lead melting point. Between 400 and about 620°F, there is a rapid loss in ductility at all strength levels. From 620 to 890°F, embrittlement is maximum but there appears to be three groupings of strength levels on the basis of per cent of R. A. loss. High strength materials, i.e., 240 to 200 ksi, show a zero ratio. For low to intermediate strength levels, i.e., 120 to 160 ksi, the ratio is about 0.4. Above 160 ksi there is a rapid change from the moderately embrittled condition to the zero ductility situation. Plots of elongation, e , in Figures 67 to 69 show essentially the same effect of strength level on the extent of the ductility trough. Reduced ductility above the lead melting point is also accompanied by substantial decreases in fracture strength. This loss in strength due to lead is seen in Figures 70 through 75 which are individual and ratio plots of σ_{UTS} and $\bar{\sigma}_F$, respectively, as a function of test temperature. Ultimate strength ratios show losses only above the lead melting point and then only for high-strength materials having no ductility in this region. Fracture strength ratios, which reflect R.A. losses in the leaded material, show substantial embrittlement even below 621°F and, unlike σ_{UTS} , $\bar{\sigma}_F$ losses are apparent for low strength materials. Above 621°F the lowest value of $\bar{\sigma}_F$ or σ_{UTS} for the high strength L24 leaded material was 103 ksi, compared to N24 non-leaded values of 260 ksi and 175 ksi for $\bar{\sigma}_F$ and σ_{UTS} , respectively. Measurements of σ_{YS} and σ_{PL} , shown in Figures 76 to 79, show that the gross transition from elastic to plastic behavior is not noticeably influenced by the lead addition.

Elastic modulus, E , was measured for all specimens; however, no significant differences were found between leaded and non-leaded steels at any strength level. The data for the "as-received" material only, are shown in Figures 13 and 16 for comparison.

In addition to the standard tensile bar used for these tests, Figure 5, a number of leaded and non-leaded fatigue type longitudinal tensile specimens (Figure 10) were also tested at 75 and 750°F. Two strength levels were used,

200 and 220 ksi, to determine initial property data on this specimen geometry necessary for static fatigue testing. A property comparison for the two longitudinal specimen types is given in Table 2. This table also contains data on the transverse tensile specimens pertinent to the static fatigue program.

6.2.2. IMPACT TESTS

The effect of test temperature on Charpy "V" notch absorbed energy is plotted in Figure 80 for the high-strength level leaded, L20, and non-leaded, N20, material. The leaded steel is of slightly lower toughness at room temperature, and there is a slight increase in toughness for both types as test temperature is increased up to 550°F. In the temperature range of 550 to 621°F, the leaded material shows a rapid loss in toughness. At the higher temperature, the leaded material absorbs twelve to fourteen foot-pounds compared to 27 to 30 foot-pounds for the non-leaded steel. Above 720°F the leaded material shows little change in absorbed energy. However, impact energy of the tougher non-leaded steel decreases continually with increasing temperature above 720°F. Although the ratio of leaded to non-leaded impact energy increases from the minimum value of 0.44 at 720°F, there is no return of properties at temperatures above 900°F in contrast with the recovery of tensile ductility at this temperature for tensile properties. Impact curves at higher strength levels show a greater maximum loss in toughness, i.e., 0.39 for the L24 as compared to N24 steels, Figure 81, but the general features of the impact energy-temperature plot are similar to that of the 200 ksi steel. In comparatively low strength alloy steels, e.g., 140 ksi tensile strength, the sharp ductile-to-brittle transition just below the lead melting point is absent, Figure 82. Absorbed energy values for the low strength material are lower than those for non-leaded type above 621°F and equal to or slightly higher than non-leaded below 621°F. For an intermediate strength steel, e.g., L18 and N18, Figure 83, the embrittlement is still quite evident above 621°F. The ratio plot for all strength levels tested appear in Figure 84. It is interesting to note that Charpy curves for the low strength 4145 material are similar to Swindon's results on the intermediate strength manganese-molybdenum steel.

6.2.3. TENSILE TESTS ON TRANSVERSE SPECIMENS

Tensile properties of fatigue type transverse specimens heat treated to the strength levels listed in Table 1 are plotted in Figures 85 through 97. A comparison of room-temperature σ_{UTS} values for non-leaded 4145 shows that transverse specimens are generally about 20 ksi higher than equivalent longitudinal ones (see Table 2). σ_{UTS} values of leaded transverse specimens are equal to those obtained on equivalent longitudinal specimens above 200 ksi. Below this strength level, transverse σ_{UTS} values are about 15 ksi greater than those for the equivalent longitudinal specimens. The fatigue type transverse specimen configuration, which accounted in part for the increased σ_{UTS} of non-leaded material, did not permit measurement of \bar{E} or \bar{e} . Nevertheless, the elastic extensometer was used on all specimens and the value of total elongation to fracture, $\bar{\delta}$, was recorded. A plot of $\bar{\delta}$ rather than \bar{e} is, therefore, included on the figures showing transverse properties. Ductility, as measured by R.A. and $\bar{\delta}$, at all strength levels was quite low for both leaded and non-leaded material. At 200 ksi and above, leaded material showed less than one per cent R.A. at all testing temperatures. Fracture strengths were much closer to ultimate tensile values and were thus included on the plot of common engineering tensile properties. Values of σ_{YS} at 0.2 per cent offset were not obtained due to the inability to measure \bar{e} on a fatigue type specimen. Autographic records obtained on fatigue type transverse specimens were quite different from those obtained on either standard or radiused longitudinal test bars. Figures 98 through 109 are autographic engineering stress-strain and stress-deflection plots, obtained on standard longitudinal, fatigue-type longitudinal and fatigue-type transverse tensile specimens pulled at room temperature and selected elevated temperatures. First, these figures show that a fatigue type specimen has less ductility than a standard uniform gage length type. In addition to this expected constraint effect, high strength leaded transverse specimens show no measurable flow prior to brittle fracture in the embrittlement trough region of temperature. Fracture strengths of leaded transverse specimens in the trough region (Table 2) are also considerably lower than equivalent longitudinal specimens.

The lower ductility of the non-leaded transverse specimens compared with longitudinal ones is, therefore, a result of both the notch constraint in the non-uniform cross-section bar and to the effect of testing perpendicular to the

processing-oriented stringers. In leaded transverse specimens, ductility values at room temperature are lower than non-leaded transverse specimens because of the greater size and larger number of inclusions. At temperatures in the embrittlement trough, i.e., 700°F, the effect of lead, as well as the unfavorable inclusion orientation, further reduces the ductility of the leaded transverse specimens. However, the already low ductility masks this additional loss, due to lead. Thus, the effects of lead are less evident on a ratio plot of R.A. than for longitudinal specimens. The combined effects of notch constraint, stringer orientation, and lead embrittlement reduces the strength of leaded transverse specimens in the embrittlement range to half that of equivalent longitudinal specimens.

6.2.4 THERMAL EXPANSION

Determination of dilatometric expansion was carried out on high strength, L20 and N20, leaded and non-leaded steels up to 900°F. The value of α , the linear coefficient of thermal expansion was $6.9 \mu\text{-in./in./}^\circ\text{F}$ for the leaded material and $7.0 \mu\text{-in./in./}^\circ\text{F}$ for the non-leaded steel, Figure 110. Errors are generally about \pm five per cent for the dilatometric method of measurement so that these values can be considered identical. There were no anomalous slope changes at any temperature, including 621°F, the lead melting point, for either steel. The values of α agree closely with reported values for steels of this carbon and alloy content.

6.2.5 STATIC FATIGUE

The results of static fatigue exposure using radiused longitudinal specimens of L20 and L22 steel are shown in Figures 111 and 112. Stress levels up to the engineering yield point, determined from Table 2, were used in this test program. Due to the change in specimen geometry there were slight changes in properties as noted in the table. At room temperature for both steel types there is little difference in σ_{UTS} , $\bar{\sigma}_F$, and σ_{PL} , between the fatigue type specimens and those tested earlier with a uniform gage length. However, there is a three to five per cent R.A. decrease for all materials. At 750°F, the non-leaded radiused specimen shows an increased σ_{UTS} and σ_{PL} . There is the expected decrease in R.A. but no change in $\bar{\sigma}_F$. For radiused leaded steel specimens at 750°F, R.A. drops to zero, while σ_{UTS} is higher for both

strength levels than for uniform gage length specimens. The specimen fractures essentially without plastic flow so that a proportional limit cannot be detected. The L22 material failed in a brittle manner at 123 ksi. The L20 material also fractured with nil ductility at 142 ksi. Thus, when a comparison is made with uniform gage length specimens having equivalent intrinsic strengths, the change in configuration is seen to account for an increase in σ_{UTS} of more than 20 ksi for leaded material at both strength levels in the trough region.

For both strength levels, the lengths of exposure time to fracture varied from seconds to several hundred hours. There were, however, only small differences in stress between similarly exposed specimens that differed in time-to-fracture by several orders of magnitude. For the lower strength leaded steel, e.g., 200 ksi (Figure 111), a stress level of 130 ksi resulted in fracture at 750°F in less than a minute. At 120 ksi, the specimen lasted several hundred hours. The higher strength leaded steel, 220 ksi (Figure 112), was more susceptible to delayed failure than the 200 ksi material and showed delayed failure in less than a minute when the exposure stress at 750°F was 120 ksi. A static stress level of 105 ksi produced fracture only after more than 300 hours.

Comparison of time to failure in static fatigue for the two strength levels shows that the higher intrinsic strength steel failed in shorter times at a given stress level than did the lower intrinsic strength material. This is typical of the static fatigue behavior of liquid metal embrittlement couples.

Exposure of similarly heat treated, fatigue type transverse leaded specimens was also attempted at stress levels within seven per cent of the fracture stress, Table 2. Surprisingly, no delayed failures were noted although the inclusion orientation effect, observed in tensile tests, was substantial. Apparently the lower maximum stress level used for the transverse specimens was not sufficient to initiate flow and fracture.

6.3 FRACTOGRAPHY

6.3.1 MACRO-FRACTOGRAPHY

Fractographically, the embrittlement effect of lead is most easily seen

for longitudinal tensile specimens. However, each of the three testing modes — longitudinal tensile, transverse tensile, and impact — produced a different type of fracture appearance. Both transverse tensile and impact fracture surfaces showed no differences between leaded and non-leaded steels even in regions of severe embrittlement. Transverse tensile fractures always showed a "woody" appearance at all test temperatures for both steels at all strength levels, Figure 113. As test temperatures are increased, impact fractures of both steels did change from the more flat fracture to one that contained an exaggerated shear lip, Figures 114 and 115. Note that the leaded material also shows shear lip fractures at embrittlement temperatures even though the absorbed energy is comparatively low.

The longitudinal tensile fracture appearance of non-leaded alloy steels has been described in detail by Larson and Carr.¹⁷ Their nomenclature has been adopted here to classify various fracture areas for both steel types. At low temperatures, below 400°F, leaded and non-leaded steel fracture appearances are similar and typical of 4145 behavior generally, e.g., Figure 34. These fractures, denoted radial, propagate from an approximately central region of fibrous appearance. There is a minimum of sheared cup and cone area. From 400 to 600°F, the non-leaded material loses the radial appearance in the flat fracture region and gains additional shear area. Leaded steel fractures in this temperature range have a large number of quite small, about 0.010 in., flat fracture areas surrounded by a matrix of sheared material. Surrounding this region are the more familiar shear surfaces typical of tensile fracture; these occupy about one fourth the total fracture area. At 621°F and above, non-leaded steel, while increasingly more ductile, has about the same ratio of cup and cone shear area to flat fracture area. Leaded steels, which are quite brittle in this region, show one or more of the large flat fracture areas, called "fish-eyes," which approximate the small flat fracture areas seen below 621°F at low strengths. A closer examination of the large flat "fish-eye" area shows a small orange or golden-brown colored area which is apparently the origin of fast crack propagation. This small area, generally near the specimen surface, has a number of streaks emanating from it into the main flat area. It is this small spot that appears to be the lead affected initiation and slow crack growth site. Above 900°F leaded and non-leaded steels have an identical cup and cone fracture appearance.

6.3.2 ELECTRON FRACTOGRAPHY

A determination of fracture morphology in the region of embrittlement was undertaken by R. Zipp as an electron fractographic study in partial fulfillment for the Master of Science degree in metallurgical engineering. In order to simplify the electron microscope study, each of the fracture types described in the macro-fractography section was given a specific designation by Zipp, viz:

- 1) Low temperature "cup-and-cone" (A)
- 2) Rough, golden-brown, little shear lip (B)
- 3) Small, golden-brown "fish-eyes" on shear surface (C)
- 4) One "fish-eye" surrounded by shear lip (D)
- 5) High temperature "cup-and-cone" (E)

These classifications are illustrated in Figures 116 and 117. Fractographs demonstrating the more pertinent fracture types are reproduced in Figures 118 through 122 with the permission of R. Zipp. The fractographs that have been included are related to proposed mechanisms of embrittlement covered in the discussion chapter.

For the non-leaded steels at all strength levels, a change from A to E fractures occurred at about 550°F. While no other listed types of fracture occurred, A fractures near 550°F exhibited very large shear areas. Starting at about this temperature, a rapid rise in ductility was evidenced and the change to the E fracture type was seen.

Leaded steels tested either above or below the embrittlement trough show identical micro-fracture appearance to non-leaded material. Electron fractographs taken of fracture surfaces of leaded material tested at embrittlement temperatures below 621°F show that an intergranular fracture surface is associated with an inclusion. The extent of the embrittlement effect is a function of temperature. Since lead has been shown to be an integral part of most inclusions, it appears that lead is associated with intergranular fracturing. At temperatures above 621°F, the area of brittle fracture is greater and specific inclusions that were the origins of fracturing cannot be found.

Strength level does not influence the type of embrittlement, only its extent. Indeed, extensive fractographs of leaded steel specimens tested in the trough region all showed an intergranular fracture mode in the vicinity of the inclusion, irrespective of strength level.

Section 7

DISCUSSION

A number of observations concerning the embrittlement of leaded steel are similar to those previously reported for surface-wetted liquid-metal embrittlement experiments. In particular, the complete loss of tensile ductility above the lead melting point for high strength leaded steels strongly indicates that the embrittlement is caused by the liquid lead. The major difference between the present work and that reported for surface-wetted experiments is that substantial embrittlement is observed below the lead melting point. The explanation of this effect requires a review of liquid-metal-wetted observations with attention to the mechanisms involving the transport of the low-melting metal and its interaction at the crack tip in the high melting metal.

Typical features of liquid-metal-wetted experiments are: 1) a limited range of temperature where severe embrittlement occurs extending from above the melting point of the embrittling liquid to some higher temperature where the brittle behavior disappears and the ductility returns; 2) a lowering of the elevated temperature ductility and fracture strength with an increase in room-temperature ultimate tensile strength; 3) minimized embrittlement at high strain rates; 4) delayed failures at static stress levels below the yield stress in the brittle temperature region, i.e., static fatigue; and 5) a more effective embrittlement with increasing grain size, all other factors being equal.

Specific evaluation of the embrittlement effect of wetted liquid lead on steel is incomplete. It was reported by Rostoker (Ref. 18, p. 30) that a heat treated alloy steel, at a hardness of 45 R_c , was unaffected by lead when tested at 380°C (716°F) and he concluded that the two materials could not be classified as an embrittlement couple. On the other hand, Russian investi-

gators¹⁹ observed a reduction of tensile properties in heat treated steel similarly exposed to lead. At a strength level of 170 ksi, lead was reported to have caused a substantial loss in ductility. The disparity between Rostoker's data and those reported by the Russian investigators is possibly one of degree. The test criteria for effectiveness used in Reference 18 were based on large losses in ductility; small effects were ignored.

7.1 SIMILARITIES OF LEADED STEEL DATA TO LIQUID-METAL-WETTED OBSERVATIONS

First, the severe tensile embrittlement was largely confined to a particular temperature region: 621 to 900°F. Tensile properties at test temperatures below 400°F were relatively unaffected by the presence of lead.

Second, unstressed exposure in the embrittlement temperature range did not change mechanical properties upon subsequent testing at other temperatures.

Third, above 900°F there was a complete recovery of ductility. This return of ductility above some temperature is common to this type of embrittlement and is denoted as the "brittle-to-ductile transition temperature."

Fourth, within the embrittlement region, leaded steels of higher intrinsic strength* showed greater losses in tensile strength. As is typical of liquid-metal-embrittlement, the higher the intrinsic tensile strength the lower was the fracture strength.

Fifth, the toughness of leaded steels, determined in impact testing, drops severely in the temperature range above 600°F. As was the case with fracture strength differences, toughness differences between leaded and non-leaded steels, tested in the embrittlement region, are larger at higher intrinsic strength levels. However, the toughness losses in impact testing begin closer to the lead melting point than the onset of embrittlement observed in tensile testing. The effect of lead in the high strain rate impact tests is apparent

* The intrinsic strength of the leaded steel is considered to be the σ_{UTS} of non-leaded steel; hence, the matrix of the leaded type.

only at temperatures about 50°F below the lead melting point compared with more than 200°F for slow strain rate tensile tests. Although Charpy impact data does indicate some strain rate sensitivity, the embrittlement is still substantial. This is at variance with high strain rate data for a number of liquid-metal wetted systems, reported by Rostoker (Ref. 18, p. 49), which shows a much reduced embrittlement.

Sixth, the tendency, although slight, for static fatigue failure also is in keeping with liquid-metal-wetted experiments.

Seventh, electron fractographs of leaded steel which demonstrate brittle intergranular failures around inclusion sites are similar to observations made on the fracture surfaces of many specimens broken in the presence of an embrittling liquid-metal.

A standard method of demonstrating the effect of an embrittling metal, i.e., lead, is to plot room temperature R_C hardness versus elevated temperature σ_{UTS} for both leaded and non-leaded steels at a specific temperature in the embrittlement region, e.g., 700°F, Figure 123 (compare with Figure 4.10, Ref. 18). Each pair of leaded and non-leaded specimens was given identical quenching and tempering to achieve the same R_C . Below 38 R_C , the σ_{UTS} for the two steels are identical, but as hardness increases, the leaded curve deviates sharply from that of the non-leaded steel. The leaded specimens fail in a brittle manner, never achieving the intrinsic load bearing capacity of the matrix. This plot is typical of data indicating susceptibility to liquid metal embrittlement. Since hardness in this case has only been determined at room temperature, a more meaningful plot is obtained in terms of intrinsic strength determined at test temperature, i.e., non-leaded σ_{UTS} versus leaded σ_{UTS} at a given testing temperature. The curve for 700°F (equivalent to the curve in Figure 123) is shown in Figure 124. At this temperature leaded σ_{UTS} values equal non-leaded σ_{UTS} values up to 140 ksi. When compared to non-leaded steel, the leaded material shows a loss in ultimate tensile strength in the range between 140 and 165 ksi. As intrinsic strength in leaded material is increased above 165 ksi, there is a rapid decrease in corresponding ultimate tensile strength. It should be noted that in this temperature region, leaded σ_{UTS} equals leaded $\bar{\sigma}_F$ since there is essentially no reduction of area. The

effect of test temperature on the relationship between intrinsic strength and ultimate strength is shown in Figure 125 for several test temperatures.

These curves show that leaded and non-leaded values at all temperatures, except those found in the embrittlement trough, lie in a single scatter band around the 45° line where leaded σ_{UTS} equals non-leaded σ_{UTS} . For temperatures in the embrittlement region, increases in intrinsic strength result in decreases in ultimate strength of the leaded steels, similar to those shown in Figure 125. The effect of intrinsic strength level on ductility, as measured by the ratio of leaded R.A. to non-leaded R.A., is shown in Figure 126 for the same temperature parameters used in Figure 125. Note that the ductility of equivalent but low intrinsic strength leaded steels is still seriously lowered at temperatures in the trough region.

7.2 DISSIMILARITIES OF LEADED STEEL DATA TO LIQUID-METAL-WETTED OBSERVATIONS

First, though most of the data for temperatures above the lead melting point are similar to data for an externally applied liquid metal on other metal systems, the literature does not clearly define lead as an effective embrittling agent on steel. The experiments by Rostoker, et al¹⁸ indicate that high purity lead does not have any effect on steels at high strength levels. On the other hand, those of Potak, et al¹⁹ indicate that externally applied lead (of unreported purity) has some effect on ductility. While it is well known that alloys of lead, notably solders, cause substantial liquid-metal embrittlement (Ref. 18, p. 6), chemical analysis of the lead inclusions, using the microprobe analyzer, does not indicate the presence of any of these elements. The sensitivity of this instrument assures that the quantities of embrittling metals present in the lead are smaller than those reported to cause embrittlement.

Second, at temperatures ranging as much as 200°F below the lead melting point, substantial ductility losses are observed. This differs from observations made on liquid-metal-wetted tensile specimens, which show that, in order for embrittlement to occur, a sufficient supply of liquid metal must be available to supply the extremities of the growing crack.

Third, the reduced impact toughness of the leaded steel compared to non-leaded steel at temperatures in the trough region are not in keeping with the high strain rate recovery of ductility reported for liquid-metal-wetted experiments.

Fourth, the relatively high level of stress required to cause static fatigue failure, at temperatures where embrittlement is maximum in the tensile test, is not typical of the liquid-metal-wetted data reviewed to date.

The above differences between usual liquid-metal-embrittlement phenomena and those found on leaded steels may be due to the differences in availability of the embrittling agent to an area containing or generating defects. In leaded steels, inclusions, which are the nuclei for crack generation, are also the location of the embrittling medium. It is assumed that effects which are not manifested at temperatures below the melting point and at high strain rates, for usual liquid-metal-wetted experiments, can appear when the embrittling metal is finely dispersed in the metal matrix.

The fact that leaded steels are degraded well below the lead melting point, i.e., at 400°F, is the most important difference between liquid-metal-wetted experiments and those reported here. The only difference between the two experimental methods is that the embrittling metal in leaded steels is in intimate contact with the matrix and finely dispersed throughout. This difference in location of the embrittling metal suggests a number of possible causes for the anomalous low temperature behavior.

If the lead is alloyed with trace elements, either present in the lead prior to addition or scavenged from the steel during solidification, the alloy might be responsible for the embrittlement effect not seen for lead alone. The onset of embrittlement at lower temperatures could occur as a result of the alloy having a lower melting point than lead. Not only does the macro- and micro-chemical analysis of the alloy steel make such a situation unlikely, but if a much lower melting alloy were present, the complete loss of tensile ductility at the melting point of pure lead would then be coincidental. In addition, the beginning of extensive migration of lead does not occur below 621°F as shown by the electron fractographs taken above and below this temperature. These low temperature fractographs indicate that only the immediate site of the lead inclusion is embrittled. Fractographs above 621°F are not associated

with any specific inclusion as would be expected for a completely liquid embrittling agent.

It is well known that steels with a relatively large percentage of inclusions have poorer tensile properties than clean steels of similar composition. Thus, at temperatures below the lead melting point, the "dirtier" leaded steel has poorer properties than the non-leaded steel as a result of both an inferior inclusion morphology and the effect of solid lead on tensile fracturing. In a tensile test on ductile material, the slip or shearing deformation common to metals is accompanied by the formation of microscopic voids. These voids occur at discontinuities in the metal matrix, e.g., inclusions, where flow is impeded.^{20,21} Once the tensile strain becomes localized in necking, both the size and number of voids increases in the minimum section. As the true stress level increases, the isolated voids join to form a macroscopic crack. Ductility losses in leaded steels below 621°F could result from a lowering of the energy necessary for this crack formation process or the replacement of normal tensile fracturing by a completely new lower energy process. The onset of this crack propagation localizes further plastic flow to the region of the crack tip until complete separation. It is proposed by the author that solid lead in the inclusion cavities is transported to the high strain region where crack formation occurs, reducing flow and encouraging slow intergranular crack growth after gross tensile strain becomes localized in necking and stresses become critical. Electron fractographs taken of leaded steel tensile specimens broken below 621°F, which show that intergranular fracturing is localized to the region of the inclusion, indicate that the above conclusion is likely. The mechanics of transport and the interaction at the crack tip are covered in the following paragraphs.

7.3 MECHANISMS OF LIQUID-METAL-EMBRITTLEMENT

Recently several mechanisms describing the role of liquid metal in producing embrittlement have been postulated. Stoloff and Johnston²² proposed that a stress, σ_F , necessary to extend a crack in a liquid metal environment be calculated on the basis of the rupture of atomic bonds by tensile stresses at the crack tip.

This assumption results in an expression for σ_F in which a surface energy term, γ , is multiplied by a dimensionless ratio proportional to the energy of plastic deformation. This expression is clearer than earlier ones describing the mechanism of embrittlement, which involved the addition of a relatively small surface energy term to a much larger plastic deformation energy term. In describing the actual atomic interaction, Westwood and Kamdar²³ suggested that the liquid metal atoms were chemisorbed at sites of high strain concentration and, thus, caused a localized reduction in cohesion. The two areas suggested as likely for strain activated chemisorption were those of high dislocation density, where crack nucleation might be facilitated, and at the tip of an initiated crack, where propagation would be enhanced.

A review of typical liquid-metal-wetted observations indicates that the liquid metal enters a deformation or flaw initiated crack and penetrates to the region of the crack tip. Since the contact angle in the couple system is generally greater than zero, the liquid metal cannot penetrate to the exact site of new surface formation and thus there must always be a small amount of vapor present in the cavity. In order to cause embrittlement, then, the fusible metal atoms must migrate to the area where solid metal atoms are being separated. The appearance of embrittling metal atoms at the crack tip can occur as a result of either surface diffusion or vapor condensation from the exposed liquid. While no experimental evidence of surface diffusion has been presented as yet, experiments have shown that the vapor phase of an embrittling metal, alone, can lower the ductility of the couple metal (Ref. 18, p. 24). Observed cracking rates, though, are much lower than in the case where the liquid itself contacts the site of cracking. However, neither the physical or chemical interactions between the two metals nor the transport of the embrittling metal atoms to the area of the crack tip are well defined.

In addition to the uncertainty regarding the atomic interaction that results in embrittlement, there is still speculation as to the nature of the "brittle-to-ductile" recovery in the presence of the embrittling liquid. The prevailing mechanism suggests that this recovery comes about because of large changes in the dislocation flow stress, σ_D (Ref. 18, p. 115). It is stated that at embrittlement temperatures σ_D is large compared with the fracture stress σ_F , determined from the surface energy term γ . The rapid decrease in σ_D with

increasing temperature, compared to σ_F , results in a crossover temperature above which flow can occur prior to fracture (Ref. 18, p. 75). Although numerical values for either σ_F or σ_D are not available, it is assumed that the brittle-to-ductile transition occurs when σ_D falls below σ_F .

This mechanism is not completely satisfactory to explain the experimental results obtained on leaded steel, Figure 126. First, Figure 126 shows that leaded steels heat treated to low strength levels, while not totally brittle, have considerably lower ductility in the trough region than at temperatures above or below this region. Second, electron fractographs indicate that this lower ductility is associated with brittle crack extension from the lead inclusions (as was the case for higher strength steels tested between 400 and 600°F) and not a change over to a ductile fracture mode. Lastly, the fact that the temperature at which recovery occurs is independent of strength level is not consistent with a single valued flow stress criterion for embrittlement.

It is expected that the role of intrinsic strength or flow stress in determining the degree of ductility loss has not been determined from surface-wetted experiments because of the nature of this test. For these experiments, materials which exhibit ductility values different from zero, show substantially no effect of the liquid-metal due to the restriction of brittle crack extension to the surface region alone.

7.4 ATOM TRANSPORT TO THE CRACK TIP

At temperatures below the melting point, gross mass flow of the liquid is impossible and indeed no embrittlement reported below the fusible metal melting point has ever been considered credible. The observed ductility losses, in the present work, at temperatures below the lead melting point strongly suggests that the fine dispersion of lead throughout the steel matrix provides an appreciable source of lead to the newly forming crack through the vapor phase. It is proposed that the decrease in ductility with increasing temperature up to the lead melting point is related to the rising vapor pressure of lead with increasing temperature. In the times to fracture typical of the tensile test, an equilibrium of lead vapor cannot be established due to the kinetics of the solid-to-vapor phase change. Thus, the extent of embrittlement would then be a function of

the concentration of lead atoms present at micro-crack nucleating sites. Once the lead melting point is reached, however, the liquid lead can follow the growing crack and the concentration of lead vapor approaches equilibrium more rapidly due to the smaller void between the crack tip and the supply of lead atoms. The mobility of the liquid maintains this small void near the crack tip resulting in the greatest loss in ductility at or somewhat above the melting temperature. Above the lead melting point, the phenomenon thus appears to be quite similar to that of surface applied liquid-metal embrittlement experiments where the liquid metal can follow a surface generated crack. Below 621°F, the dispersion of lead in areas where cracks are being generated results in a loss of properties due to an accelerated effect of vapor transport to uncontaminated surfaces. This loss in ductility has not been reported in the literature describing experiments in the general field.

The return of ductility at elevated temperatures has been attributed to the decrease, with increasing temperature, in energy necessary to cause dislocation motion (Ref. 12, p. 115). Assuming, however, that vapor transport of fusible metal atoms to the crack tip is responsible for the observed embrittlement, both the low temperature loss in ductility and the apparently anomalous return of properties at elevated temperatures are at least qualitatively predictable from the kinetics of the vapor-solid interaction as a function of temperature. Although the degree of embrittlement most likely depends upon the extent and exact nature of surface coverage, e.g., adsorbed population and condensate morphology, a less detailed model is sufficient to demonstrate the probability of vapor interaction embrittlement. Using such a model, it is assumed that the lead atoms, adsorbed or condensed on a clean surface, are uniformly distributed then the average surface concentration of lead atoms covering a given surface area, per unit time at a specific temperature, is a function of two variables; the number of atoms striking the surface per unit time and the probability that the atoms will remain on the surface. Under isothermal conditions, the flux is directly related to the vapor pressure at the temperature of interest.

The vapor pressure of lead as a function of temperature is given by:
 $\log P = 5 - 10^4/T$, where P is the vapor pressure in atmospheres, and T is the

absolute temperature in degrees Kelvin (see Appendix 1 and Figure 127). This expression is reasonably accurate over the temperatures interest in this work. There are no discontinuous changes from room temperature to temperatures well above the lead melting point. On the other hand, the probability of capture for an atom striking a clean surface decreases with increasing temperature.²⁴ The theoretical probability, α_c , of an atom striking a surface and then being incorporated is low at high temperatures, but cannot be measured quantitatively. However, the macroscopic sticking coefficient, β , i.e., the total mass on the surface at the end of the experiment divided by the total mass impinging during the experiment, can be determined. This macroscopic sticking coefficient, β , while not well defined numerically for lead on iron, has always been shown, both theoretically and experimentally, to decrease to very small values with increasing temperature and increasing residual gas pressure for other systems including metals.^{25,26,27,28} The availability of lead atoms and the probability of adsorption determines the presence or absence of the surface concentration assumed to be required for embrittlement. At low temperatures, even though β has a relatively high value, P is too low to supply sufficient lead atoms for embrittlement. As temperature is increased, P increases such that some embrittlement can occur. Since the crack extends in a near perfect vacuum, the lead vapor saturates the area of the growing crack very rapidly. At high temperatures, although P continually increases with increasing temperature, β decreases rapidly to very small values. Thus, at these higher temperatures, the high kinetic energy of the lead atoms causes β to approach zero. While a large number of lead atoms are available, none remain long enough to cause embrittlement by interaction with the growing crack. This results in the brittle-to-ductile recovery at elevated temperature. Verification of this approach is difficult experimentally due to an inability to evaluate β to the accuracy necessary to determine whether embrittlement will occur. If for convenience, however, we assume β to be near unity, the likelihood of a vapor transport mechanism is predictable simply from an examination of the surface flux of lead atoms at temperatures in the embrittlement region. It can be seen from the following calculations that the probability of embrittlement by the vapor phase would remain essentially unchanged if β were assumed to be of the order of 0.1.

A calculation of the probable surface concentration in the embrittlement region under isothermal conditions can be made using the ideal gas law, which is applicable at these low pressures, and kinetic theory which states:

$$I = P/(2\pi mkT)^{1/2} \quad (1)$$

where: I = flux of atoms to the surface
(particles/sec/cm²)

m = number of grams per atom
= $\frac{\text{atomic weight (grams/mole)}}{\text{atoms/mole}}$

$$= 207.2/6.03 \times 10^{23}$$

$$= 3.43 \times 10^{-22} \text{ grams/atom}$$

P = equilibrium vapor pressure (dynes/cm²;
1 atmosphere = 10^6 dyne/cm²)

k = Boltzmann's constant
= 1.38×10^{-16} ergs/atom/°K

T = Temperature (°K)

Rewriting (1) in terms of the vapor pressure in atmospheres we obtain:

$$\begin{aligned} I &= 10^6 P / (2\pi \times 3.43 \times 10^{-22} \times 1.38 \times 10^{-16} T)^{1/2} \\ &= 1.823 \times 10^{24} P / (T)^{1/2} \end{aligned} \quad (2)$$

Substituting the expression for P as a function of T (Equation 6, Appendix I) we obtain:

$$\begin{aligned} I &= 1.832 \times 10^{24} \times \frac{10^5 \times 10^{-10,000/T}}{\sqrt{T}} \\ &= 1.832 \times 10^{29} \times \frac{10^{-10,000/T}}{\sqrt{T}} \end{aligned} \quad (3)$$

Taking logs this expression can be written as:

$$\log I = \log 1.832 + 29 - 10^4/T - 1/2 \log T \quad (4)$$

Over the temperature range from approximately 100 to 1,000°F (300 to 800°K), the term $1/2 \log T$ varies from 1.24 to 1.45 while the term $10^4/T$ varies from 33 to 12.5. Thus, a plot of $\log I$ versus $1/T$ will yield an approximately straight line, Figure 128.

If we assume that the tensile test takes place in a time period, t_m , of the order of 100 seconds, the surface concentration in atoms per cm^2 , C_o , can be calculated from:

$$C_o = t_m I \quad (5)$$

This allows Figure 128 to be used to determine the assumed surface concentration as a function of temperature. It should be pointed out that the calculated surface concentration is an average value and neglects the known adsorbed condensate equilibrium reactions. For example, when I is 10^{12} atoms/ cm^2/sec , C_o is 10^{14} atoms/ cm^2 . In the embrittlement region, i.e., 400 to 900°F (487 to 764°K), I varies from approximately 10^9 to 10^{16} atoms/ cm^2 . Assuming the degree of embrittlement is related to how much of the available surface area is covered with lead atoms, a calculation must be made of the number of atoms that cover the total area; e.g., the number of atoms required in a cm^2 to obtain an average monolayer. An estimate of the number of monolayers, M_o , can be made by examining the relative sizes of the lead and iron atoms. For iron the close packed spacing is approximately 2.5 \AA while for lead this distance is 3.5 \AA . Considering primary binding alone, the monolayer formed can be assumed to be made up of lead atoms spaced 10 \AA apart. The value of C_o for a monolayer, C_m , would then be 10^{14} atoms/ cm^2 . If secondary interactions are considered, this spacing would be somewhat greater. Thus, in Figure 128, one of the ordinates is labeled M_o and the number of monolayers at any temperature can be estimated.

The assumption of t_m equal to 100 seconds predicts that a complete monolayer will be formed at 600°F in the time period of the tensile test. The

loss in ductility observable at 400 to 500°F suggests that embrittlement occurs before a complete monolayer is attained.

Observations of the way in which foreign atoms cover a clean surface indicate that, well before the surface concentration equals a monolayer, widely separated "islands" or patches of atoms appear which cover a given area for several hundred atomic diameters.²⁷ These islands could then be responsible for the low temperature degradation by sufficient alteration of the crack tip binding energy. The surface concentration where island formation becomes important in influencing crack extension is necessarily quite small at low temperatures. For example, the average surface concentration at 500°F, where considerable embrittlement is seen in the tensile test is 10^{10} atoms/cm²/sec. or of the order of 0.01 monolayers in the assumed 100 seconds for the test.

If a specific value of C_o is a requirement for embrittlement at all test speeds, a plot of temperature versus test time, t_m , with C_o as a parameter should be able to be used to predict embrittlement temperatures for higher rate tests, Figure I29. A comparison of tensile and impact test data shows that tensile embrittlement is substantial at 500°F while a reduction of impact properties occurs closer to 621°F. This temperature difference, from Figure I29, would result in a time to fracture, t_m , difference between the two tests of the order of 10^3 seconds, for example, if impact test fracturing occurs in 10^{-3} seconds, tensile fracture would take place in one second at a constant value of C_o . This difference in test times is not unreasonable for the two test types.

The vapor-phase transport hypothesis of embrittling metal atoms to the crack tip can also be examined for mercury, a well known embrittling liquid metal. If we examine the pressure-temperature relationship of mercury, a common liquid-metal embrittling agent, the approximate expression is found to be: $\log P = 5.9 - 3420/T$, which has been plotted in Figure I30. A comparison of this expression with that obtained on lead shows that the vapor pressure of mercury at -25°F equals the vapor pressure of lead at 900°F. Thus, the deleterious effect of mercury on a number of materials at room temperature, e.g., aluminum, is as likely to be dependent on a vapor transport of embrittling metal atoms to the crack tip as is assumed to be the case for lead embrittlement of steel.

APPENDIX A

VAPOR PRESSURE OF LEAD AS A FUNCTION OF TEMPERATURE

The compiled values of equilibrium lead vapor pressure, \underline{P} , as a function of temperature, \underline{T} ,²⁸ can be used to construct a \underline{P} - \underline{T} curve (Figure 127). In addition, \underline{P} , ΔF_T , and ΔH_T data, included in Reference 28, suggest that the curve be plotted as $\log \underline{P}$ versus $1/T$. Thermodynamically we have the expression:

$$\frac{d \ln P}{d(1/T)} = \Delta H_T / R \quad (1)$$

Changing natural logs to the base 10 and solving for the ratio of pressure to temperature we obtain:

$$\frac{d \log P}{d(1/T)} = \Delta H_T / 2.3R \quad (2)$$

Since the increase of ΔH_T is five per cent in a 500°F temperature interval somewhat above the lead melting point, the slope of the $\log \underline{P}$ versus $(1/T)$ curve will be constant within a per cent per 100°F. Substituting numerical values into equation (2) we obtain for the approximate slope:

$$\frac{d \log P}{d(1/T)} = \frac{47,000 \text{ cal/mol}}{2.3 \times 1.99 \text{ cal/mol/deg}} \approx 10^4 \quad (3)$$

If we assume this slope is constant over the temperature range of interest, we can integrate equation (3) and obtain an approximate expression for the vapor pressure temperature relationship:

$$\log P = C - 10^4/T \quad (4)$$

putting in experimentally determined values for \underline{P} and \underline{T} , \underline{C} is found to be

approximately 5.0. Thus, the complete expression for lead vapor pressure as a function of temperature:

$$\log P = 5 - 10^4/T \quad (5)$$

Solving explicitly for P we obtain:

$$P = 10^5 \times 10^{-10,000/T} \quad (6)$$

BIBLIOGRAPHY

1. Kates, N. Personal Communication.
2. Gordon, P. Personal Communication.
3. Dolan, T. J. and Price, B. R. "Properties and Machinability of a Lead Steel." Metals and Alloys, January, 1940, pp. 20-27.
4. Swindon, T. "Lead Manganese Molybdenum Steel." Journal of the Iron and Steel Institute, 11, 1943, pp. 441-447.
5. Nead, J. E., Simes, C. E. and Harder, O. E. Metals and Alloys, 10, pp. 68, 109.
6. Woolman, J. and Jacques, A. "Influence of Lead Additions on the Mechanical Properties and Machinability of Some Alloy Steels." Journal of the Iron and Steel Institute, 175, July, 1950, pp. 257-267.
7. Weaver, A. P. "Impact Characteristics and Mechanical Properties of Lead and Non-lead C-1050 and C-1141 Steels." Transactions of the American Society for Metals, 1956, pp. 464-481.
8. Simon, W. "Fatigue and Tensile Properties of High Strength Lead and Non-lead SAE 4140 Steel." Paper 220 A, SAE National Farm Construction and Industrial Machinery Meeting, Milwaukee, Wisconsin, September, 1960.
9. Brock, G. W., and Sinclair, G. M. "An Investigation of the Fatigue Characteristics of Lead Alloy Steels." University of Illinois, T and AM Report No. 105, Bu. Ord. Contr. No. NORD-16417, September, 1956.
10. Brock, G. W. and Sinclair, G. M. "How Good are Lead Steels in Fatigue." Iron Age, January 9, 1958, pp. 59-62.
11. Suhre, J. R. and Brock, G. W. "A Comparison of the Fatigue Behavior of Lead and Non-lead AISI 4340 Steel at High Hardness Levels." University of Illinois, T and AM Report No. 570, Bu. Ord. Contr. No. NORD 17735, February 1959.
12. Vetrano, J. Personal Communication.
13. Chalfant, G. M. "Revealing Lead Inclusions in Lead Steels." Metal Progress, September, 1960, pp. 77-79.

14. Schreiber, T. P. "The Electron Probe: An Instrument for the Chemical Analysis of Microscopic Samples." General Motors Engineering Journal, 11, No. 4, 1964, pp 2-7.
15. Zipp, R. Unpublished M.Sc. Thesis, Illinois Institute of Technology, 1968.
16. Peterson, J. L. "Strain Age Hardening in Hypoeutectoid Steels." American Society for Metals Transactions Quarterly, Vol. 56, No. 3, September, 1963, pp. 304-317.
17. Larson, F. R. and Carr, F. L. "Tensile Fracture Surface Configurations of a Heat Treated Steel as Affected by Temperature." American Society for Metals Transactions Quarterly, Vol. 55, 1962, pp. 599-611.
18. Rostoker, W., McCaughy, J. M. and Markus, H. "Embrittlement by Liquid Metals," Reinhold Publishing Company, New York, 1960.
19. Potak, Y. M. and Shchlegakov, I. M. "The Effect of Molten-Metal Coatings on the Mechanical Properties of Steel and Alloys." Zhurnal Tekhnicheskoi Fisiki, 1955, pp. 897-907.
20. Puttick, K. E. "Ductile Fracture in Metals." Philosophical Magazine, Vol. 4, Ser. 8, 1959, pp. 964-969.
21. Bluhm, J. I. and Morrissey, R. J. "Fracture in a Tensile Specimen." AMRA-MS-66-06 Monograph Presented at International Conference on Fracture, Sendai, Japan, September, 1965.
22. Stoloff, N. S. and Johnston, L. "Crack Propagation in a Liquid Metal Environment." Acta Metallurgica, Vol. 11, No. 4, April, 1963, pp. 251-256.
23. Westwood, A. R. C. and Kamdar, M. H. "Concerning Liquid Metal Embrittlement Particularly of Zinc Mono-Crystals by Mercury." Philosophical Magazine, Vol. 8, Ser. 8, No. 1, May, 1963, pp. 787-804.
24. Hirth, J. P. and Pound, G. M. "Condensation and Evaporation Nucleation and Growth Kinetics." Progress in Materials Science, Vol. 11, Pergamon Press, MacMillan Publishing Company, New York, 1963.
25. Gretz, R. P. "Nucleation of Silver and Cadmium on Tungsten Field Emitter Substrates." Proceedings of the International Symposium on Condensation and Evaporation of Solids, Gordon and Breach Publishing Company, New York, 1964, pp. 575-599.

26. Pound, G. M. and Hirth, J. P. "Heterogeneous Nucleation on Substrates." Ibid., pp. 474-502.
27. Moazed, K. L. and Pound, G. M. "Field-Emission Microscopy of Metal Crystal Nucleation." Transactions of the American Institute of Mining, Metallurgical and Petroleum Engineers, Vol. 230, 1964, pp. 234-239.
28. Wexler, S. "Deposition of Atomic Beams." Review of Modern Physics, Vol. 30, No. 2, 1958, pp. 402-409.
29. Hultgren, Orr, Anderson and Kelly. "Selected Values of Thermodynamic Properties of Metals and Alloys." Wiley, New York, 1964.

Table 1. Materials List, Heat Treatment and Code for Use on Figures.

Material:

"As-received" warm drawn (650°F) leaded and non-leaded AISI 4145. σ_{UTS} of "as-received" material, 200 ksi.

Heat Treatment:

One hour at 1525°F. Quench in 140°F oil. Tempered for one hour as follows:

Tempering Temperature $T_t, ^\circ F$	Room Temperature $\sigma_{UTS},$ ksi	Figure Code For series
770	240	24
880	220	22
940	200	20
1030	180	18
1130	160	16
1200	140	14
1280	120	12

Prefix N or L preceding code number indicates heat treated Non-leaded or Leaded longitudinal series. No prefix indicates comparison curves between the series Leaded to Non-leaded. No suffix indicates comparison of a property as a function of strength level. LO or NO prefix indicates material as warm drawn. A suffix T after the number indicates a transverse specimen.

Table 2. Influence of Tensile Specimen Orientation and Specimen Configuration on the Mechanical Properties of Lead and Non-Leaded Steels Heat Treated to Two Strength Levels and Tested at Room Temperature and in the Embrittlement Trough.

Matl.	Specimen Configuration (1)	Test Temp. °F	σ_{UTS} ksi	σ_F ksi	σ_{YS} ksi	σ_{PL} ksi	R.A. %	e %	δ (2) mils
N22	A	RT	218	308	205	198	49.8	8.22	152
N22	B	RT	224	300	NA(3)	197	41.2	NA	80
N22T	C	RT	240	258	NA	209	6.8	NA	3.94
L22	A	RT	216	297	205	188	46.6	7.0	130
L22	B	RT	228	295	RA	198	36.7	NA	68
L22T	C	RT	220	220	NA	209	0	NA	0.70
N20	A	RT	203	298	196	189	50	5.95	110
N20	B	RT	211	292	NA	188	44.1	NA	80
N20T	C	RT	222	240	NA	180	7.2	NA	6.14
L20	A	RT	193	281	189	175	45.6	7.56	140
L20	B	RT	211	282	NA	195	33.6	NA	55
L20T	C	RT	214	218	NA	181	1.4	NA	0.8

(1) Specimen configuration: A -- as figure 5 (longitudinal uniform)
 B -- as figure 10 (longitudinal radiused)
 C -- as figure 6 (transverse radiused)

(2) δ = Total elongation to fracture

(3) NA; not applicable for this specimen configuration

Table 2. (Continued).

Matl.	Specimen Configura- tion (1)	Test Temp. °F	σ _{UTS} ksi	σ _F ksi	σ _{YS} ksi	σ _{PL} ksi	R.A. %	e %	δ(2) mils
N22	A	790	158	240	132	70.7	68.8	10.2	188
N22	B	750	175	254	NA	135	58.4	NA	106
N22T	C	750	192	213	NA	120	10.4	NA	9.06
L22	A	780	111	111	NM(4)	77.2	0	0.05	0.96
L22	B	755	123	123	NA	NM	0	NA	0
L22T	C	765	76	76	NA	NM	0	NA	0
N20	A	800	150	244	136	95.5	70.7	12.4	230
N20	B	758	166	260	NA	121	63.6	NA	120
N20T	C	755	178	197	NA	120	9.8	NA	6.8
L20	A	800	112	112	NM	83.5	0	0.05	1.0
L20	B	750	143	143	NA	140	0	NA	0
L20T	C	760	75	75	NA	NM	0	NA	0

(4) NM; not measurable (specimen fractures either without apparent plastic flow or before 0.2 per cent criterion is met)

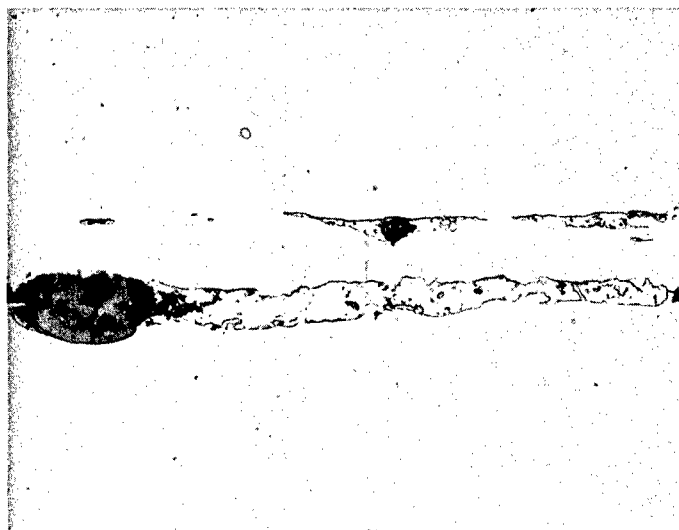


Figure 1. Photomicrographs of Leaded Cold Drawn AISI 4145 Steel Taken Parallel to Bar Axis. Unetched to Show Inclusion Morphology. 500X. Note Manganese Sulfide (Grey) and Iron or Manganese Oxides (Black) in Rounded Inclusion Surrounded by Strung Out Lead (Whitish).

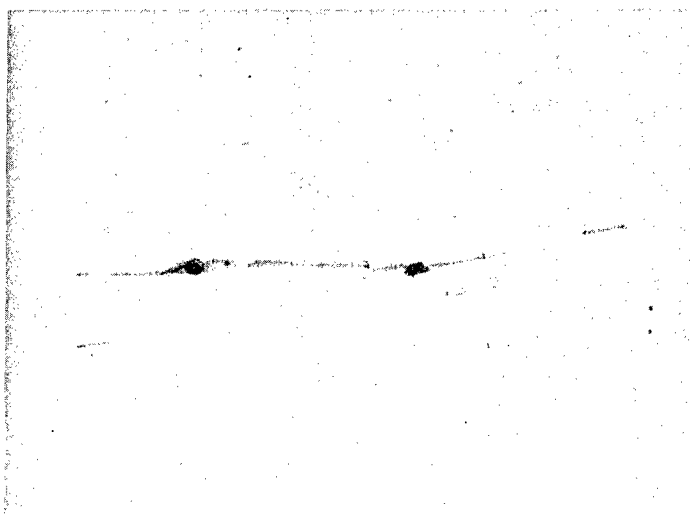
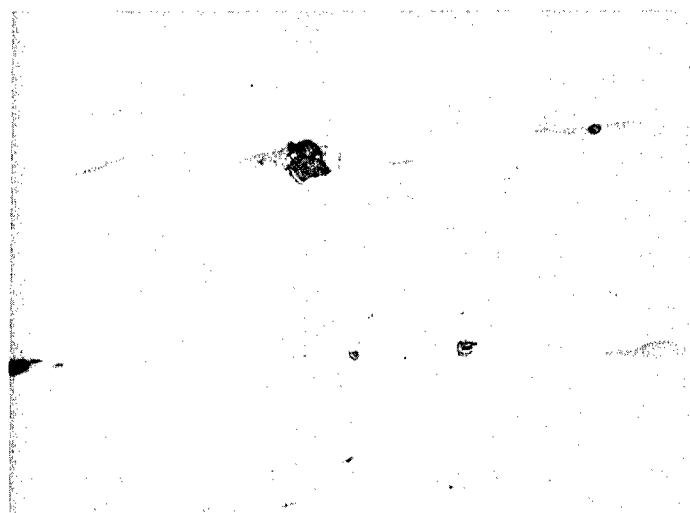
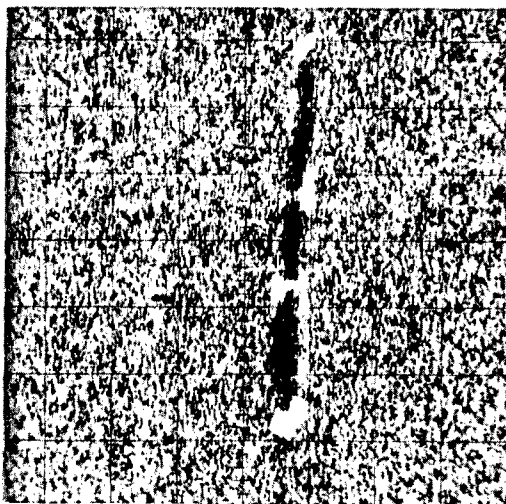
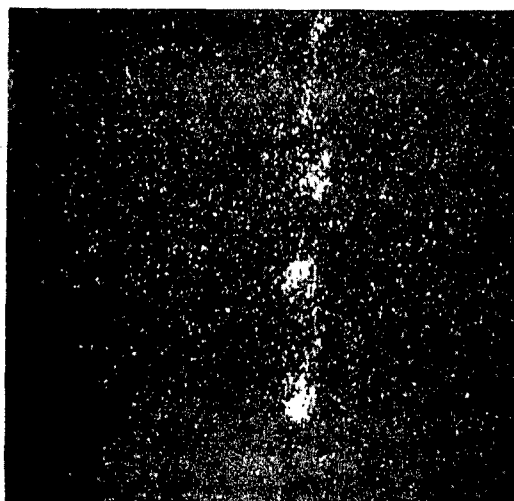


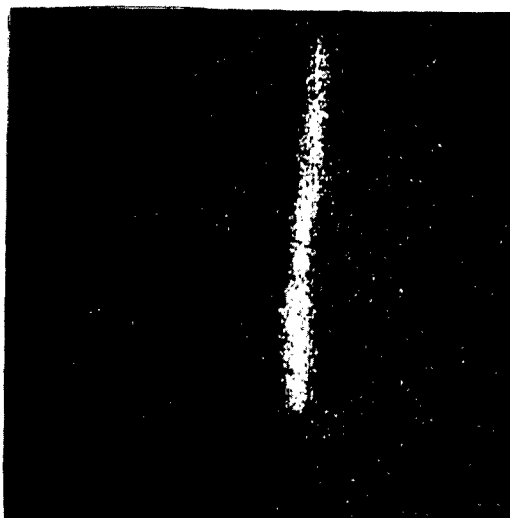
Figure 2. Photomicrographs of Non-lead Cold Drawn AISI 4145 Steel Taken Parallel to Bar Axis. Unetched to Show Inclusion Morphology. 500X. Note Manganese Sulfide as Round Black Inclusions with Strung Out Iron and Manganese Oxides Which Appear as Greyish Surroundings.



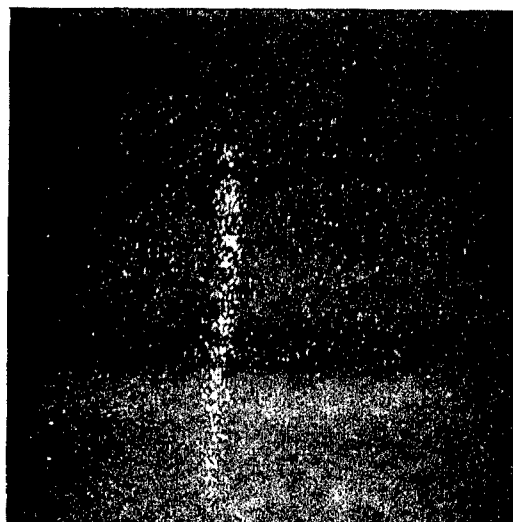
a) BSE



b) Pb-Mα



c) Mn-Kα

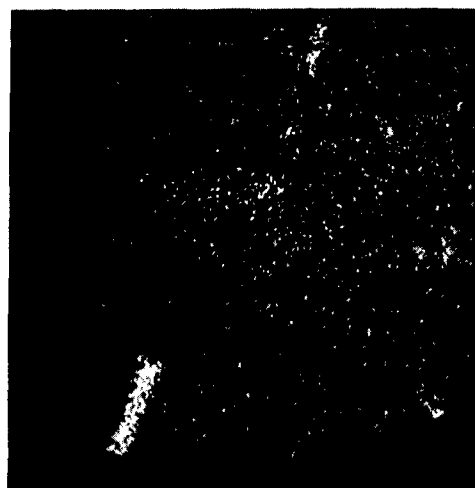


d) S-Kα

Figure 3. Electron Microprobe Scan Across a Leaded Steel Inclusion Using Back Scattered Electron, BSE, and Characteristic X-ray Counters. a) BSE, b) Pb-Mα, c) Mn-Kα, d) S-Kα. 800X.



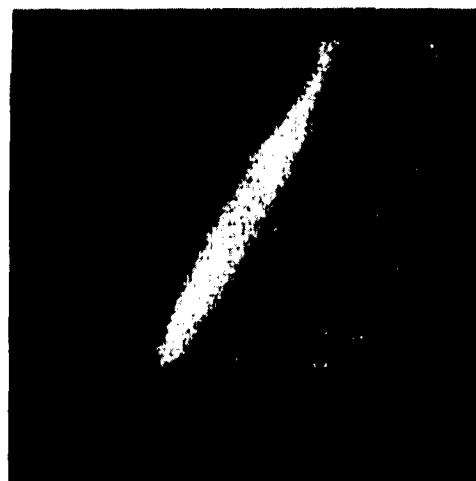
a) BSE



b) Pb-Mα

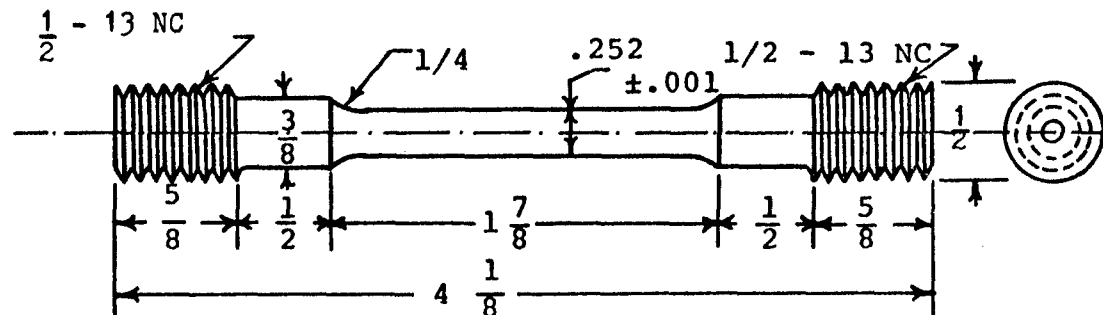


c) Mn-Kα

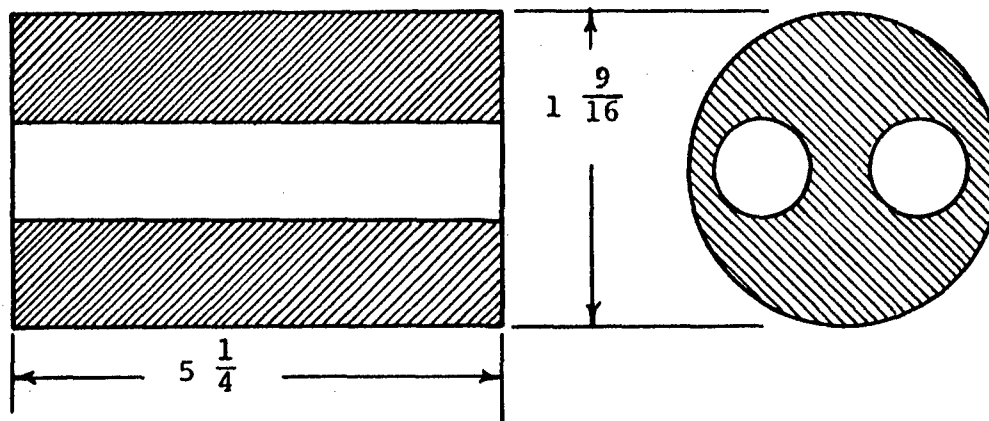


d) S-Kα

Figure 4. Electron Microprobe Scan Across a Lead Steel Inclusion Using Back Scattered Electron, BSE, and Characteristic X-ray Counters. a) BSE, b) Pb-Mα, c) Mn-Kα, d) S-Kα. 800X.



(A)



(B)

Figure 5. (A) Tensile Specimen Engineering Drawing.
 (B) As-Received Leaded and Non-leaded AISI 4140
 Steel Bar Cross-Section Showing Specimen Location.
 Note: Specimen Dimensions in Inches.

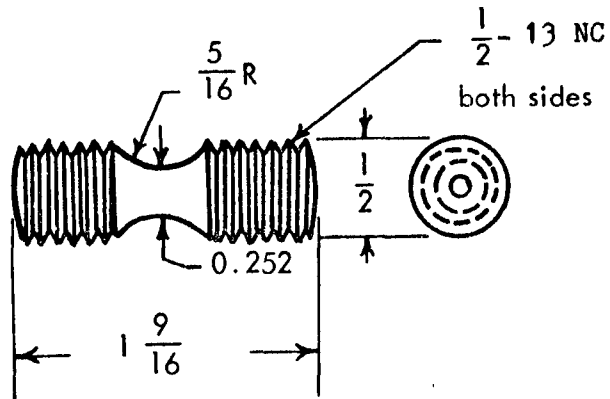
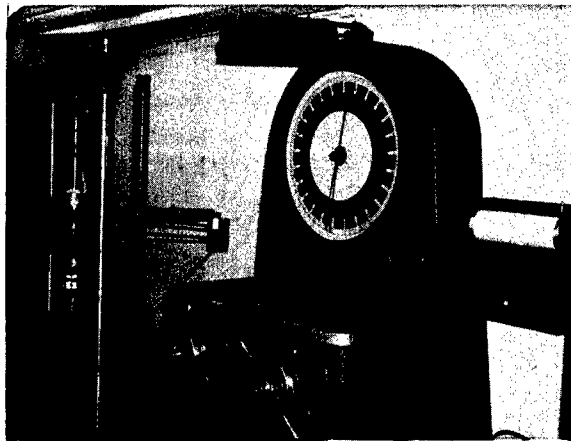
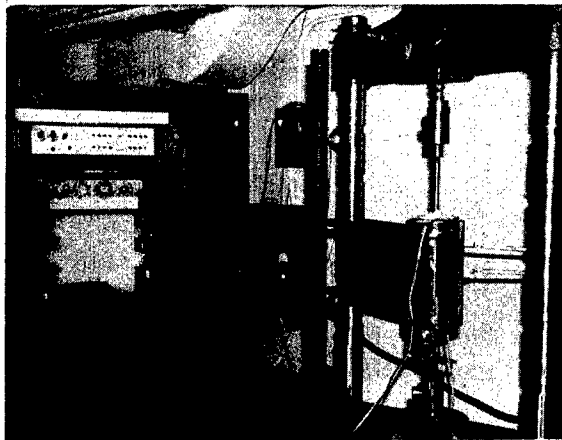


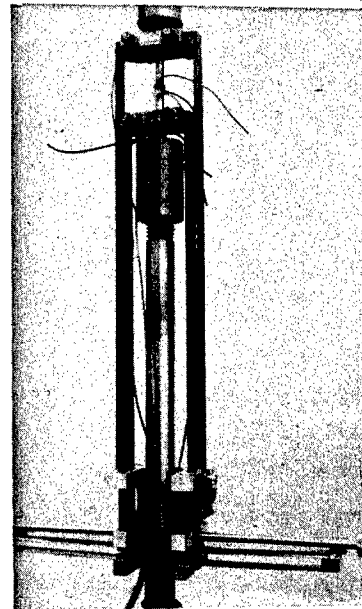
Figure 6. Radiused Transverse Tensile Specimen (Initial Bar Stock Diameter $1\text{-}\frac{9}{16}$ in.) Note: Specimen Dimensions in Inches.



a)



b)



c)

Figure 7. Room and Elevated Temperature Tensile Test Equipment: a) Baldwin 60,000 lb. cap. Tensile Machine with Autographic Recorder. b) Load Frame Equipped with Furnace: Controller and Specimen Temperature Recorder (Shown at Side). d) Load Train with Extensometer in Place Prior to Insertion in Furnace. Note Thermocouples Tied Onto Specimen.

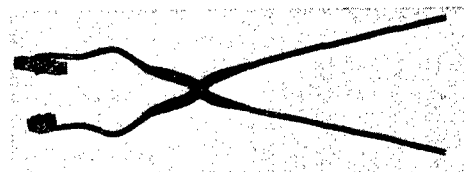
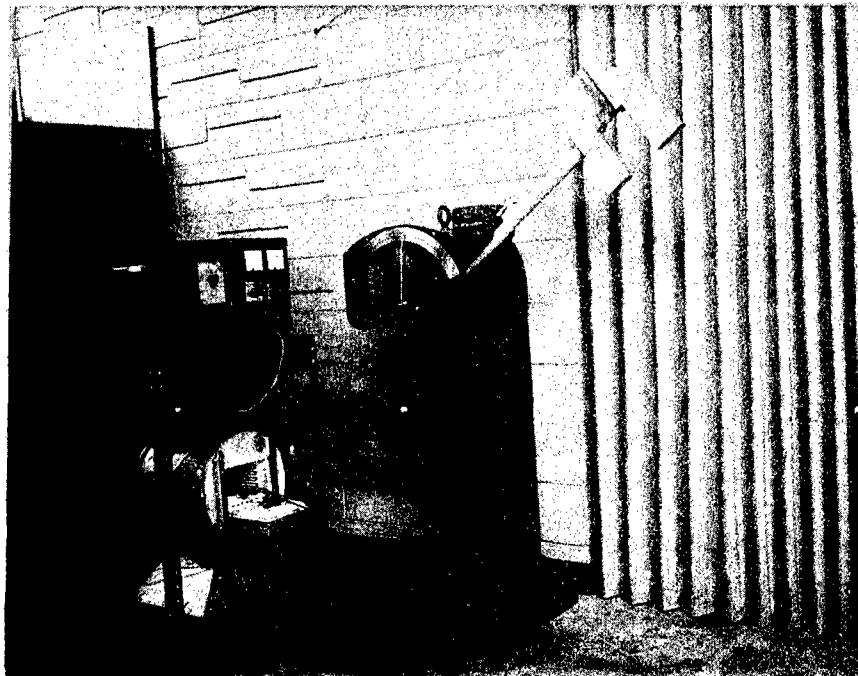


Figure 8. Room and Elevated Temperature Impact Test Equipment. Note Fitted Tongs Shown in Insert.

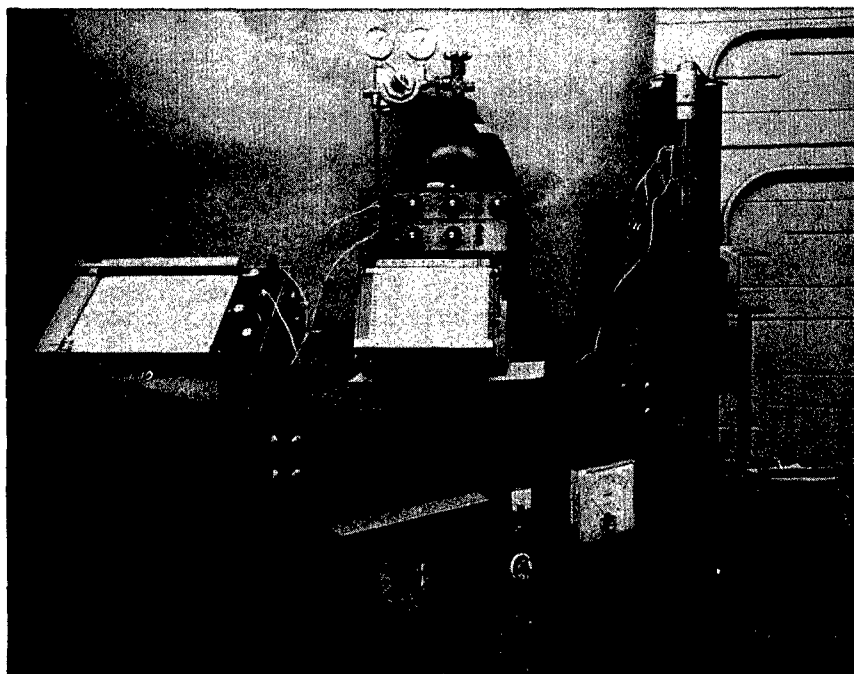


Figure 9. Apparatus for Measurement of the Thermal Coefficient of Expansion, α .

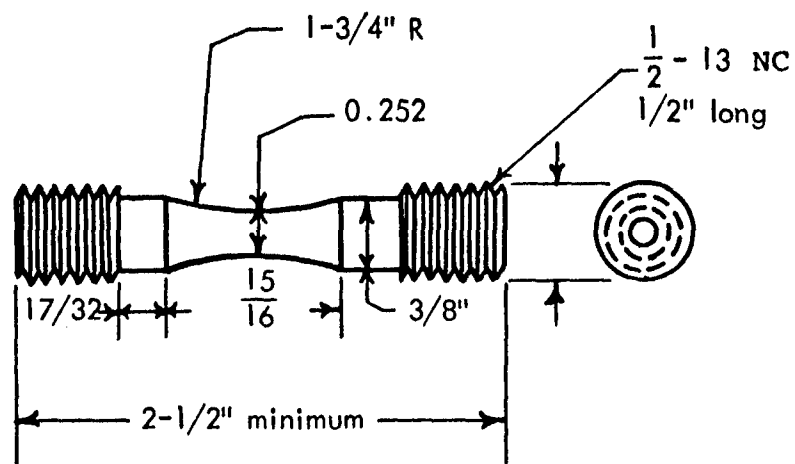


Figure 10. Static Fatigue Radiused Longitudinal Tensile Specimen Engineering Drawing. Note: Specimen Dimensions in Inches.

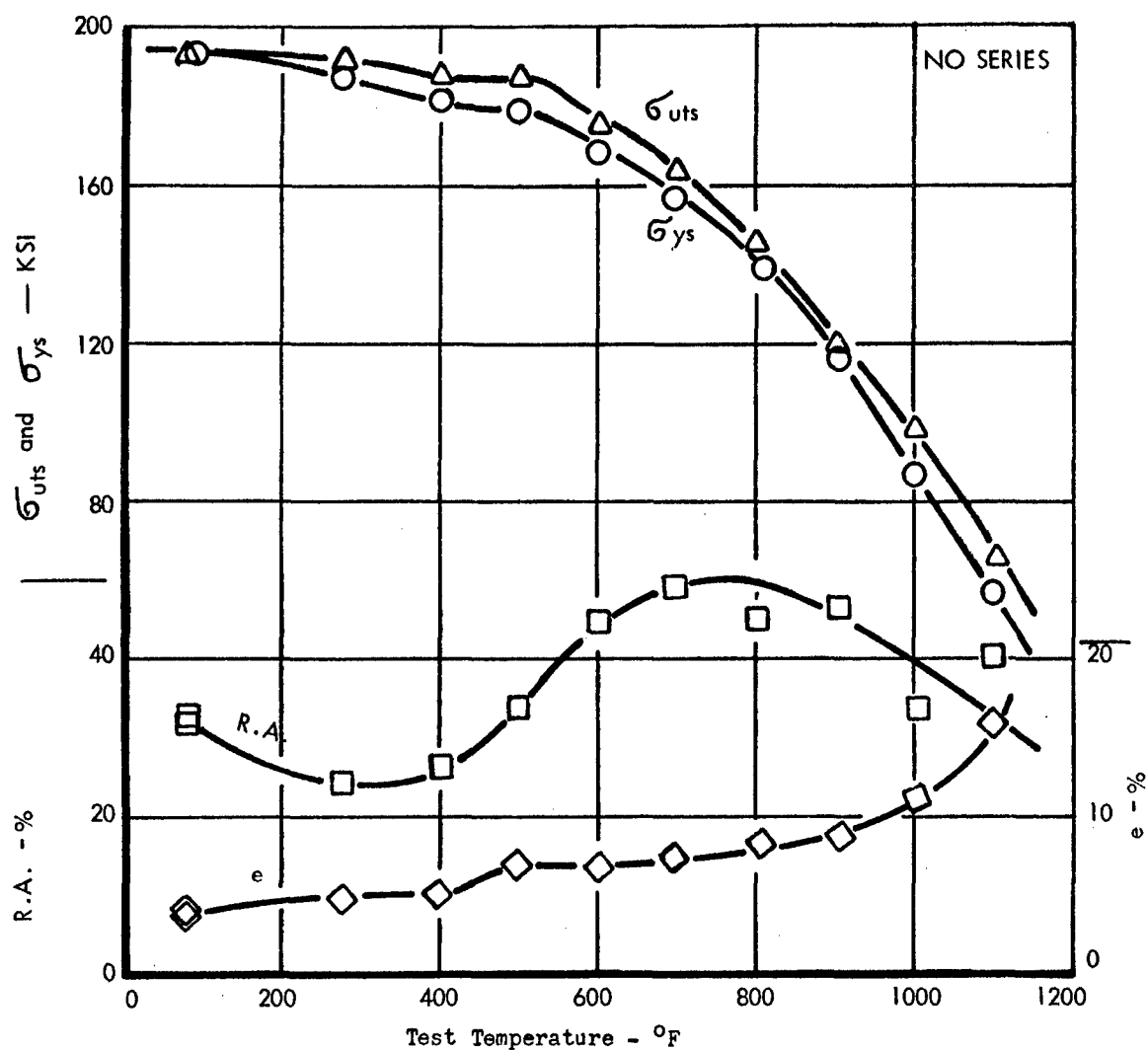


Figure 11. Engineering Tensile Properties of Cold Drawn Non-leaded AISI 4145 Steel as a Function of Test Temperature. Cross Head Rate .01 to .1 in./min. (NO Series)

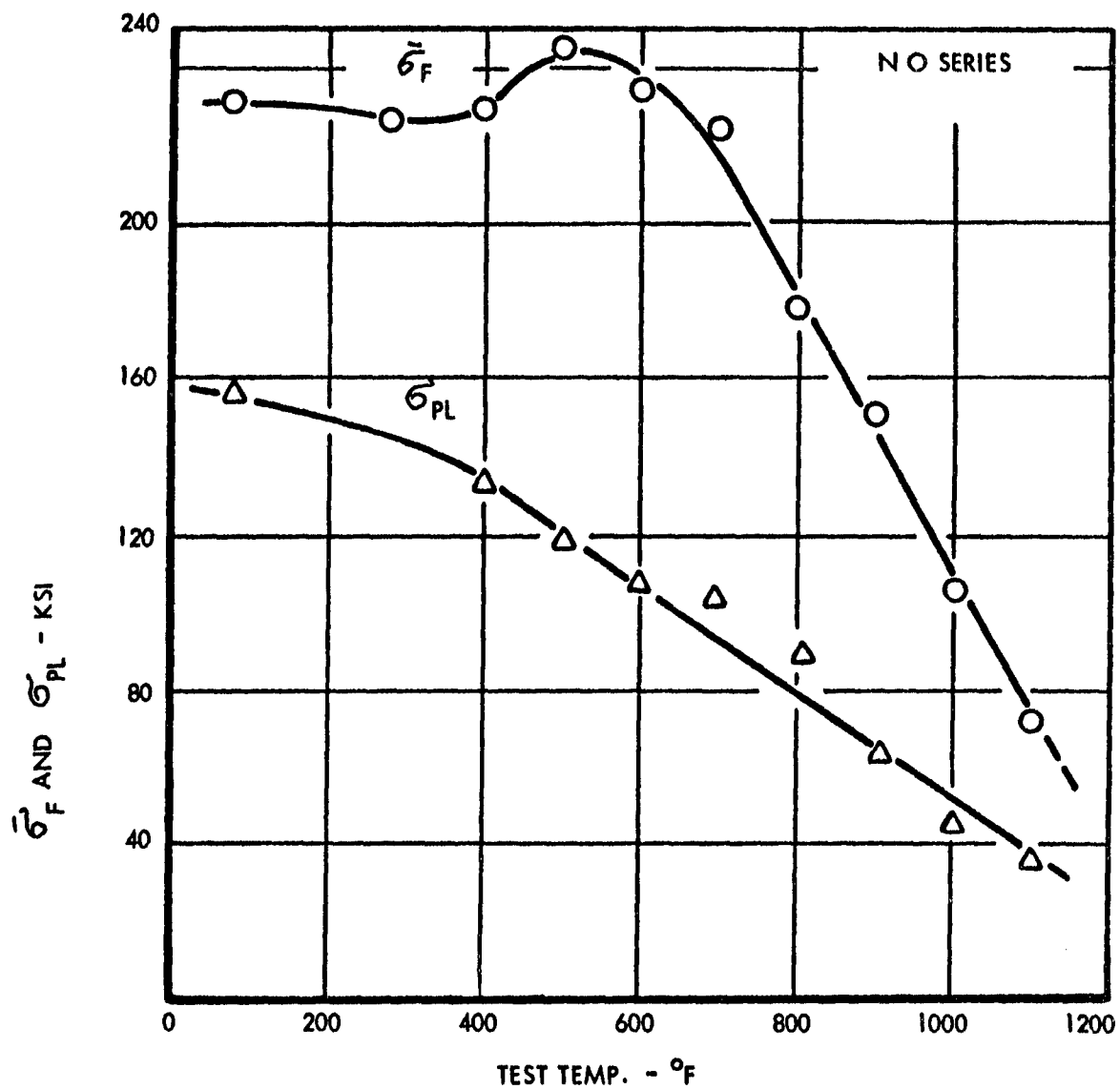


Figure 12. Effect of Test Temperature on True Fracture Stress, $\bar{\sigma}_F$, and Proportional Limit, $\bar{\sigma}_{PL}$, for Cold Drawn Non-leaded AISI 4145 Steel. (NO Series)

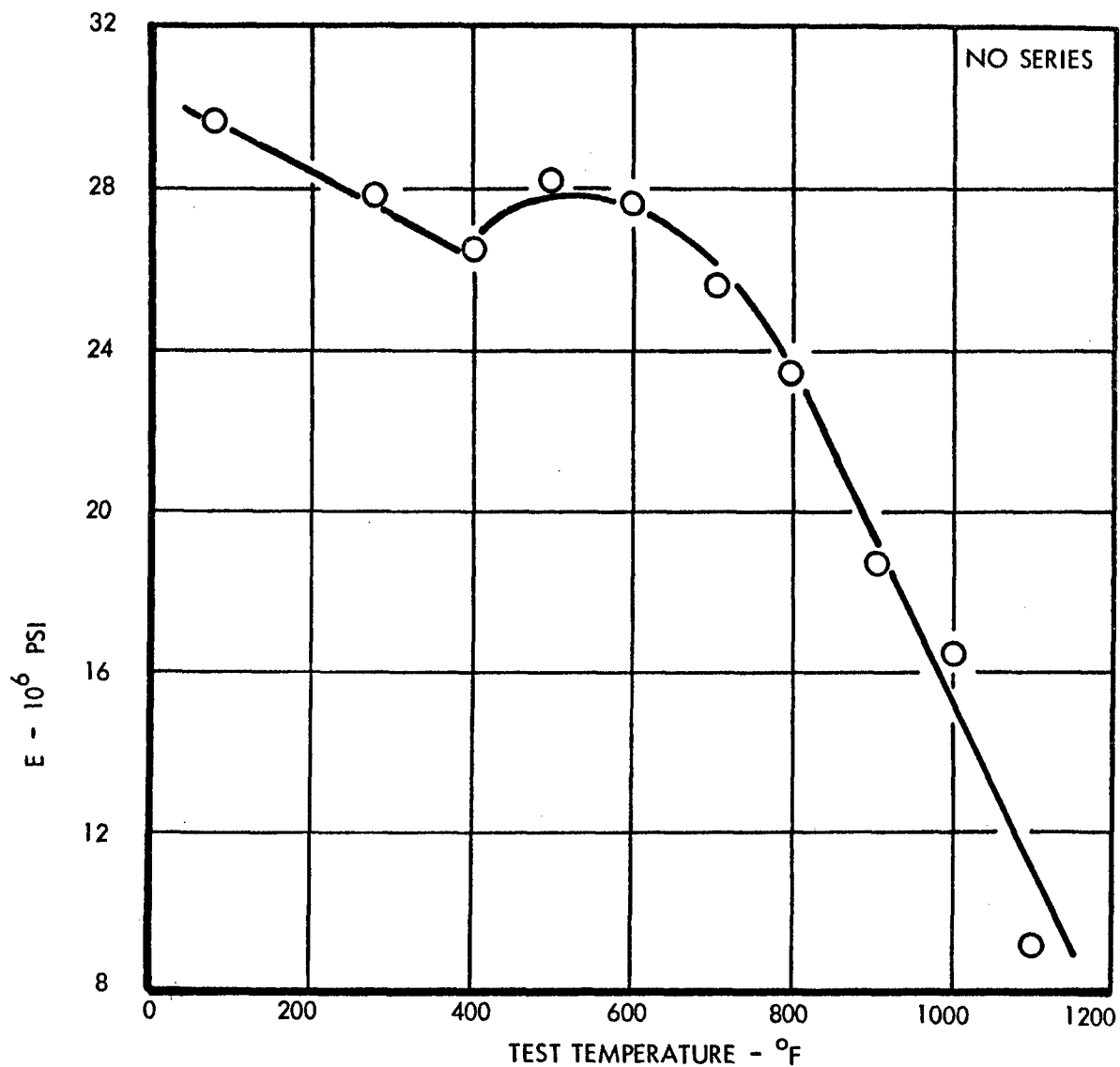


Figure 13. Effect of Test Temperature on Elastic Modulus, E, for Cold Drawn Non-leaded AISI 4145 Steel. (NO Series)

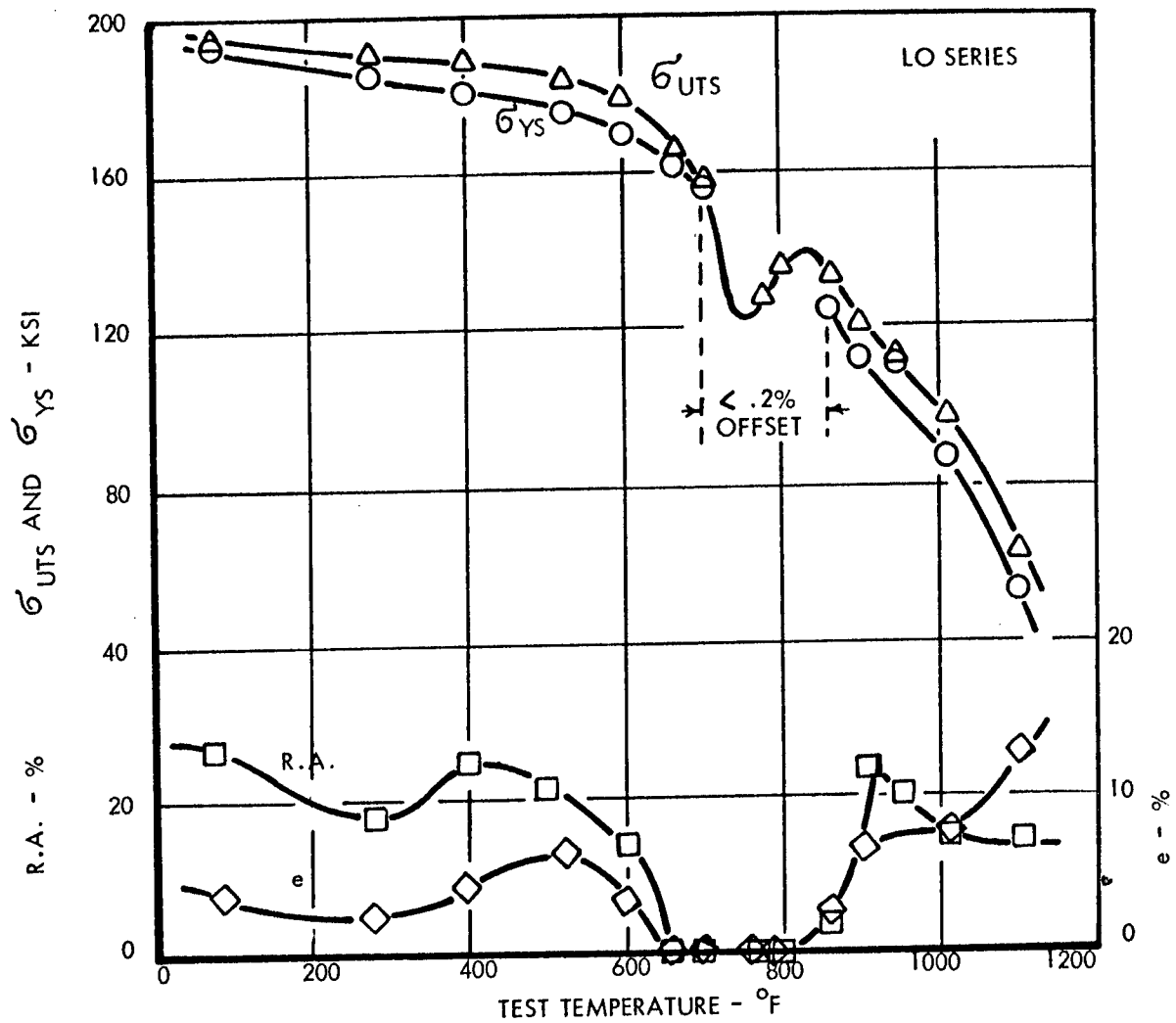


Figure 14. Engineering Tensile Properties of Cold Drawn Lead AISI 4145 Steel as a Function of Test Temperature. Crosshead Rate .01 to .1 in./min. Note that Between 700 and 850°F σ_{ys} Cannot be Measured Due to the Small Elongation in This Region. (LO Series)

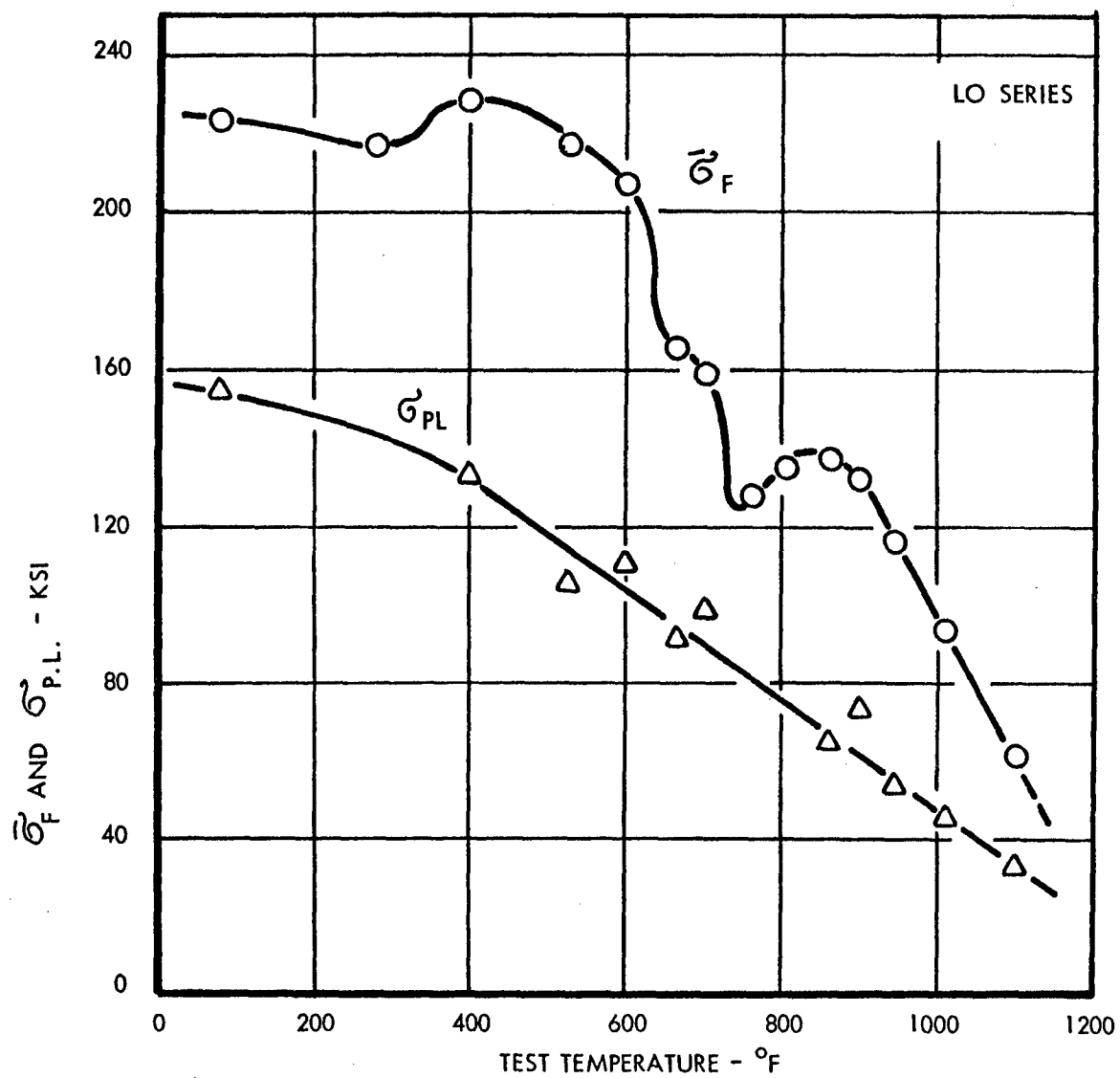


Figure 15. Effect of Test Temperature on True Fracture Stress, $\bar{\sigma}_F$, and Proportional Limit, $\bar{\sigma}_{PL}$, for Cold Drawn Leded AISI 4145 Steel. (LO Series)

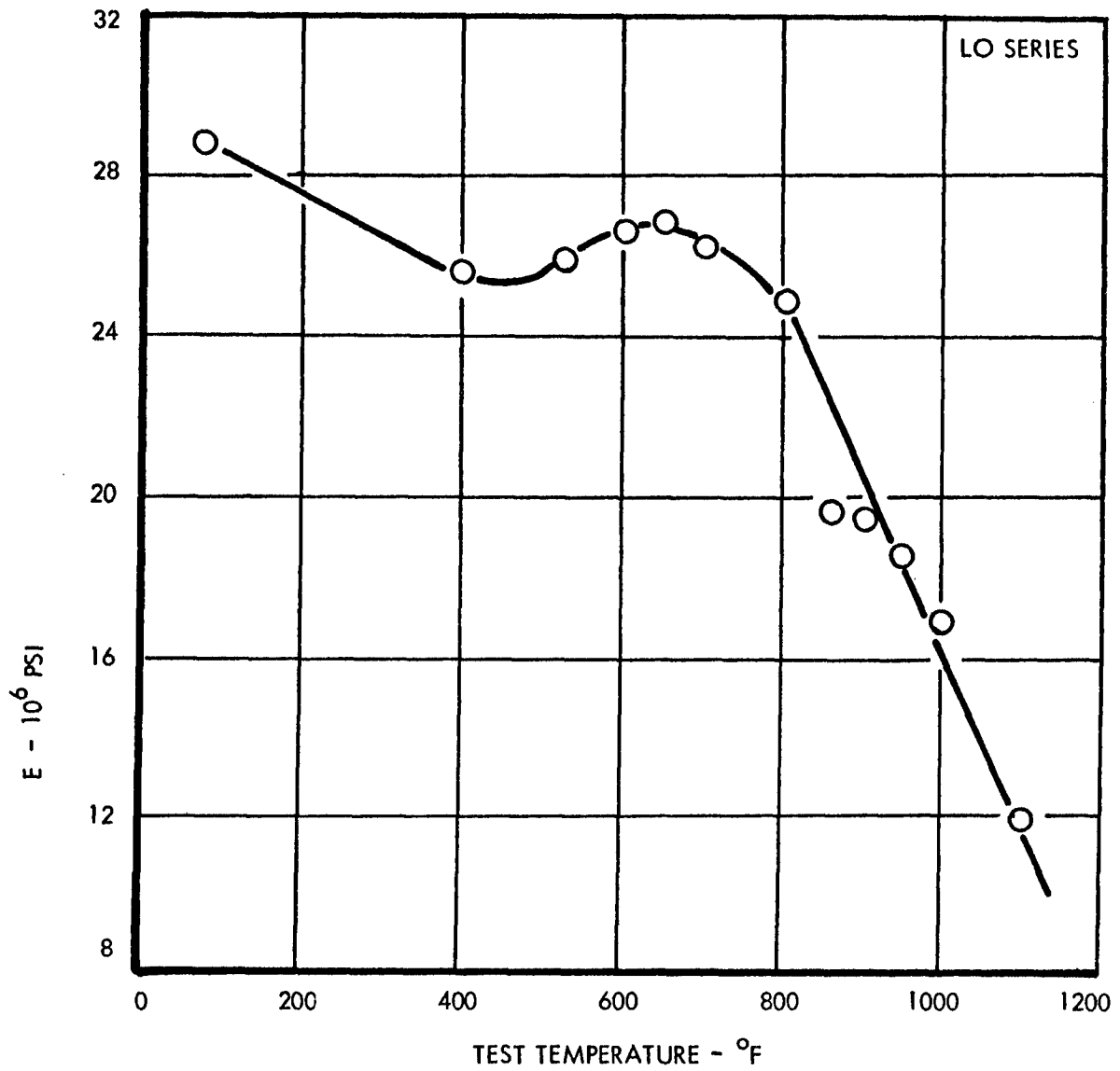


Figure 16. Effect of Test Temperature on Elastic Modulus, E, for Cold Drawn Lead AISI 4145 Steel. (LO Series)

LO Series

NO Series



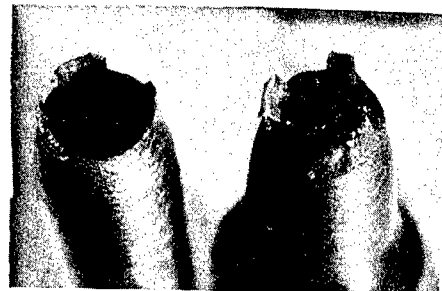
a) LO; 400°F



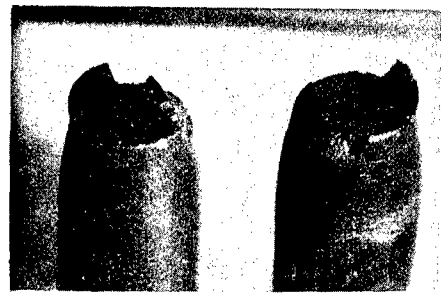
b) LO; 600°F



c) LO; 903°F



d) NO; 600°F



e) NO; 915°F

Figure 17. Effect of Test Temperature on Fracture Appearance of Ledged and Non-ledged Cold-Drawn AISI 4145 Steel Broken at Indicated Temperatures. LO Are Ledged; NO Are Not Ledged.

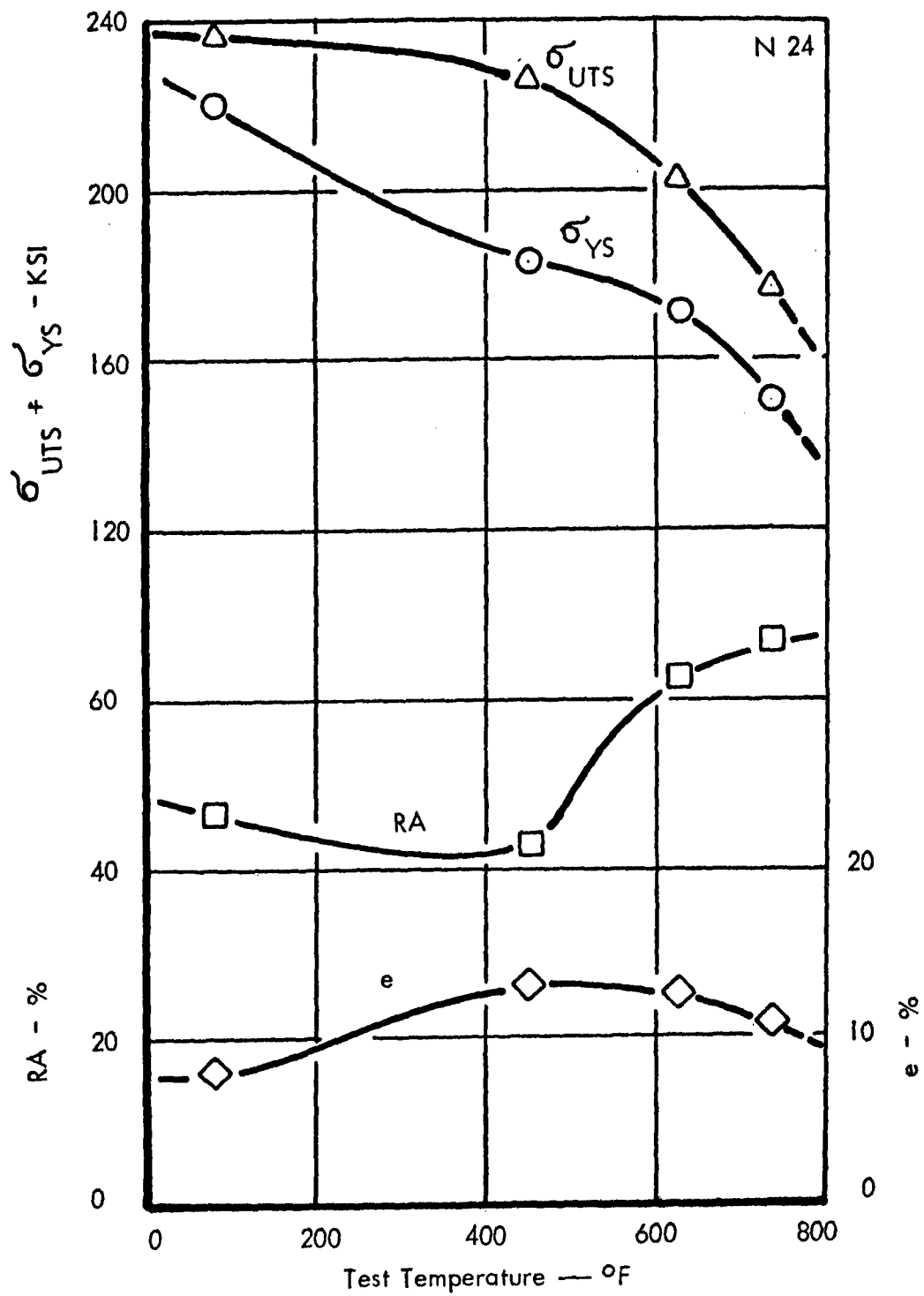


Figure 18. Engineering Tensile Properties of Non-leaded N24 Material.

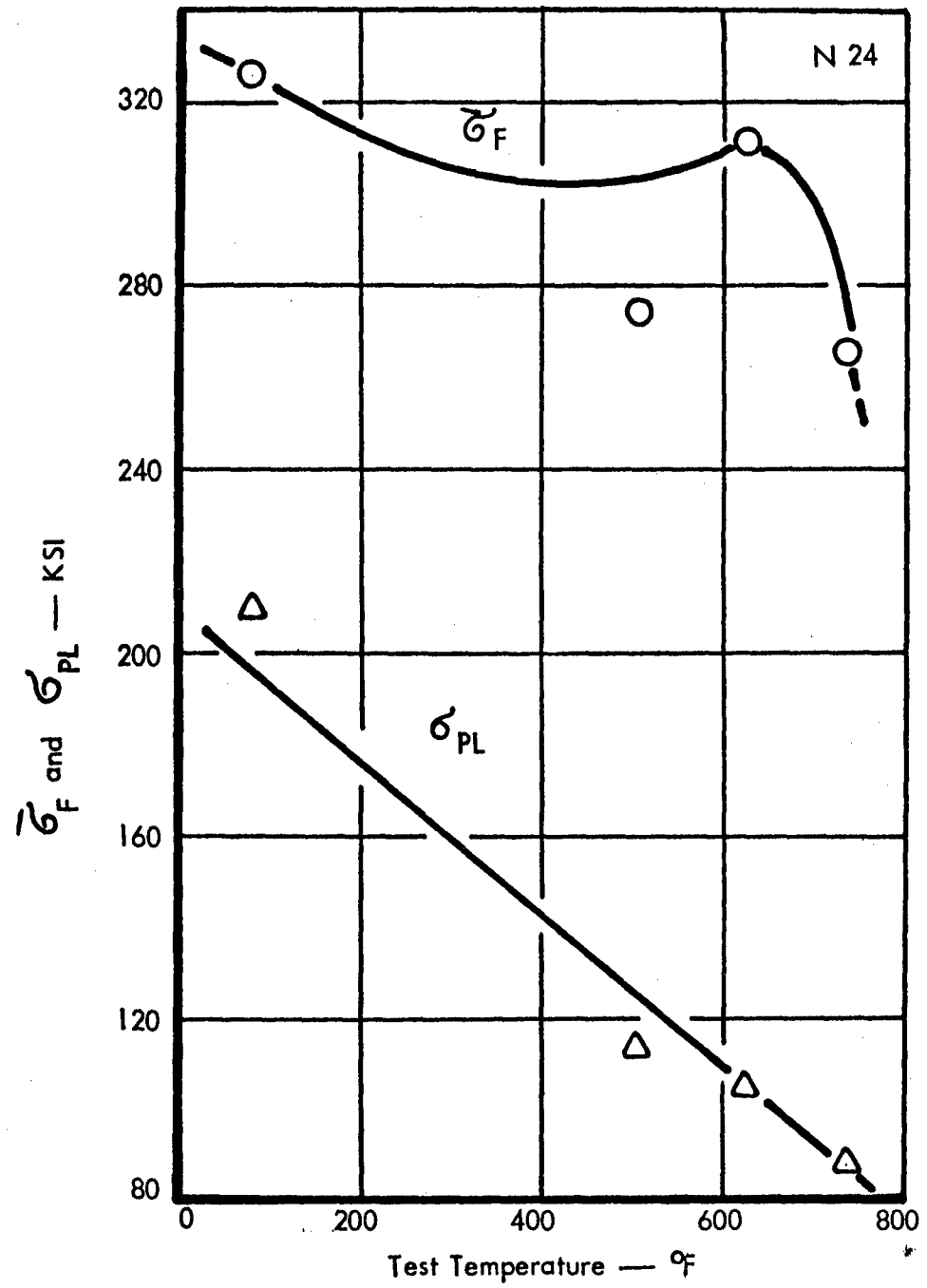


Figure 19. Effect of Test Temperature on $\bar{\sigma}_F$ and σ_{PL} for Non-leaded N24 Material.

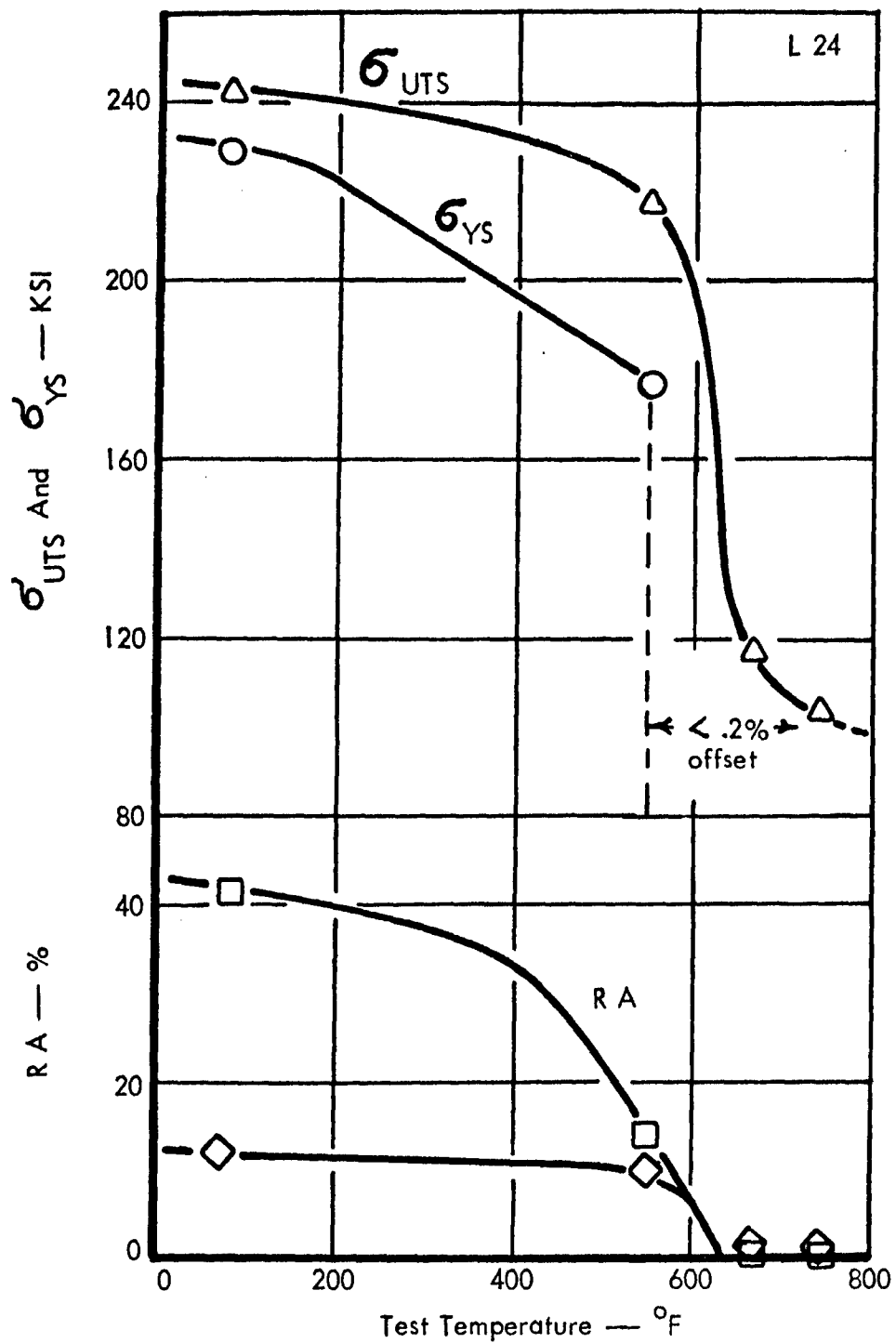


Figure 20. Engineering Tensile Properties of Lead L24 Material.

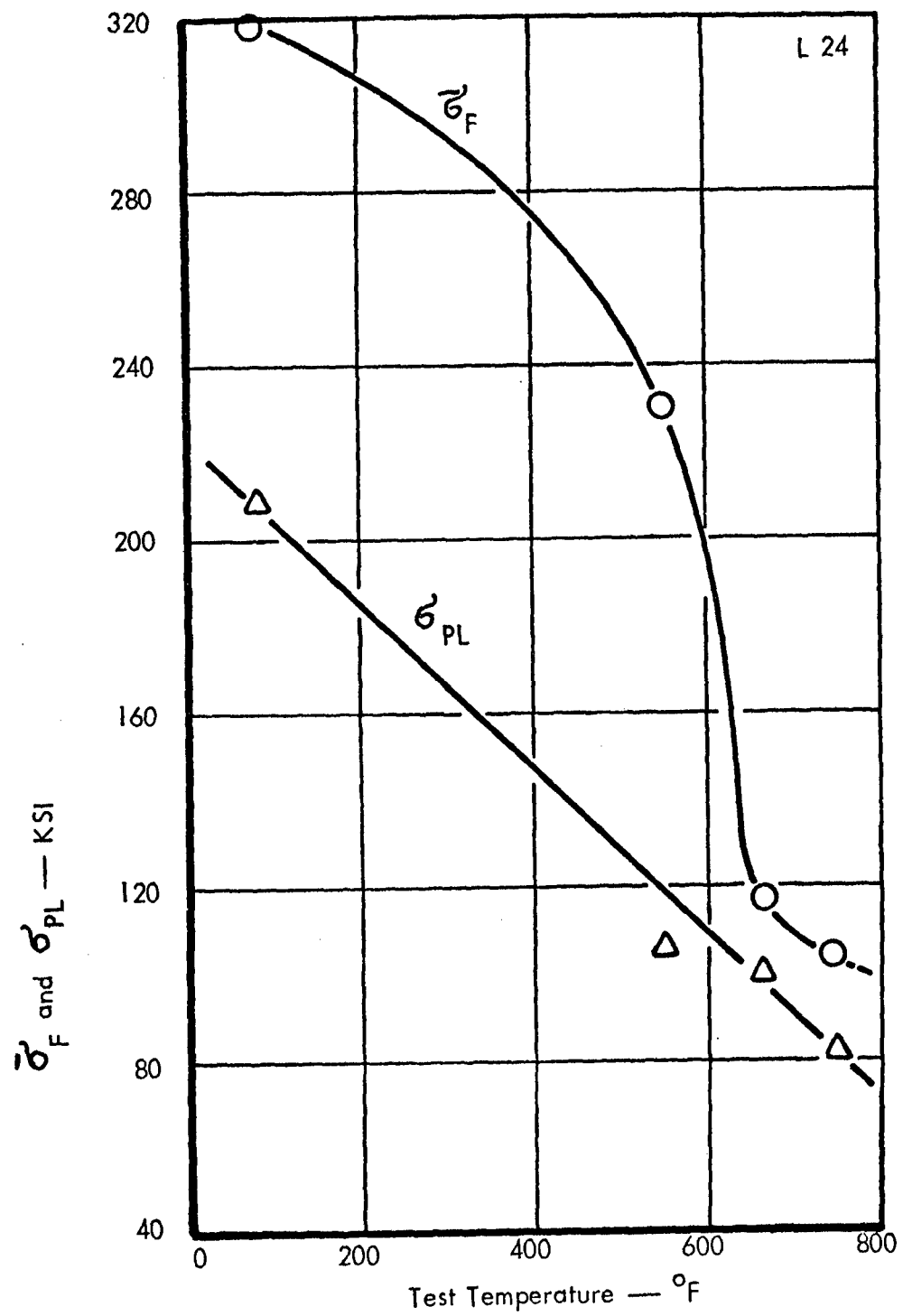
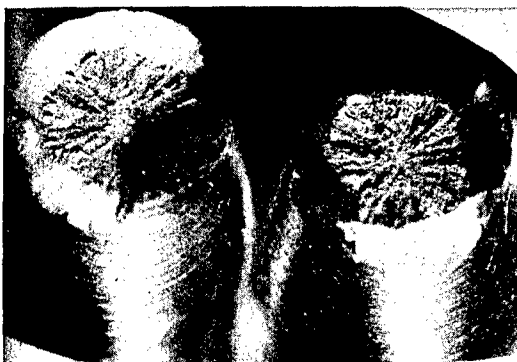


Figure 21. Effect of Test Temperature on $\bar{\sigma}_F$ and σ_{PL} for Lead L24 Material.



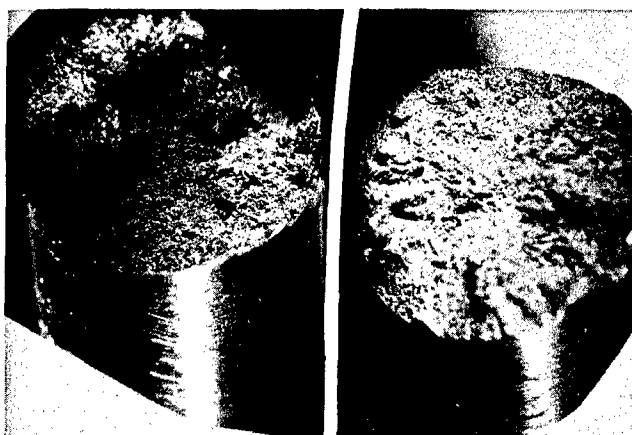
N24; RT



L24; RT



N24; 500°F

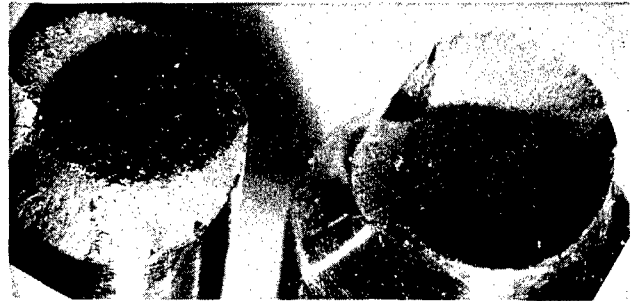


L24; 550°F

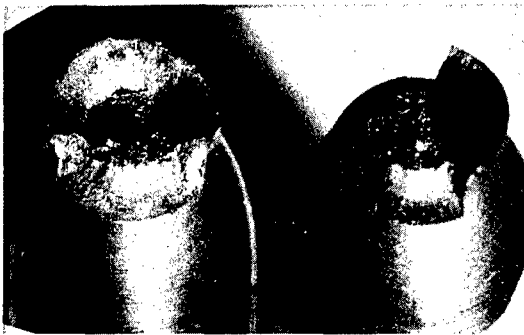
Figure 22. Tensile Fracture Surfaces of Leaded and Non-leaded N24 and L24 Material Below 620°F.



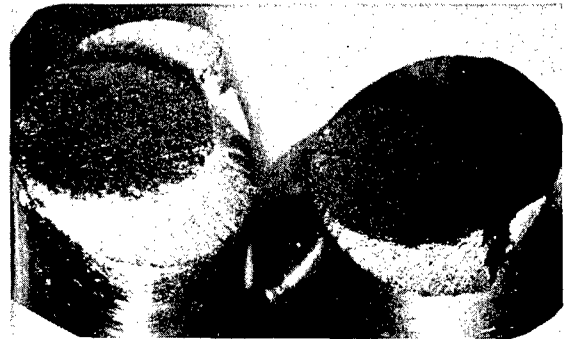
N24; 623°F



L24; 660°F



N24; 740°F



L24; 745°F

Figure 23. Tensile Fracture Surfaces of Leaded and Non-leaded N24 and L24 Material Above 620°F.

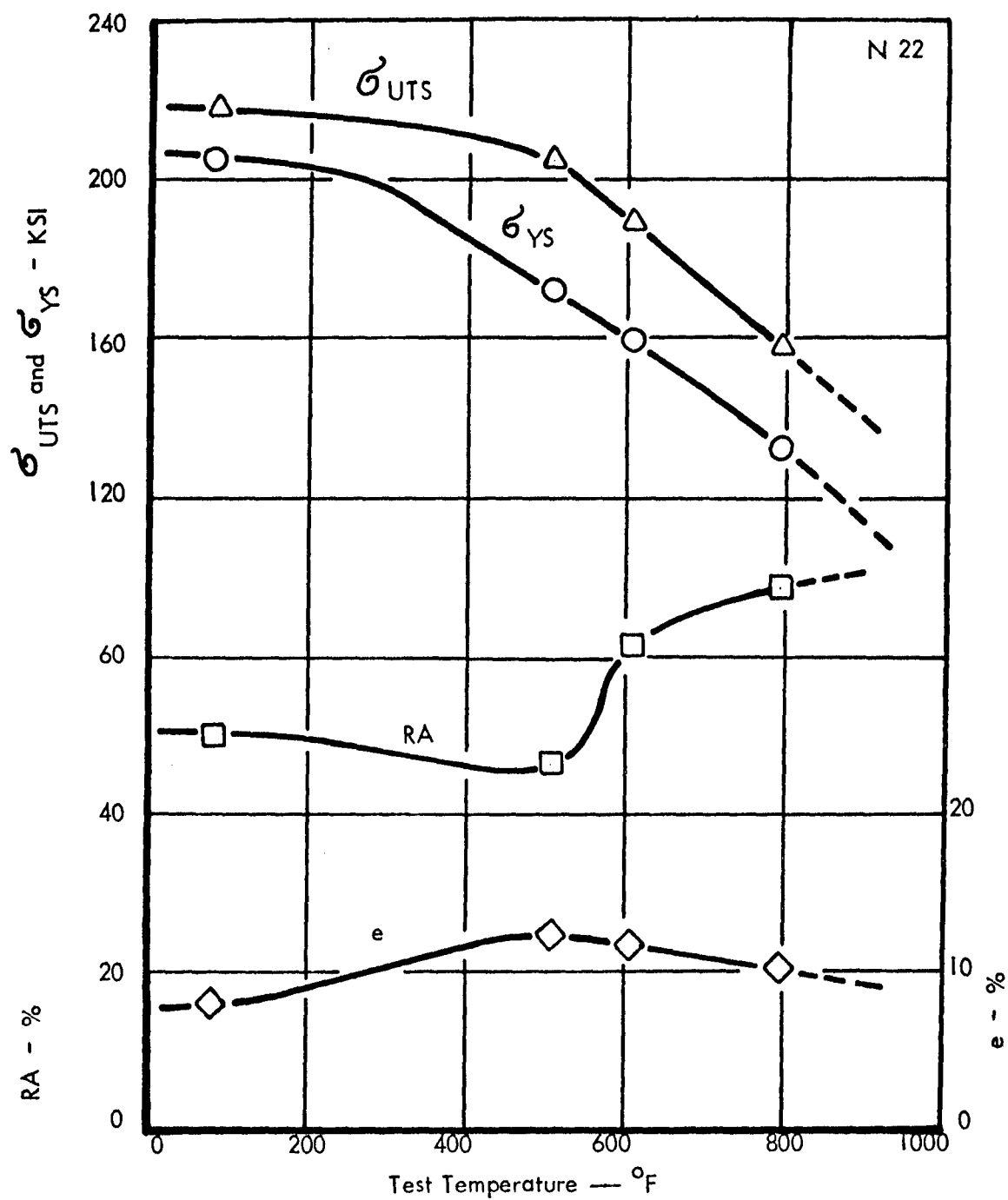


Figure 24. Engineering Tensile Properties of Non-leaded N22 Material.

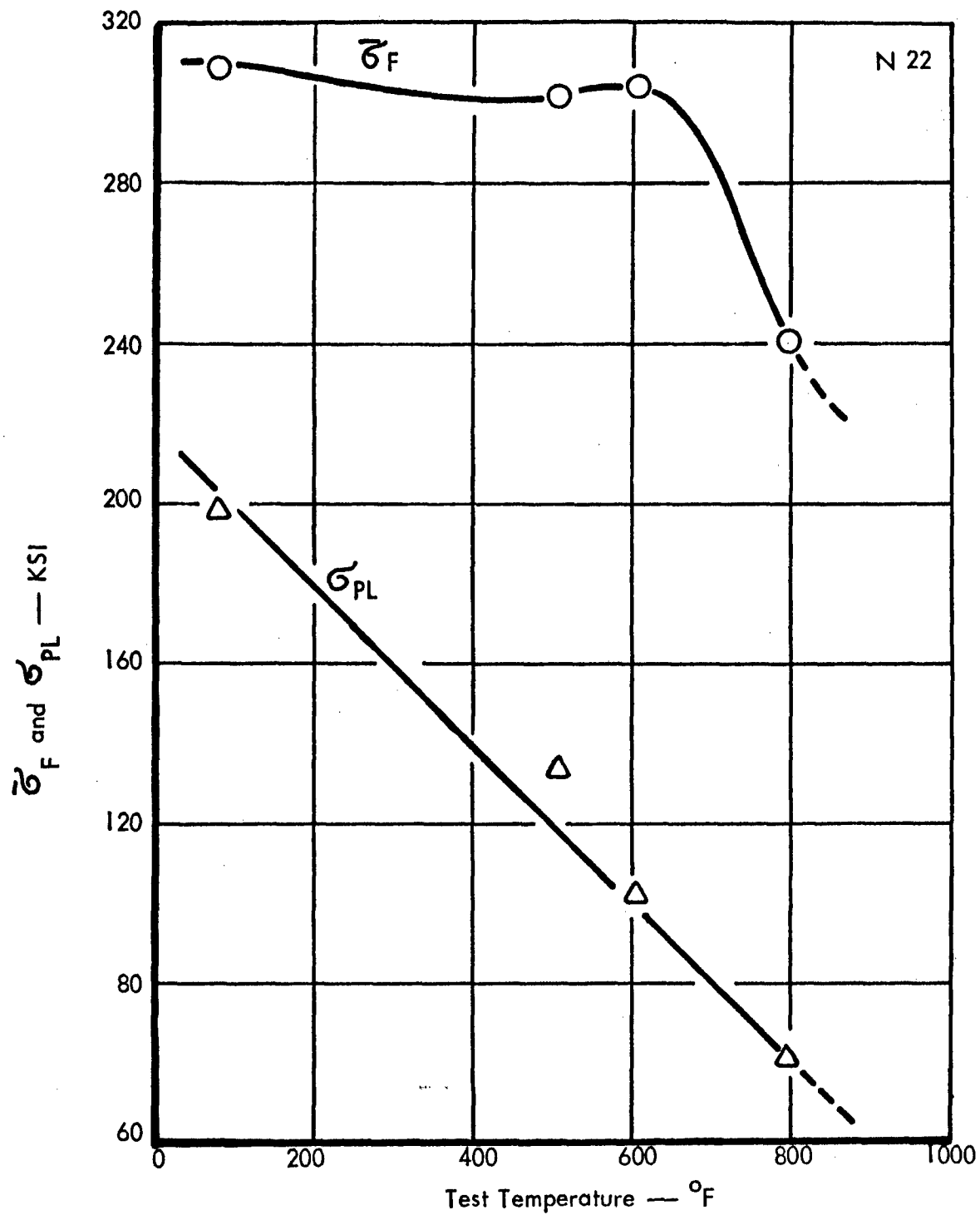


Figure 25. Effect of Test Temperature on $\bar{\sigma}_F$ and σ_{PL} for Non-lead N22 Material.

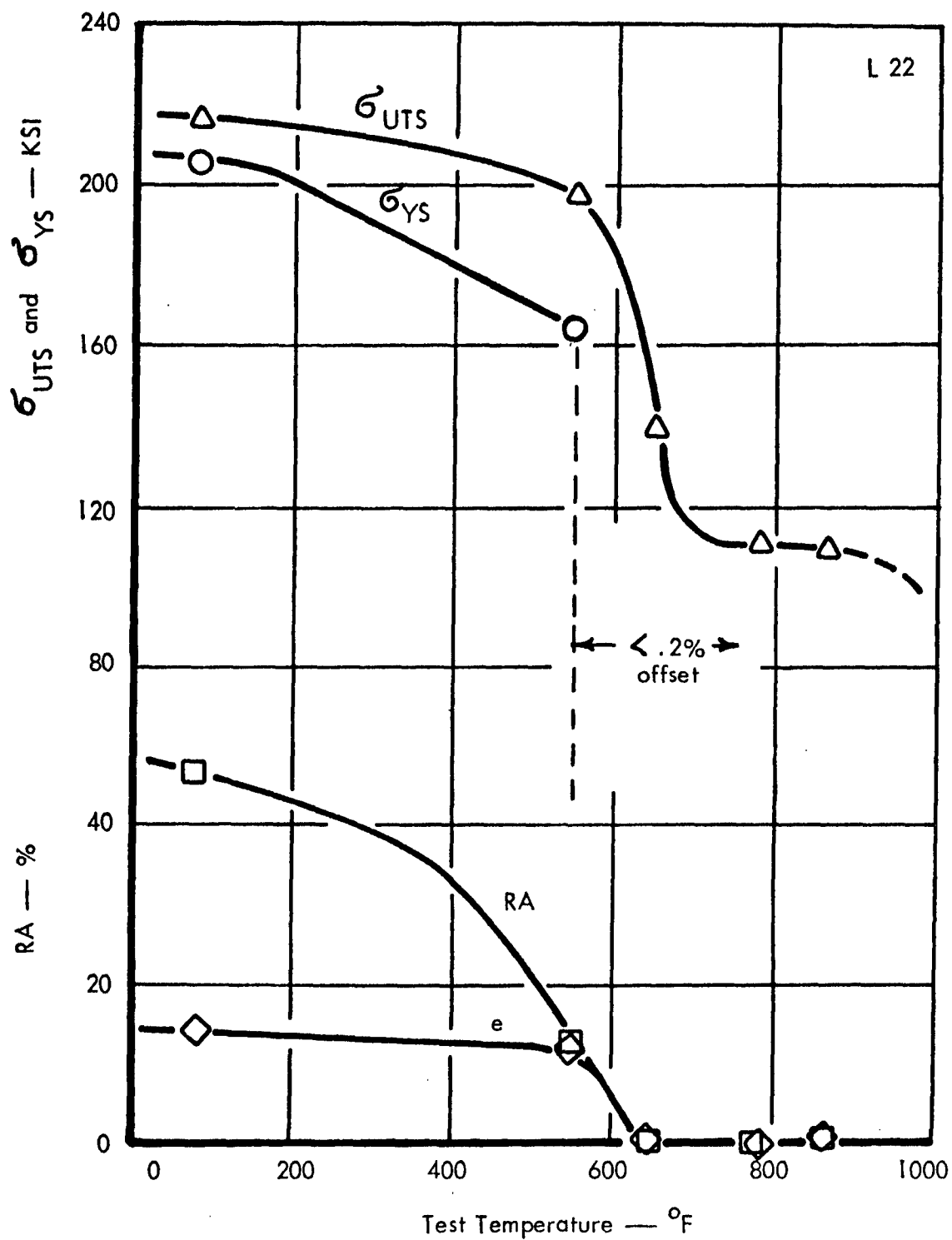


Figure 26. Engineering Tensile Properties of Lead L22 Material.

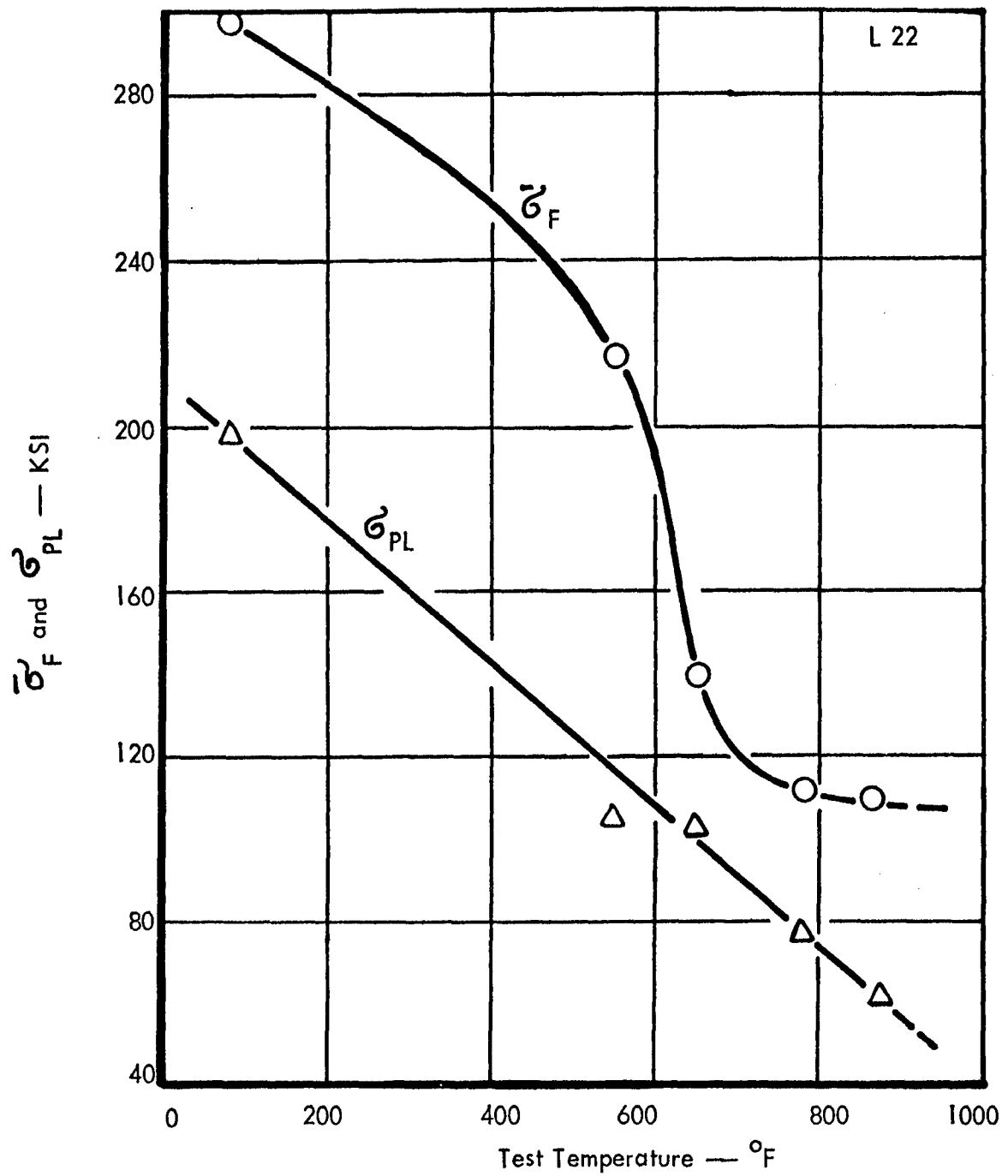


Figure 27. Effect of Test Temperature on σ_F and σ_{PL} for Leaded L22 Material.



N22; RT



L22; RT



N22; 505°F



L22; 550°F

Figure 28. Tensile Fracture Surfaces of Leaded and Non-leaded L22 and N22 Material Below 600°F.



N22; 605°F



L22; 650°F



N22; 790°F



L22; 780°F



L22; 865°F

Figure 29. Tensile Fracture Surfaces of Lead and Non-lead L22 and N22 Material Above 600°F.

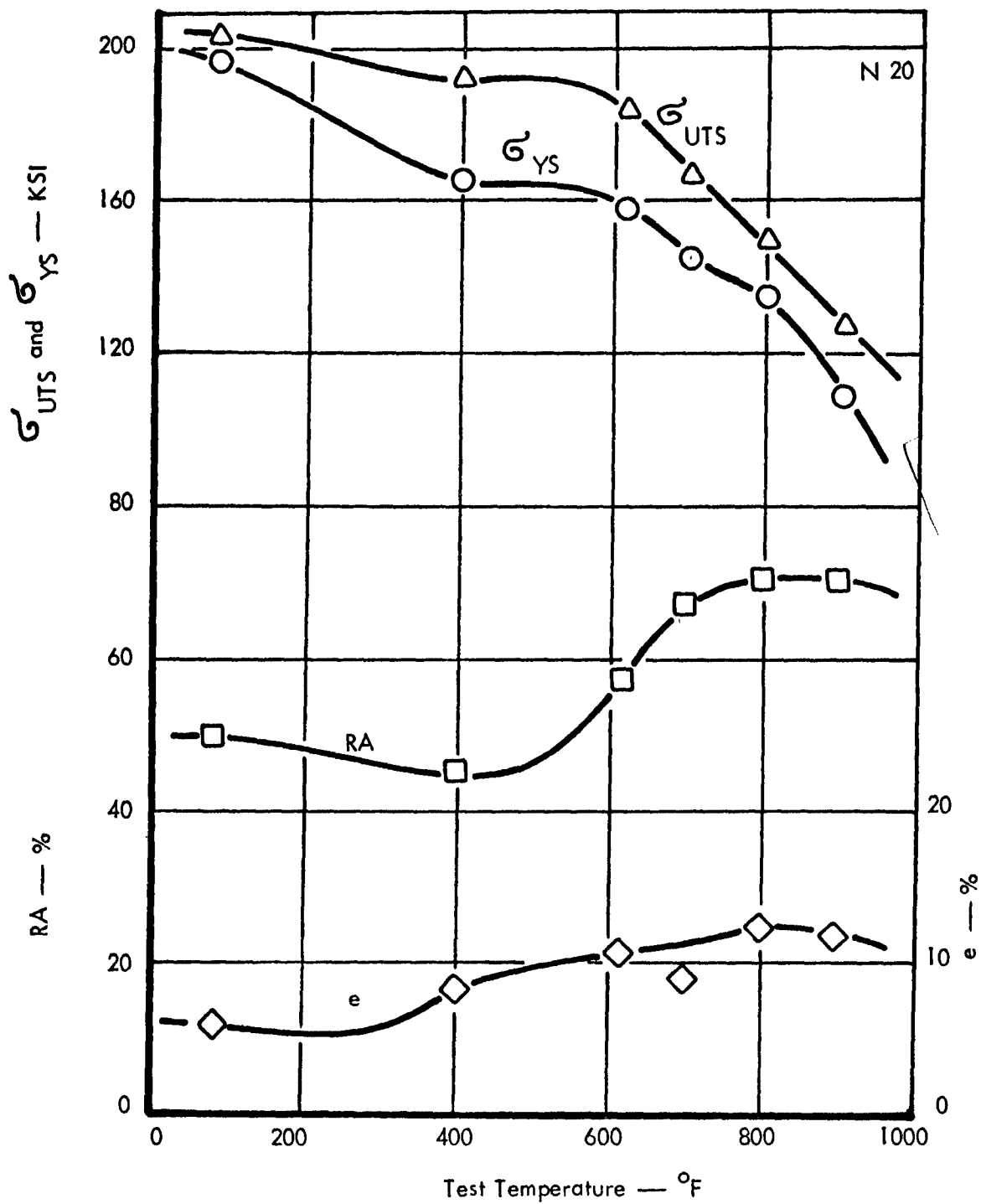


Figure 30. Engineering Tensile Properties of Non-lead N20 Material.

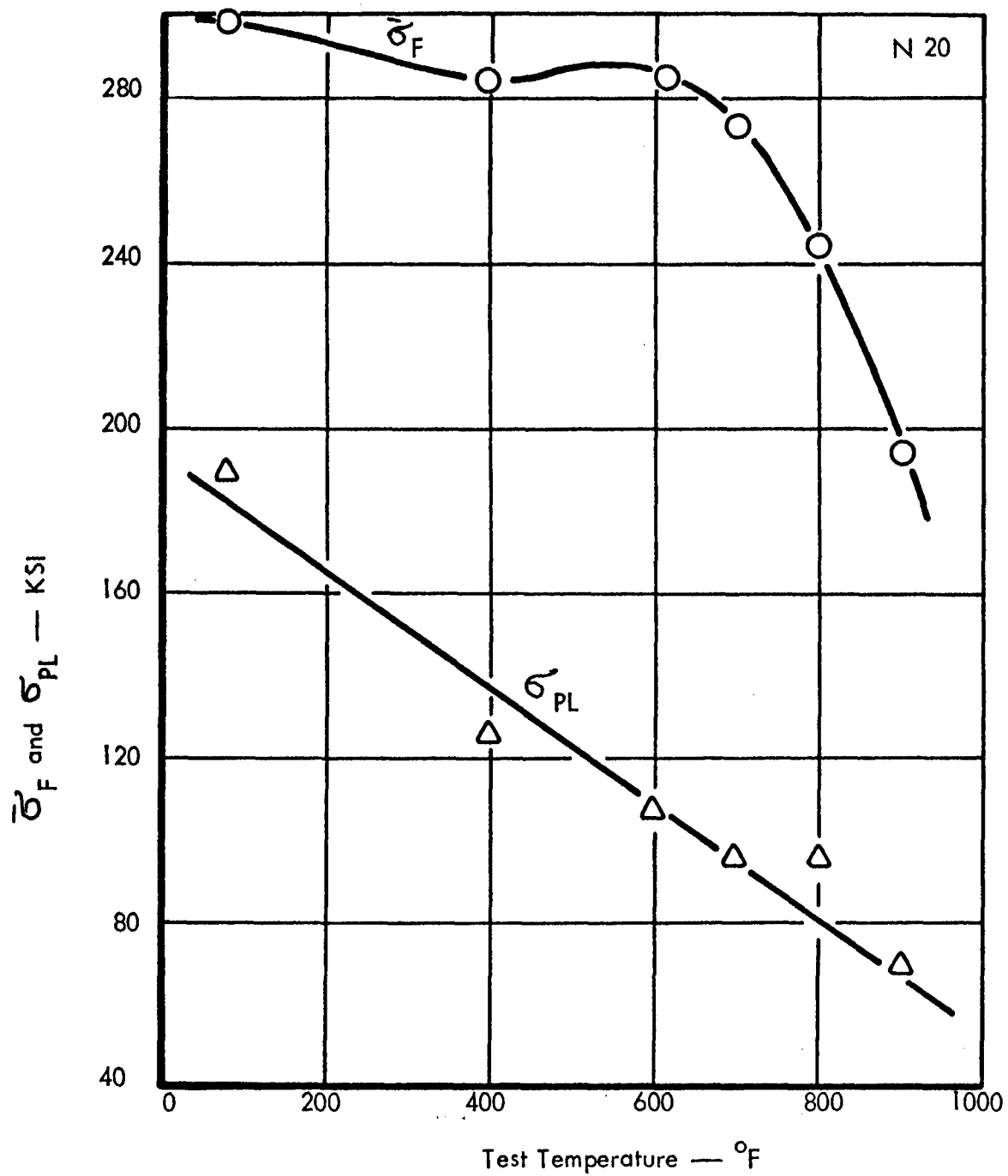


Figure 31. Effect of Test Temperature on $\bar{\sigma}_F$ and σ_{PL} for Non-lead N20 Material.

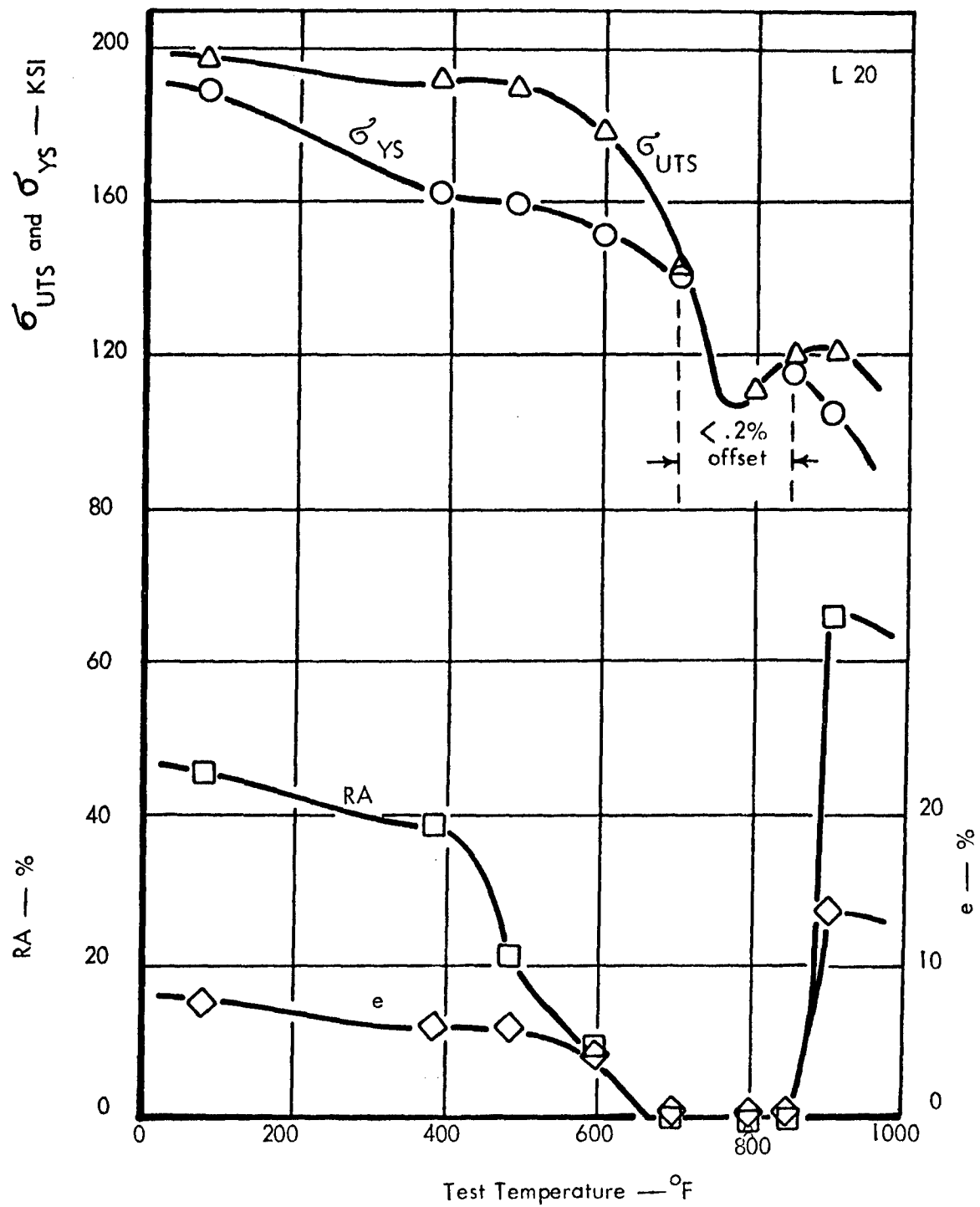


Figure 32. Engineering Tensile Properties of Lead L20 Material.

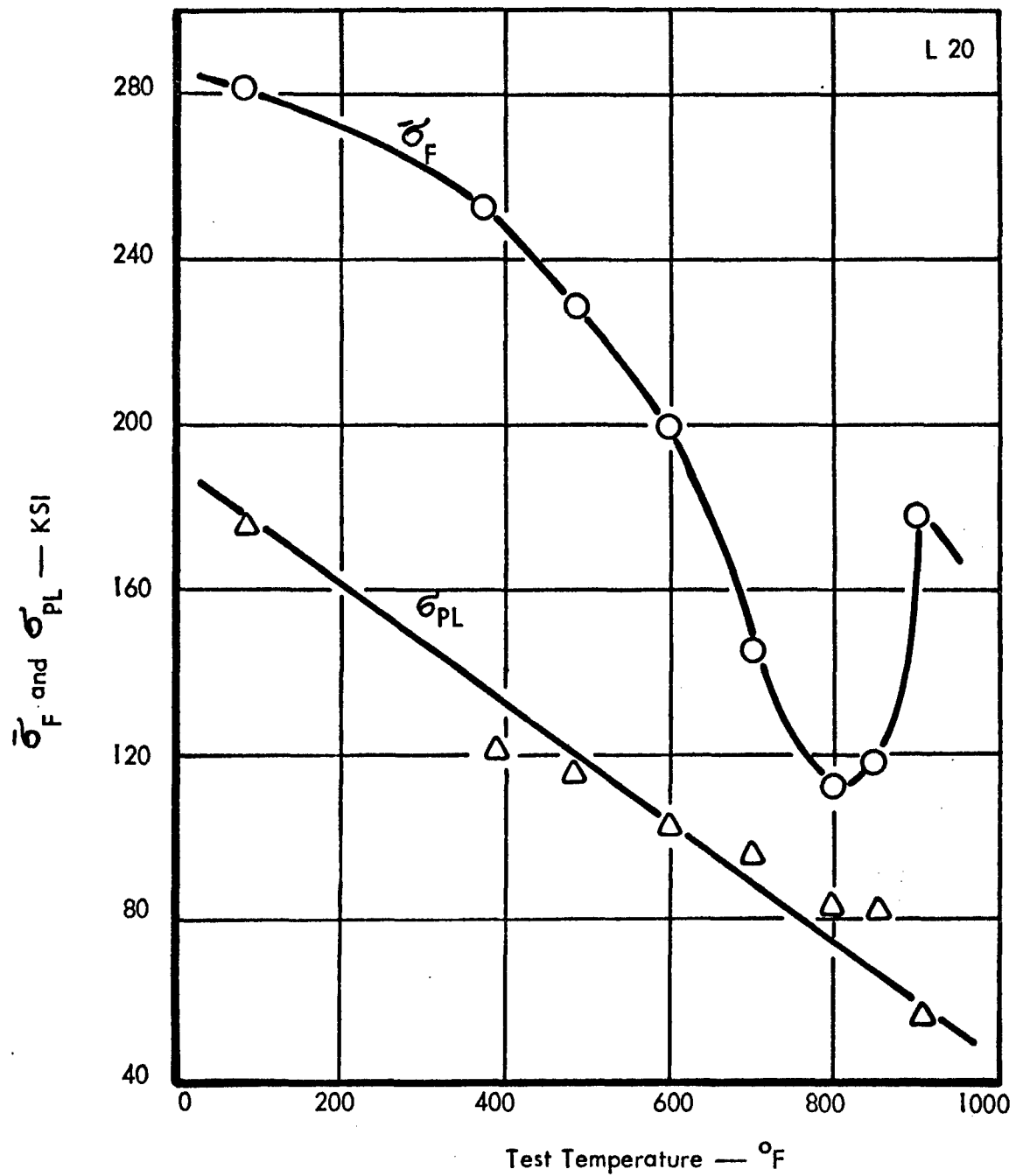
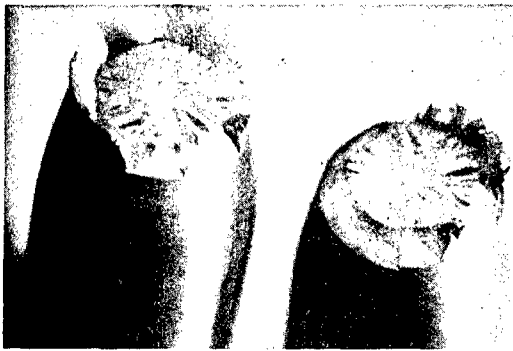
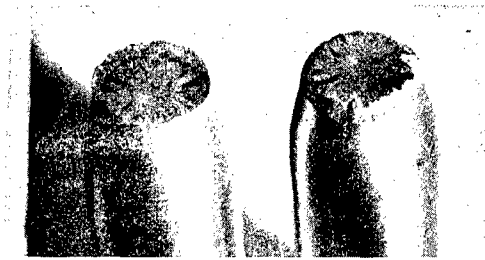


Figure 33. Effect of Test Temperature on σ_F and σ_{PL} for Leaded L20 Material.



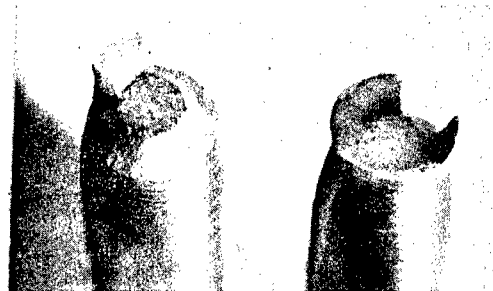
a) L20; 75°F



d) N20; 75°F



b) L20; 485°F



e) N20; 400°F

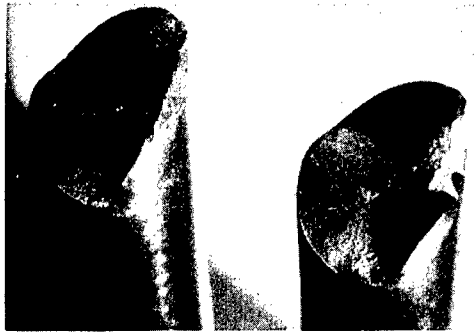


c) L20; 600°F



d) N20; 600°F

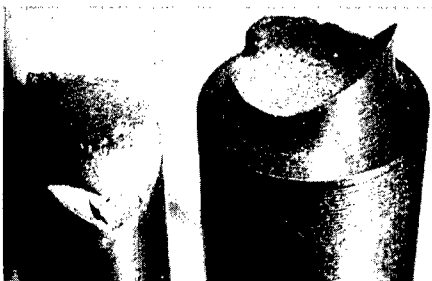
Figure 34. Effect of Test Temperature on Fracture Appearance of Leaded and Non-leaded L20 and N20 Steel.



a) L20; 710°F



c) N20; 700°F

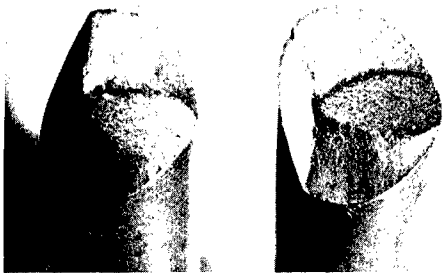


b) L20; 800°F

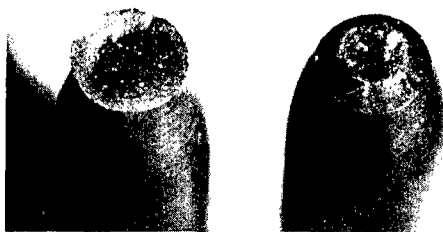


d) N20; 800°F

Figure 35. Effect of Test Temperature on Fracture Appearance of Lead and Non-lead L20 and N20 Steel.



a) L20; 850°F



b) L20; 900°F



c) N20; 900°F

Figure 36. Effect of Test Temperature on Fracture
Appearance of Lead and Non-lead AISI 4145
Steel Oil Quenched from 1525°F and Tempered at
940°F. L20 Are Lead; N20 Are Not Lead.

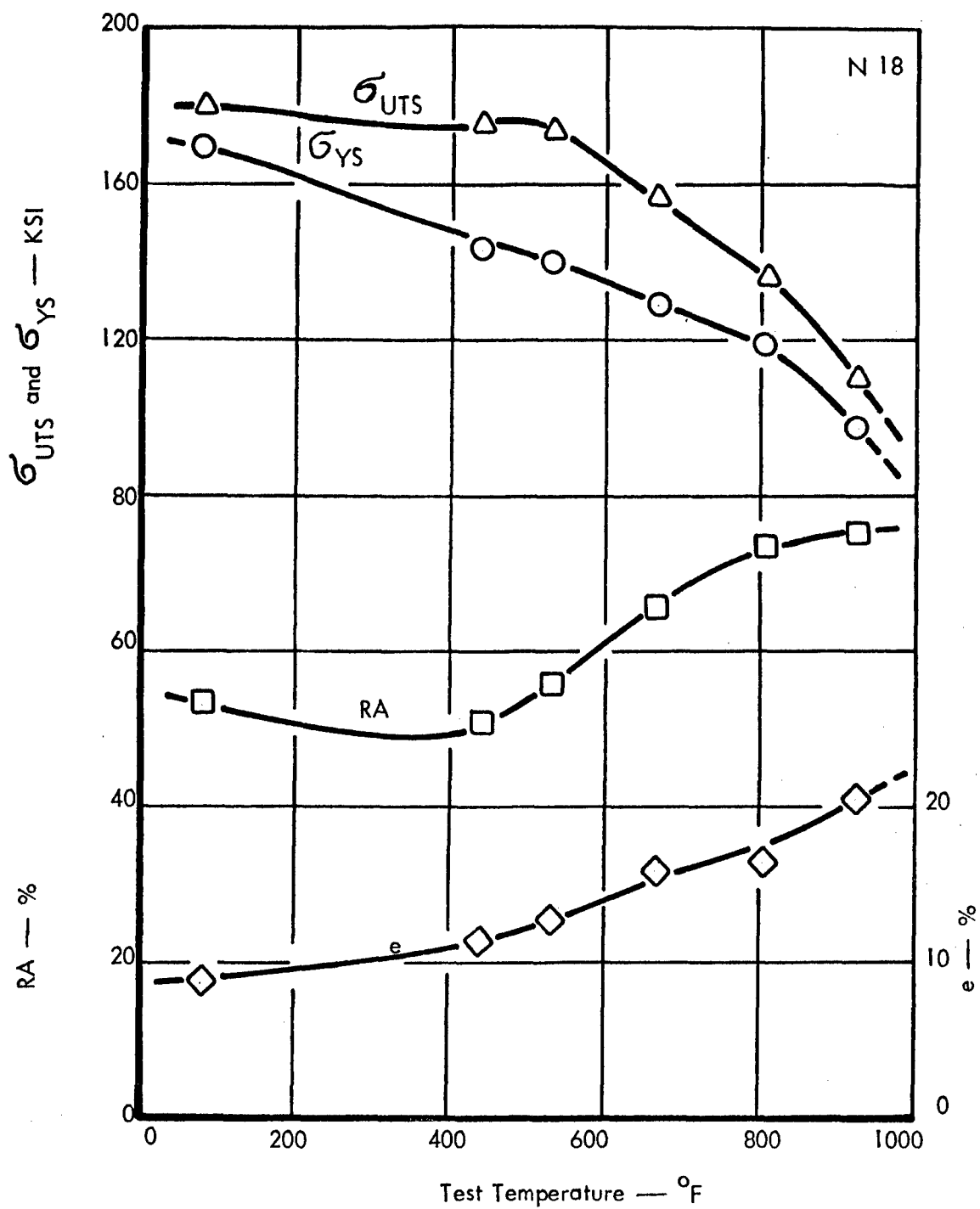


Figure 37. Engineering Tensile Properties of Non-leaded N18 Material.

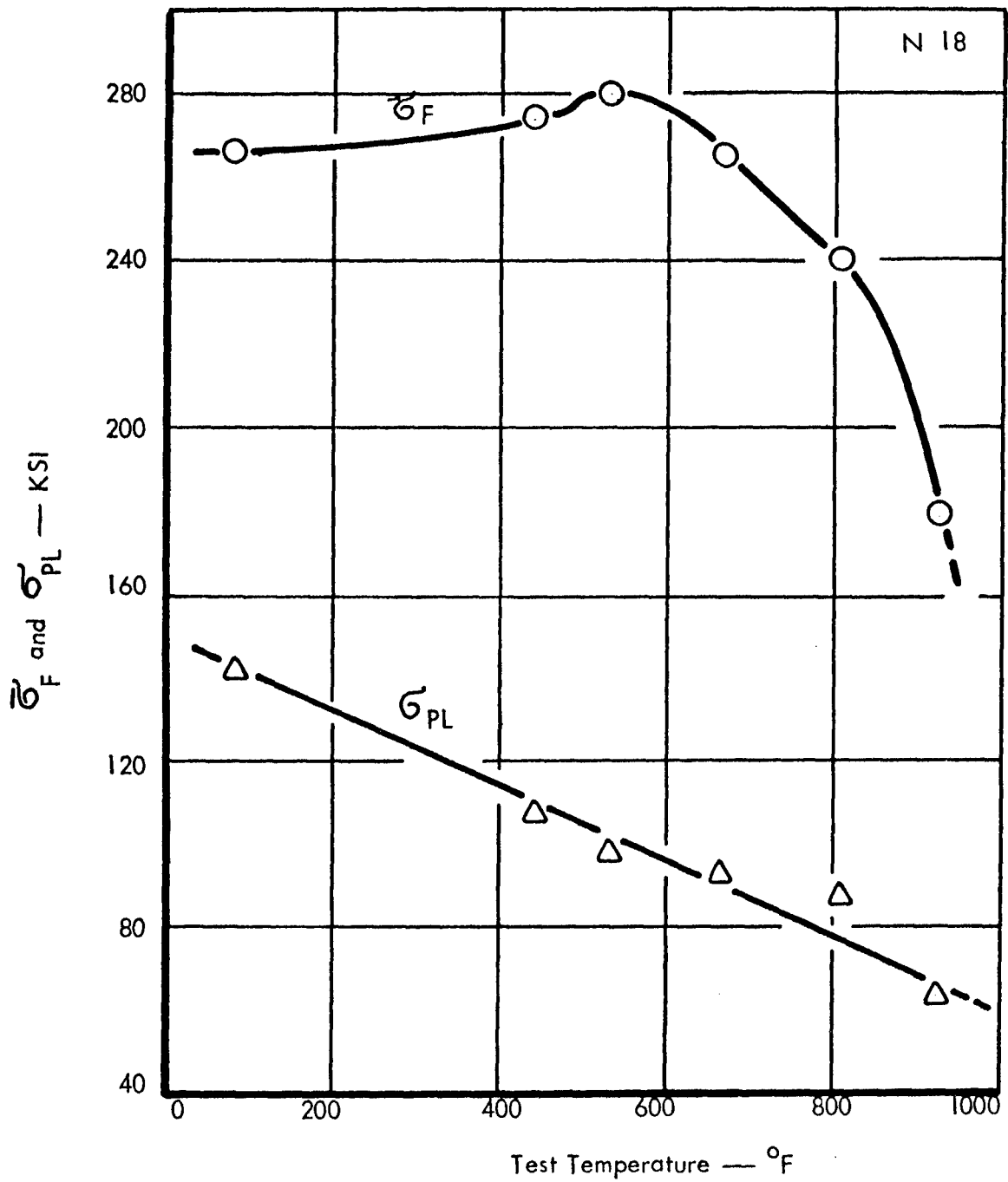


Figure 38. Effect of Test Temperature on σ_F and σ_{PL} for Non-lead N18 Material.

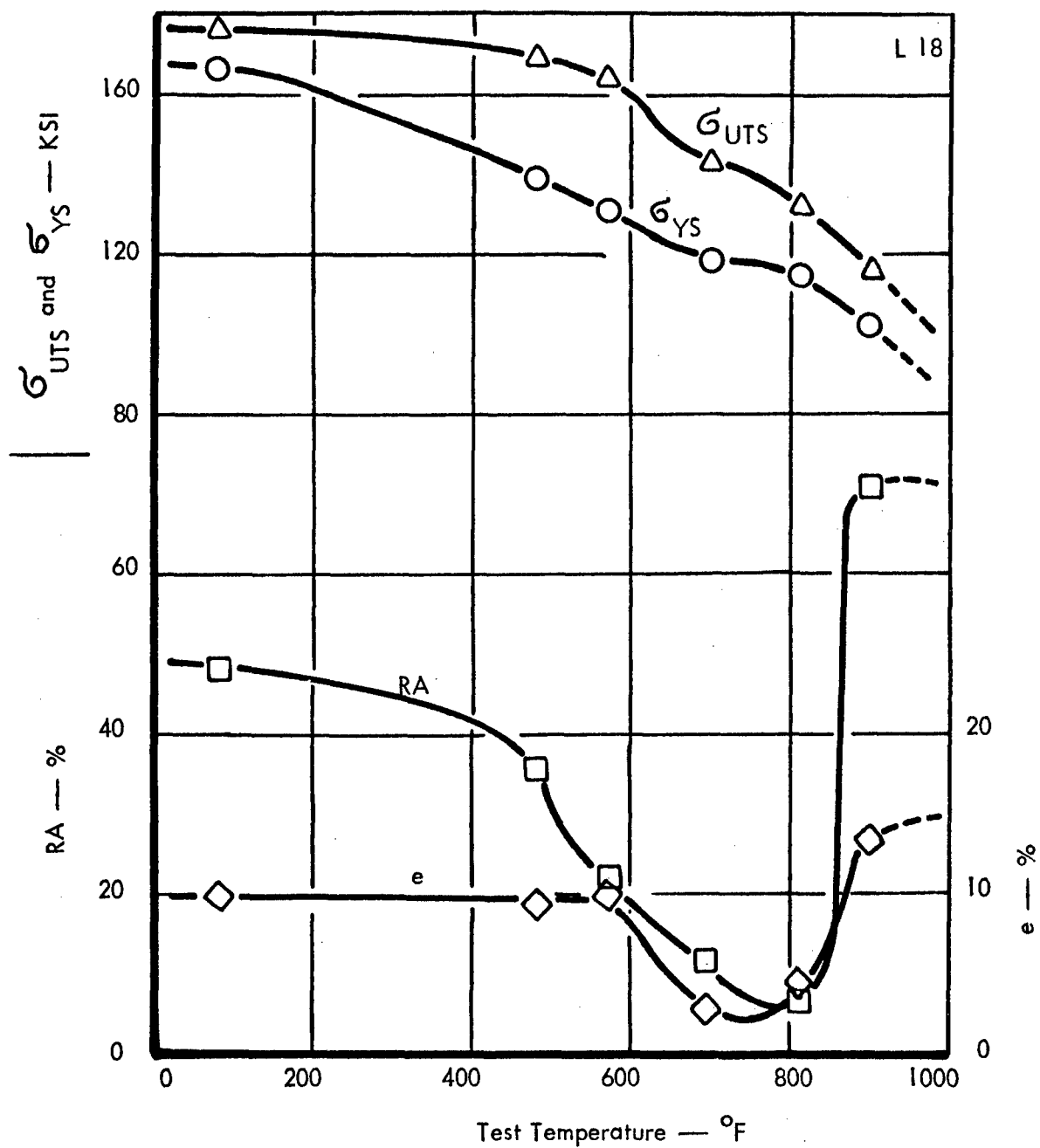


Figure 39. Engineering Tensile Properties of Lead L18 Material.

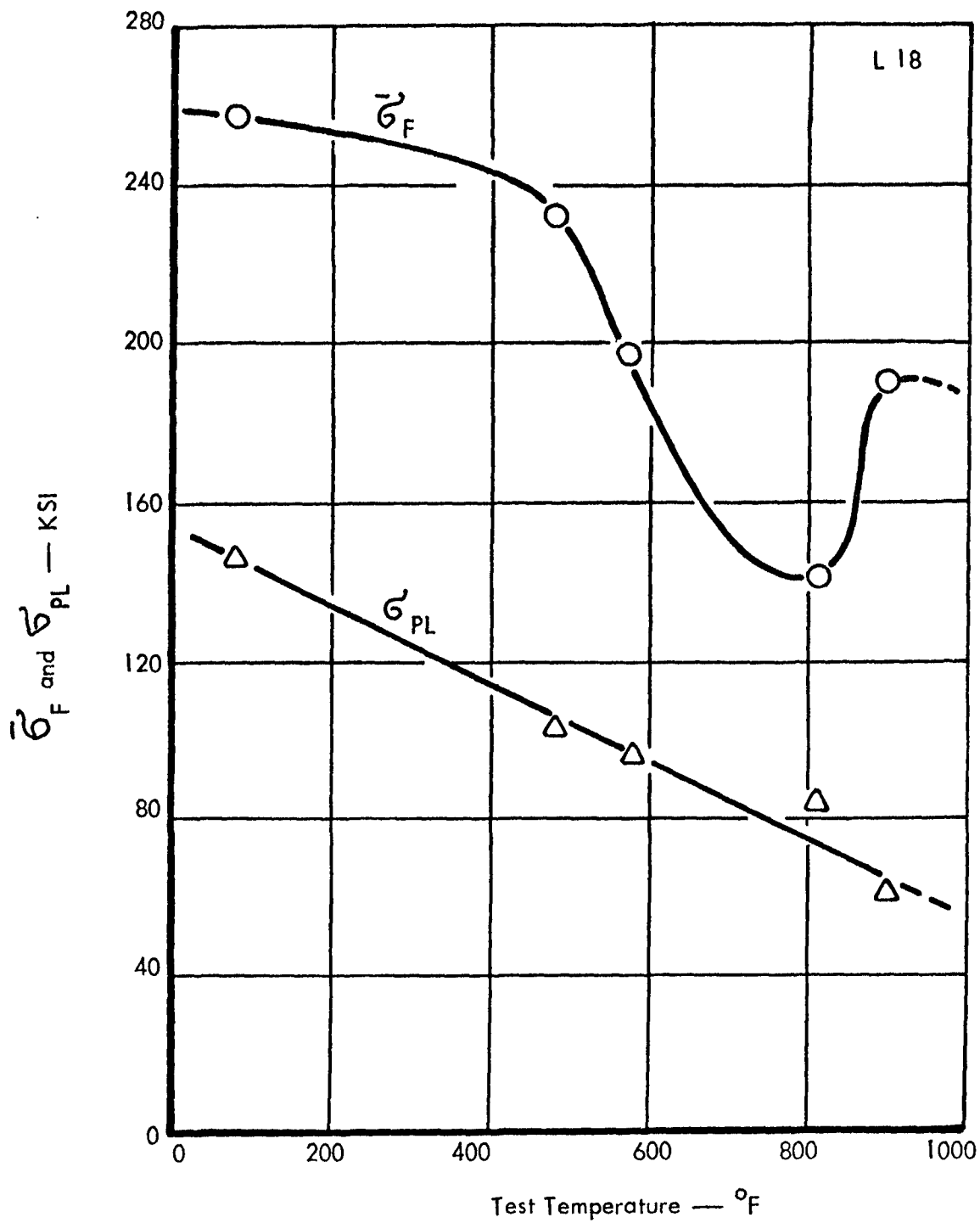


Figure 40. Effect of Test Temperature on $\bar{\sigma}_F$ and σ_{PL} for Leded L18 Material.



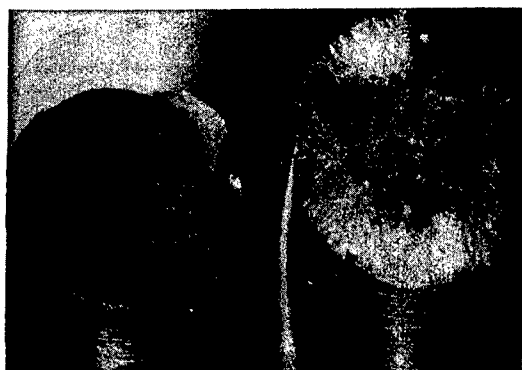
N18; RT



L18; RT



N18; 440°F



L18; 480°F



N18; 530°F



L18; 570°F

Figure 41. Tensile Fracture Surfaces of Leaded and Non-leaded L18 and N18 Material Below 650°F.



N18; 665°F



L18; 690°F



N18; 807°F



L18; 812°F



N18; 925°F



L18; 900°F

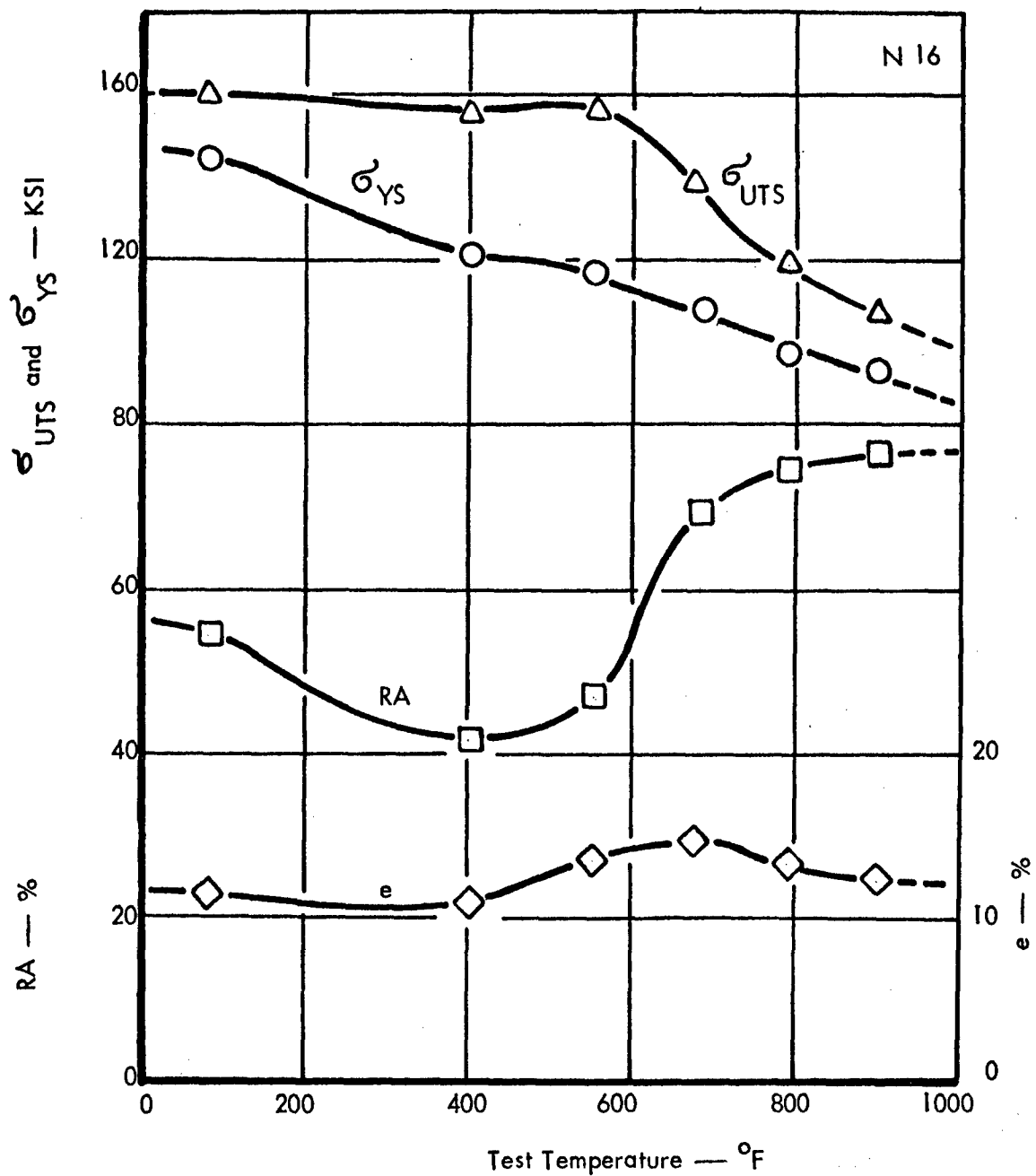


Figure 43. Engineering Tensile Properties of Non-leaded N16 Material.

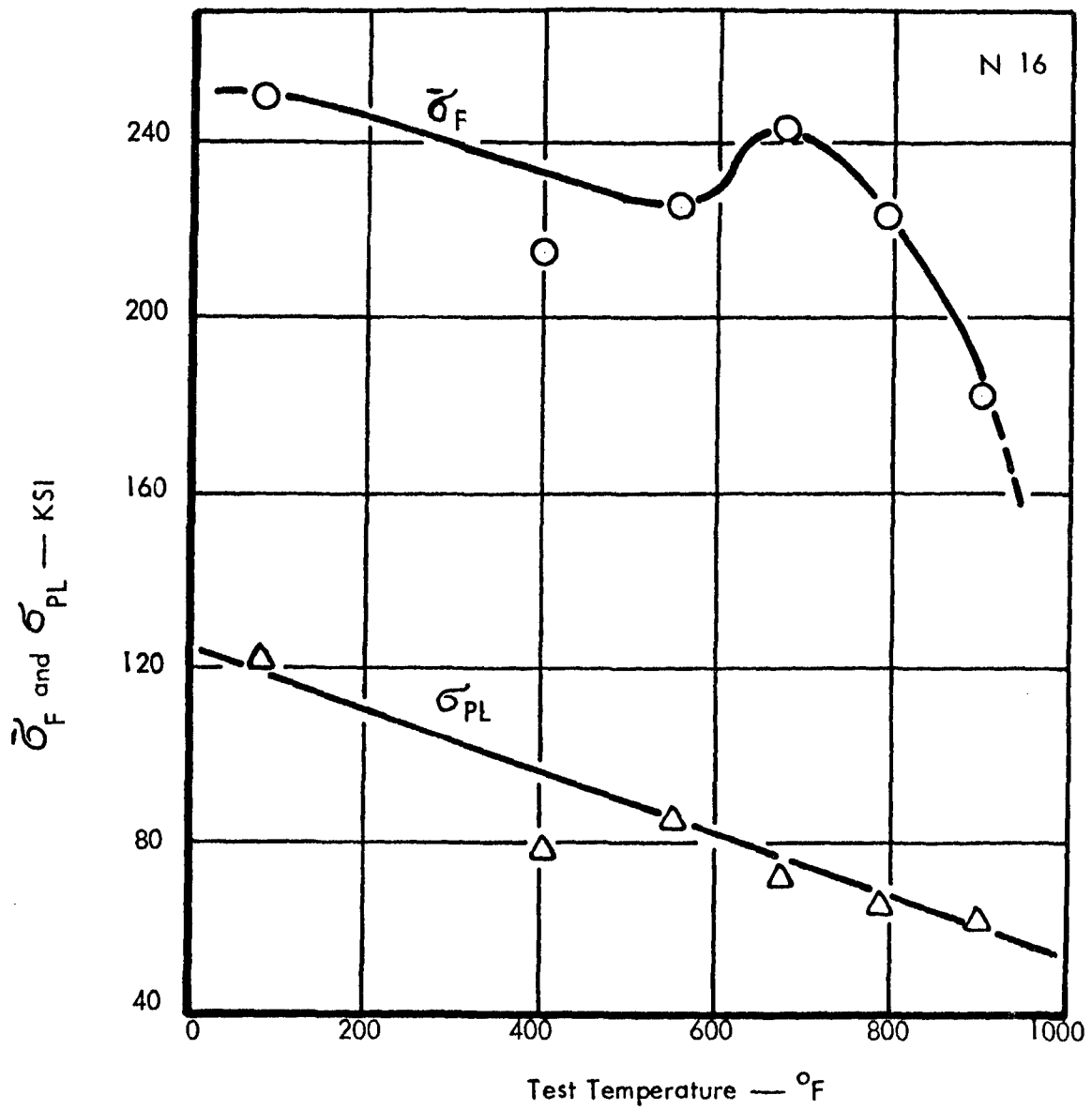


Figure 44. Effect of Test Temperature on $\bar{\sigma}_F$ and σ_{PL} for Non-leaded N16 Material.

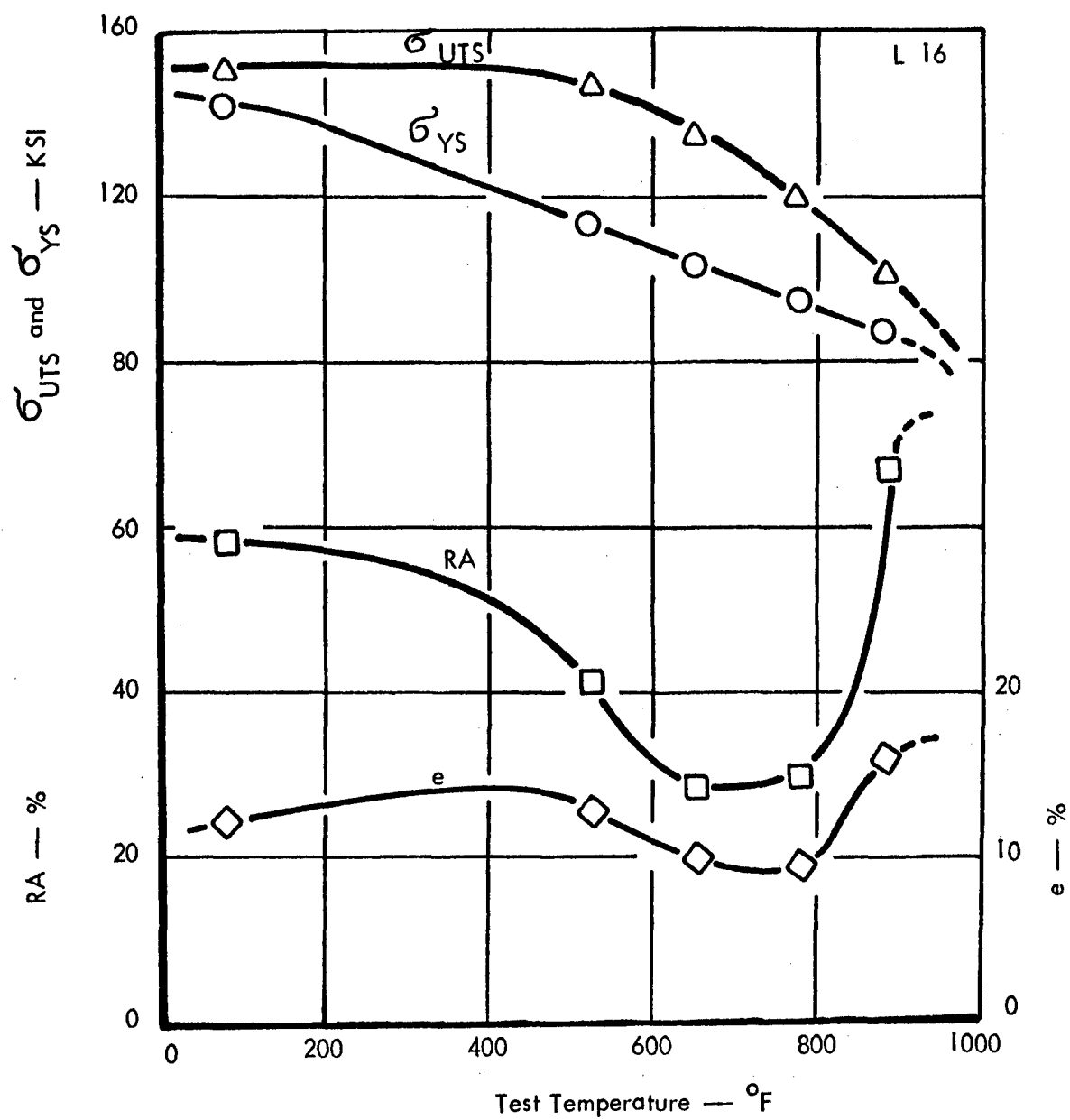


Figure 45. Engineering Tensile Properties of Lead L16 Material.

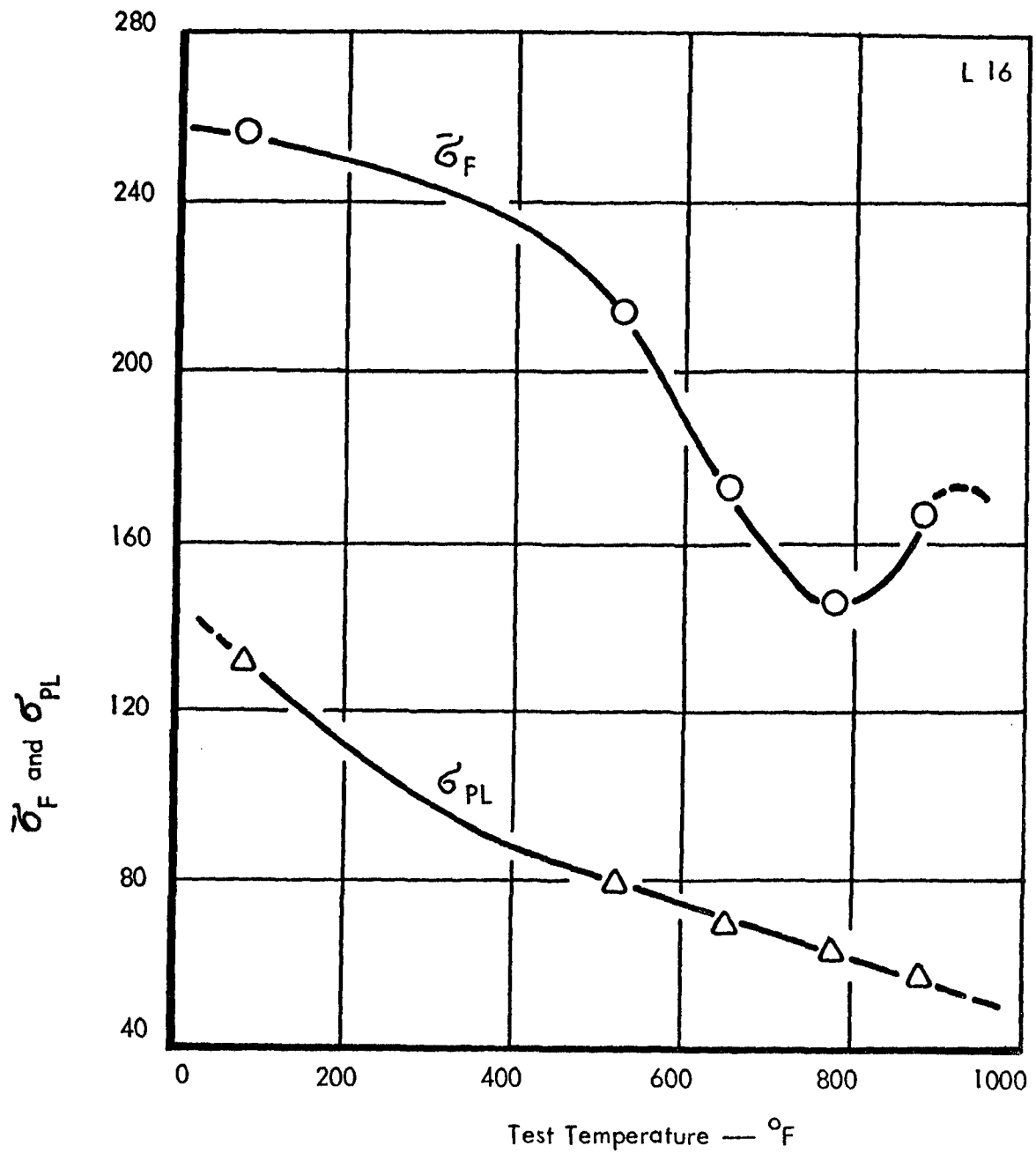


Figure 46. Effect of Test Temperature on $\bar{\sigma}_F$ and σ_{PL} for Leaded L16 Material.



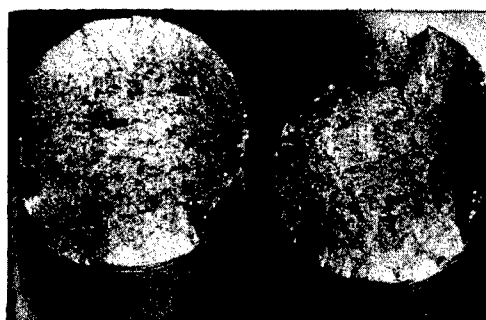
N16; RT



L16; RT



N16; 400°F



L16; 525°F



N16; 550°F

Figure 47. Tensile Fracture Surfaces of Leaded and Non-leaded L16 and N16 Material Below 650°F.



N16; 675°F



L16; 650°F



N16; 790°F



L16; 775°F



N16; 900°F



L16; 880°F

Figure 48. Tensile Fracture Surfaces of Leaded and Non-leaded L16 and N16 Material Above 650°F.

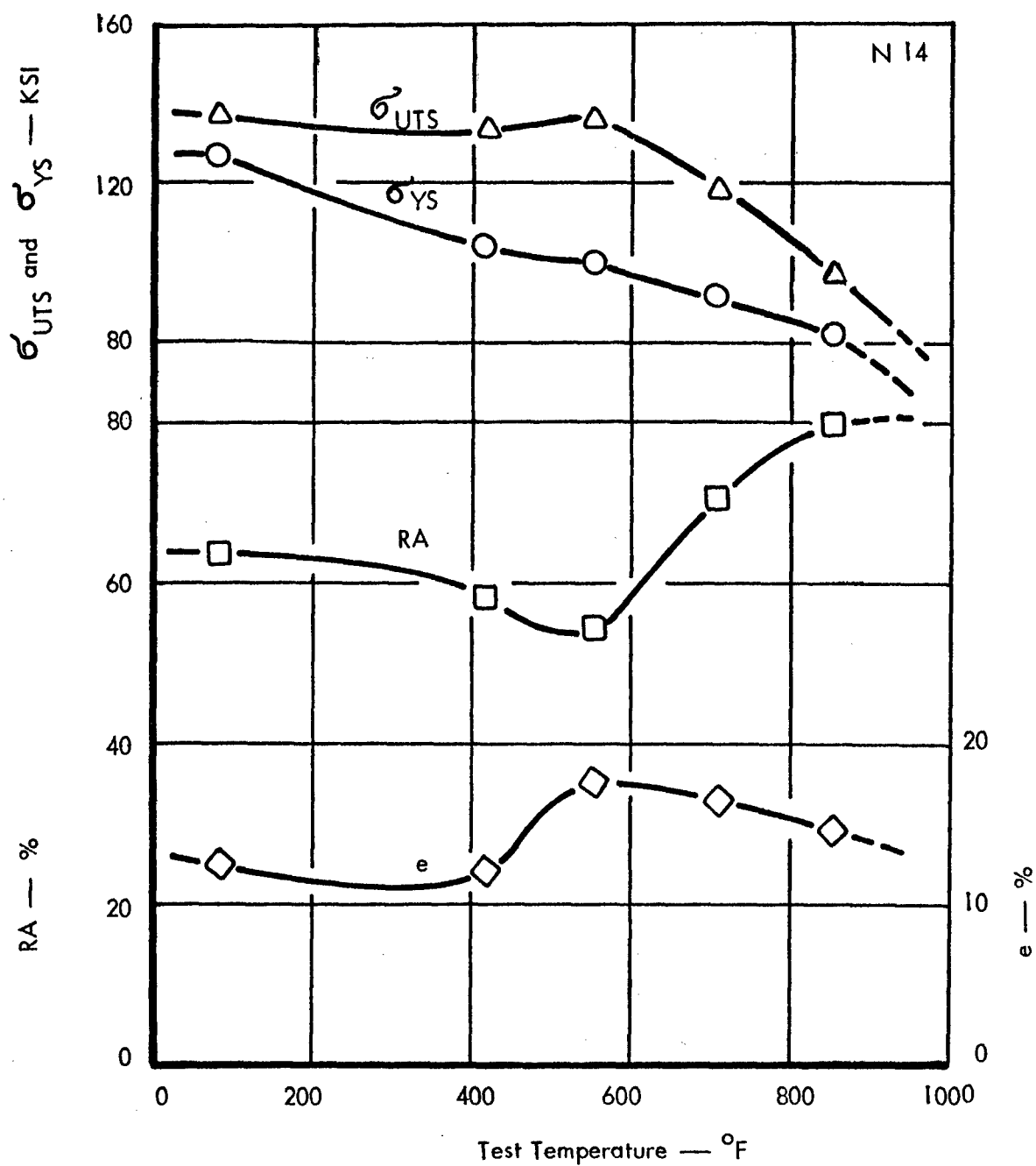


Figure 49. Engineering Tensile Properties of Non-leaded N14 Material.

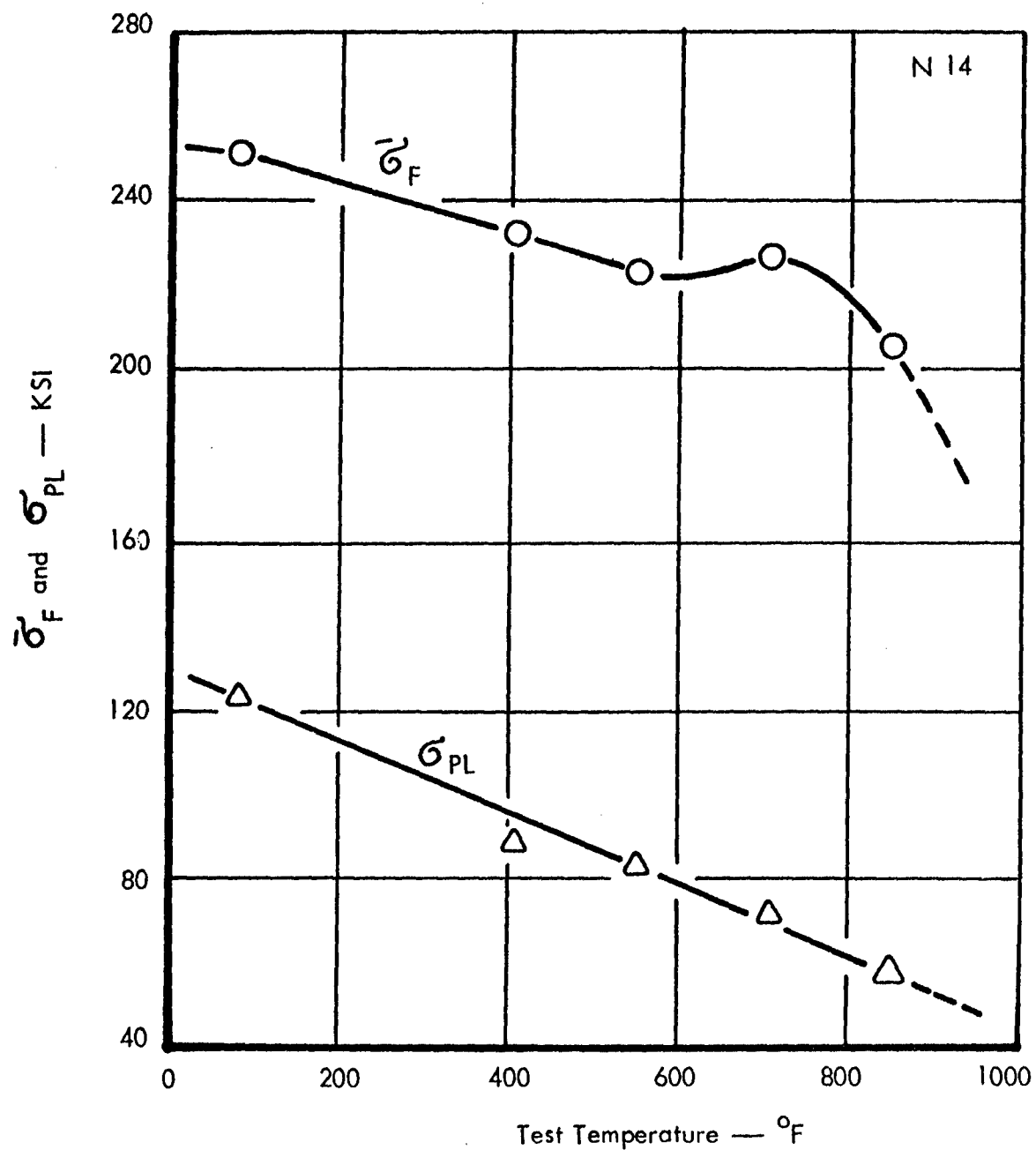


Figure 50. Effect of Test Temperature on $\bar{\sigma}_F$ and σ_{PL} for Non-leaded N14 Material.

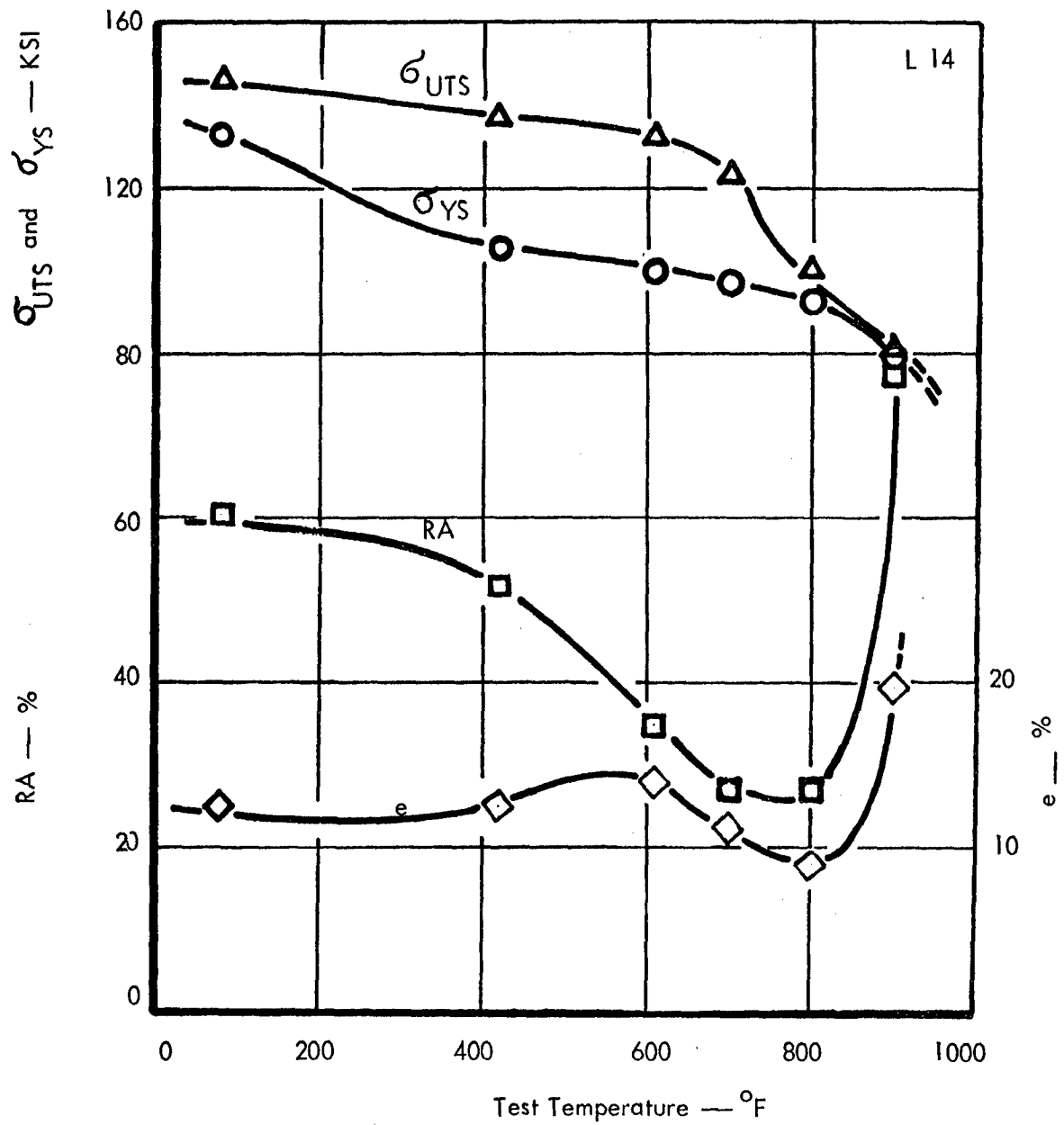


Figure 51. Engineering Tensile Properties of Lead L14 Material.

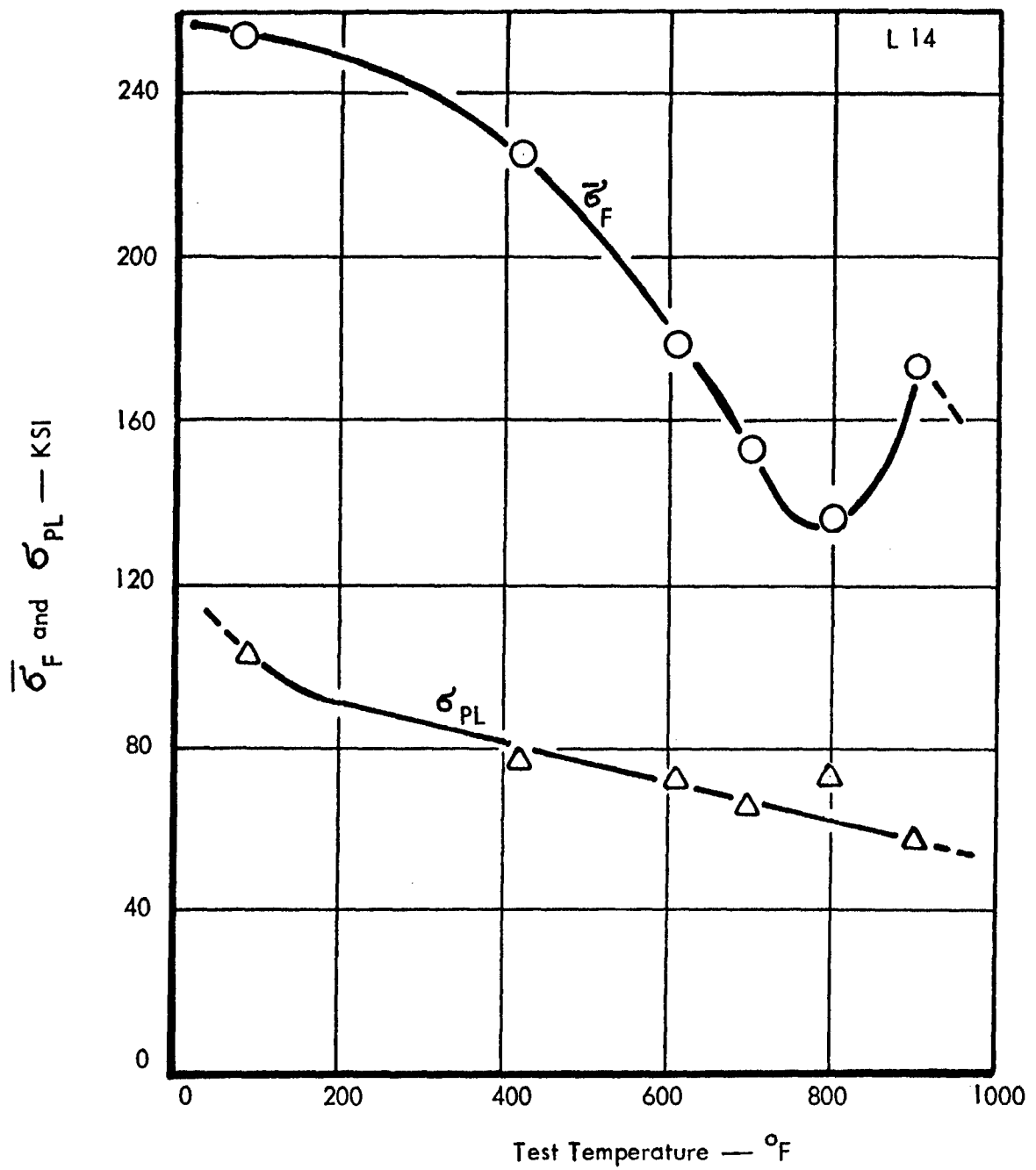


Figure 52. Effect of Test Temperature on $\bar{\sigma}_F$ and σ_{PL} for Leaded L14 Material.



N14; RT



L14; RT



N14; 415°F



L14; 420°F



N14; 550°F



L14; 610°F

Figure 53. Tensile Fracture Surfaces of Leaded and Non-leaded L14 and N14 Material Below 620°F.



N14; 705°F



L14; 700°F



L14; 800°F



N14; 850°F



L14; 900°F

Figure 54. Tensile Fracture Surfaces of Leaded and Non-leaded L14 and N14 Material Above 620°F.

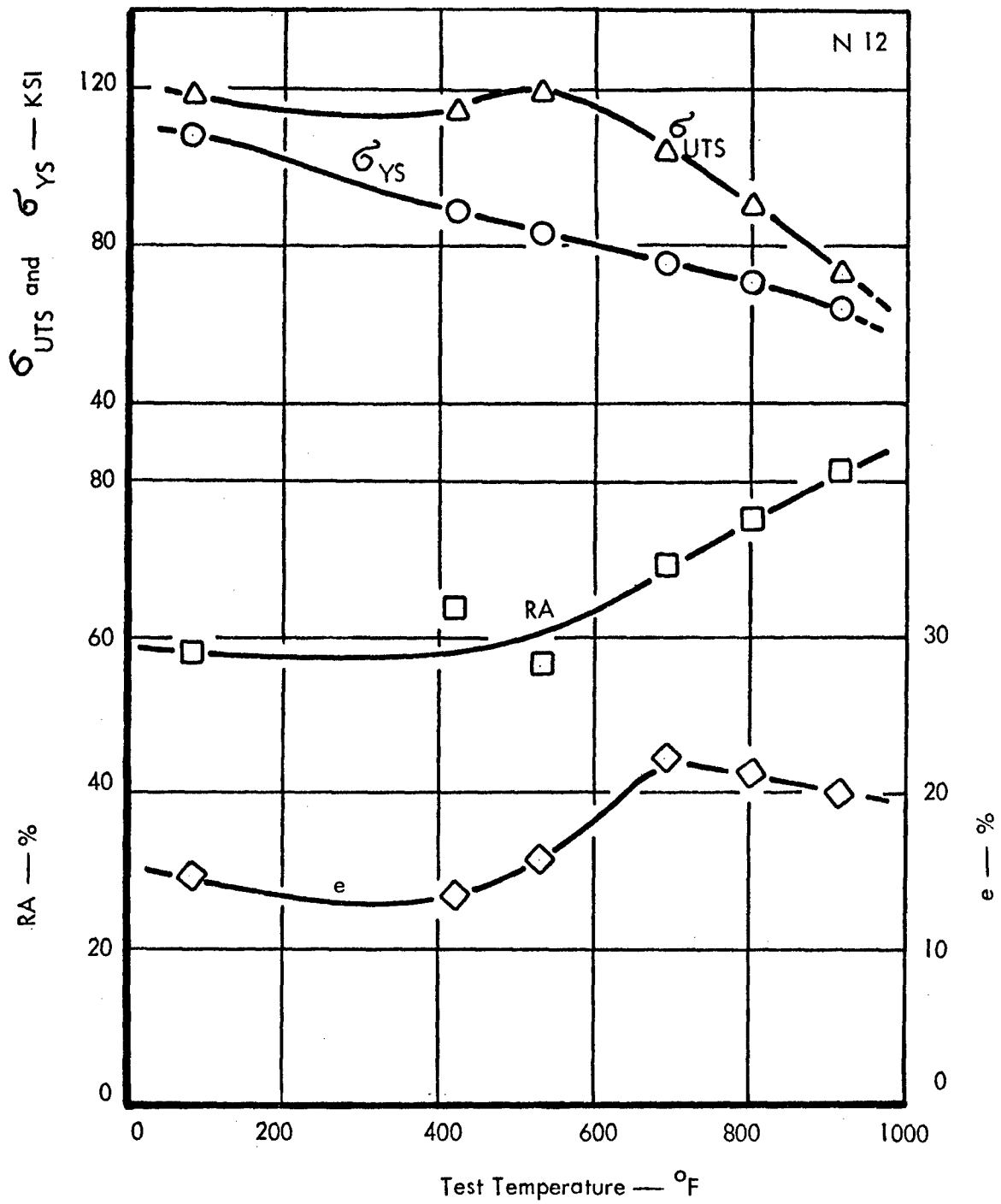


Figure 55. Engineering Tensile Properties of Non-leaded N12 Material.

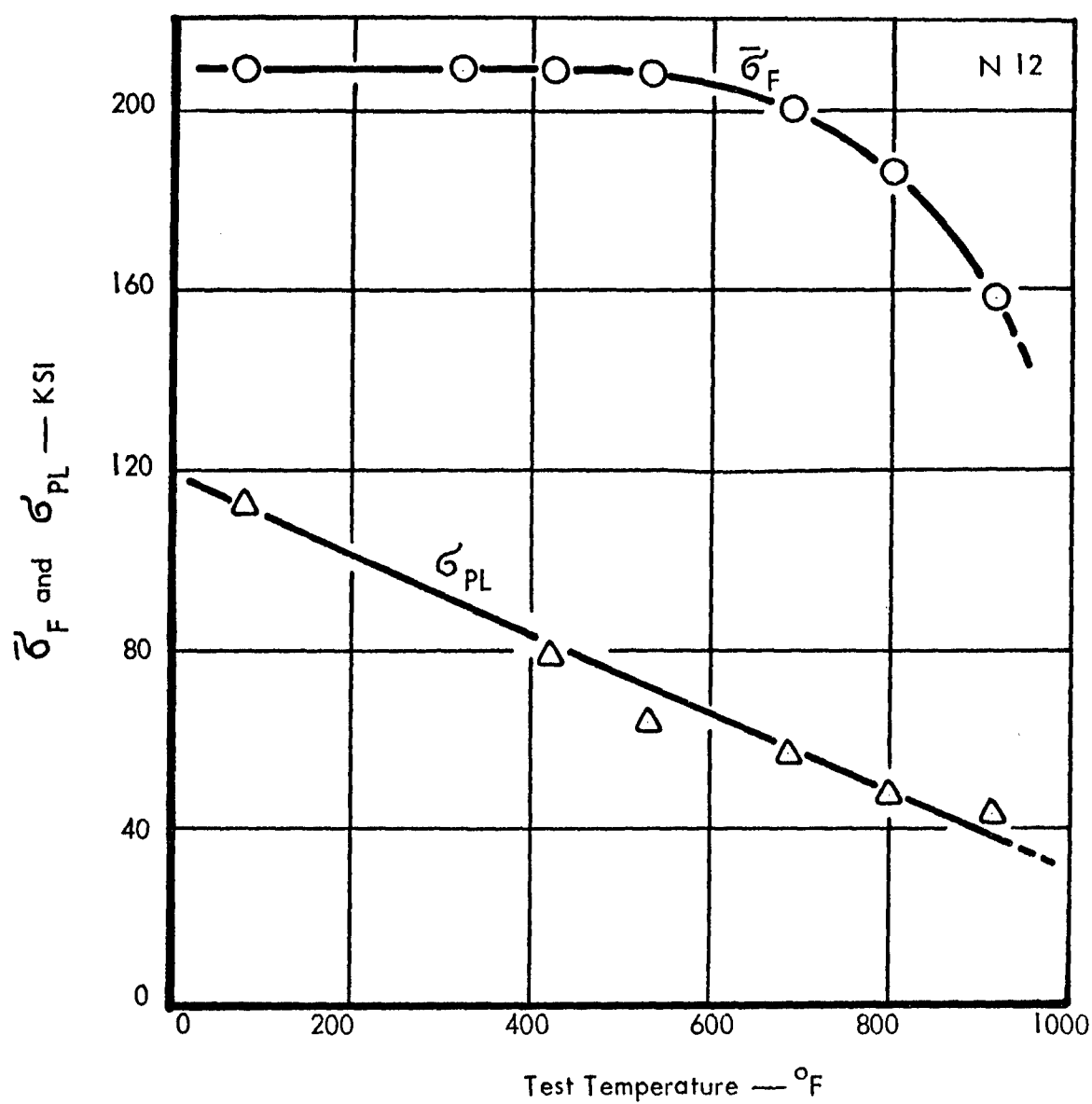


Figure 56. Effect of Test Temperature on $\bar{\sigma}_F$ and σ_{PL} for Non-leaded N12 Material.

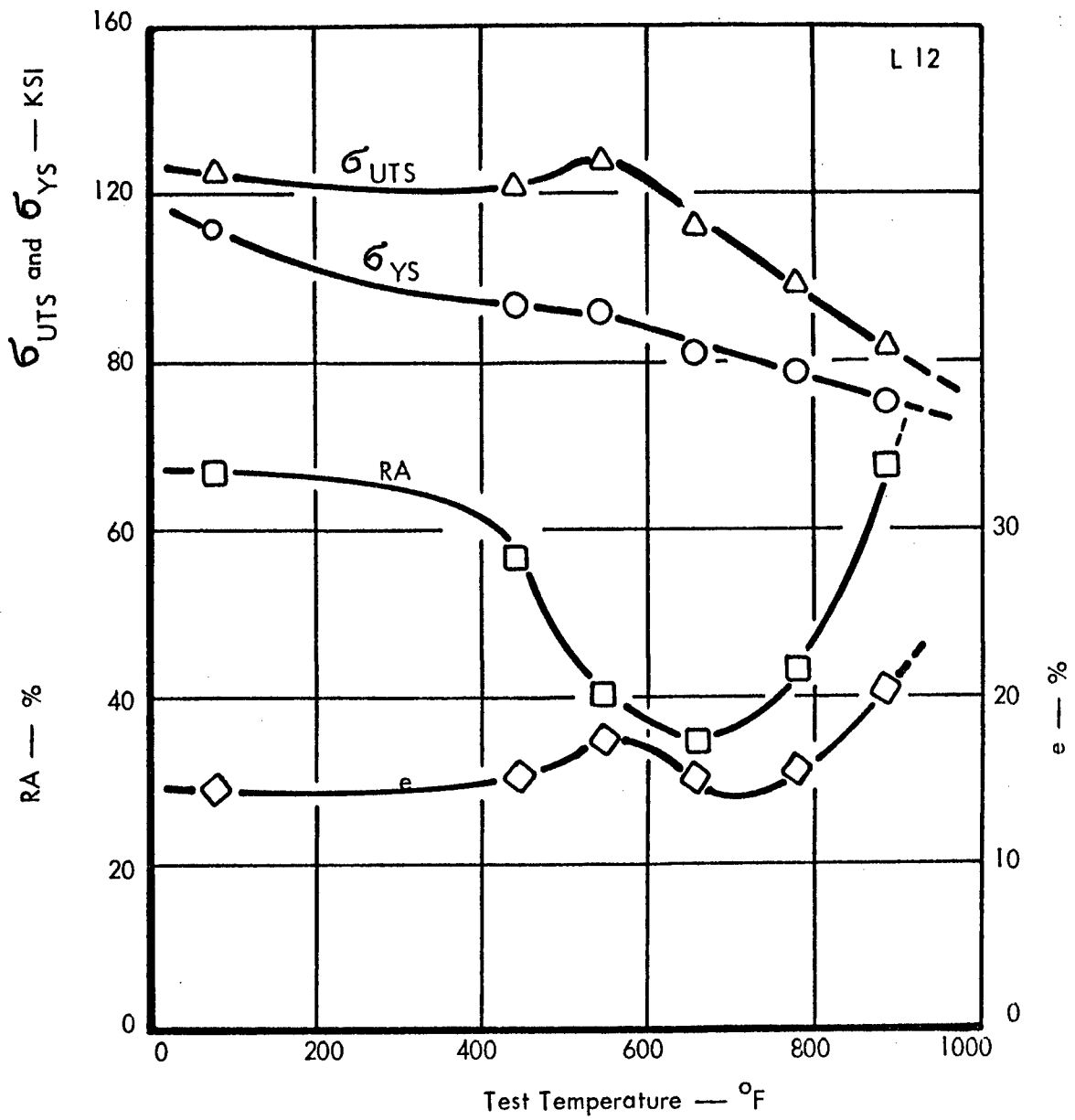


Figure 57. Engineering Tensile Properties of Lead L12 Material.

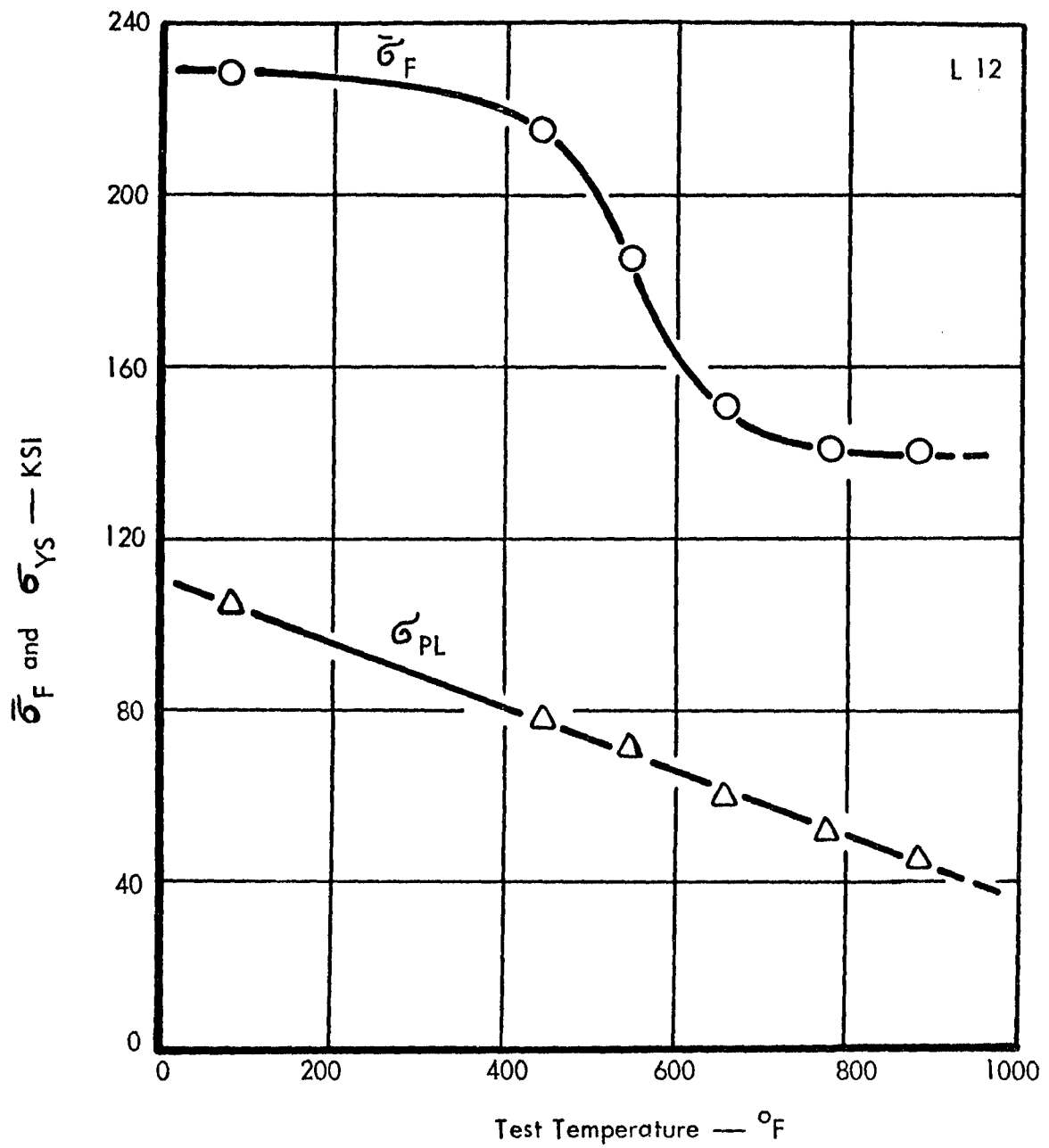


Figure 58. Effect of Test Temperature on $\bar{\sigma}_F$ and σ_{PL} for Leaded L12 Material.



N12; RT



L12; RT



N12; 420°F



L12; 440°F



N12; 530°F



L12; 545°F

Figure 59. Tensile Fracture Surfaces of Leaded and Non-leaded L12 and N12 Material Below 620°F.



N12; 690°F



L12; 655°F



N12; 800°F



L12; 775°F



N12; 915°F



L12; 882°F

Figure 60. Tensile Fracture Surfaces of Leaded and Non-leaded L12 and N12 Material Above 620°F.

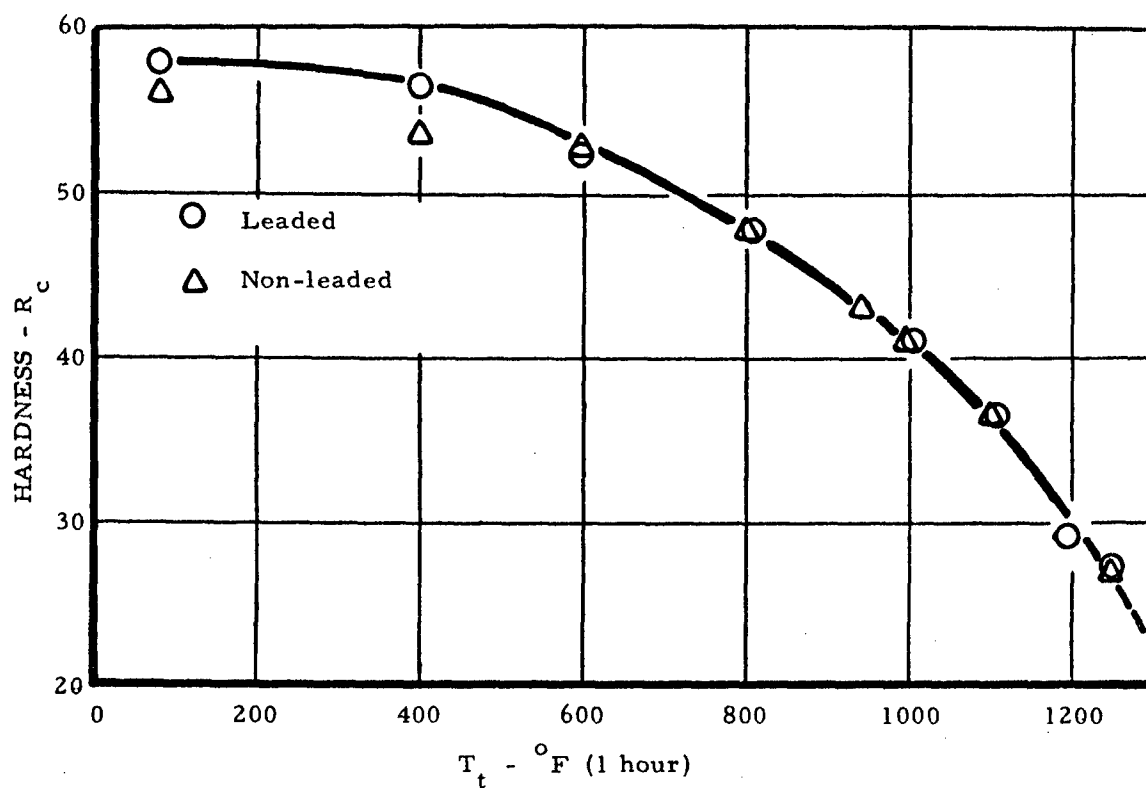


Figure 61. Hardness, R_c, vs. Tempering Temperature, T_t, for Lead and Non-lead AISI 4145 Steel Oil Quenched from 1525°F.

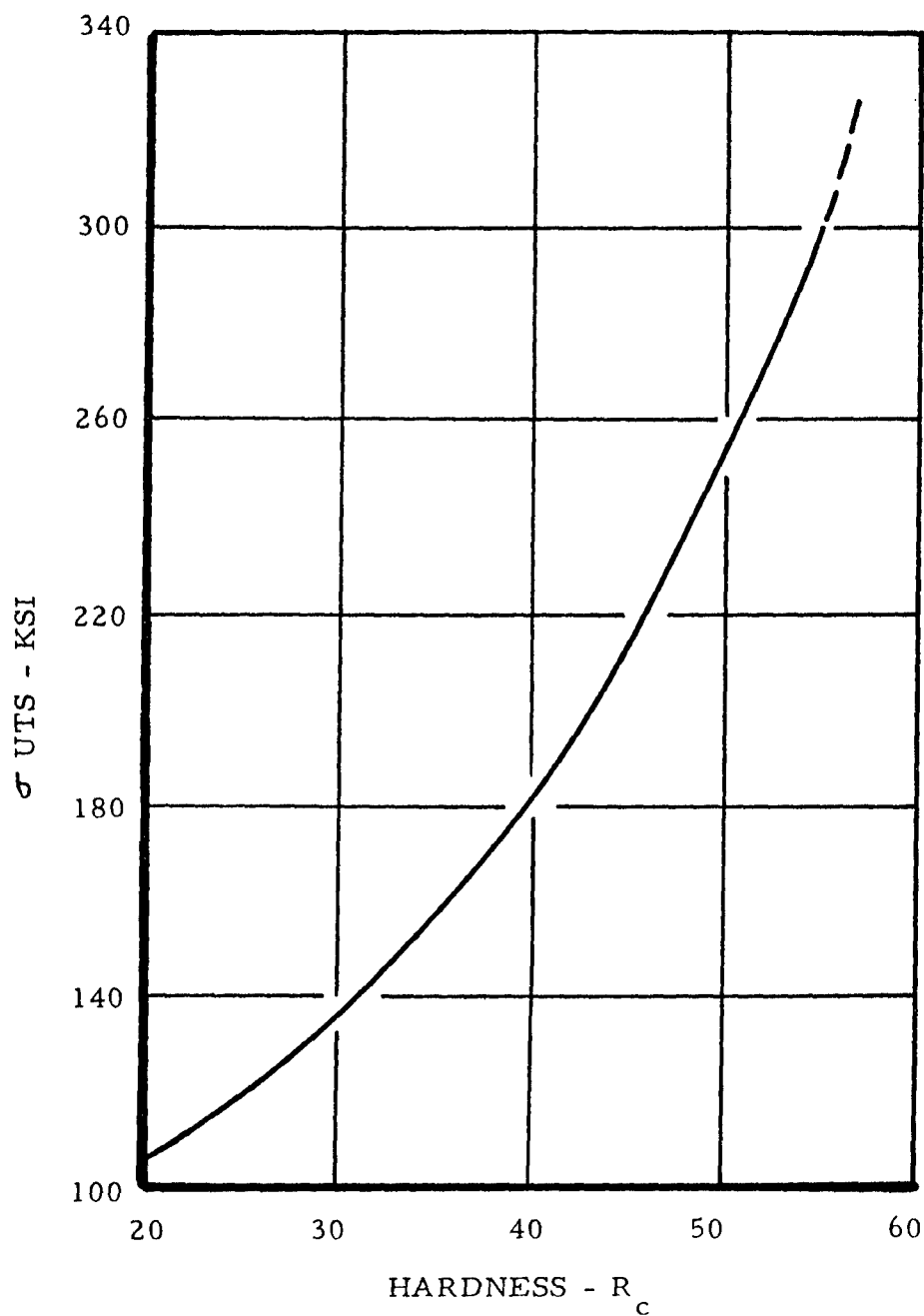


Figure 62. Empirical Relationship Between Hardness, R_c Scale, and Tensile Strength, σ_{UTS} , for Heat Treated Carbon and Low Alloy Steels.

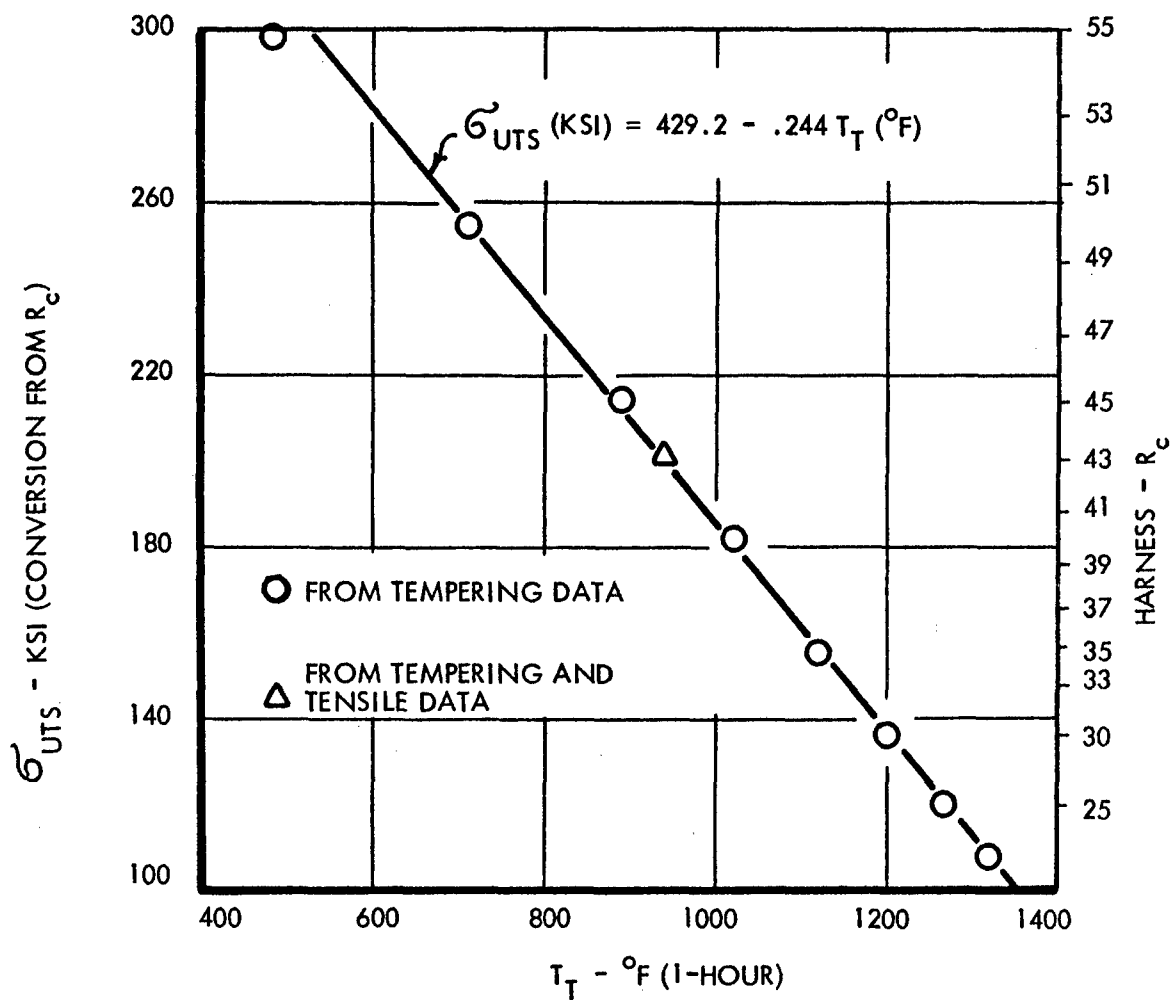


Figure 63. Ultimate Tensile Strength, σ_{UTS} , (Converted from Hardness) vs. Tempering Temperature, T_t , for AISI 4145 Steel, Lead and Non-lead. Hardness, R_C , Added for Comparison. Note that Tempering Temperature Selected for Specific σ_{UTS} Falls on Curve.

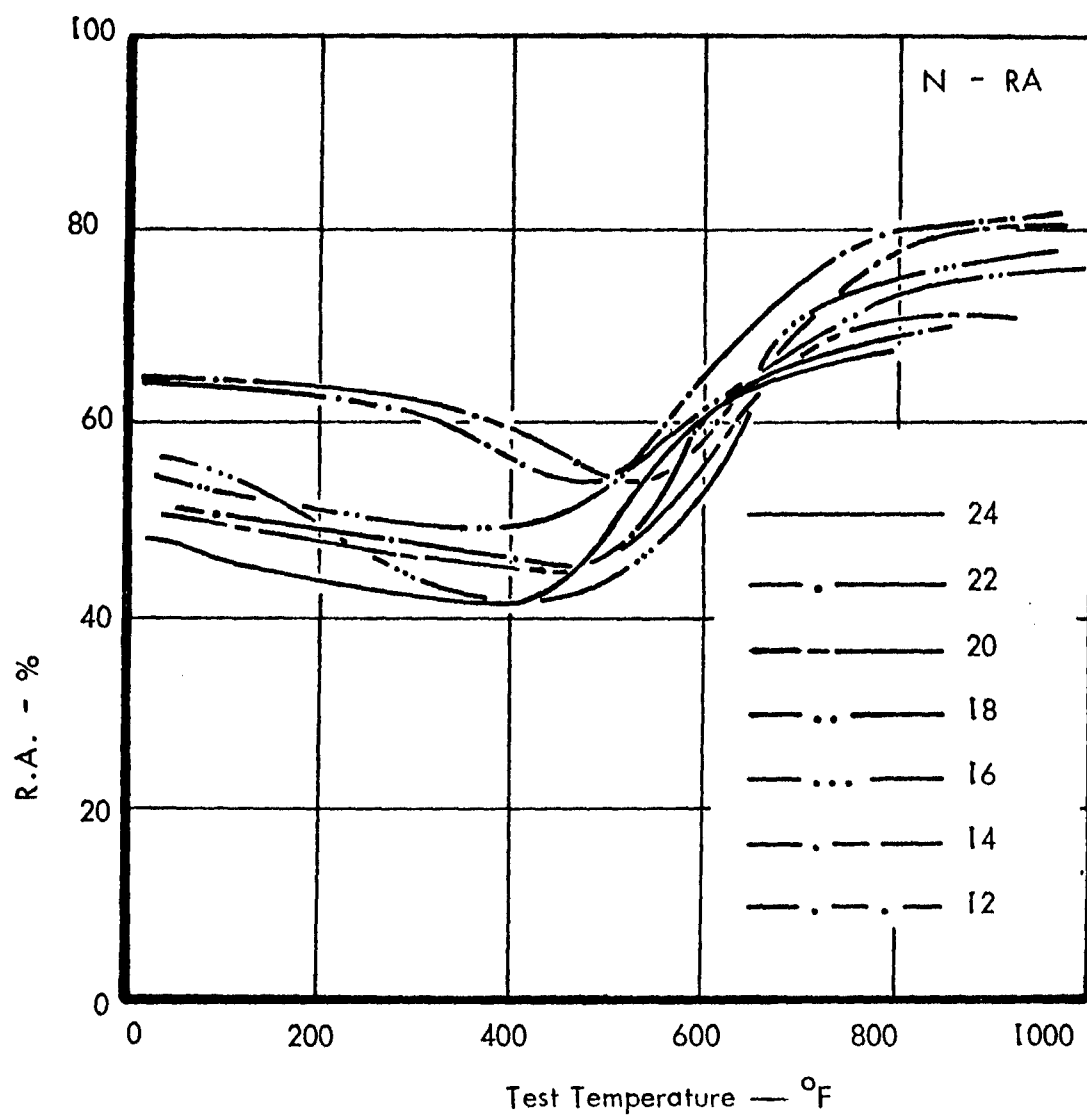


Figure 64. Comparison of R.A. for Non-leaded Material.

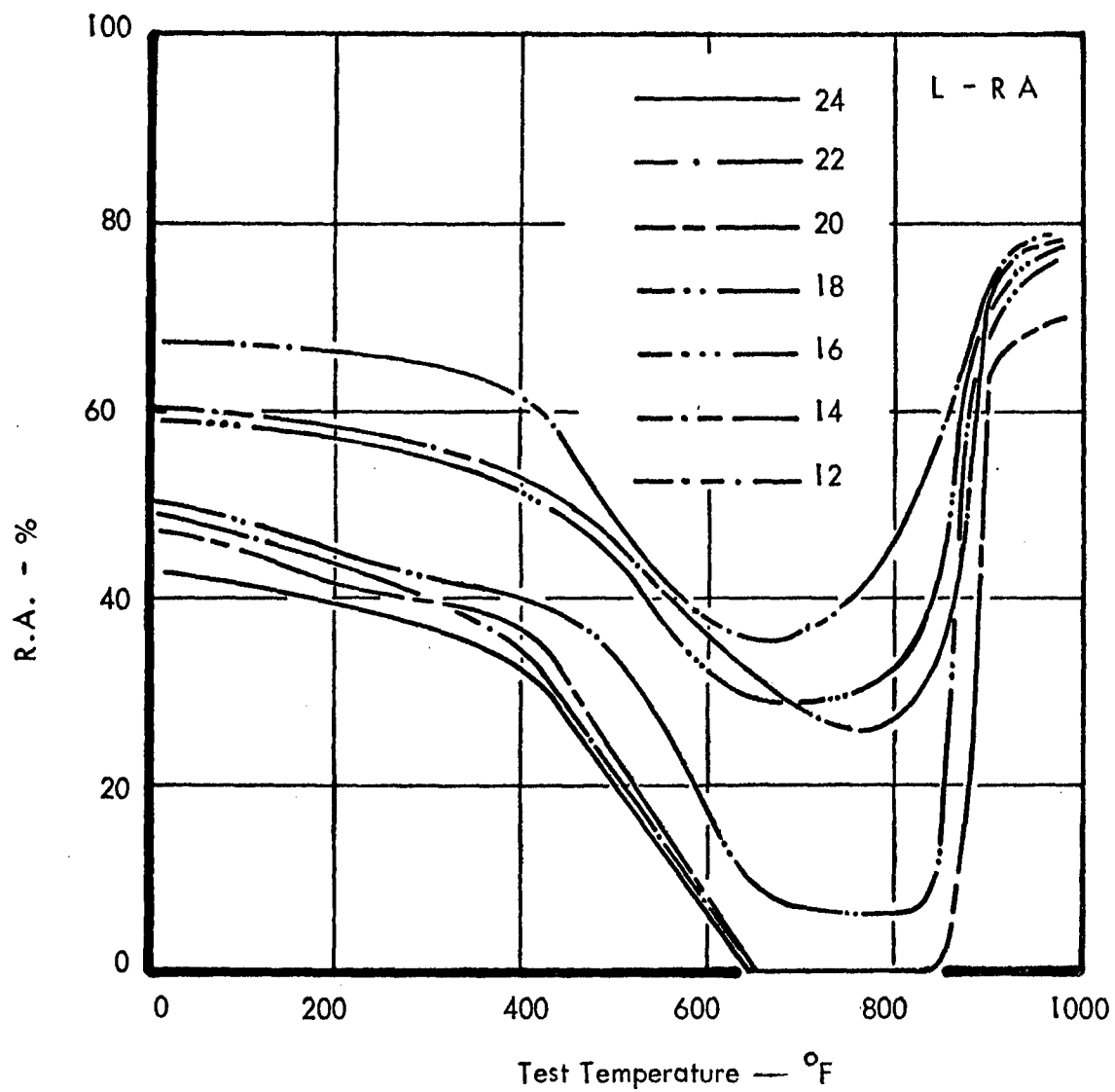


Figure 65. Comparison of R.A. for Leaded Material.

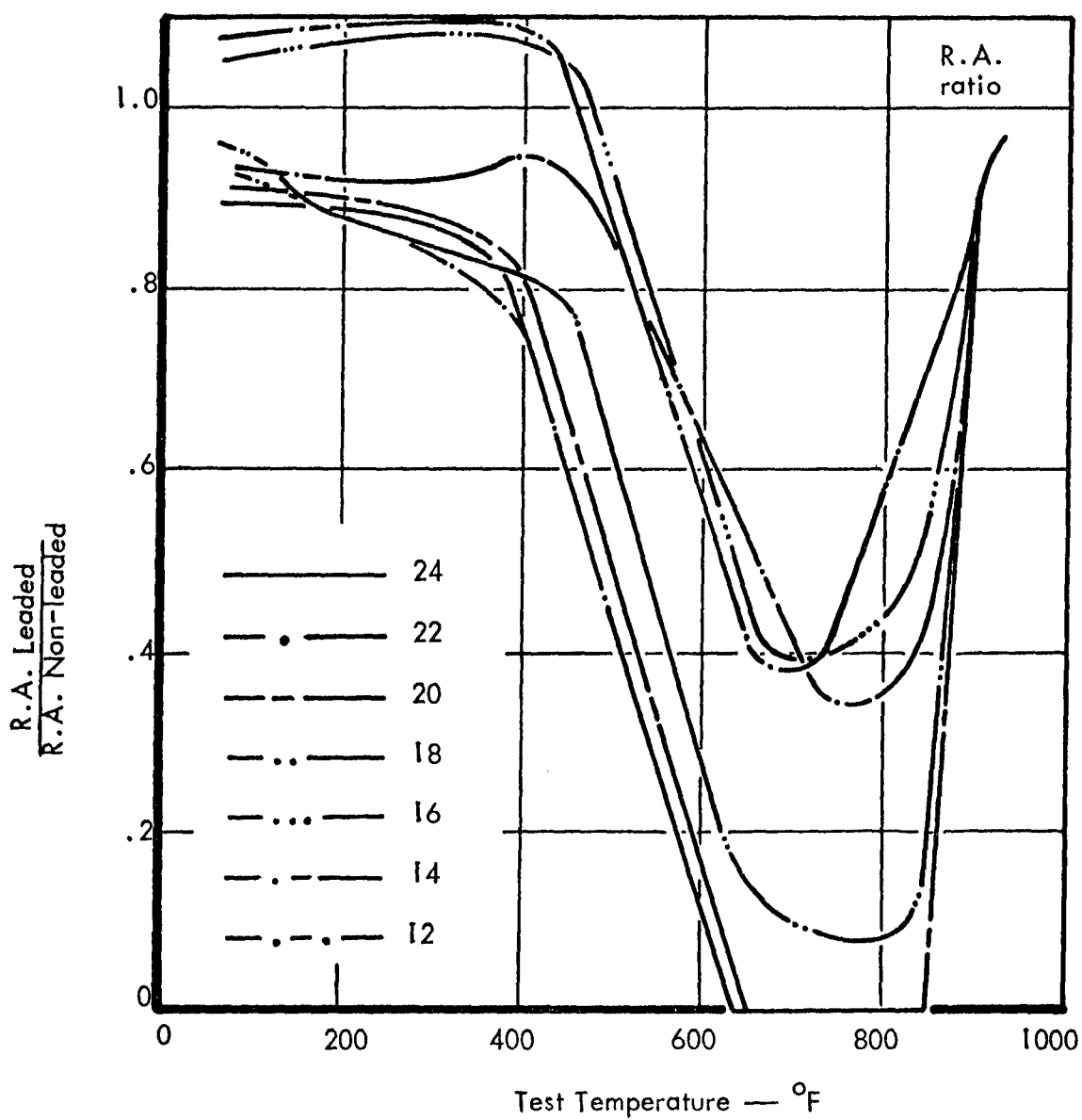


Figure 66. Ratio of R.A. for Led to Non-led Material.

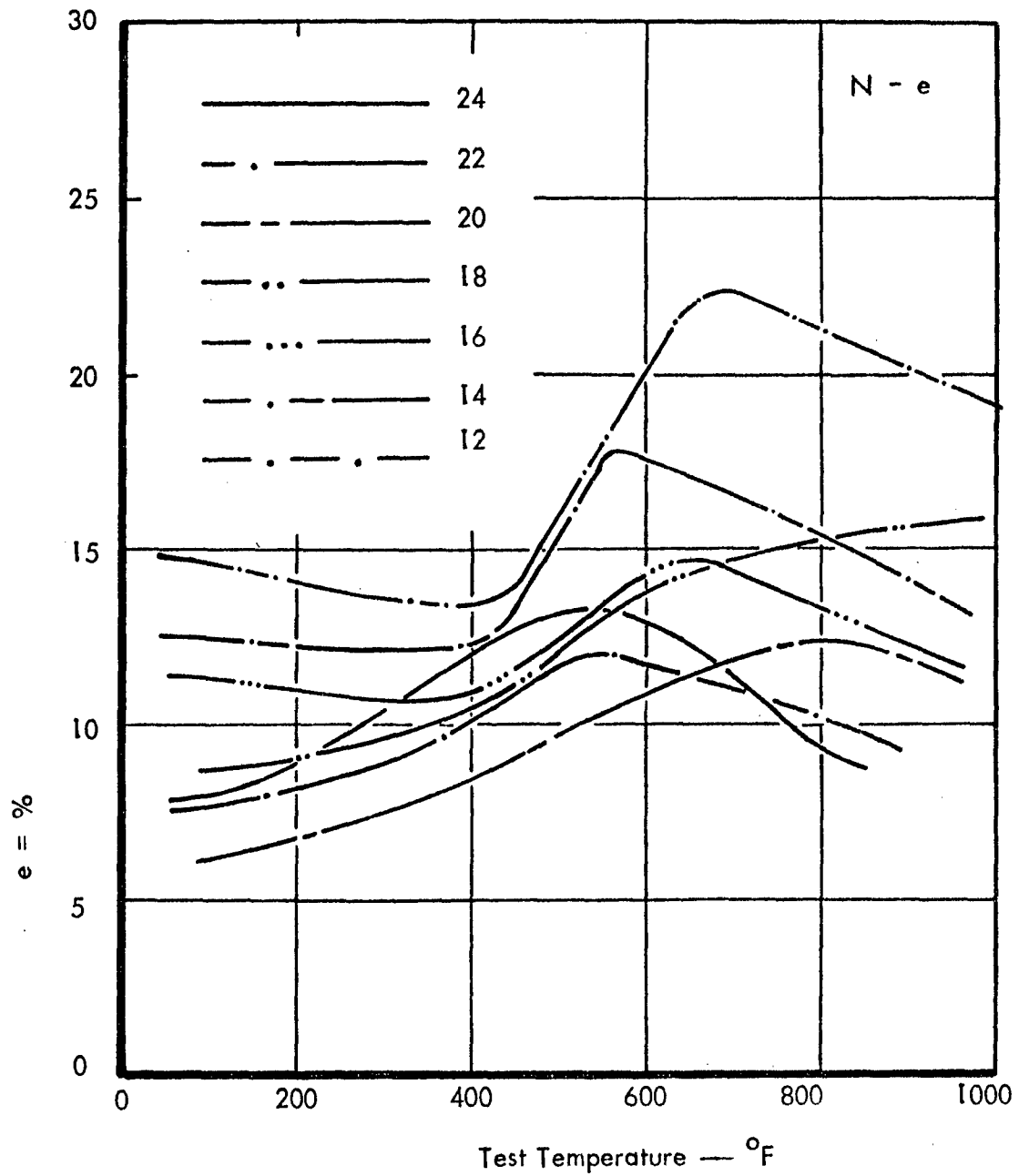


Figure 67. Comparison of \underline{e} for Non-leaded Material.

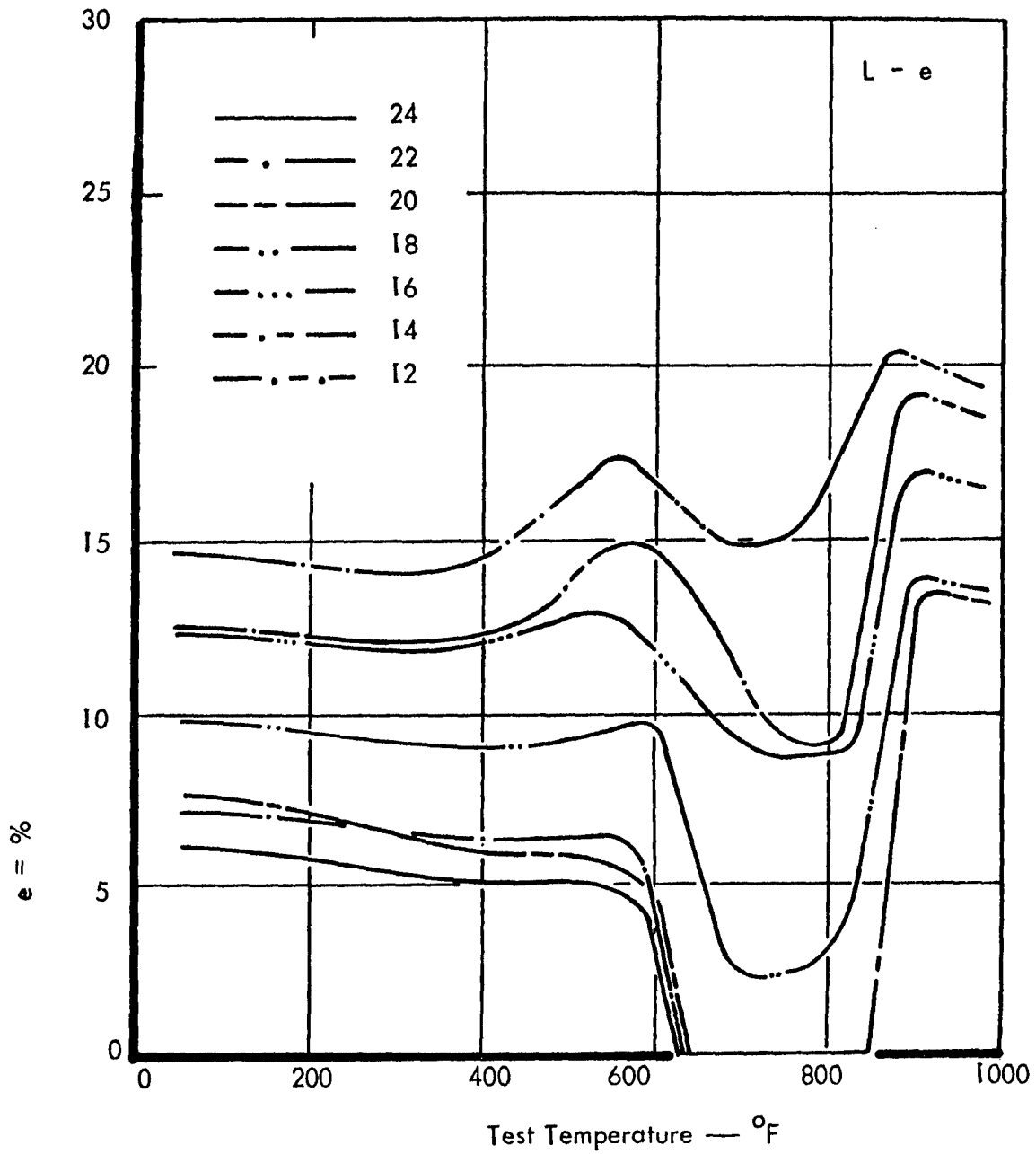


Figure 68. Comparison of \underline{e} for Leaded Material.

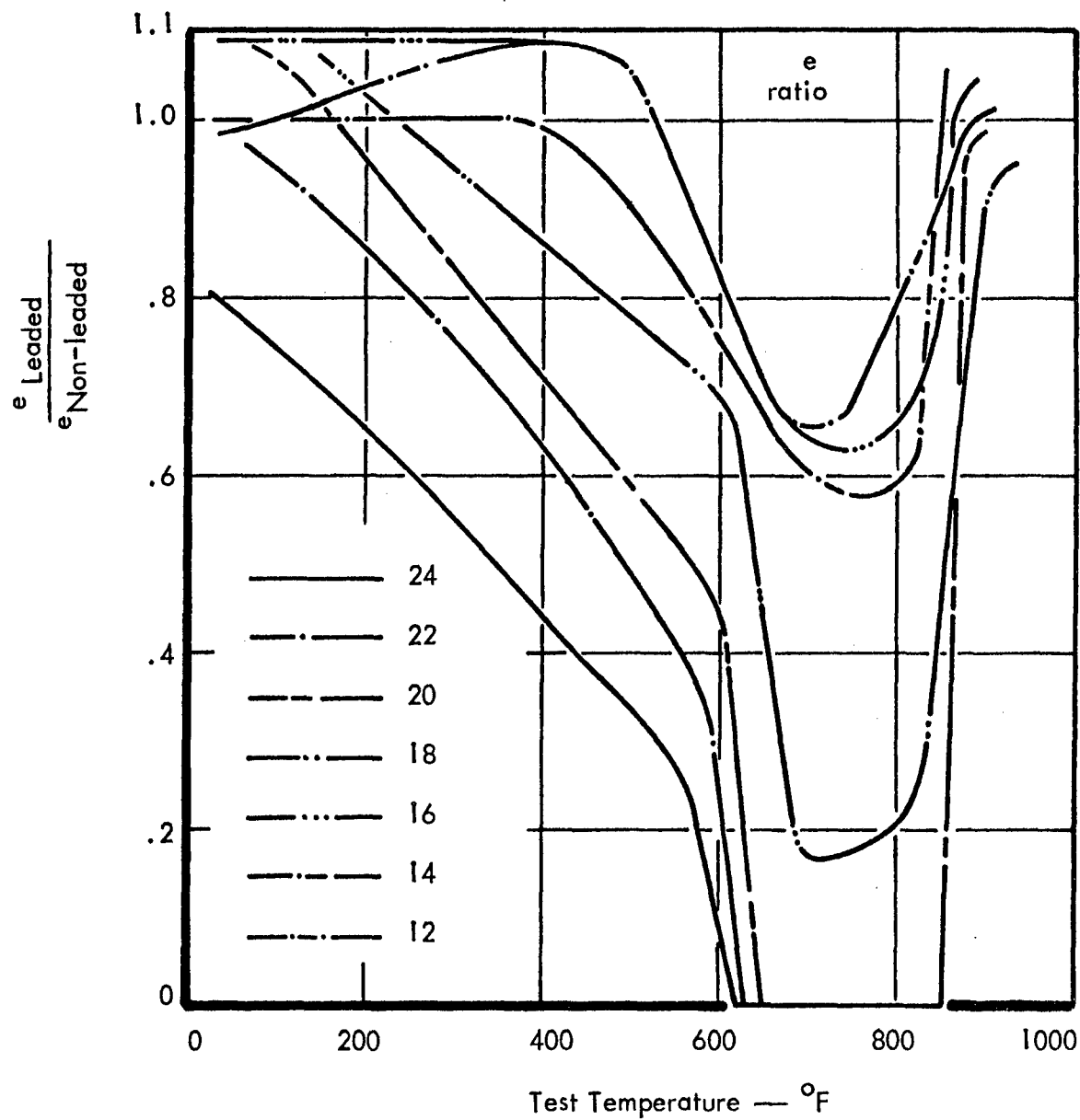


Figure 69. Ratio of e for Led to Non-led Material.

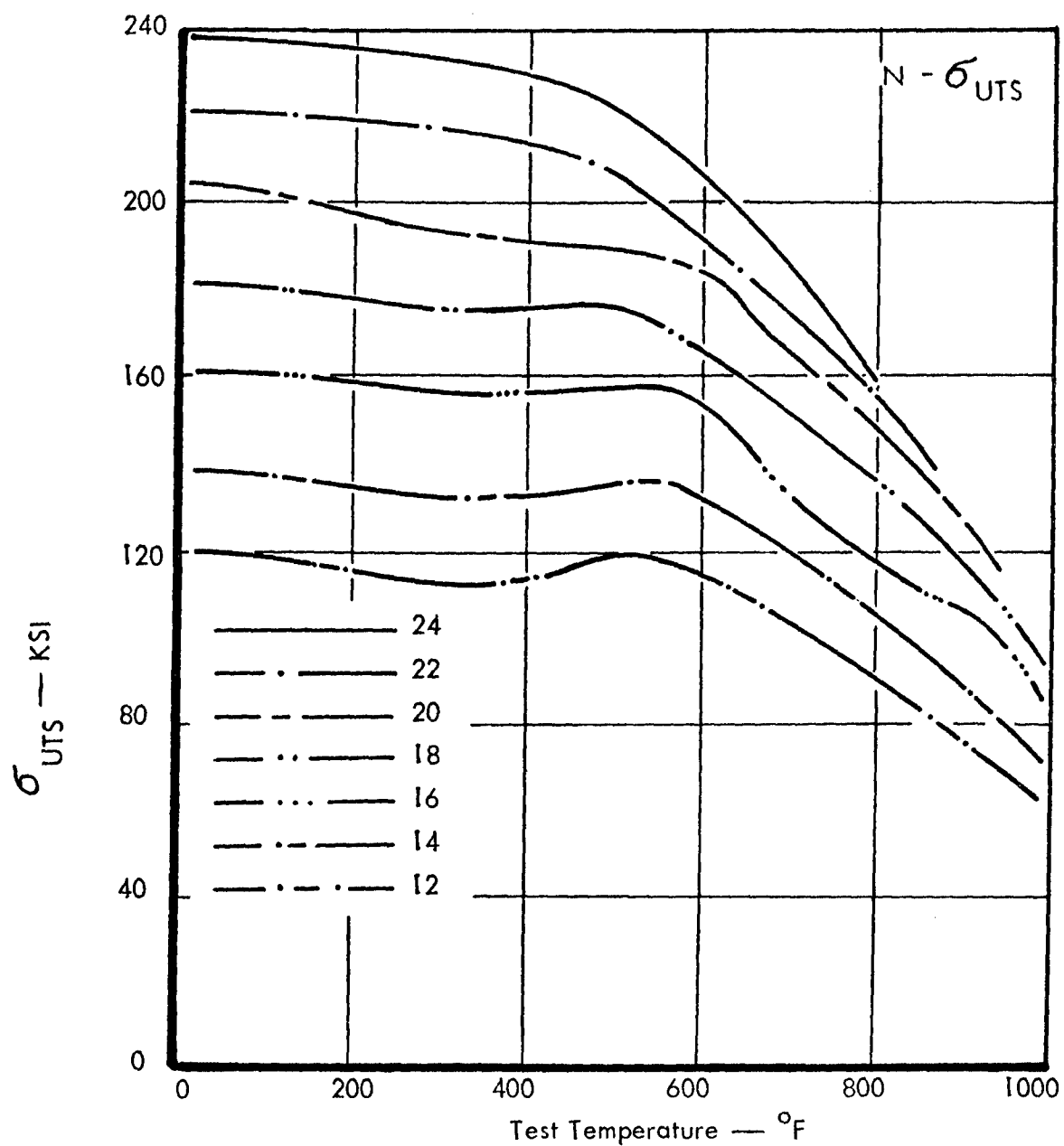


Figure 70. Comparison of σ_{UTS} for Non-leaded Material.

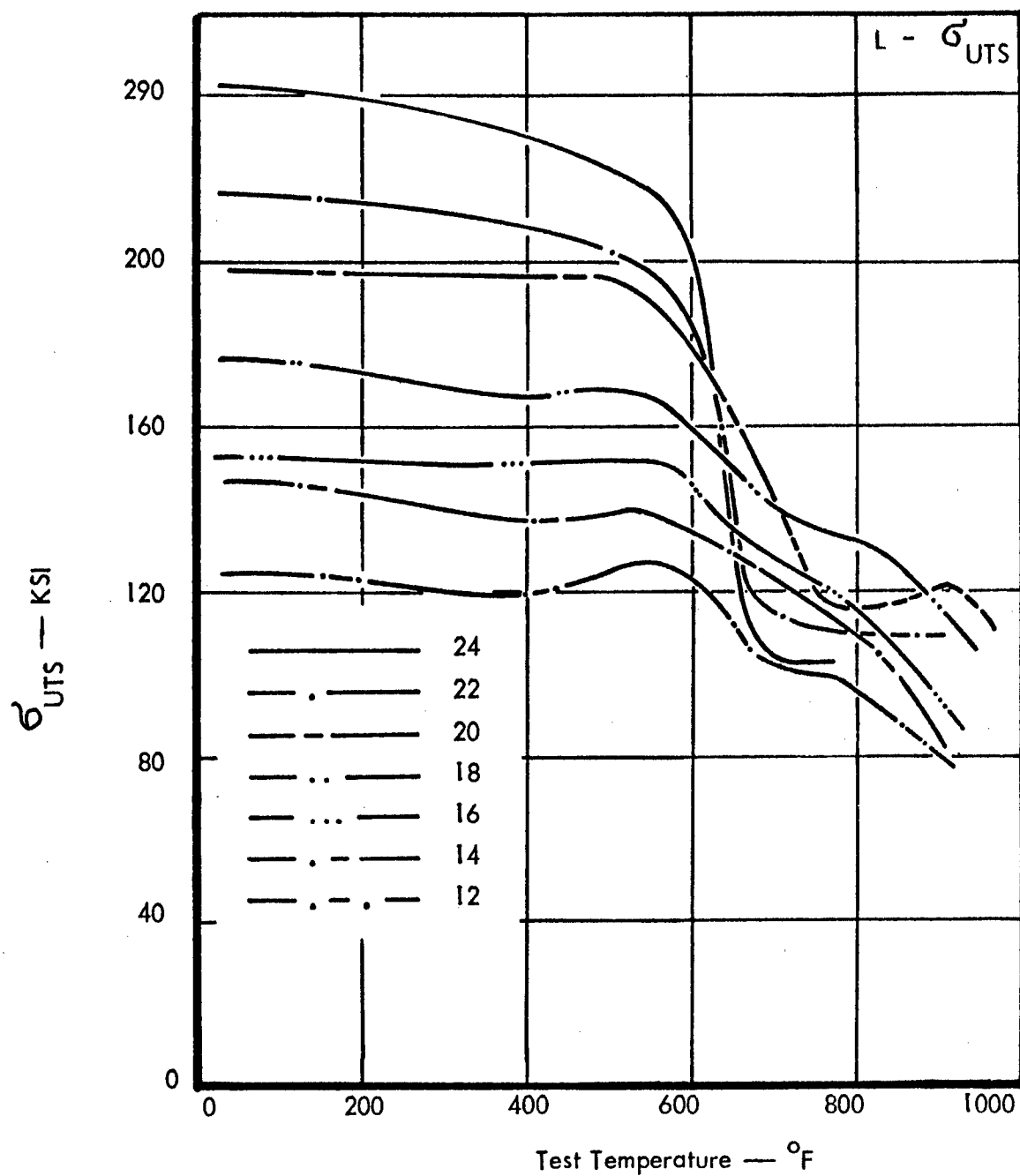


Figure 71. Comparison of σ_{UTS} for Leaded Material.

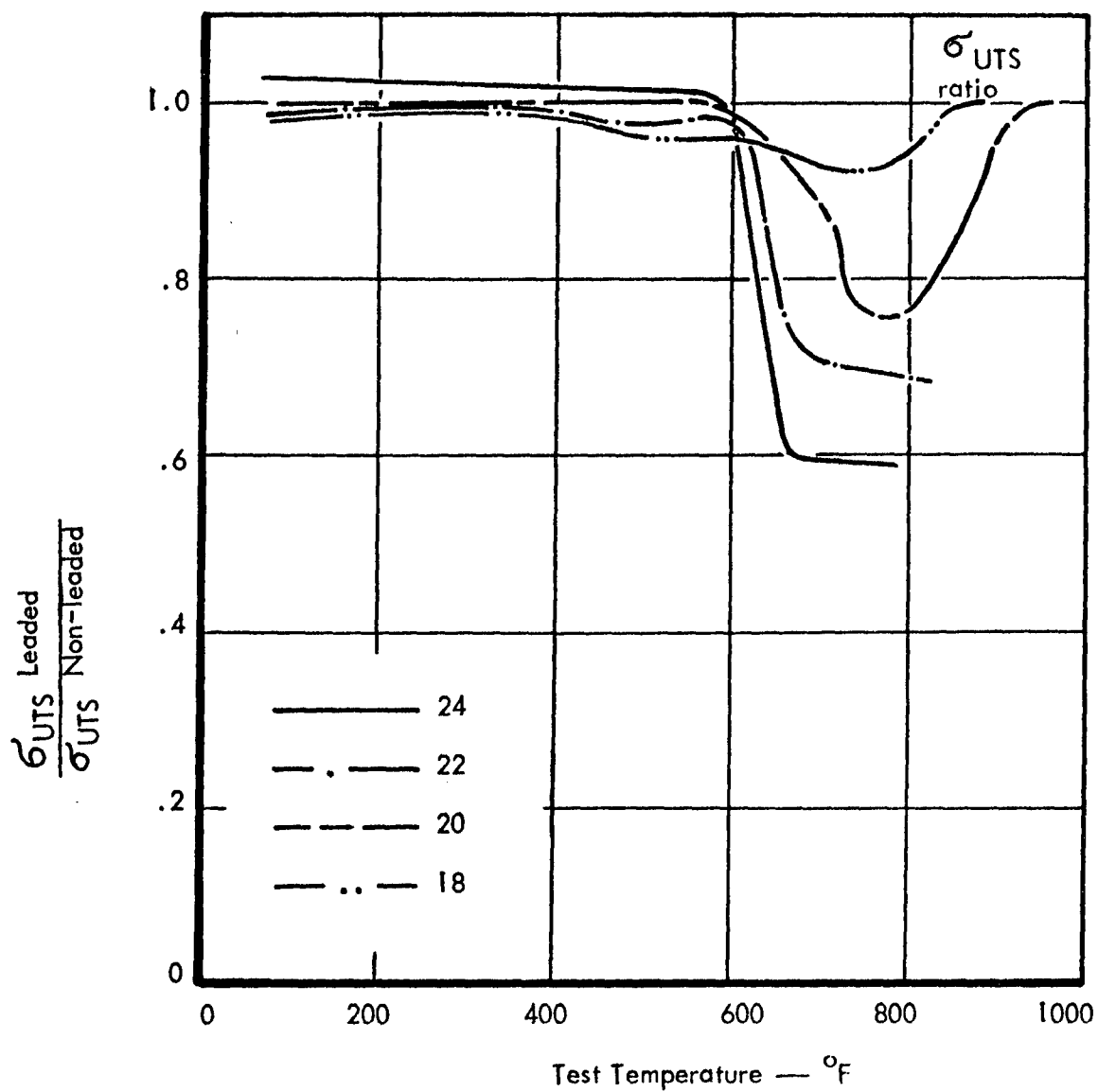


Figure 72. Ratio of σ_{UTS} for Leaded to Non-leaded Material.

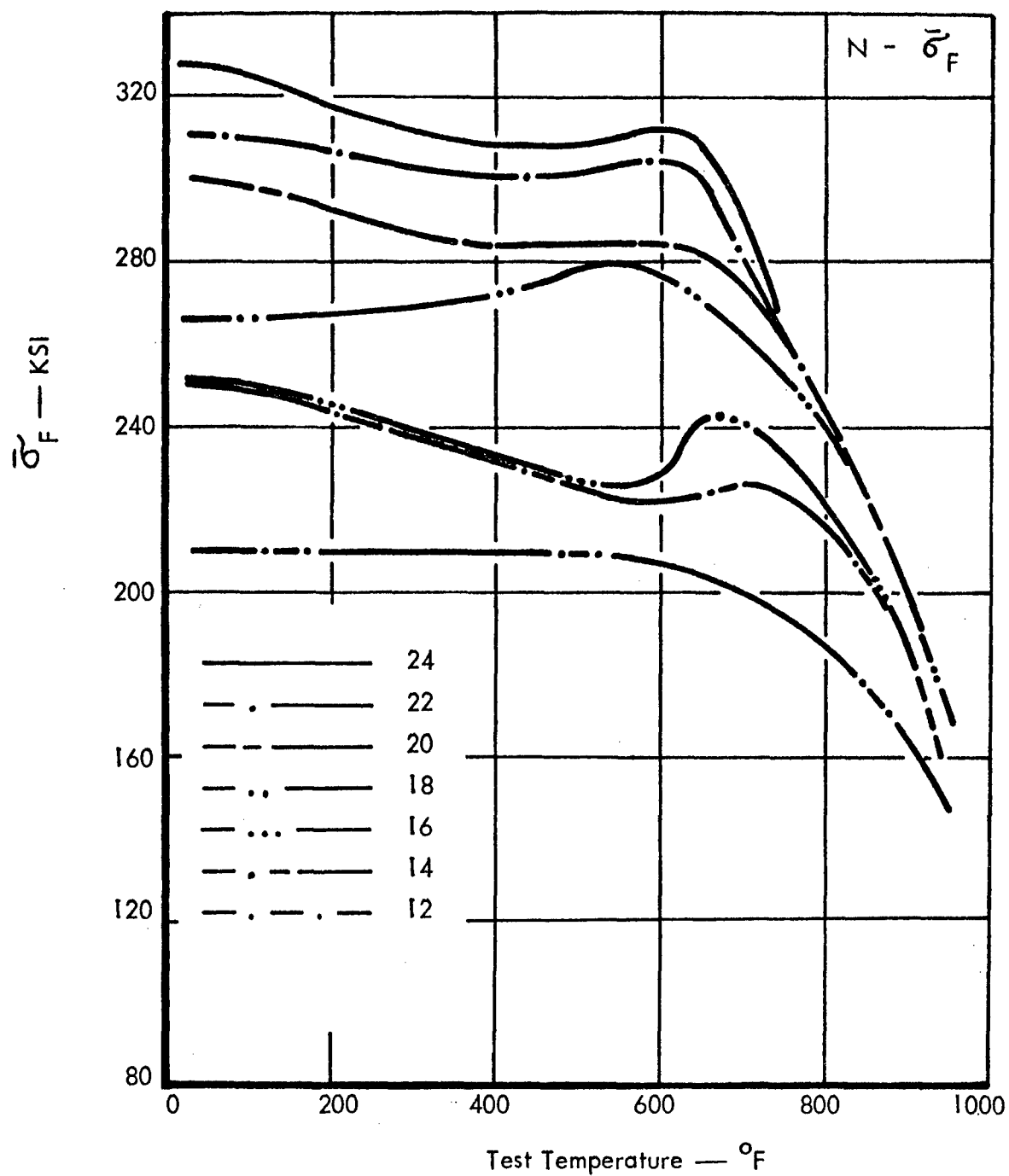


Figure 73. Comparison of σ_F for Non-leaded Material.

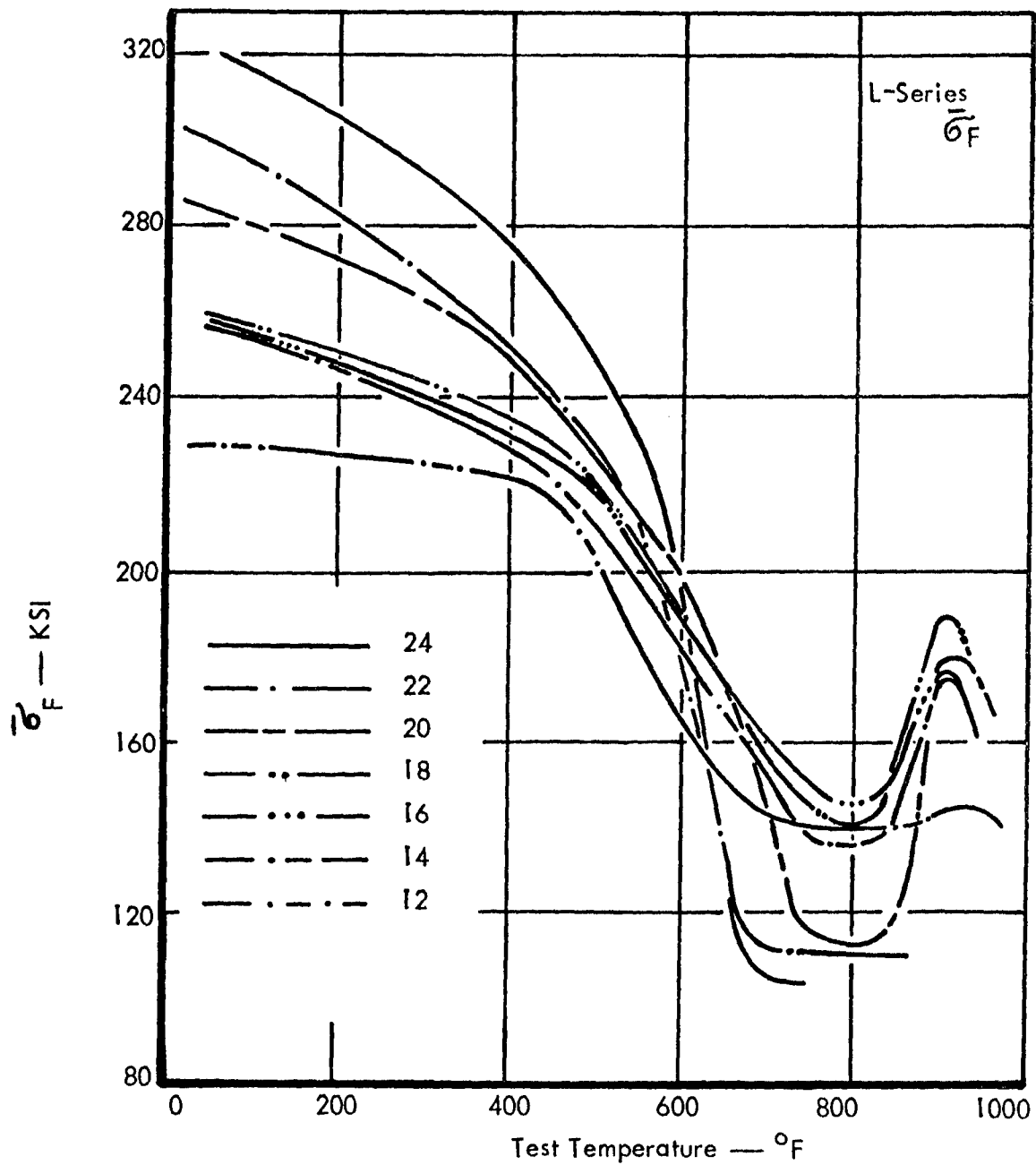


Figure 74. Comparison of $\bar{\sigma}_F$ for Leaded Material.

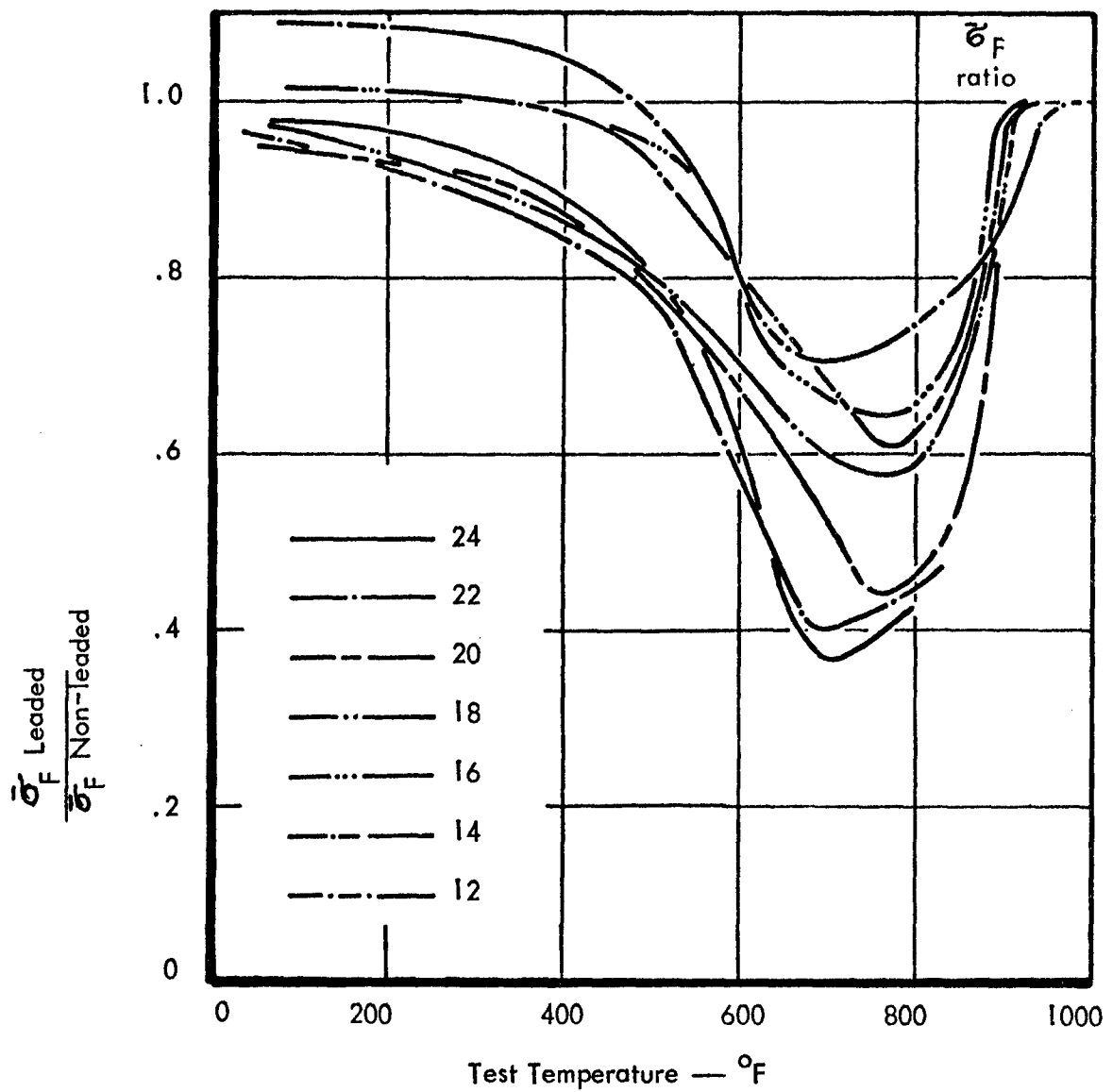


Figure 75. Ratio of $\bar{\sigma}_F$ for Leaded to Non-leaded Material.

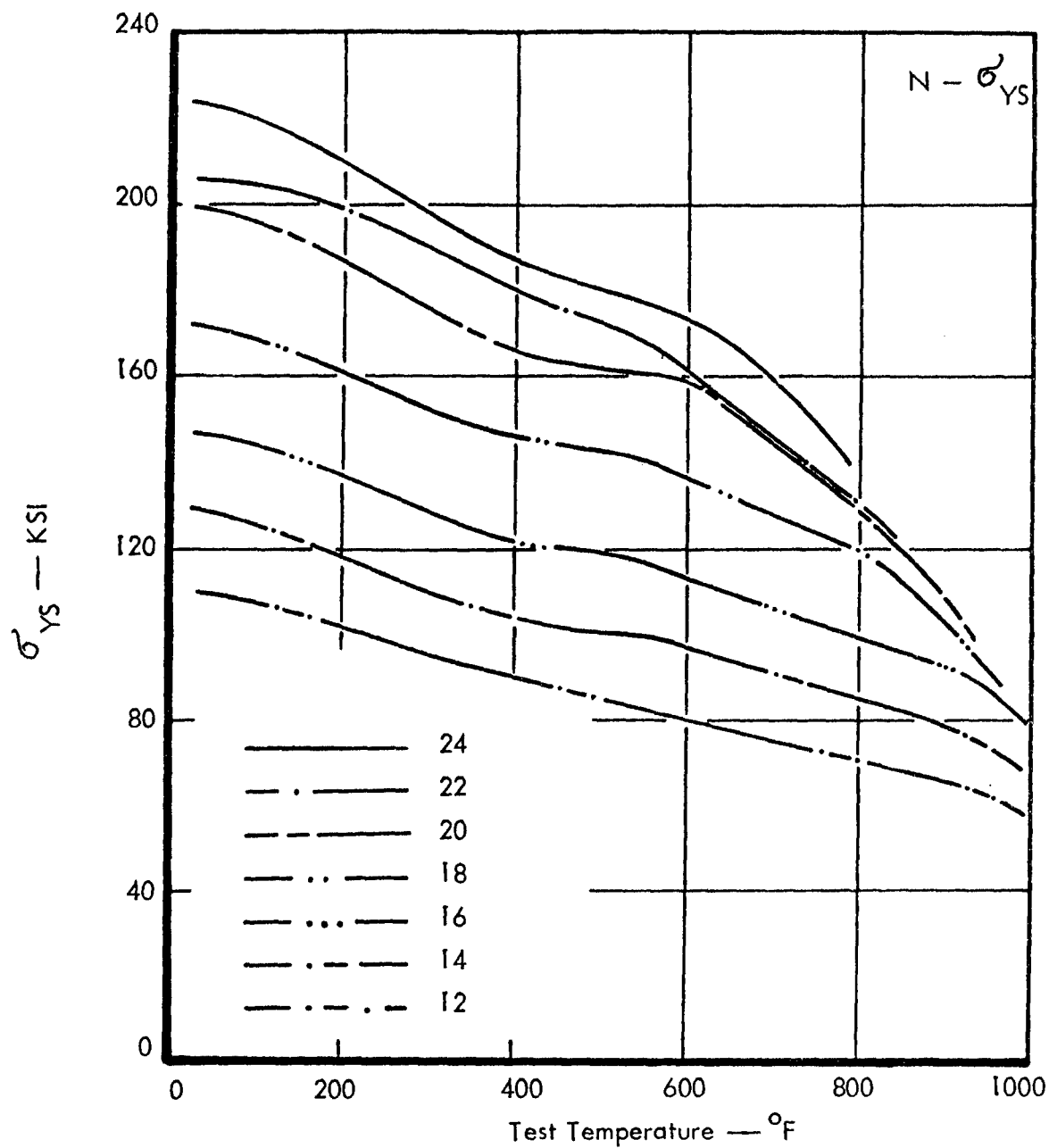


Figure 76. Comparison of σ_{YS} for Non-leaded Material.

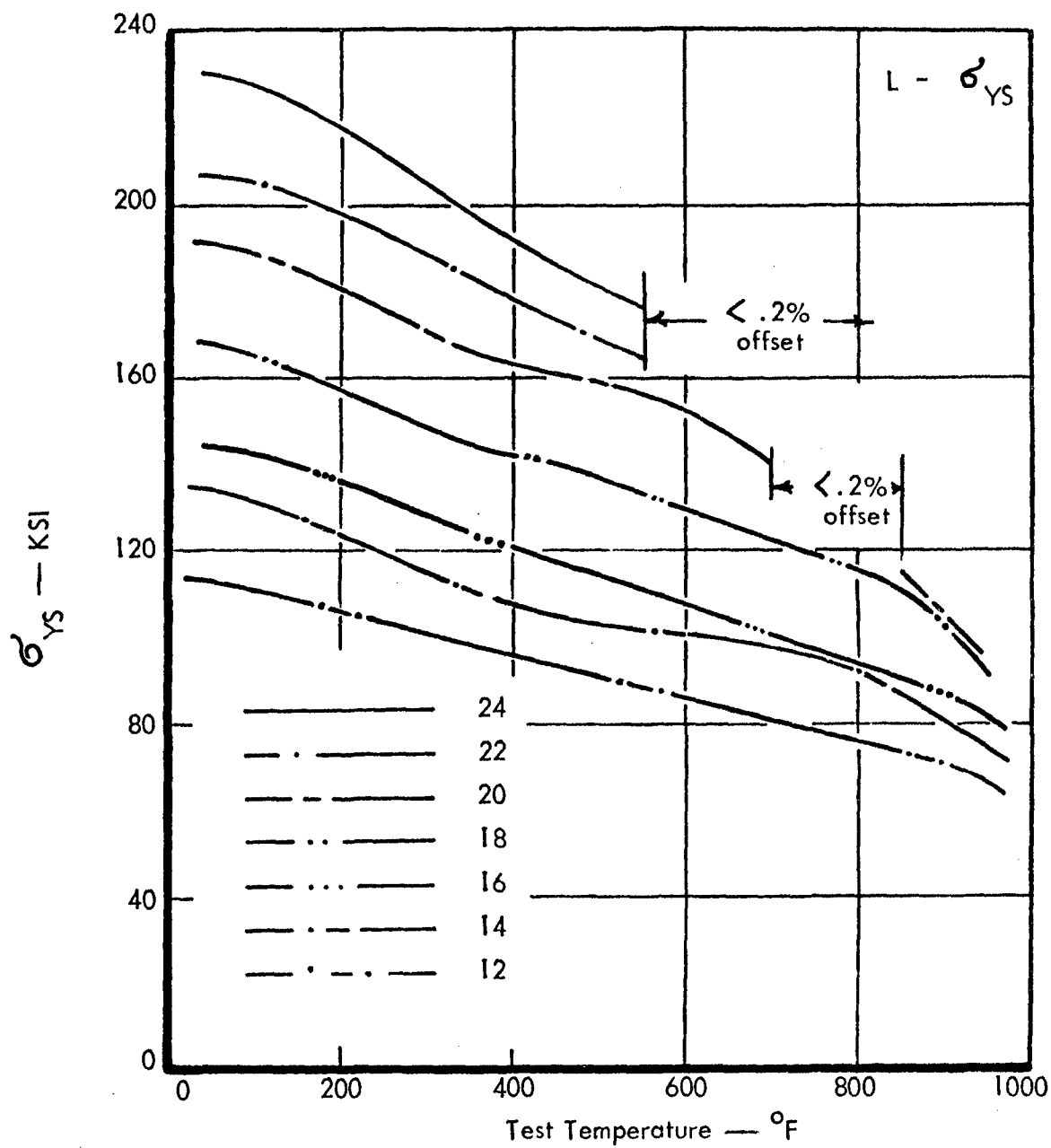


Figure 77. Comparison of σ_{ys} for Leaded Material.

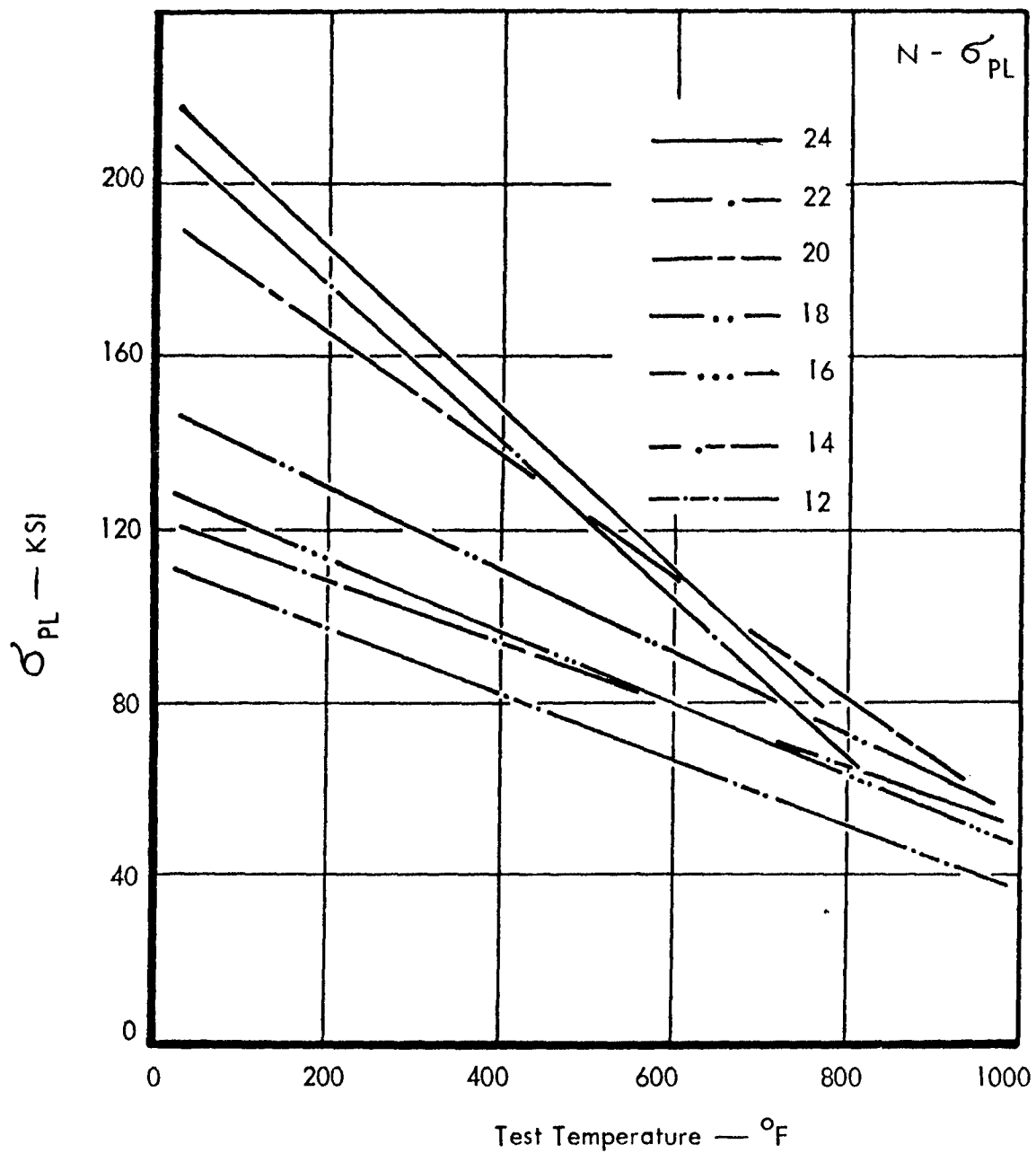


Figure 78. Comparison of σ_{PL} for Non-leaded Material.

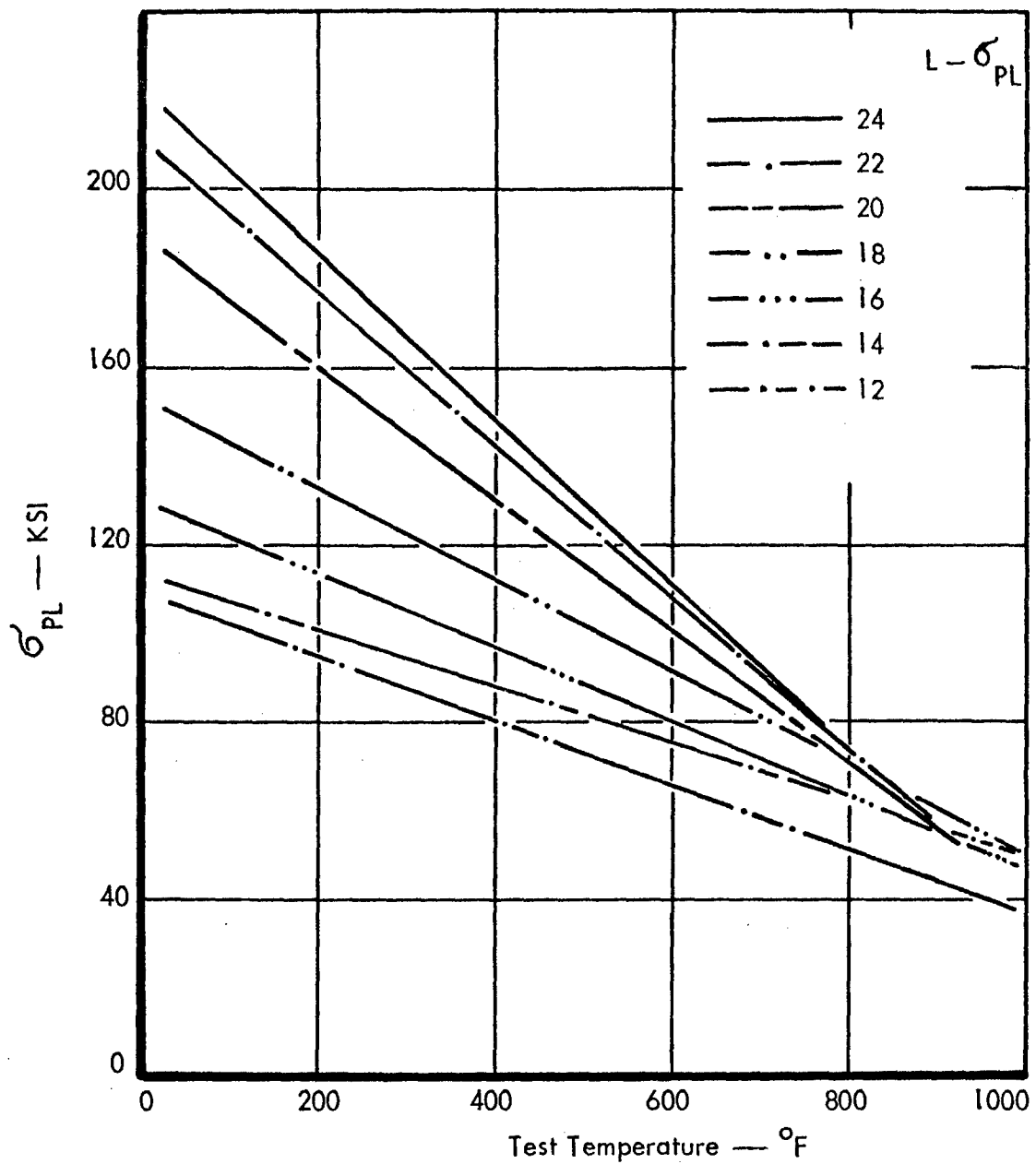


Figure 79. Comparison of σ_{PL} for Leaded Material.

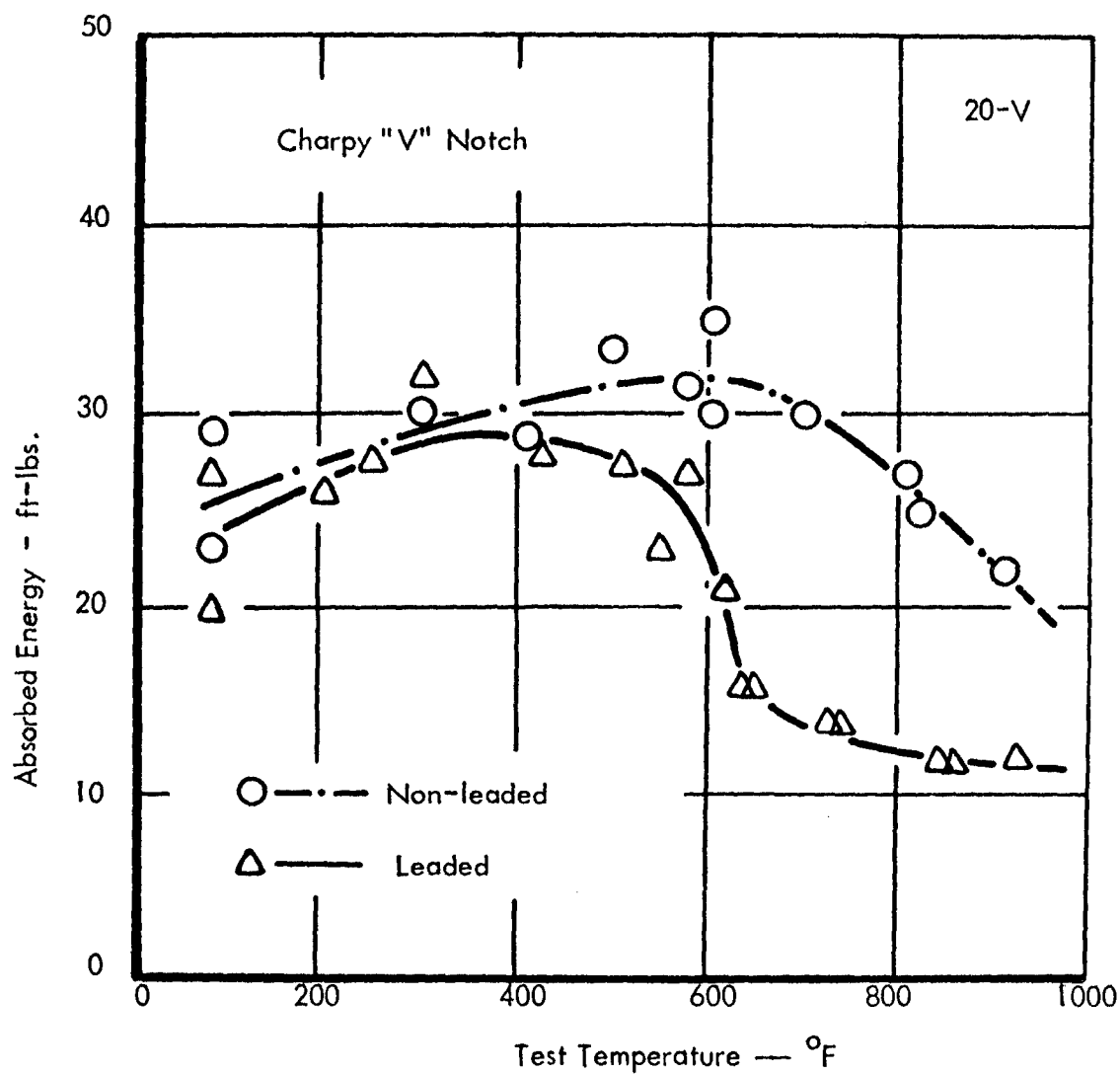


Figure 80. Effect of Test Temperature on Absorbed Energy of a Charpy "V" Notch Impact Specimen for Leaded and Non-leaded L20 and N20 Material.

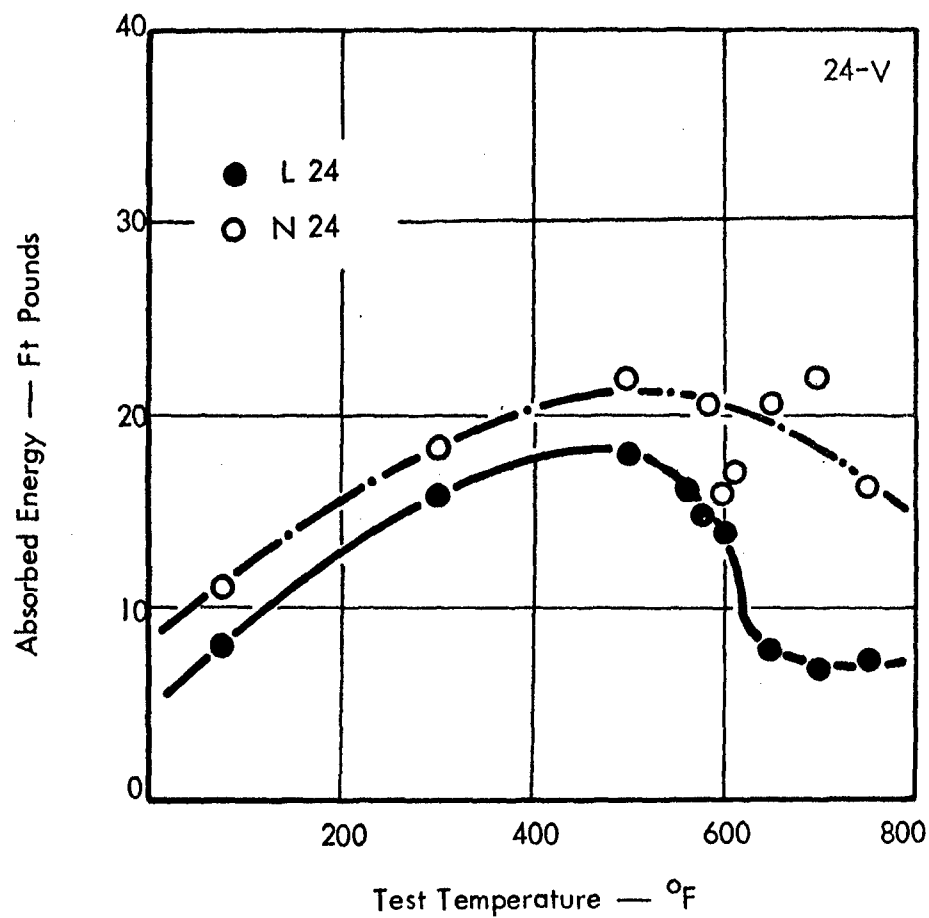


Figure 81. Effect of Test Temperature on Absorbed Energy of a Charpy "V" Notch Impact Specimen for Leded and Non-Leded L24 and N24 Material.

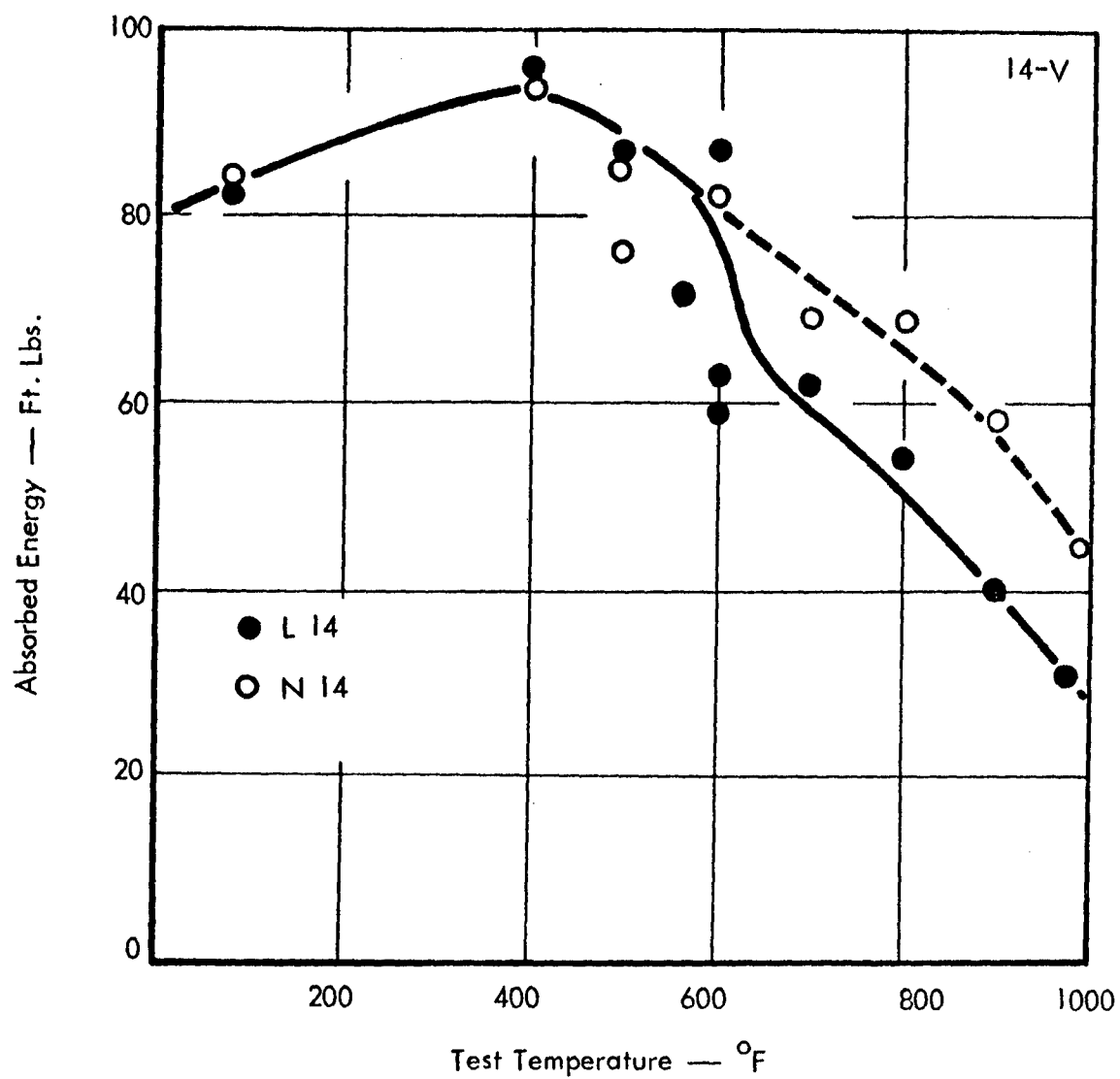


Figure 82. Effect of Test Temperature on Absorbed Energy of a Charpy "V" Notch Impact Specimen for Leaded and Non-leaded L14 and N14 Material.

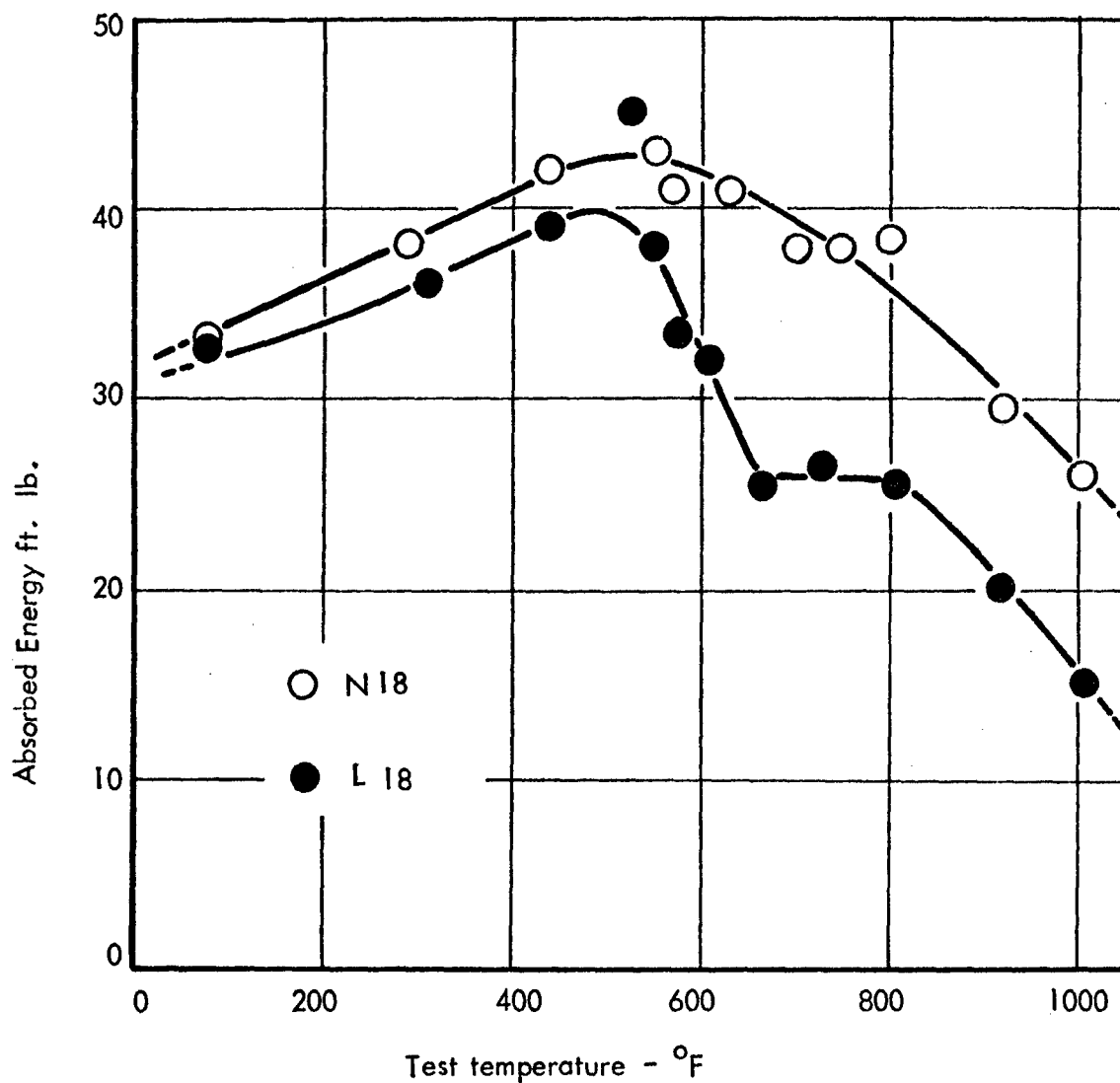


Figure 83. Effect of Test Temperature on Absorbed Energy of a Charpy "V" Notch Impact Specimen for Leaded and Non-leaded L18 and N18 Material.

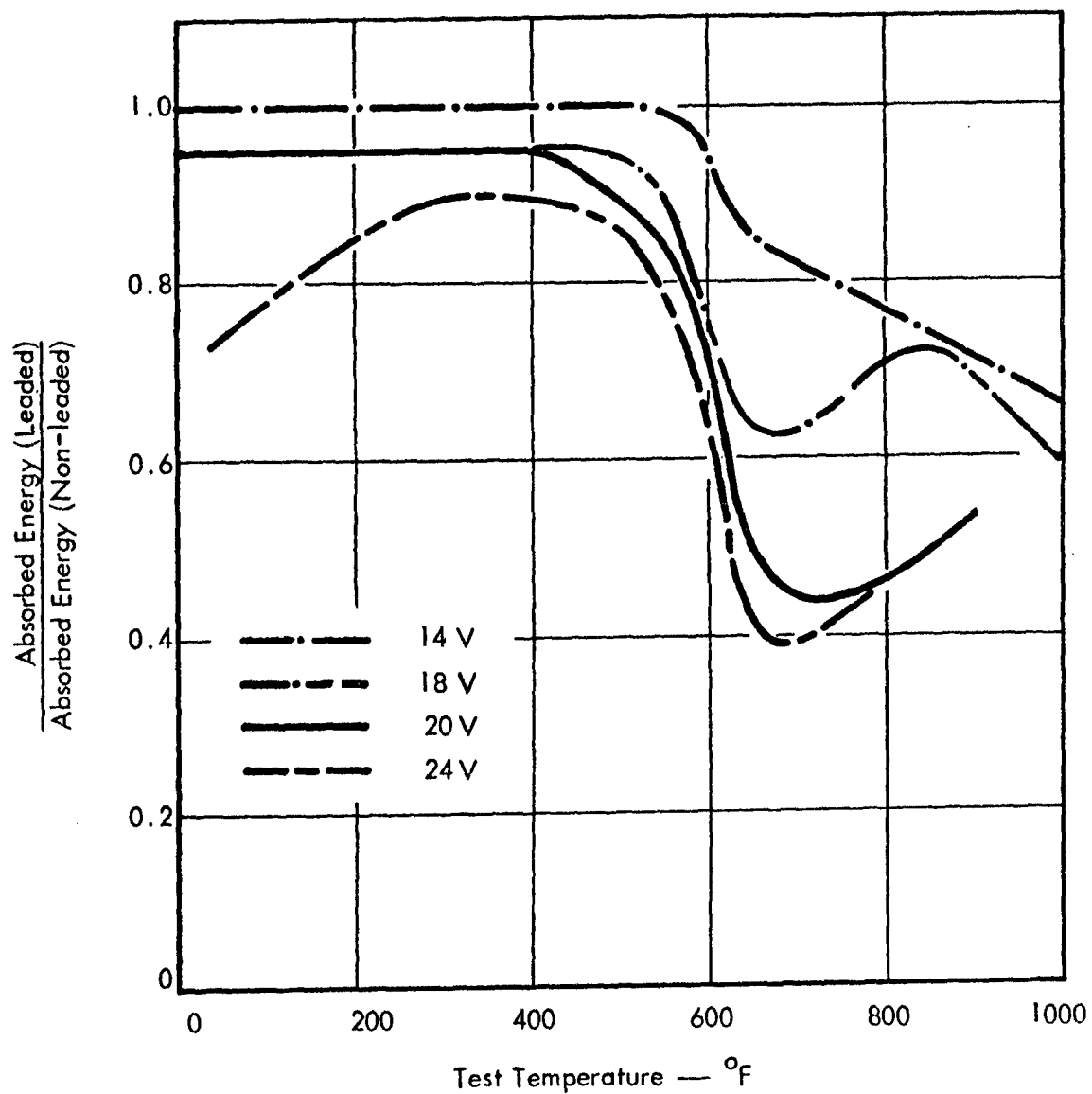


Figure 84. Ratio of Charpy "V" Notch Absorbed Energy for Leaded to Non-leaded Steels at Four Strength Levels as a Function of Test Temperature.

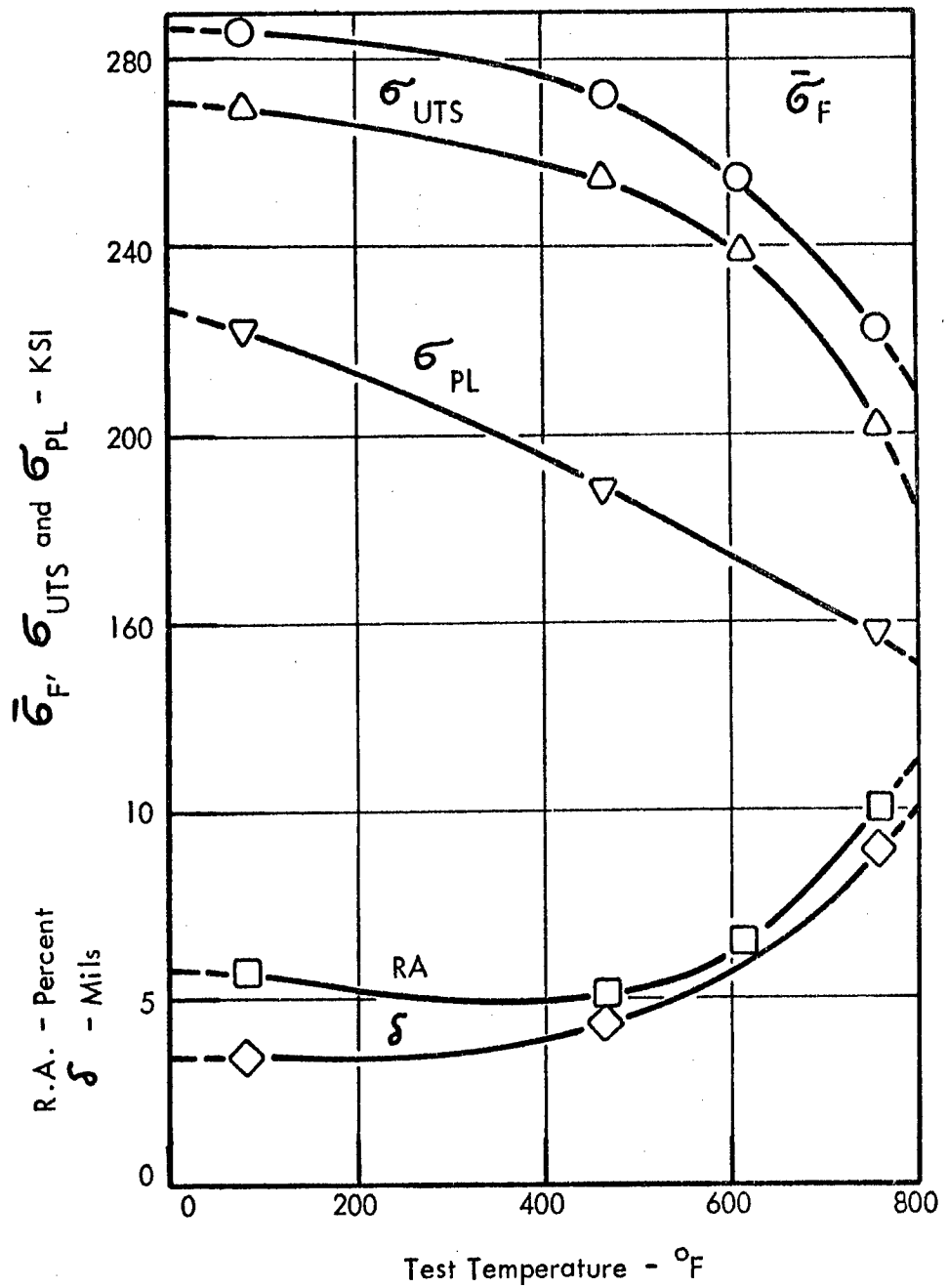


Figure 85. Tensile Properties of Radiused Transverse N24T Specimens as a Function of Test Temperature.

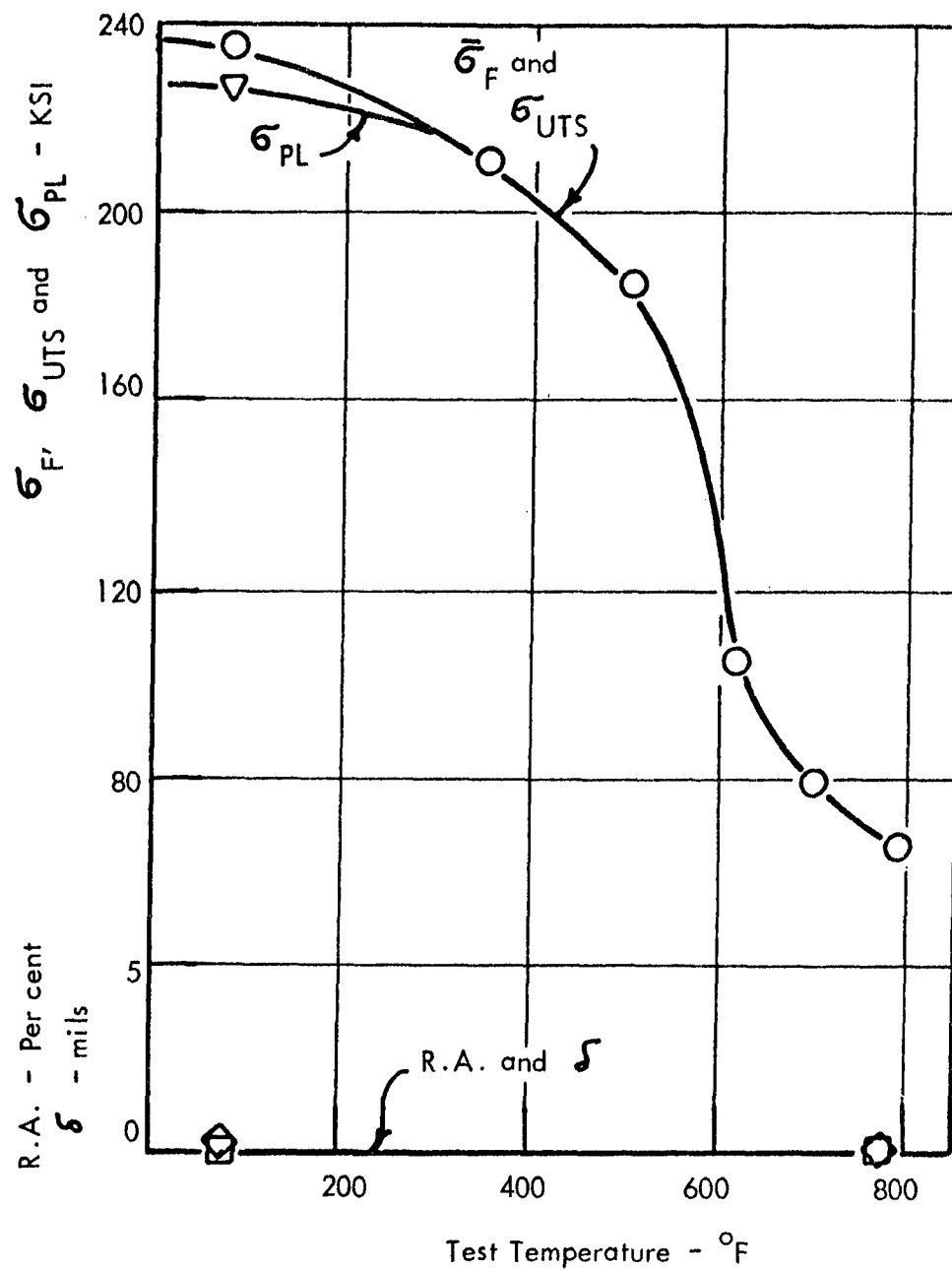


Figure 86. Tensile Properties of Radiused Transverse L24T Specimens as a Function of Test Temperature.

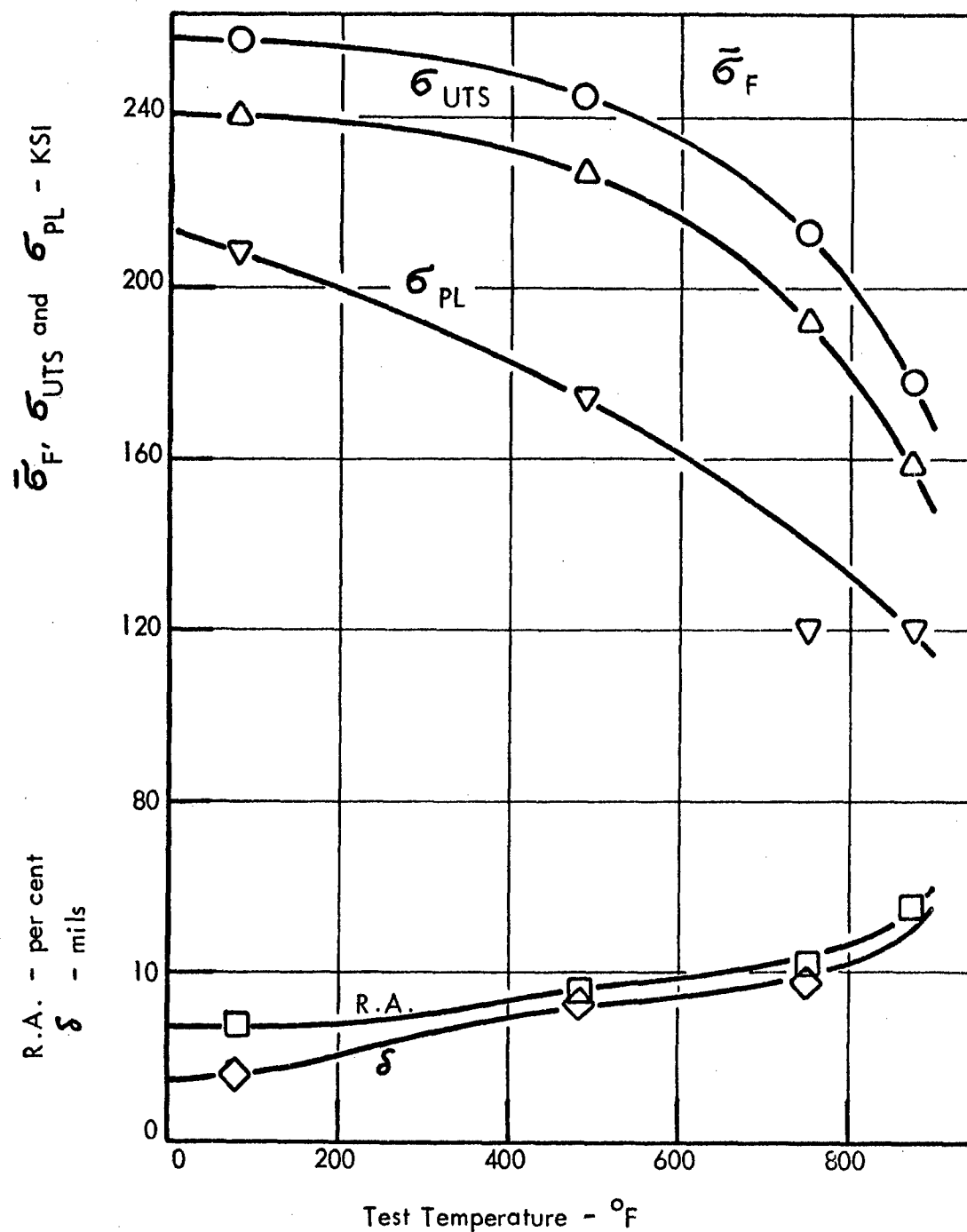


Figure 87. Tensile Properties of Radiused Transverse N22T Specimens as a Function of Test Temperature.

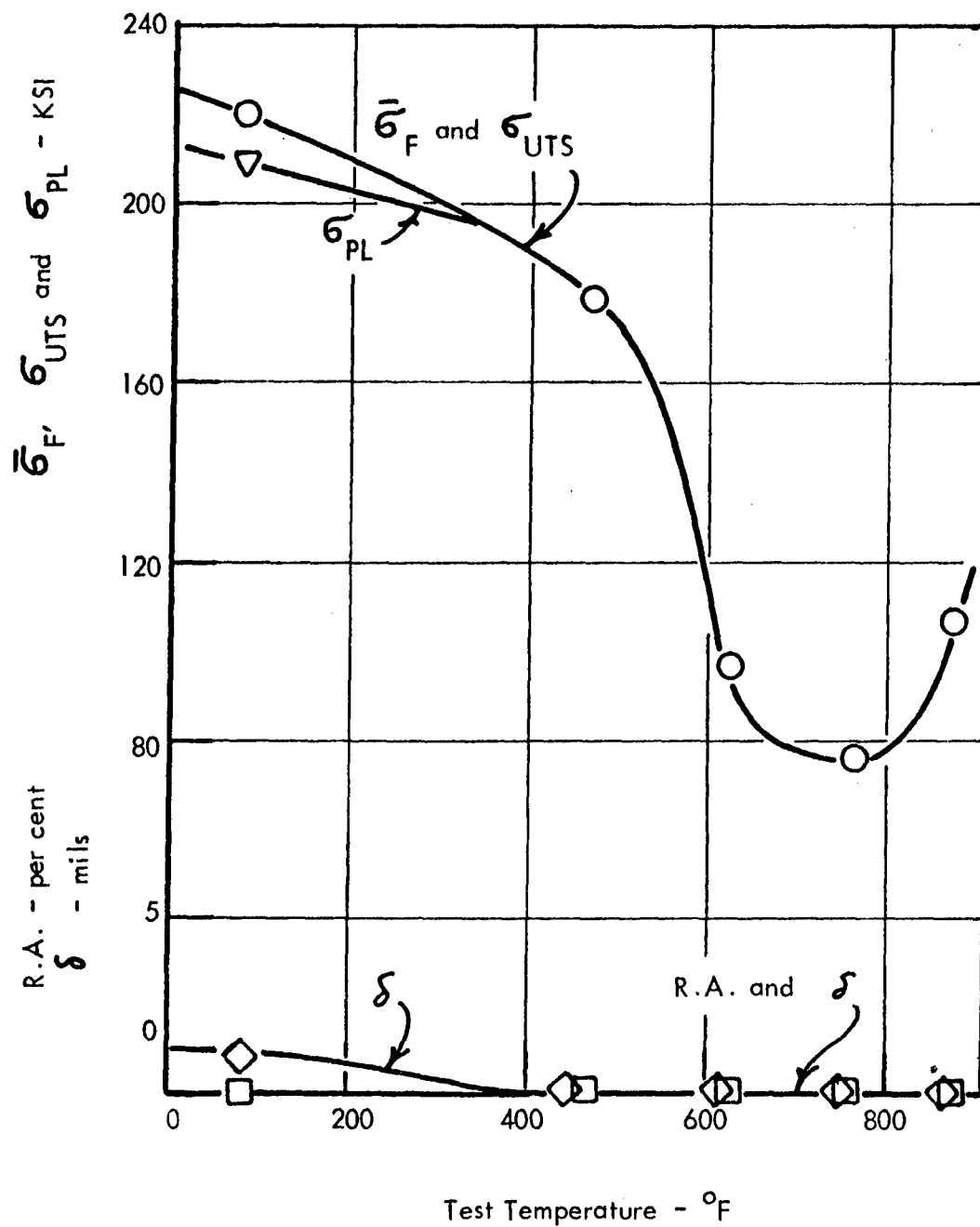


Figure 88. Tensile Properties of Radiused Transverse L22T Specimens as a Function of Test Temperature.

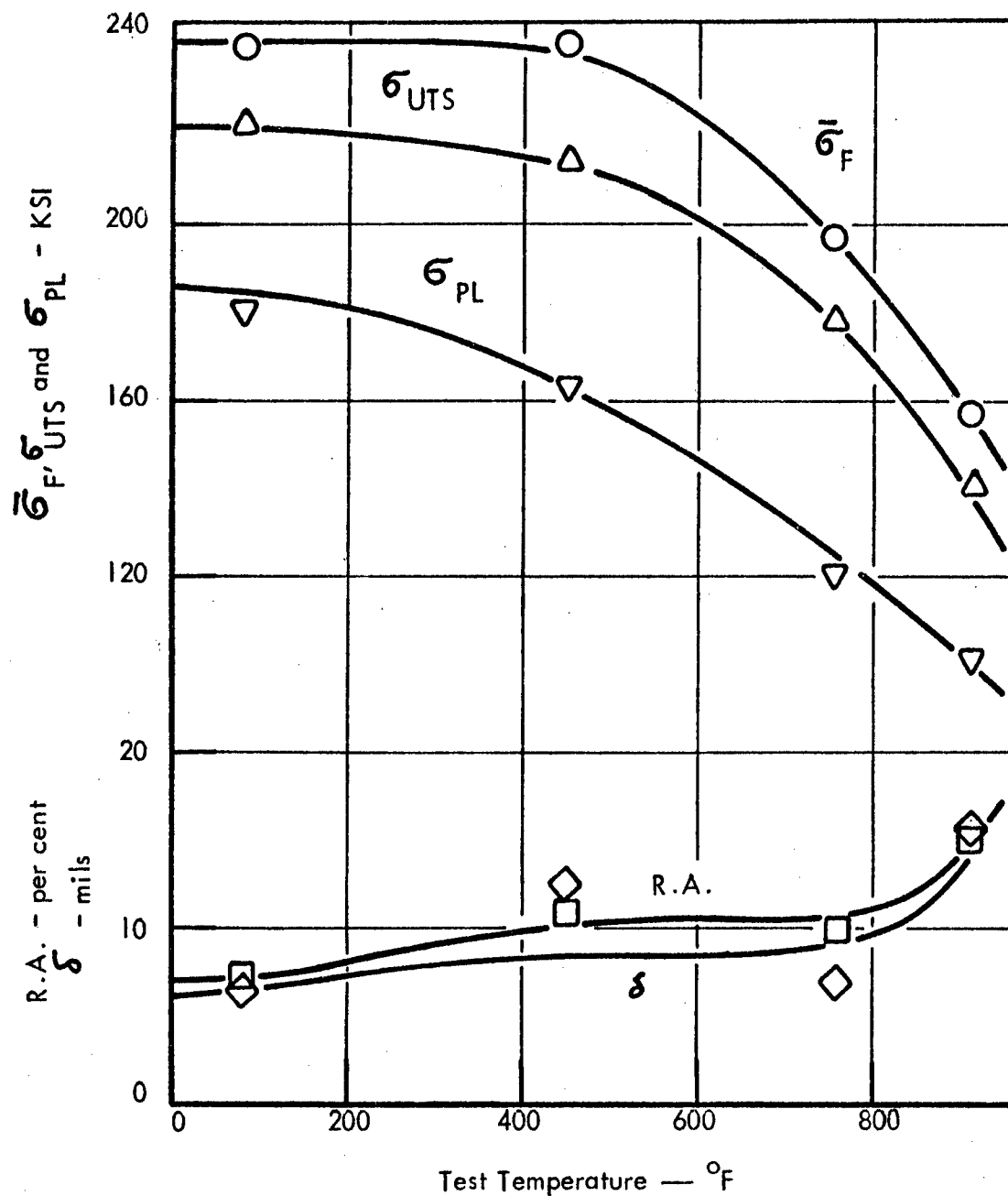


Figure 89. Tensile Properties of Radiused Transverse N20T Specimens as a Function of Test Temperature.

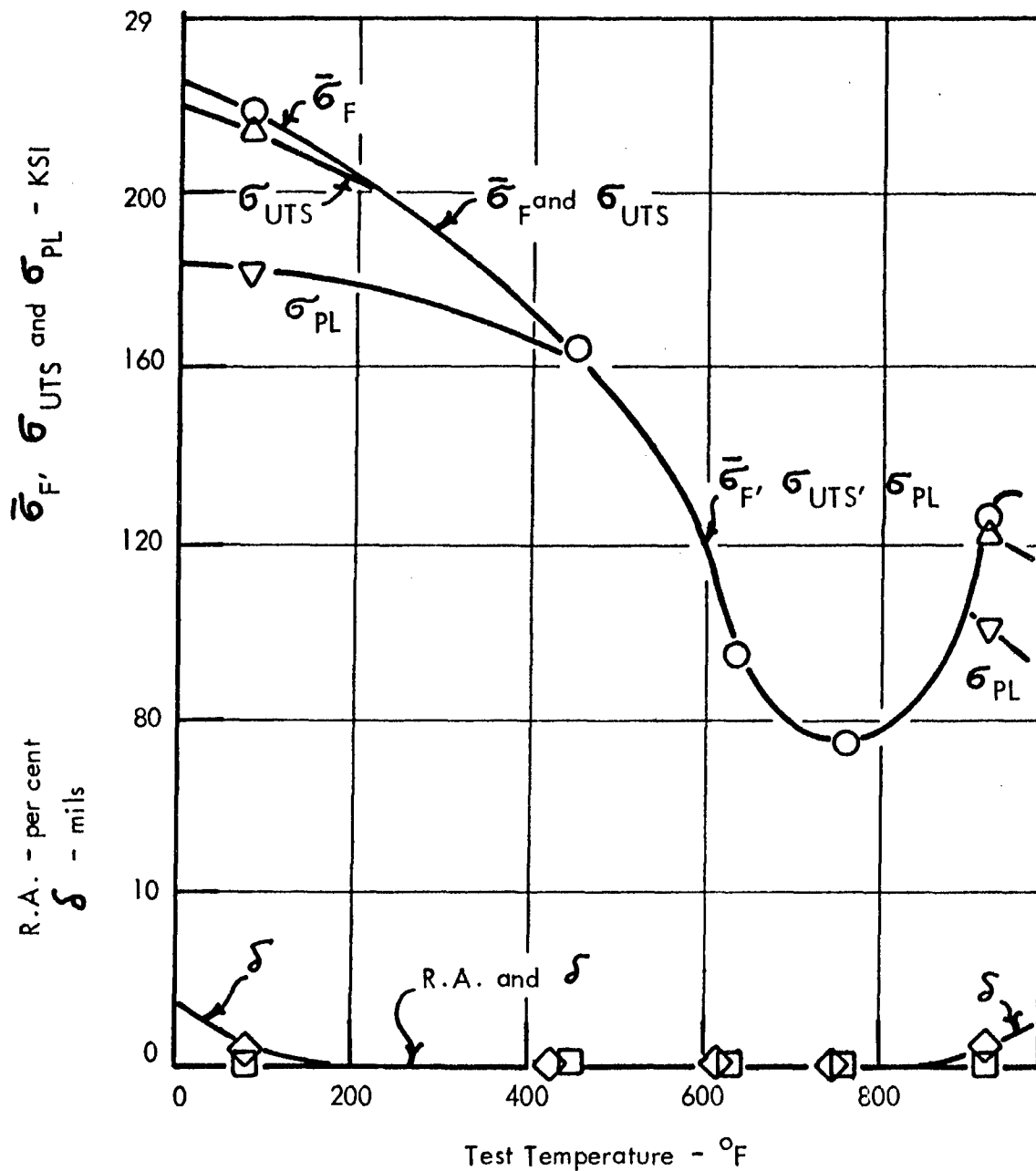


Figure 90. Tensile Properties of Radiused Transverse L20T Specimens as a Function of Test Temperature.

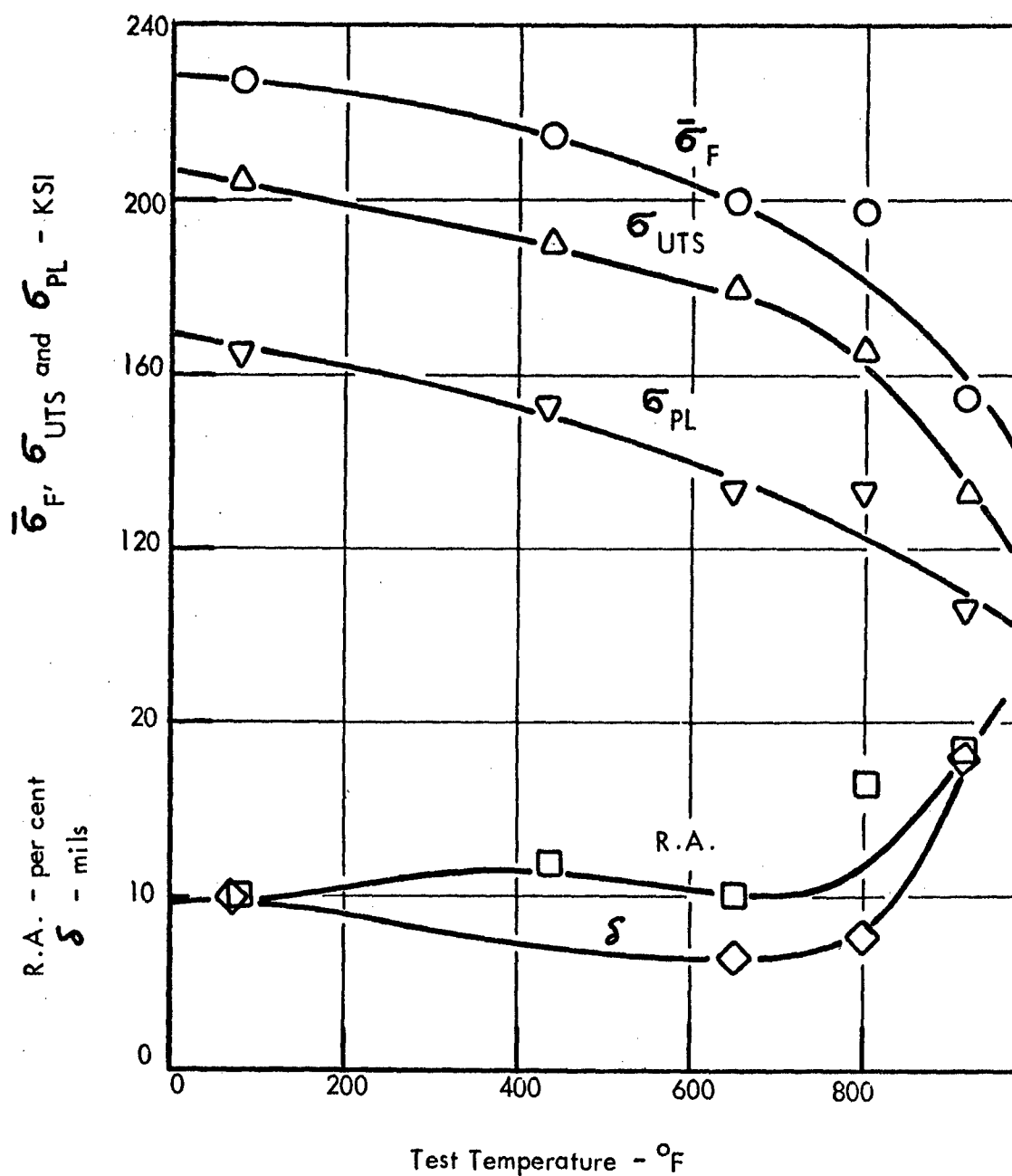


Figure 91. Tensile Properties of Radiused Transverse N18T Specimens as a Function of Test Temperature.

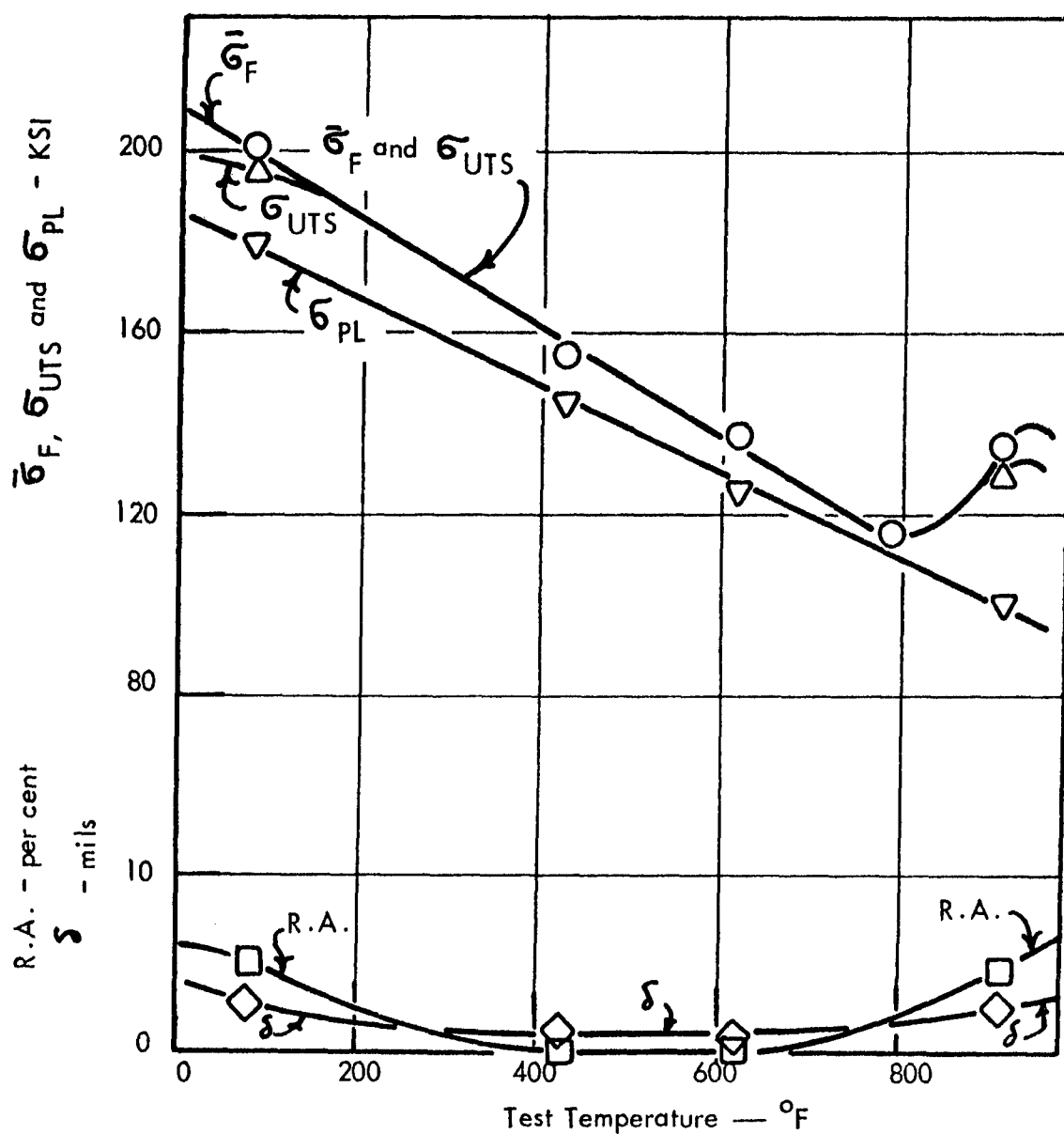


Figure 92. Tensile Properties of Radiused Transverse L18T Specimens as a Function of Test Temperature.

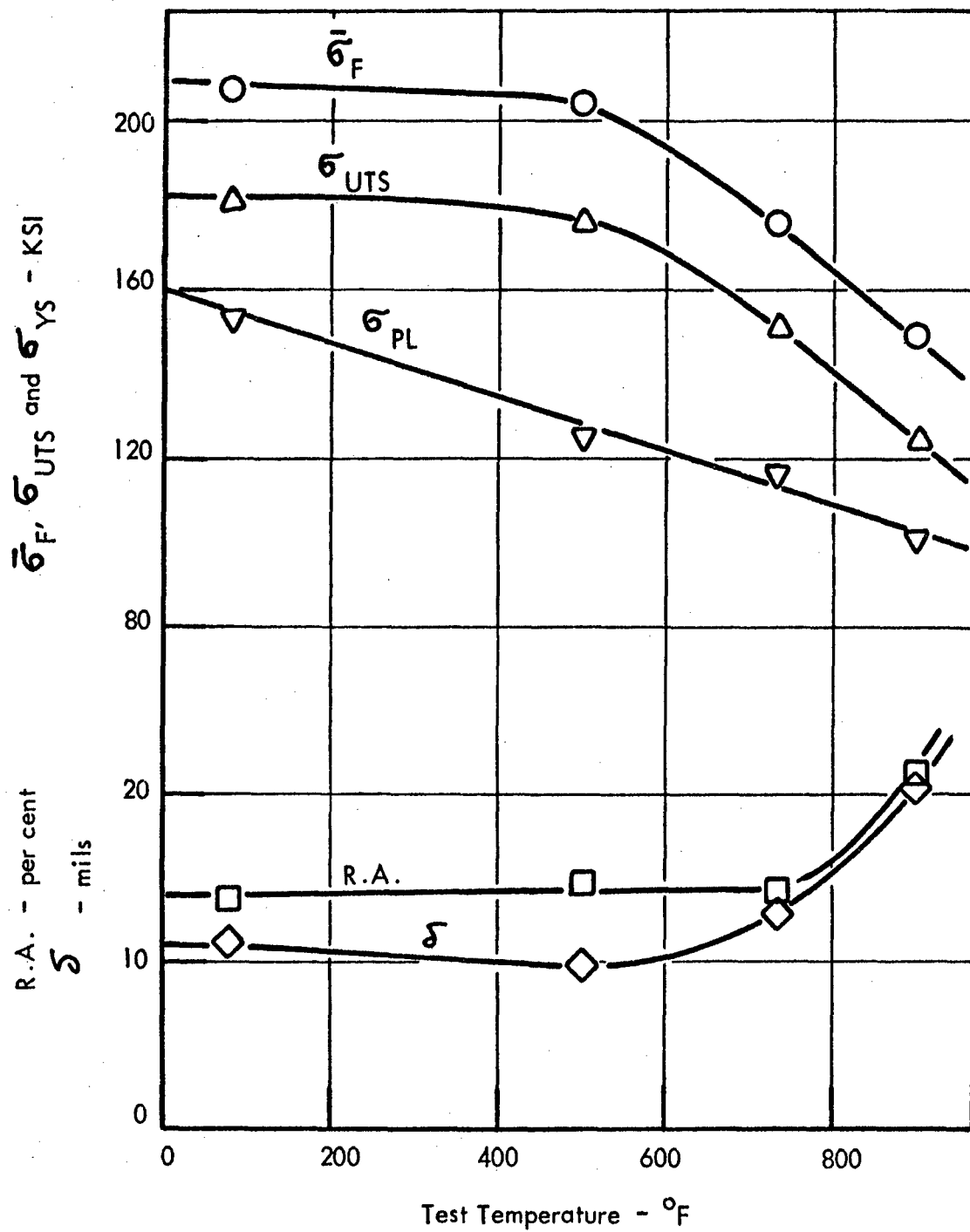


Figure 93. Tensile Properties of Radiused Transverse N16T Specimens as a Function of Test Temperature.

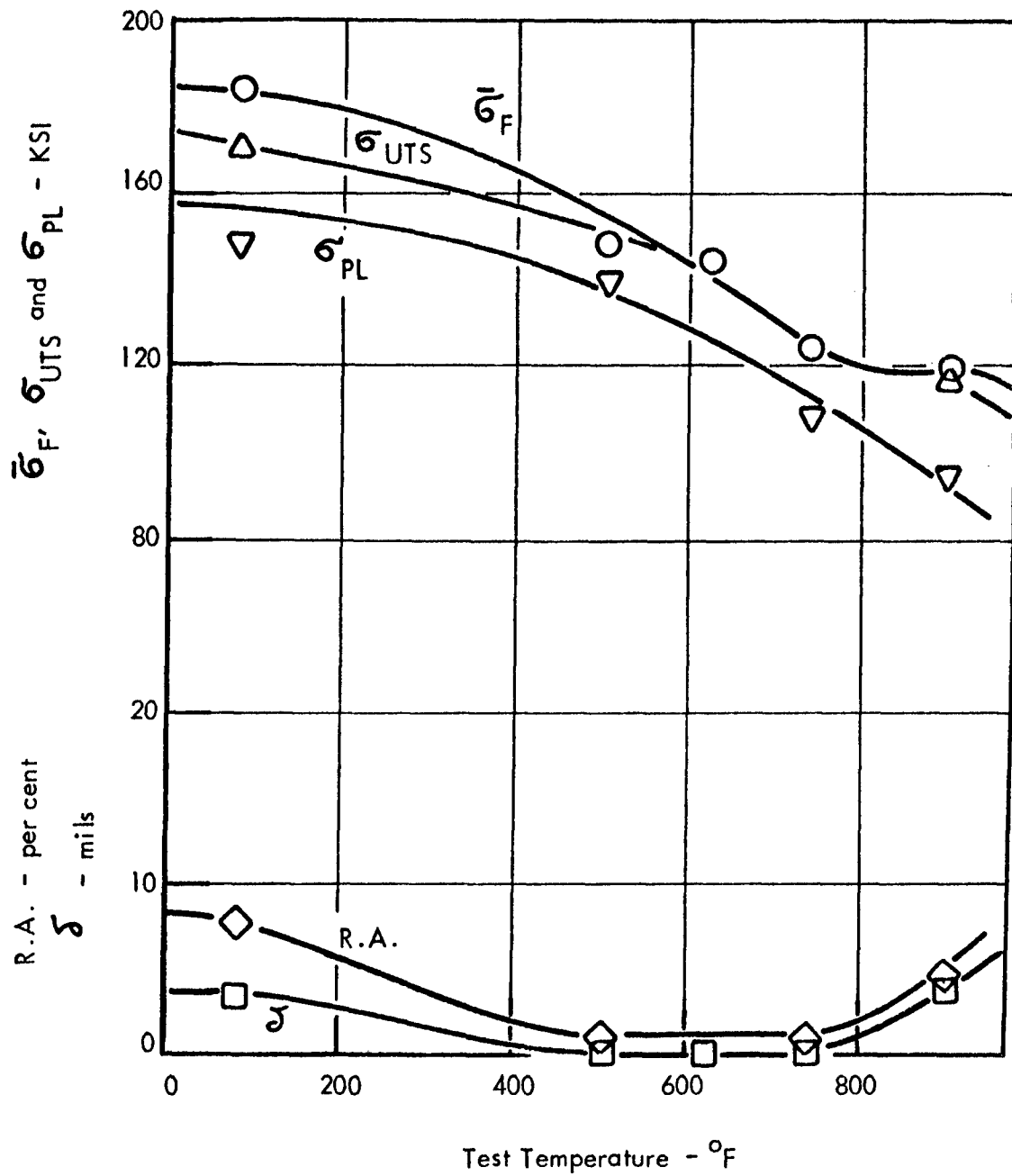


Figure 94. Tensile Properties of Radiused Transverse L16T Specimens as a Function of Test Temperature.

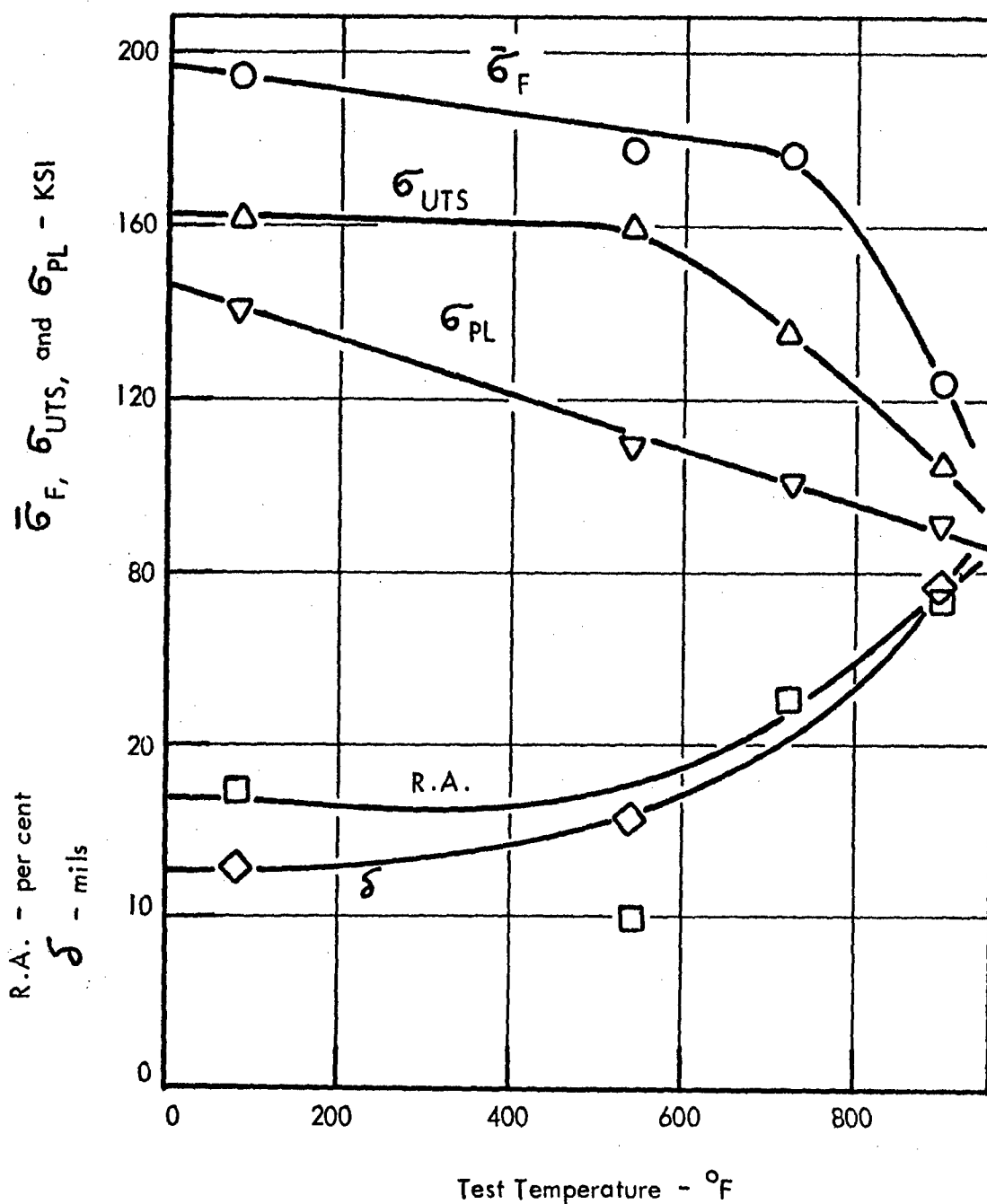


Figure 95. Tensile Properties of Radiused Transverse N14T Specimens as a Function of Test Temperature.

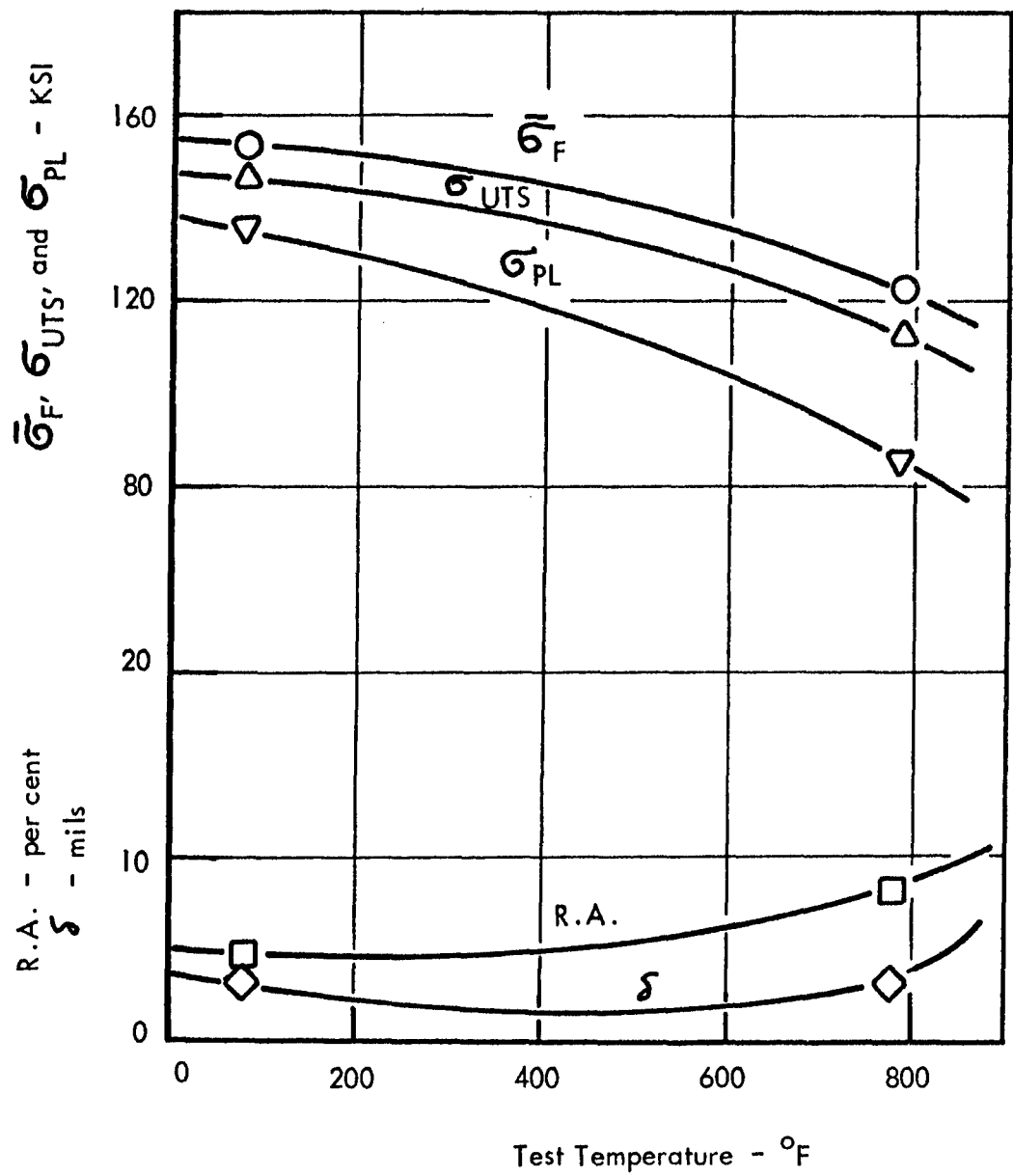


Figure 96. Tensile Properties of Radiused Transverse L14T Specimens as a Function of Test Temperature.

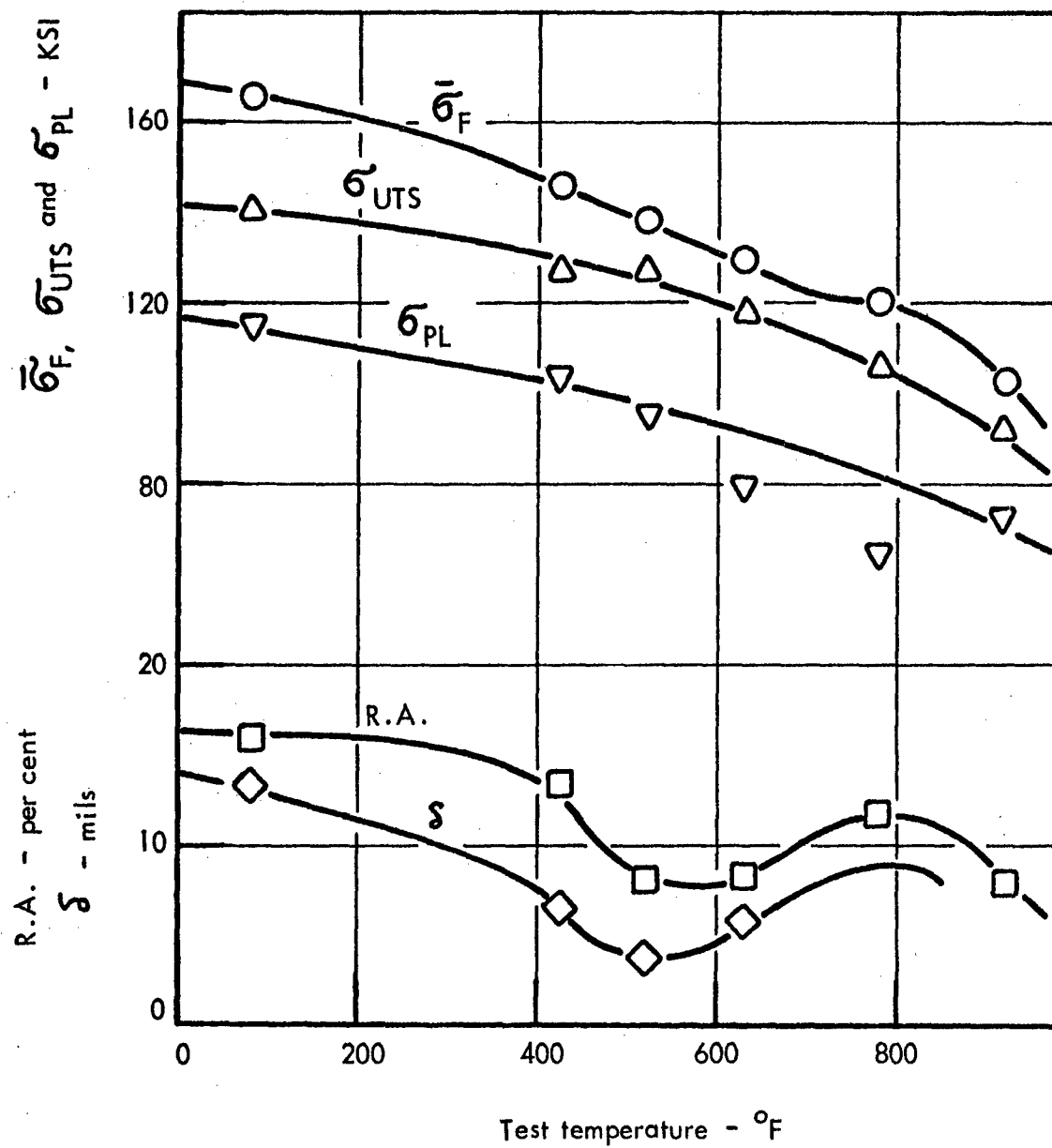


Figure 97. Tensile Properties of Radiused Transverse L12T Specimens as a Function of Test Temperature.

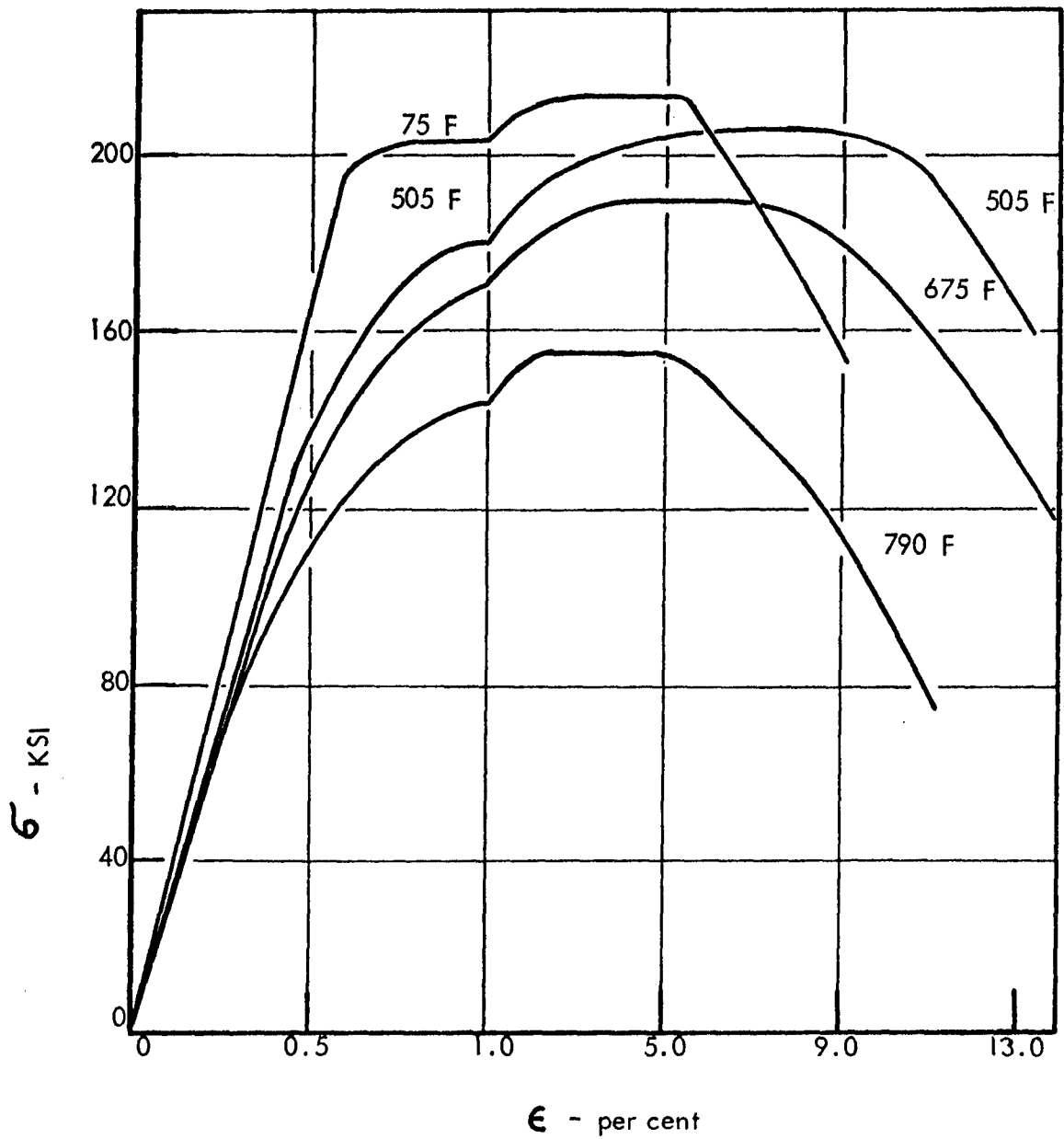


Figure 98. Engineering Stress-Strain Plots of Standard Longitudinal Specimens of N22 Material at Room and Elevated Temperatures. (Note Strain Scale Change at 1.0 per cent)

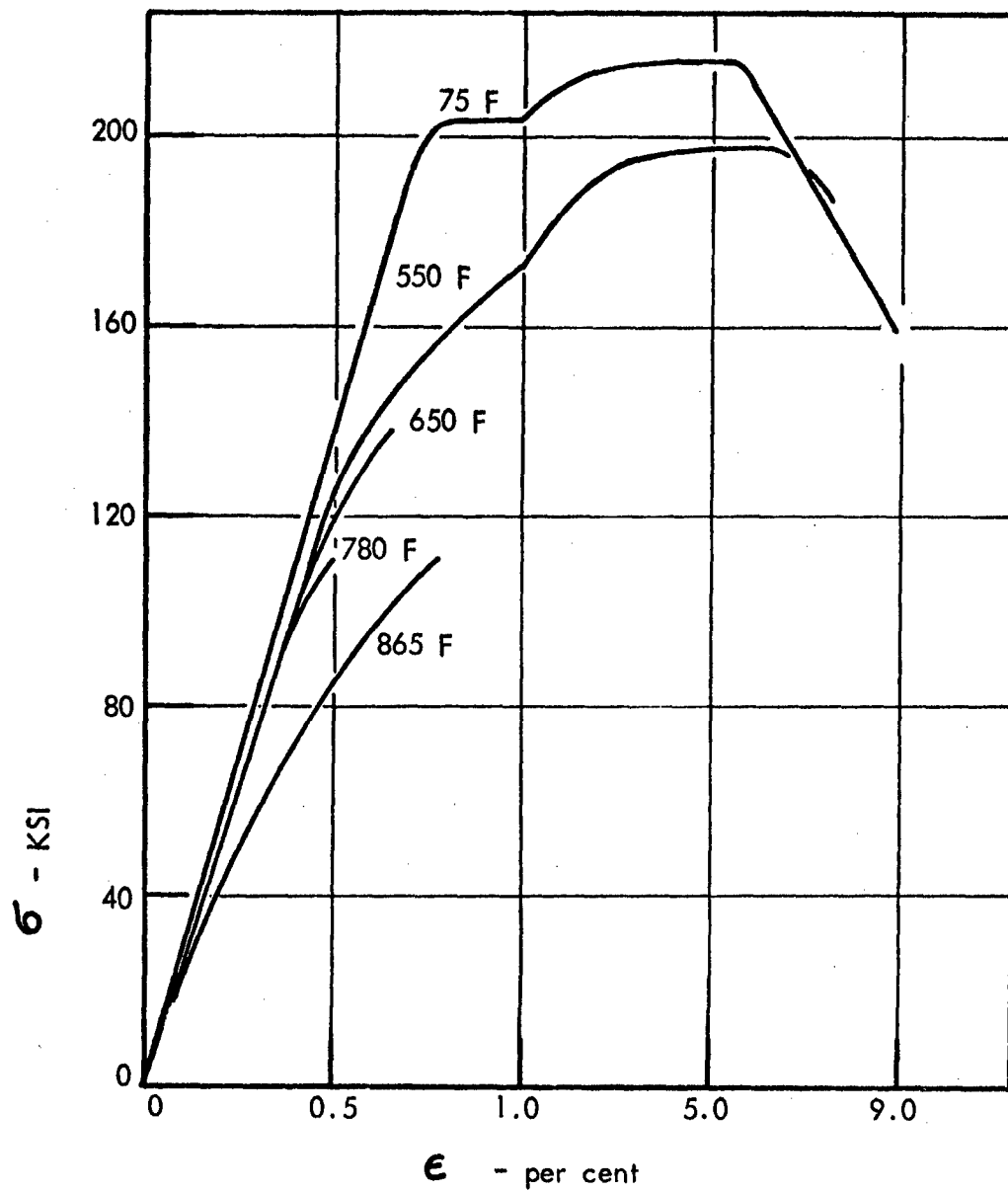


Figure 99. Engineering Stress-Strain Plots of Standard Longitudinal Specimens of L22 Material at Room and Elevated Temperatures. (Note Strain Scale Change at 1.0 per cent)

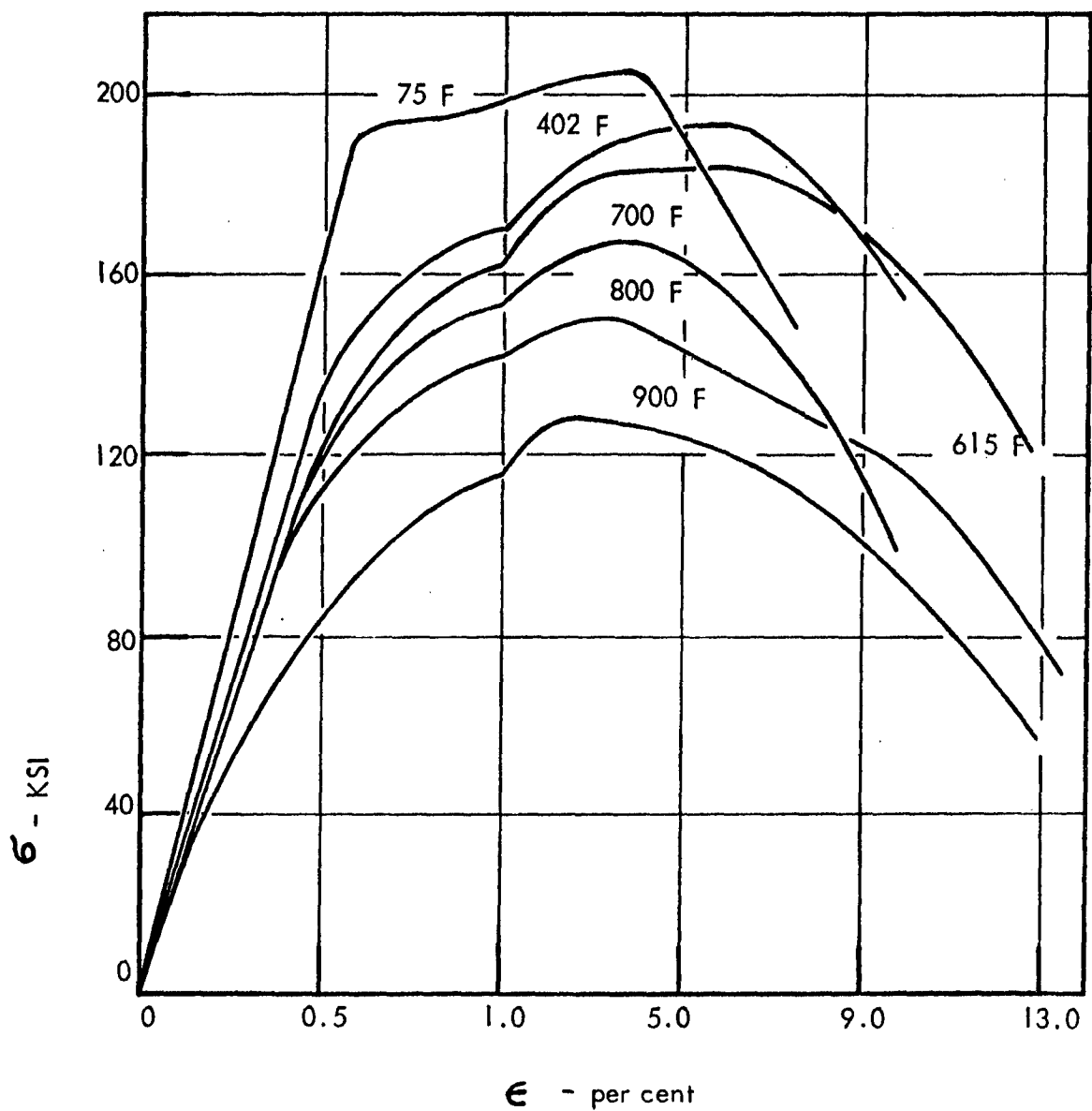


Figure 100. Engineering Stress-Strain Plots of Standard Longitudinal Specimens of N20 Material at Room and Elevated Temperatures. (Note Strain Scale Change at 1.0 per cent)

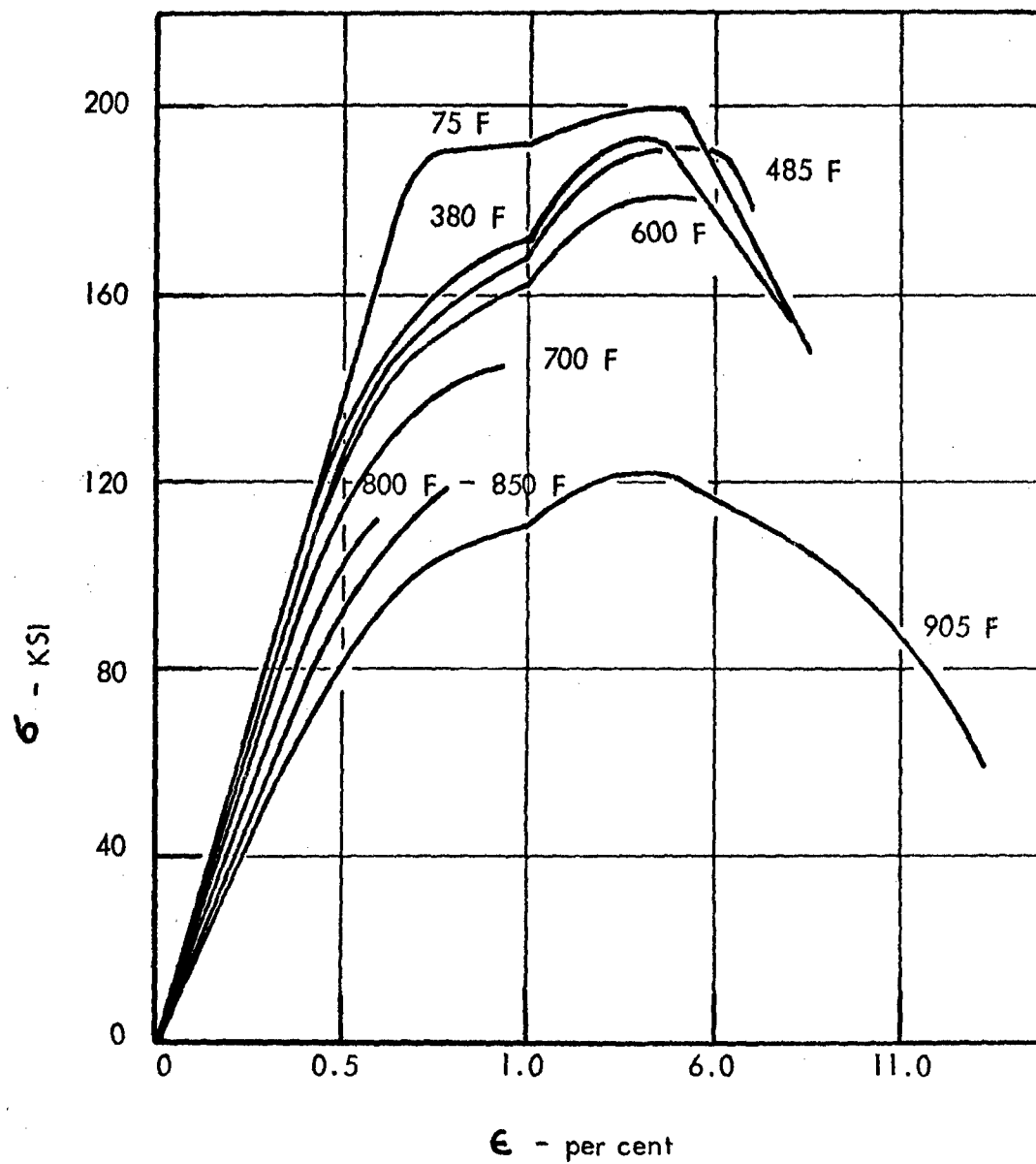


Figure 101. Engineering Stress-Strain Plots of Standard Longitudinal Specimens of L20 Material at Room and Elevated Temperatures. (Note Strain Scale Change at 1.0 per cent)

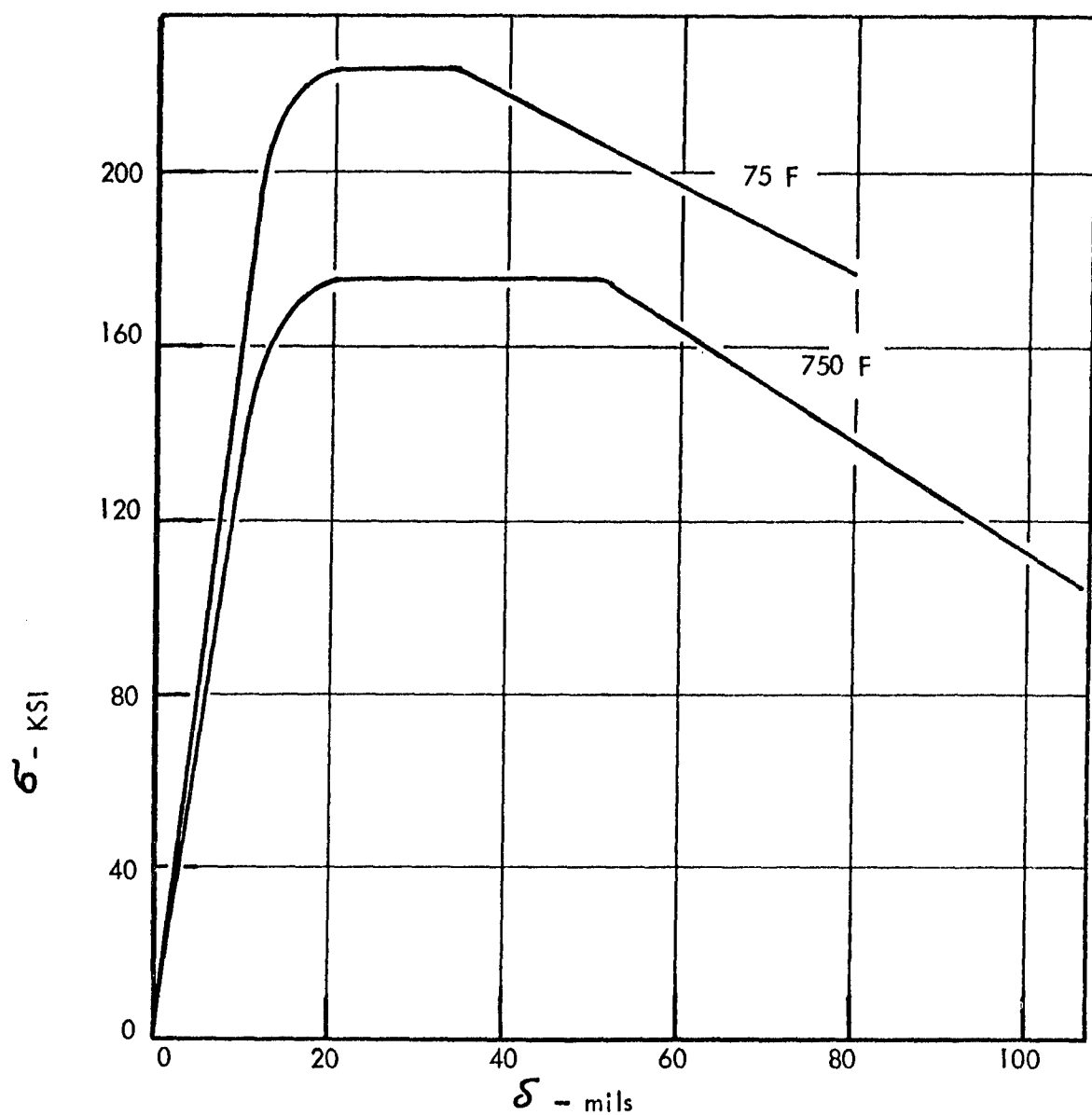


Figure 102. Engineering Stress-Deflection Plots of Fatigue Type Longitudinal Specimens of N22 Material at 75 and 750°F.

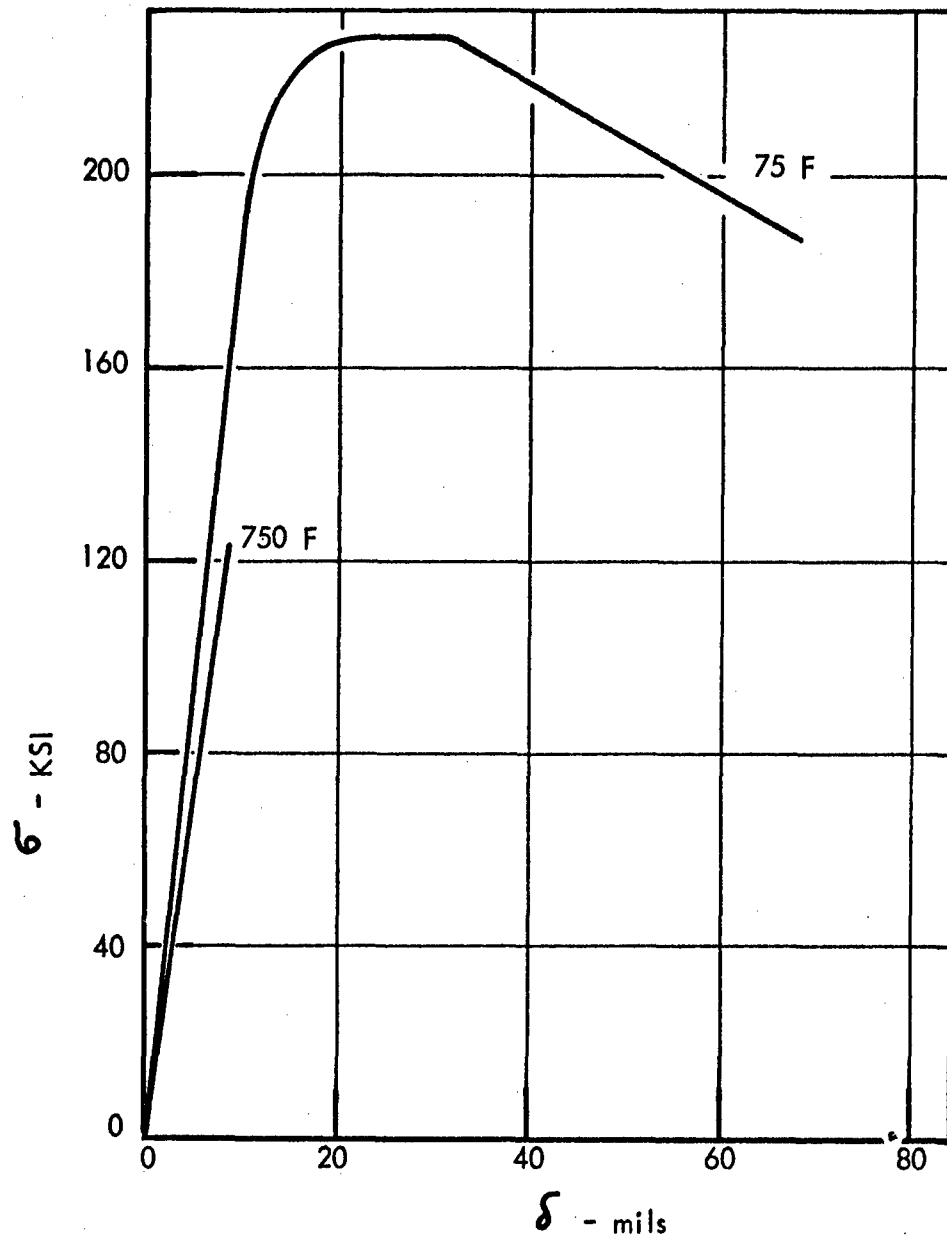


Figure 103. Engineering Stress-Deflection Plots of Fatigue Type Longitudinal Specimens of L22 Material at 75 and 755°F.

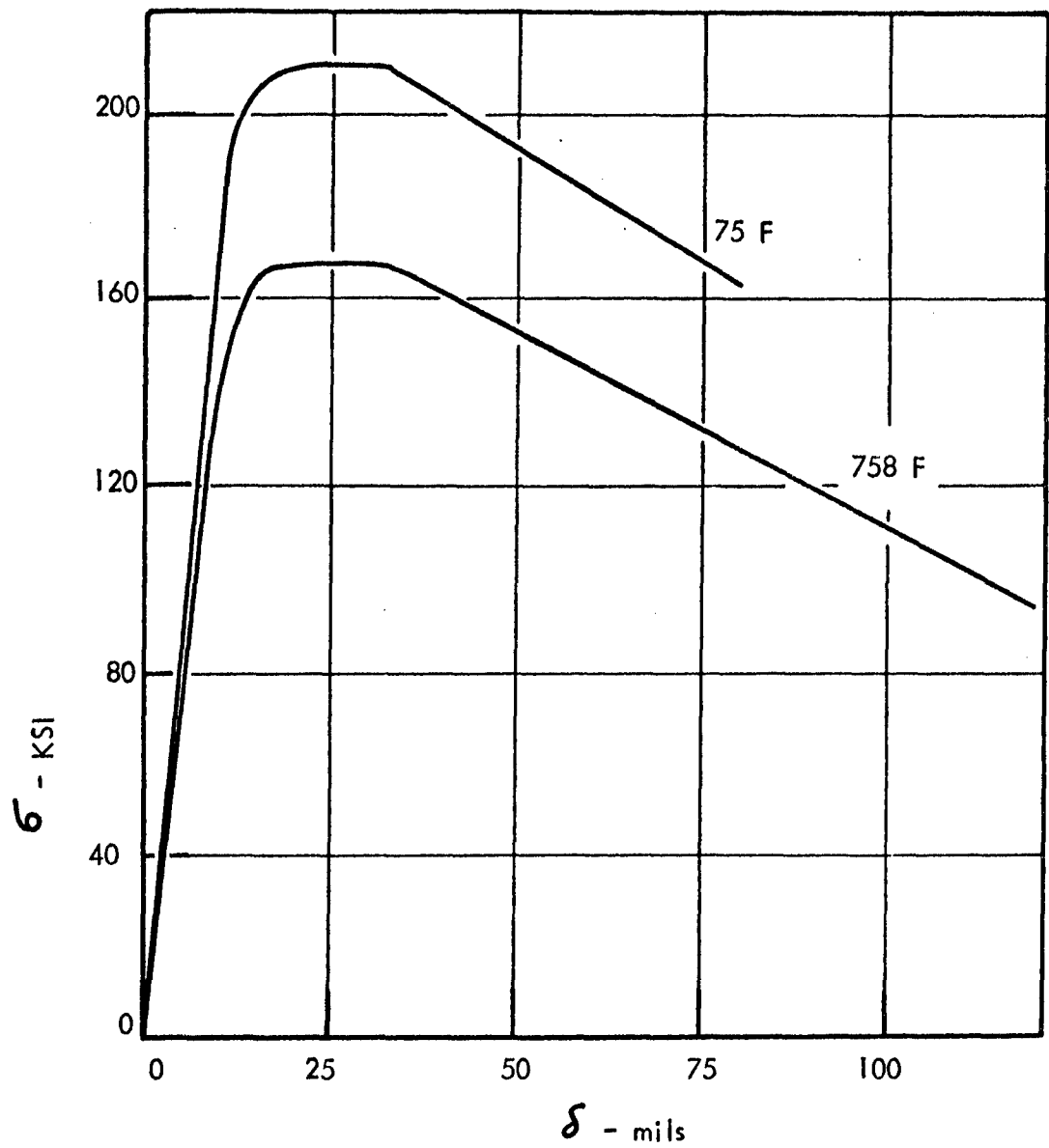


Figure 104. Engineering Stress-Deflection Plots of Fatigue Type Longitudinal Specimens of N20 Material at 75 and 758°F.

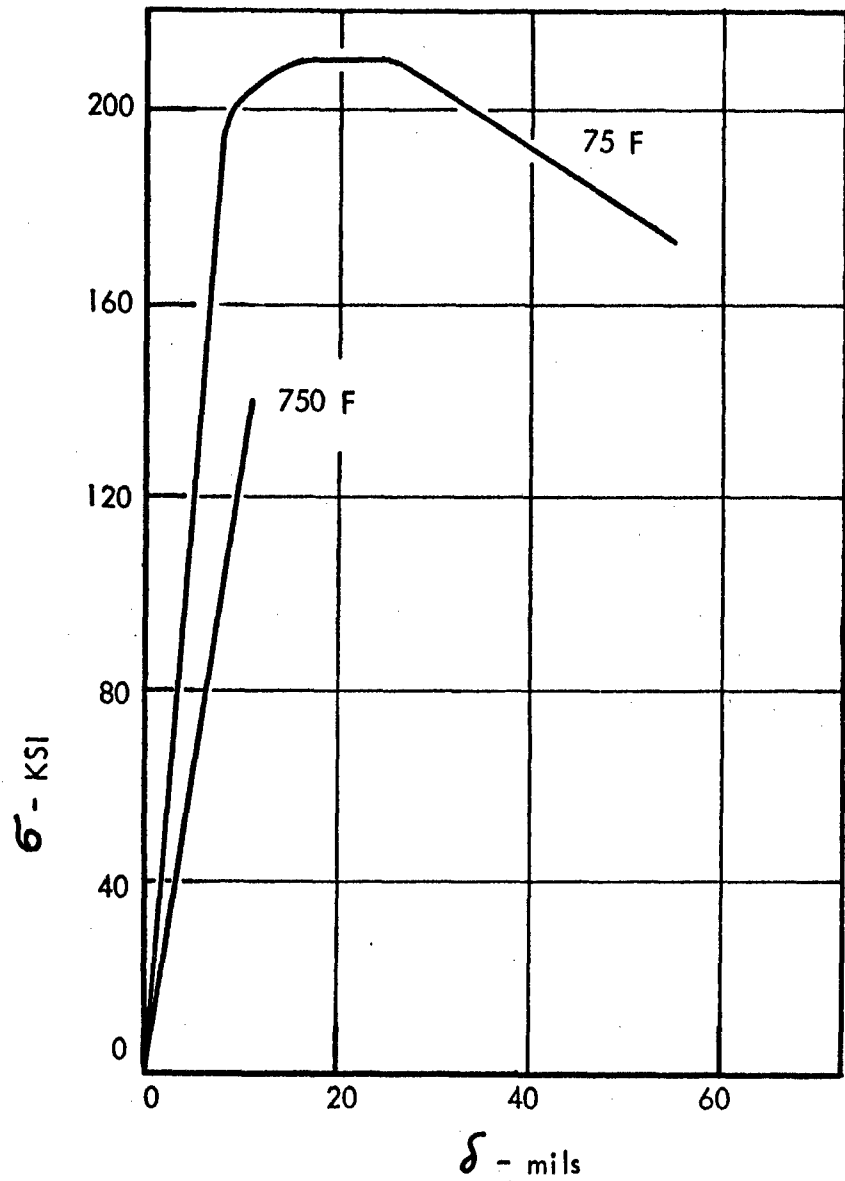


Figure 105. Engineering Stress-Deflection Plots of Fatigue Type Longitudinal Specimens of L20 Material at 75 and 750°F.

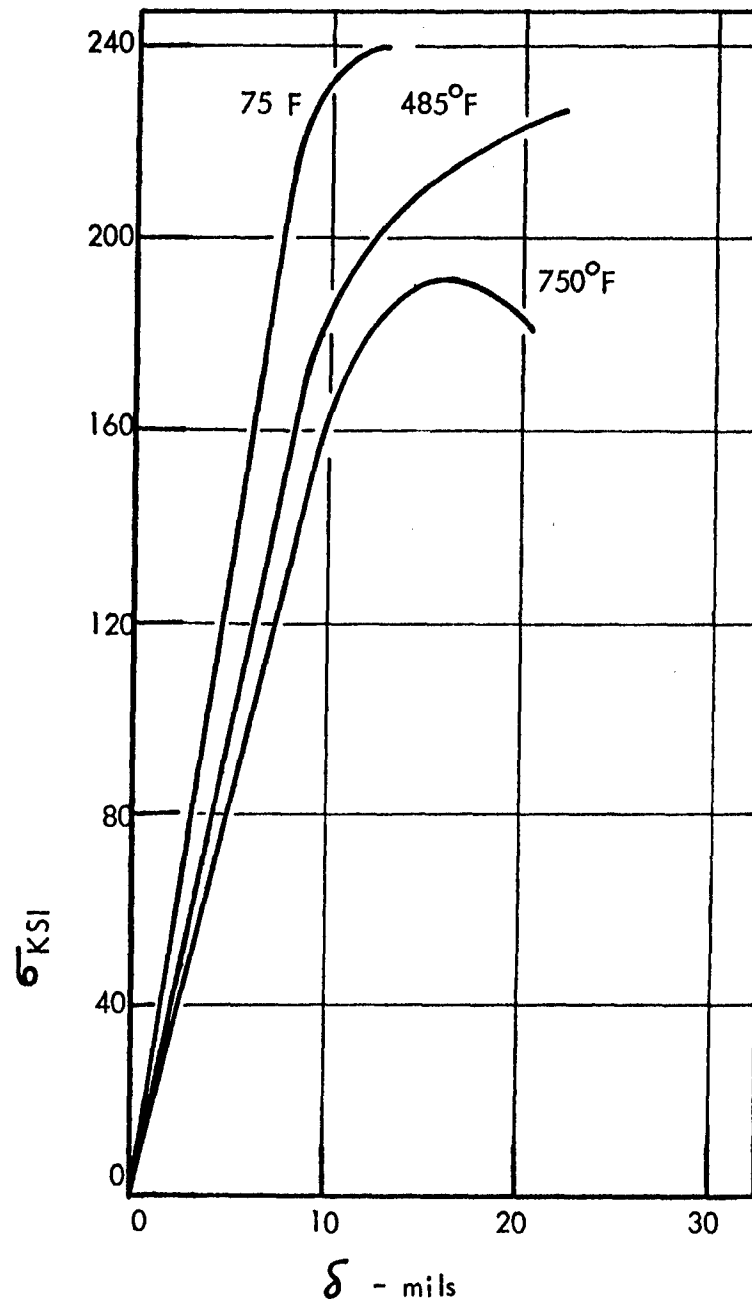


Figure 106. Engineering Stress-Deflection Plots of Fatigue Type Transverse Specimens of N22 Material at Room and Elevated Temperatures.

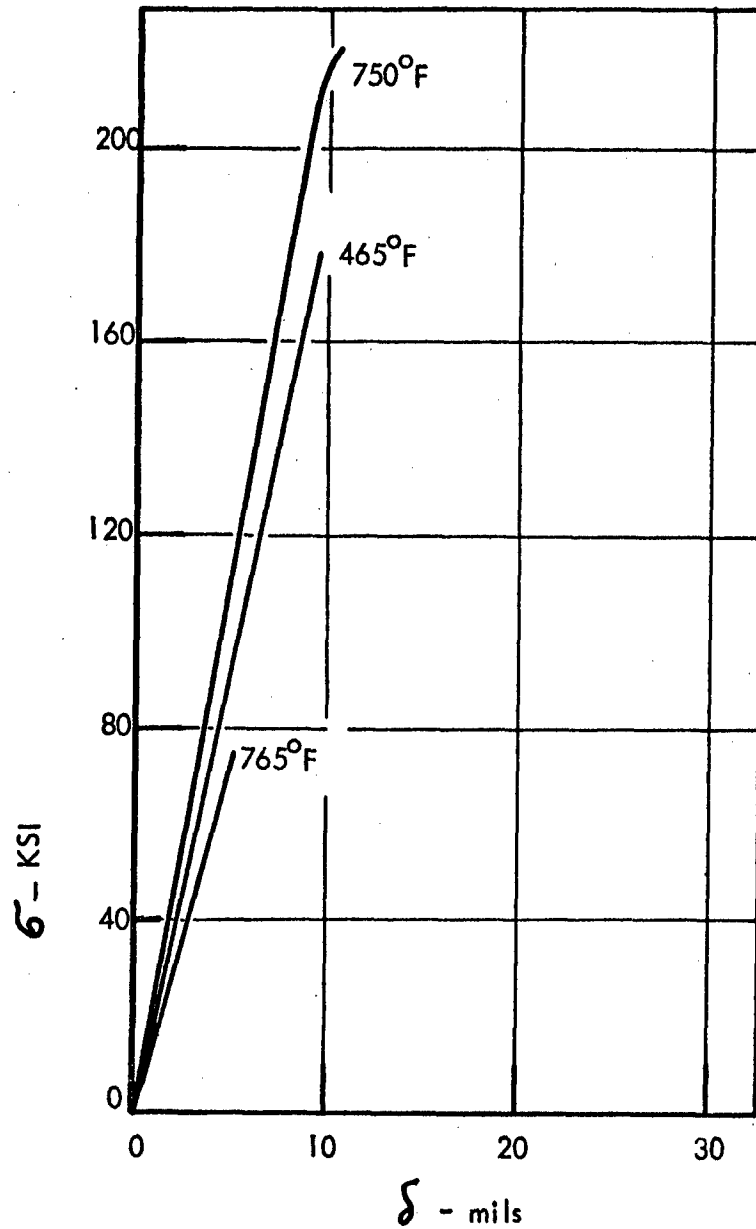


Figure 107. Engineering Stress-Deflection Plots of Fatigue Type Transverse Specimens of L22 Material at Room and Elevated Temperatures.

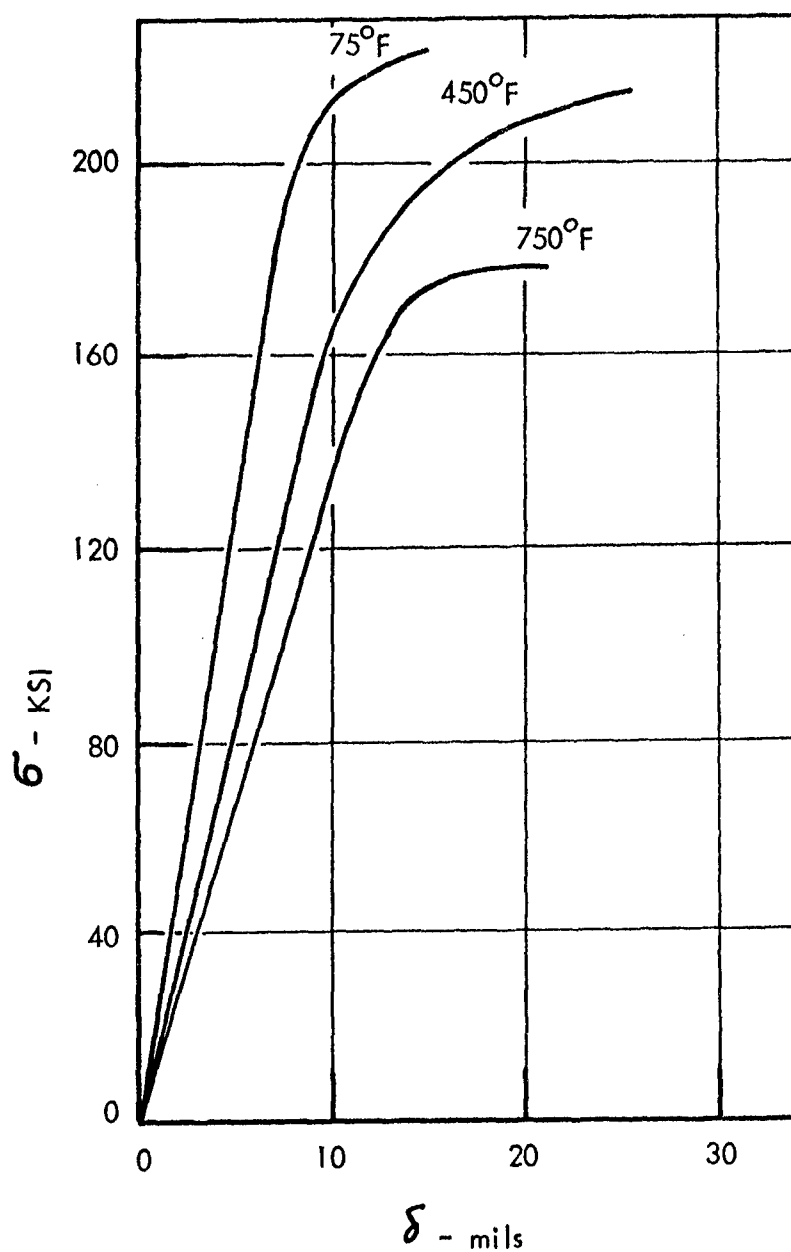


Figure 108. Engineering Stress-Deflection Plots of Fatigue Type Transverse Specimens of N20 Material at Room and Elevated Temperatures.

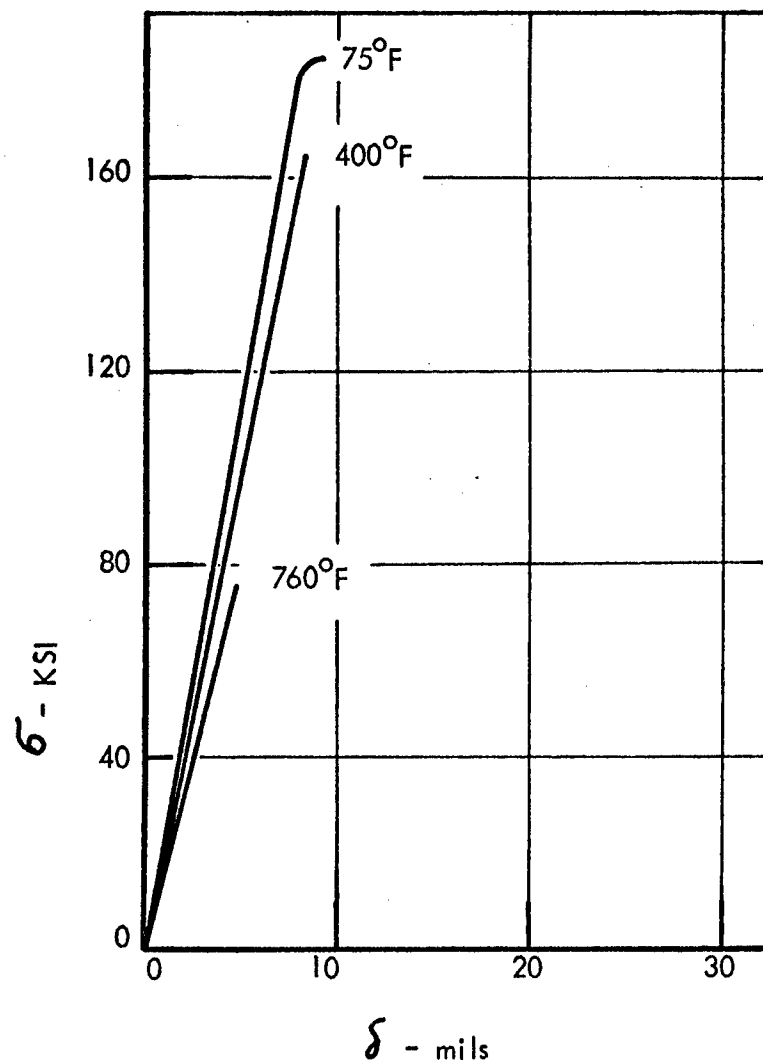


Figure 109. Engineering Stress-Deflection Plots of Fatigue Type Transverse Specimens of L20 Material at Room and Elevated Temperatures.

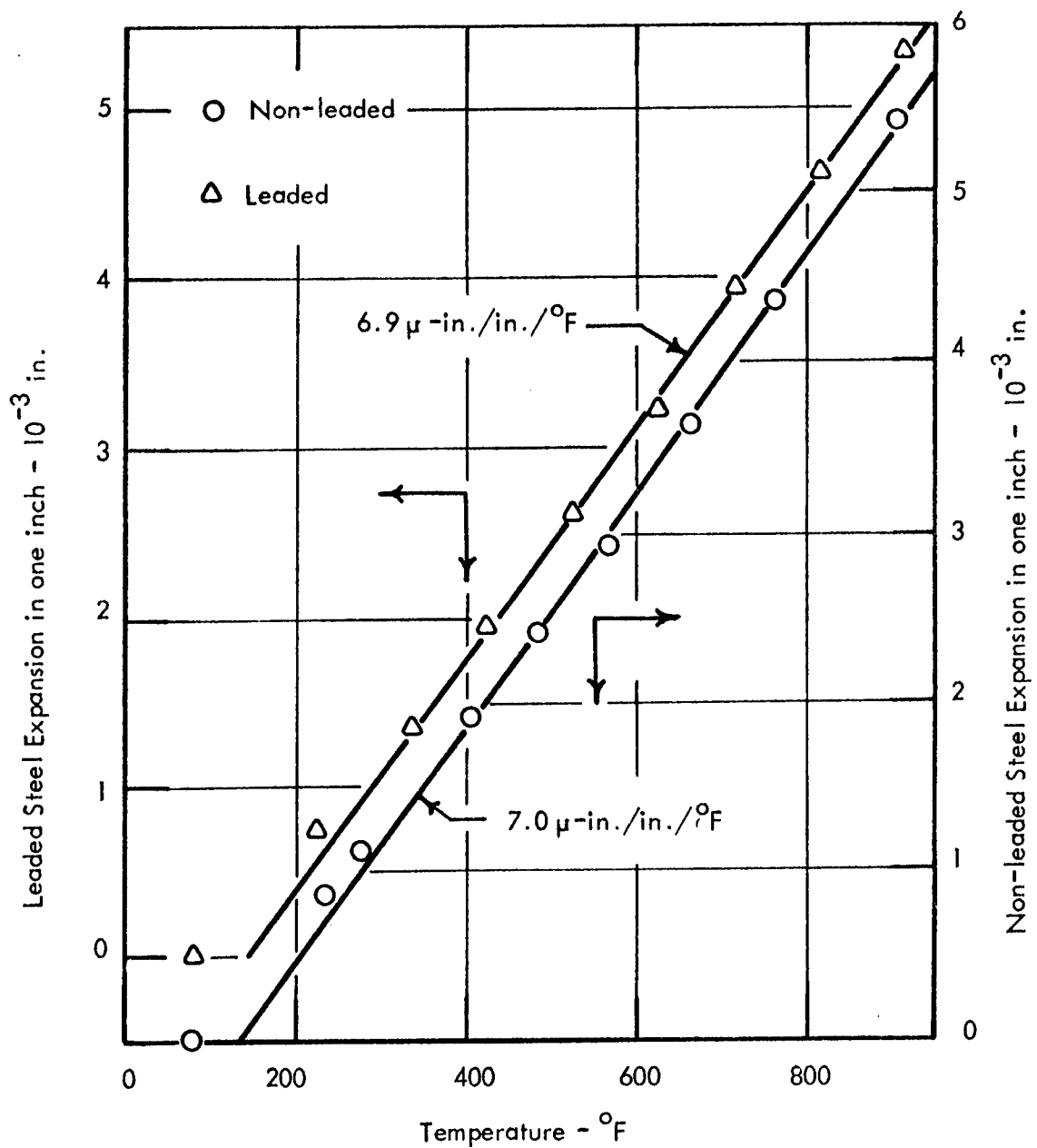


Figure 110. Thermal Expansion of Led and Non-led L20 and N20 Steel from 75 to 920°F. Note Scale Axis Separation to Separate Data Points.

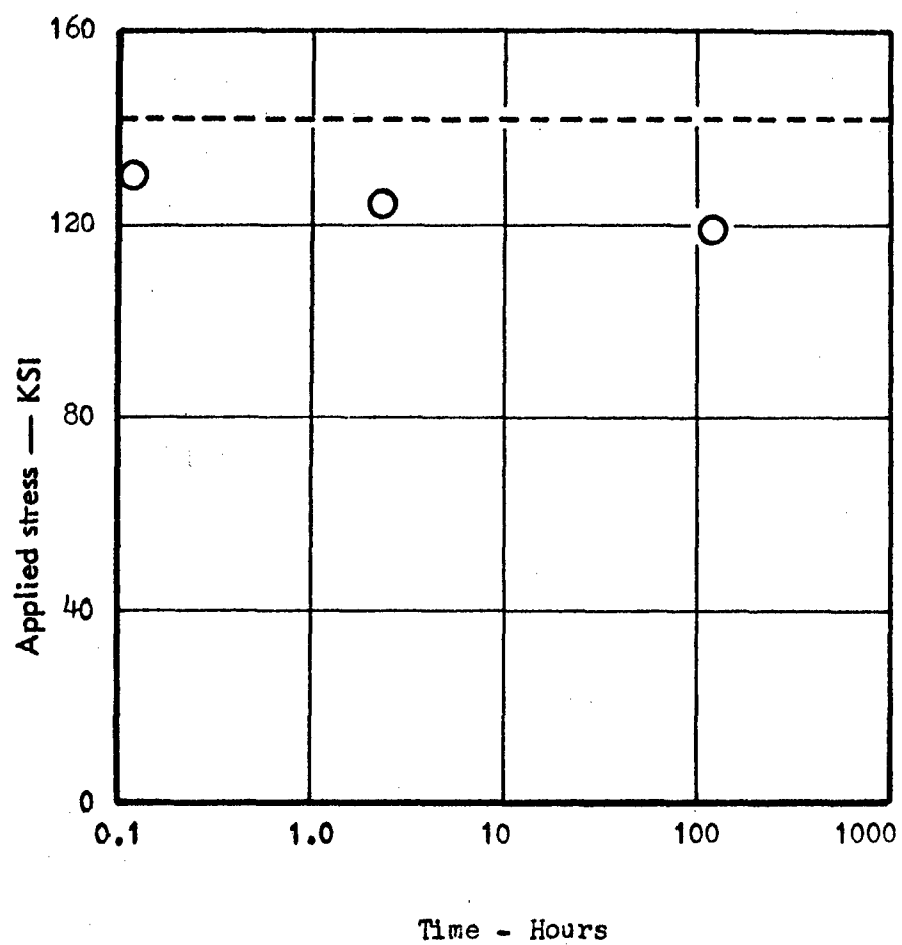


Figure 111. Applied Static Fatigue Stress at 750°F Versus Time to Fracture for L20 Material.

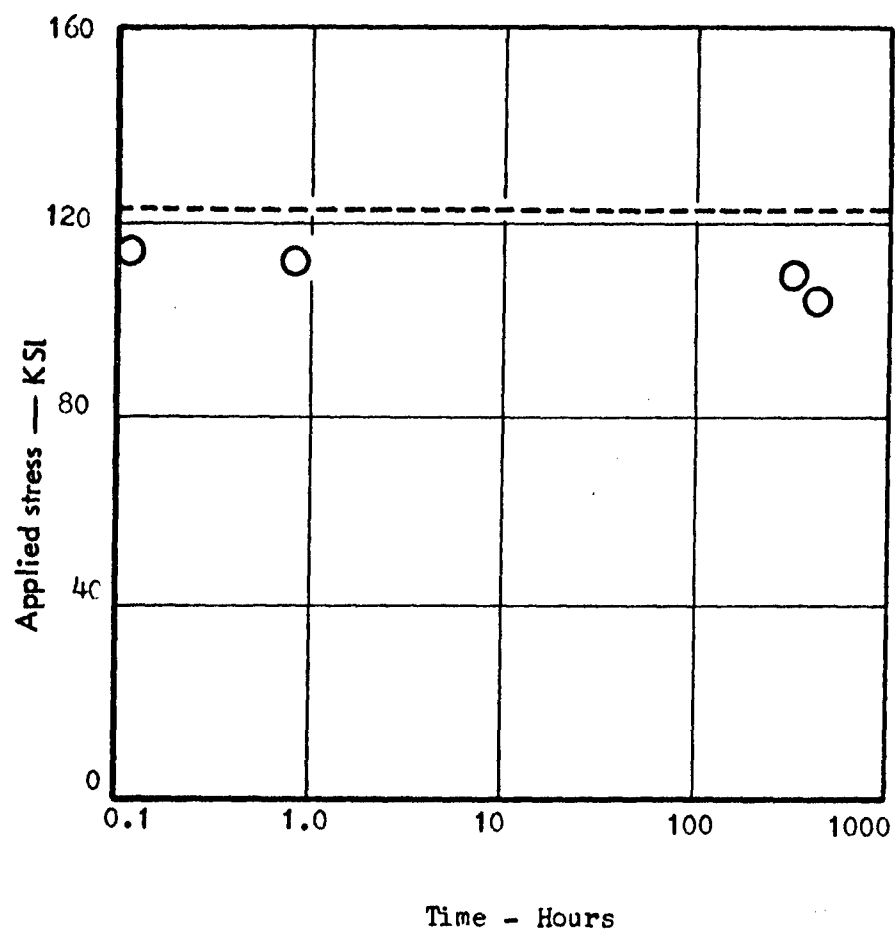


Figure 112. Applied Static Fatigue Stress at 750°F Versus Time to Fracture for L22 Material.

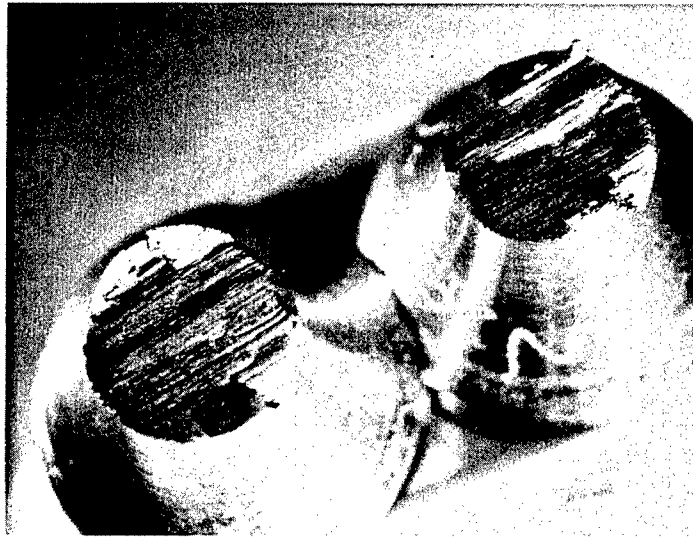


Figure 113. Fracture Surface Photographs of Transverse Tensile Specimen at (Top) 4X and (Bottom) 6X Magnification. Note These Fractures Obtained on a Leaded Material Are Typical of Those Obtained on Both Leaded and Non-leaded Steel Tested in a Transverse Direction.

Abs. Energy Ft-Lbs.	Test Temp. °F
---------------------------	---------------------

29	RT
30	250
29	408
33	500
31	580
35	602
30	606
30	700
27	810
25	820
22	913



N20 SERIES

Test Temp. °F	Abs. Energy Ft-Lbs.
---------------------	---------------------------

RT	27
200	26
300	32
425	28
510	27
550	23
580	27
620	21
637	16
728	14
843	12



L20 SERIES

Figure 114. Impact Fracture Surface Photographs of
Leaded and Non-leaded L20 and N20 Material.
Test Temperatures and Related Impact Values
Indicated Opposite Photograph.

L20 SERIES
Test Abs.
Temp. Energy
°F Ft-Lbs.

728 14

627 16

620 21

580 27

550 23

510 27



N20 SERIES
Test Abs.
Temp. Energy
°F Ft-Lbs.

700 30

606 30

602 35

580 31

500 33

408 29



Figure 115. Enlarged Oblique View of Impact Fracture Surfaces from Figure 114 in Temperature Range of Embrittlement of the Leaded L20 Material.

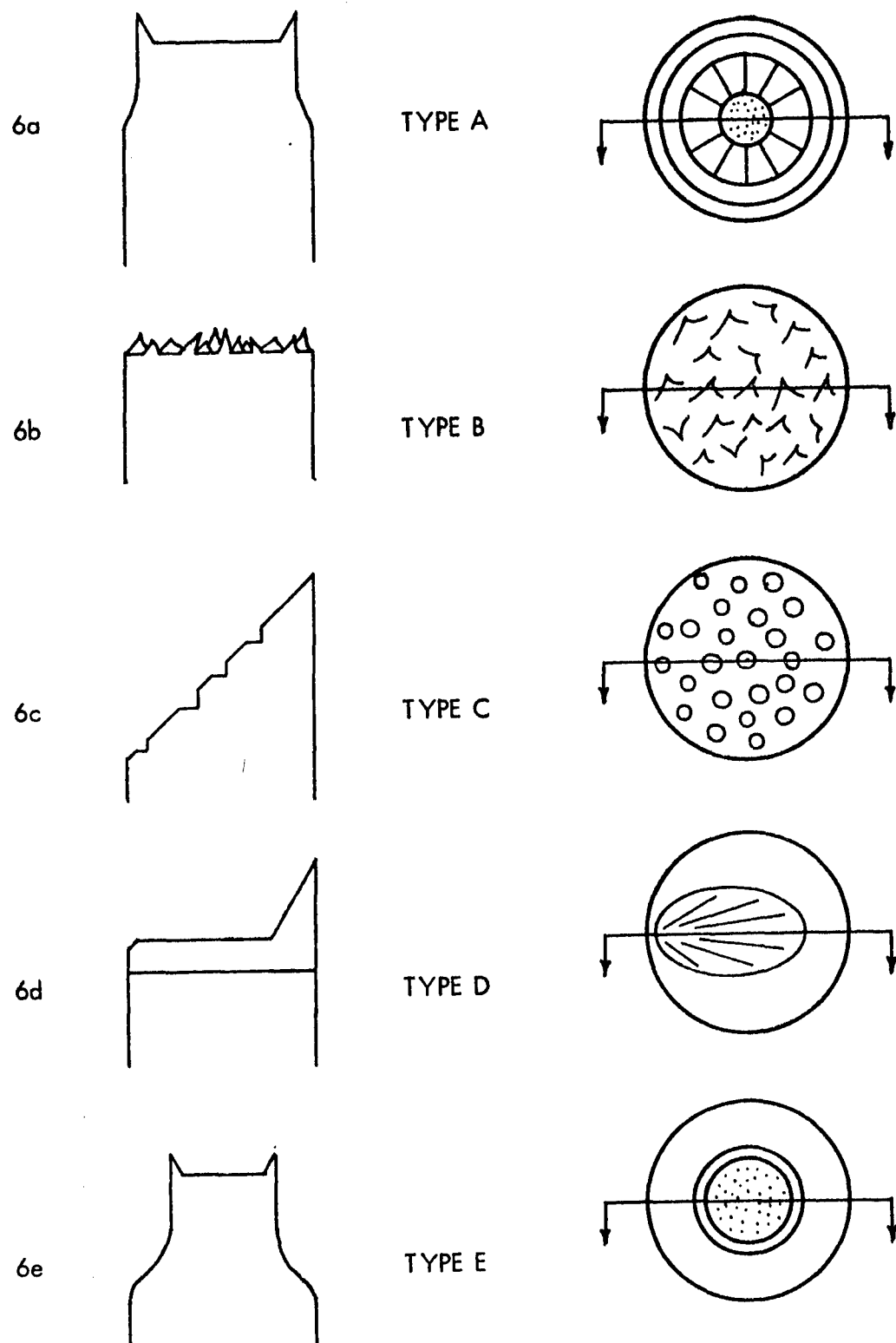


Figure 116. Fracture Surface Classification for Longitudinal Tensile Specimens.

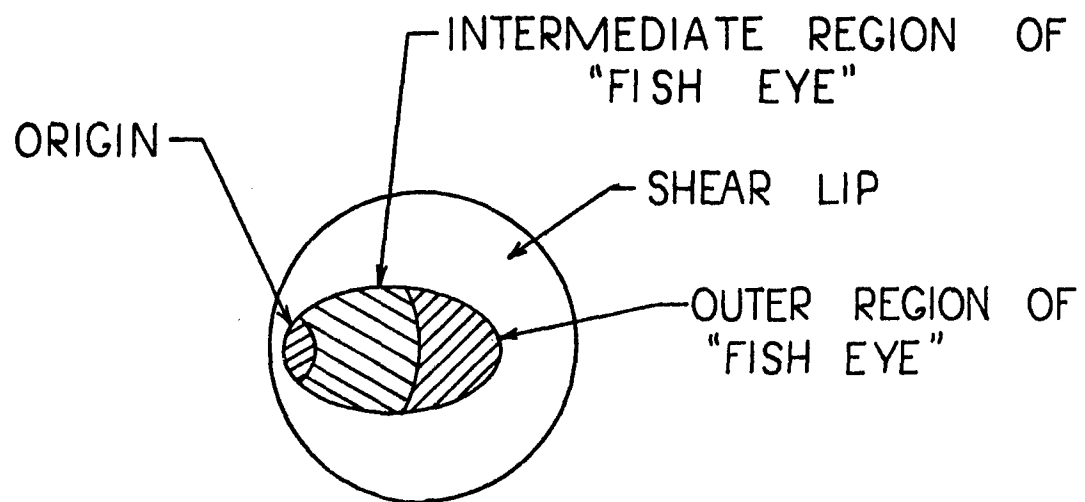


Figure 117. Schematic Drawing of Type D Fracture.

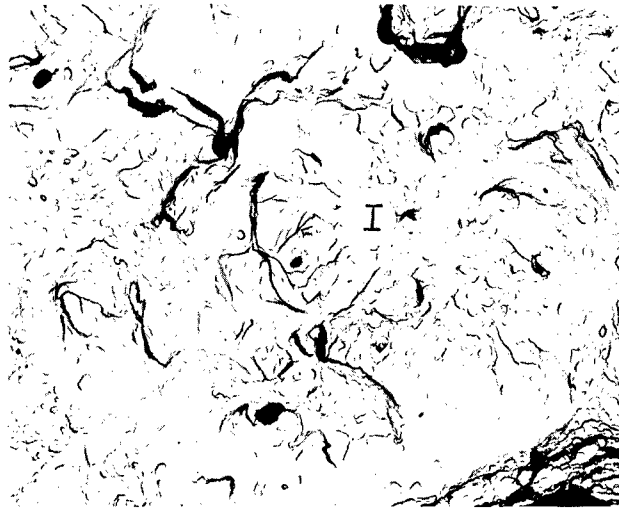


Figure 118. Electron Fractographs of Leaded Steel Showing a B Type Fracture Which Appears Intergranular in Nature. (3,000X)

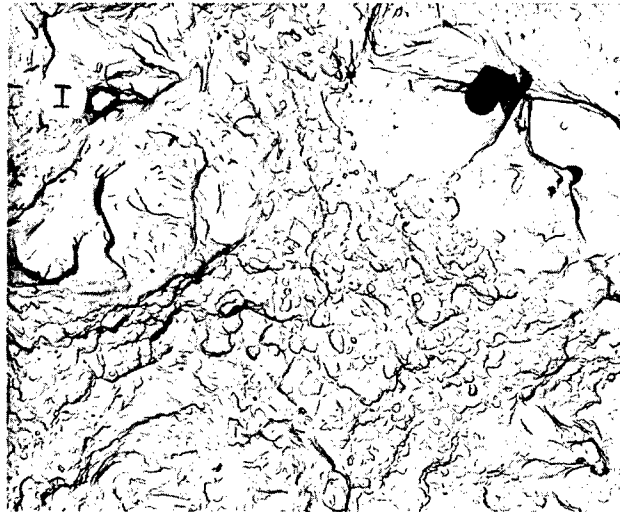


Figure 119. Electron Fractographs of Leaded Steel Showing a B Type Fracture Which Exhibits Both Intergranular and Transgranular Fracture Modes. (3,000X)

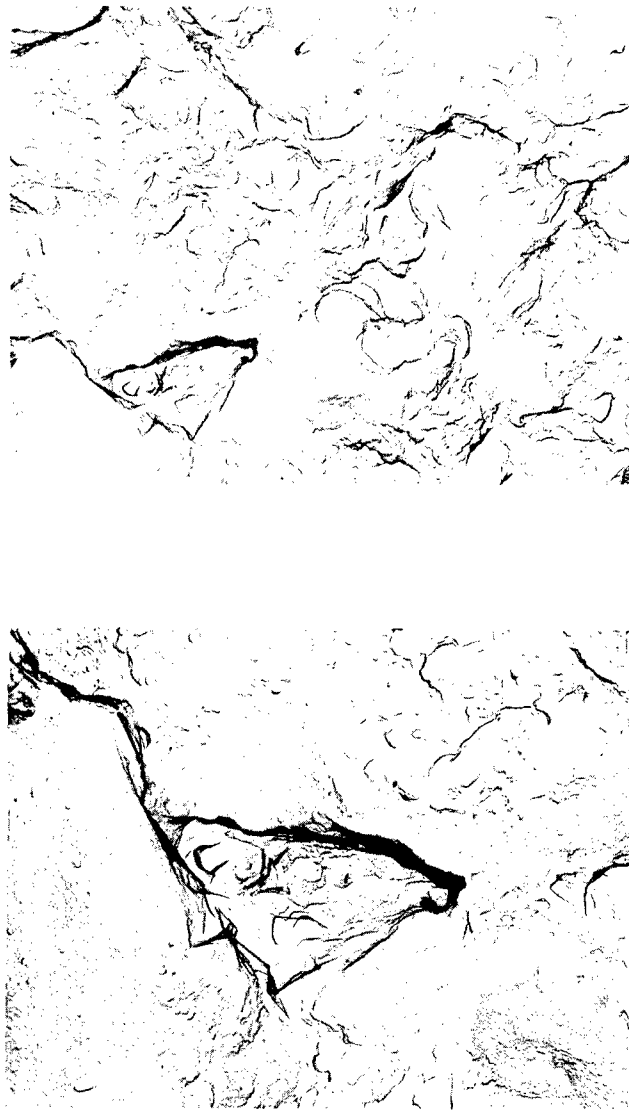


Figure 120. Electron Fractographs of Leaded Steel Showing a C Type Fracture in the Proximity of One of the "Fish-Eyes" Which Appears Intergranular in Nature. (Top, 2,000X; Bottom, 4,000X)

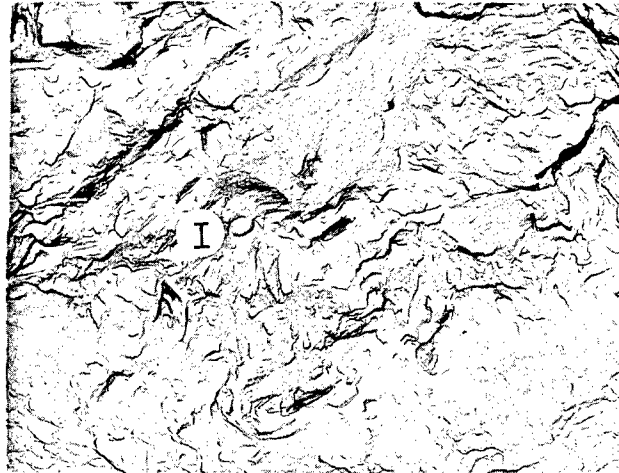
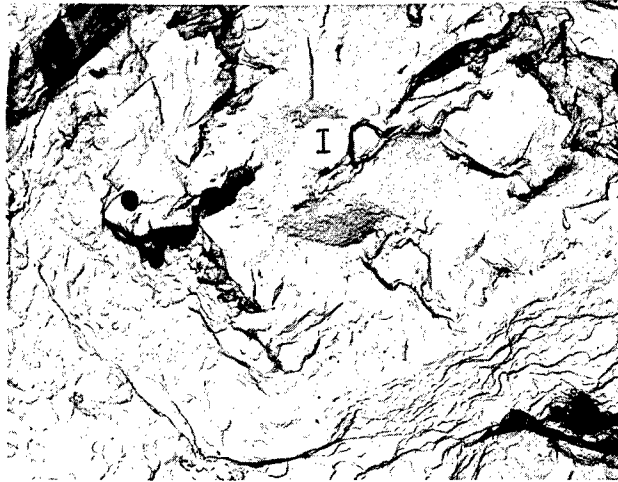


Figure 121. Electron Fractographs of Leaded Steel Showing a C Type Fracture at Some Distance from a Small "Fish-Eye" Which Exhibits Both Intergranular and Transgranular Fracture Modes. (3,000X)

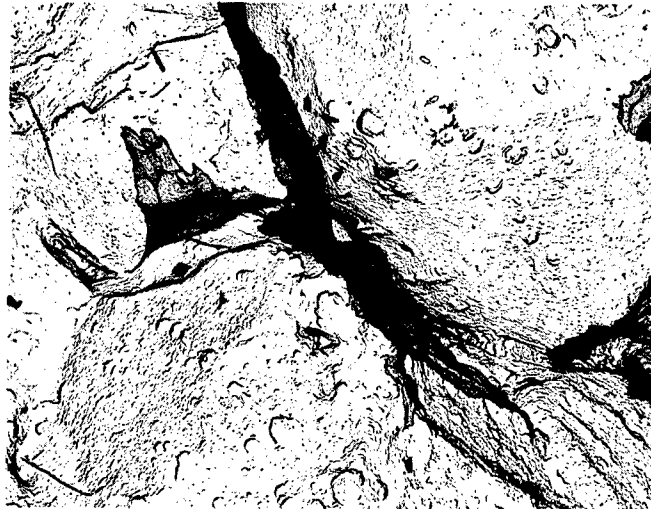
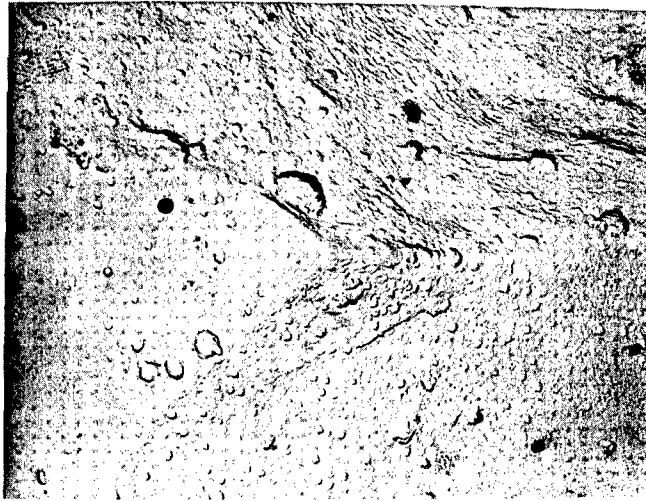


Figure 122. Electron Fractographs of Leaded Steel Showing a D Type Fracture Near the Origin of Cracking. Note That the Fracture is Completely Intergranular. (4,000X)

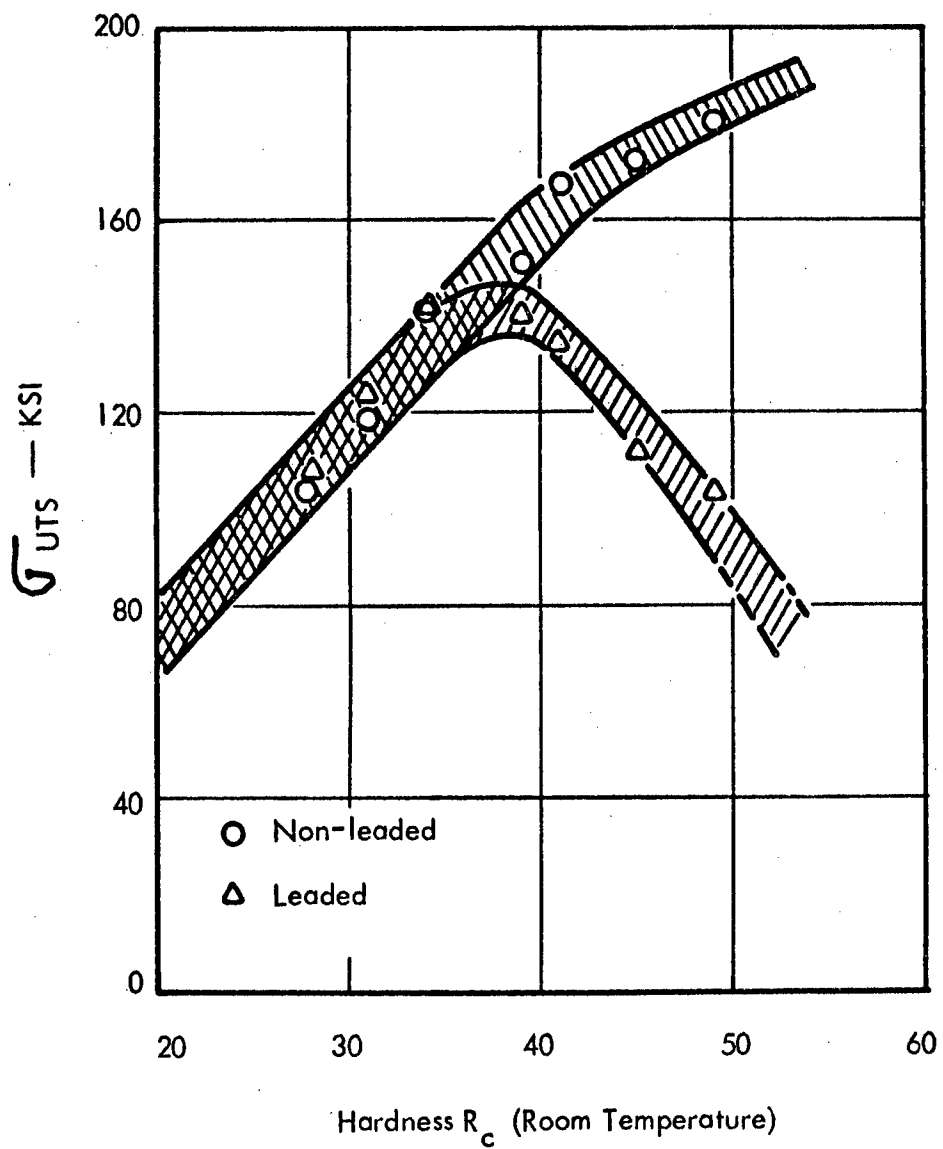


Figure 123. σ_{UTS} of Lead and Non-lead 4145 Steel as a Function of Room Temperature R_C Hardness at 700°F.

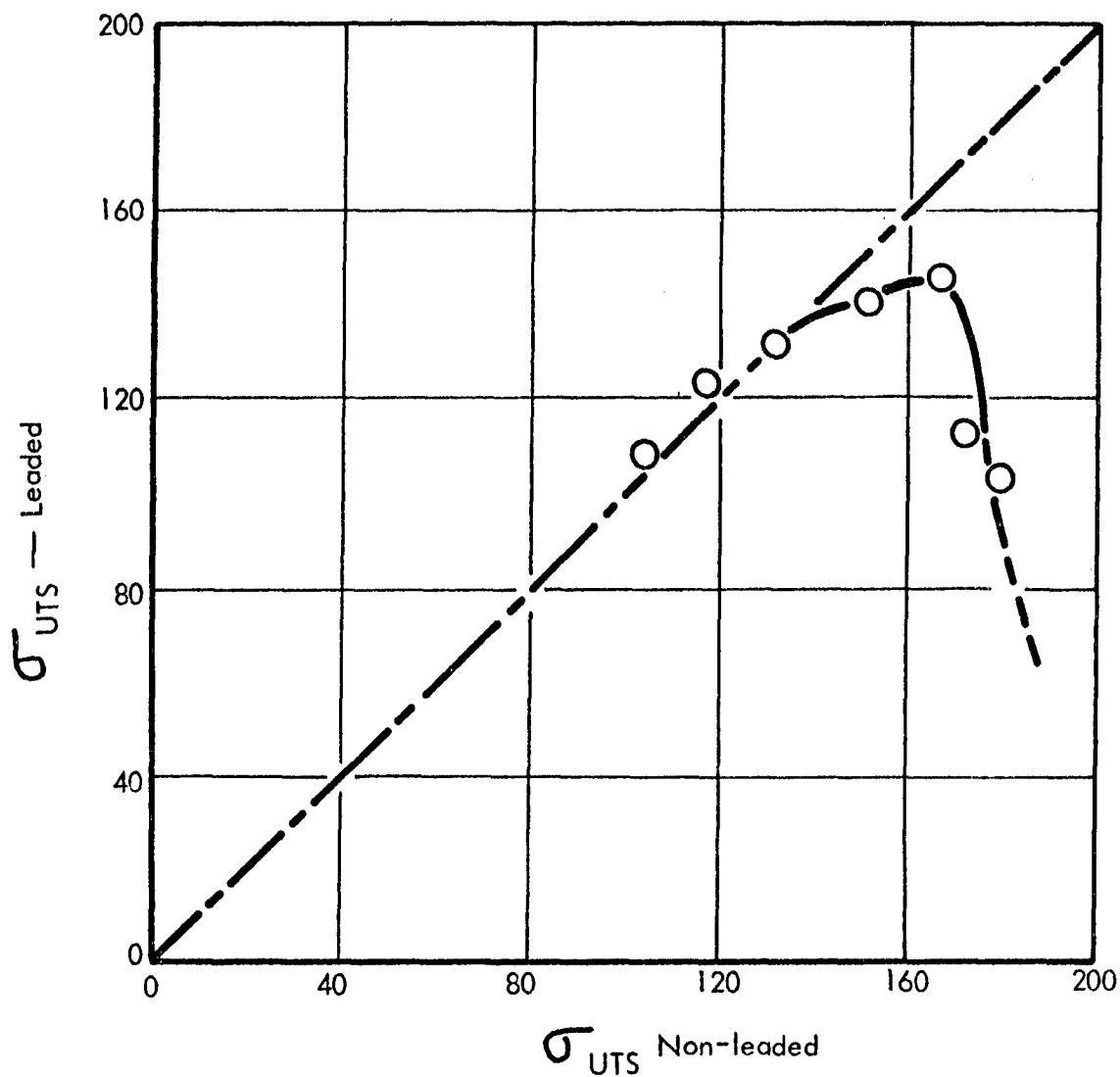


Figure 124. Ledged σ_{UTS} Versus Non-ledged σ_{UTS} at 700°F.

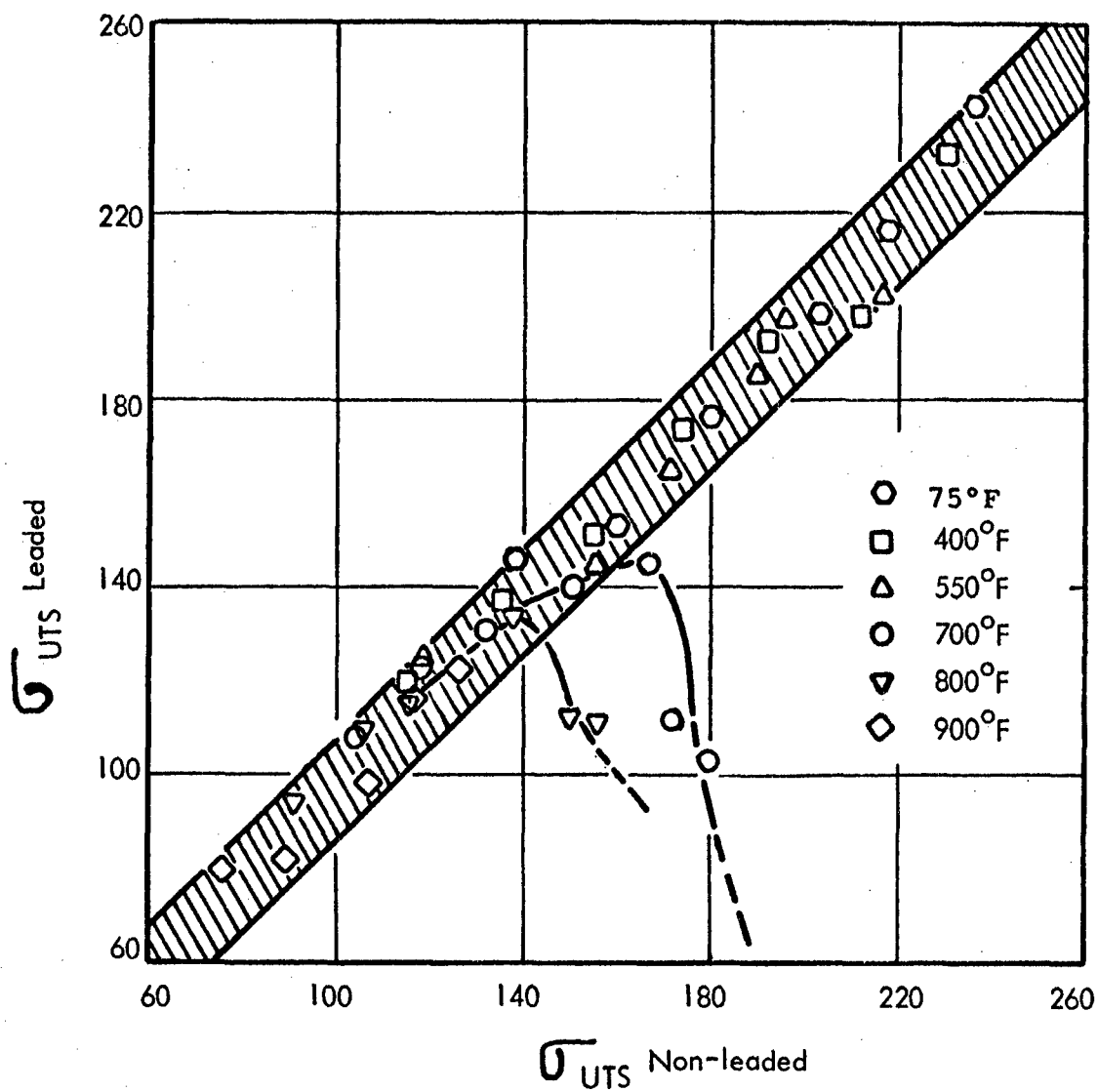


Figure 125. Ledged σ_{UTS} Versus Non-ledged σ_{UTS} with Temperature as a Parameter.

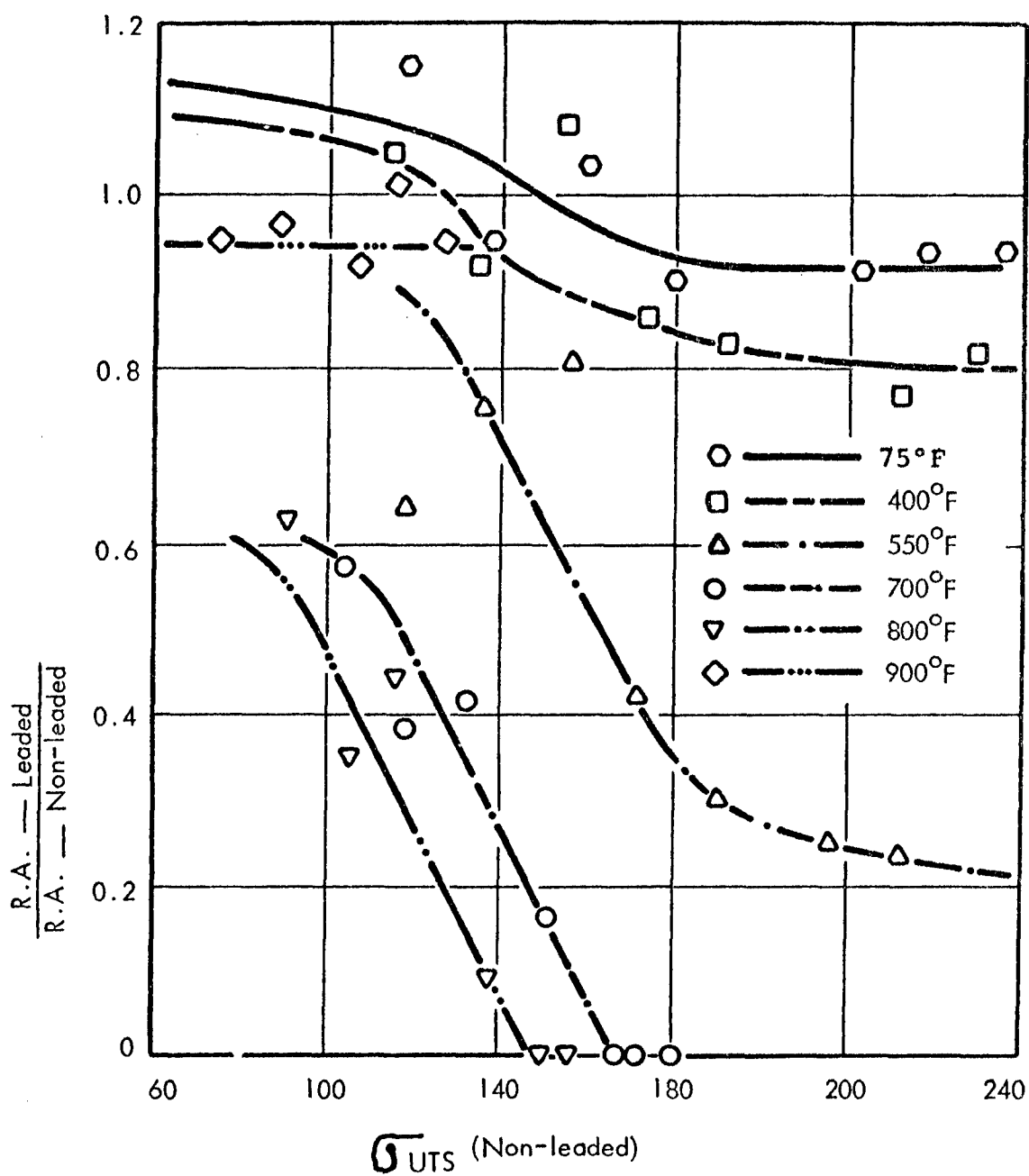


Figure 126. Ratio of R.A. for Ledged to Non-ledged Material as a Function of Non-ledged σ_{UTS} with Temperature as a Parameter.

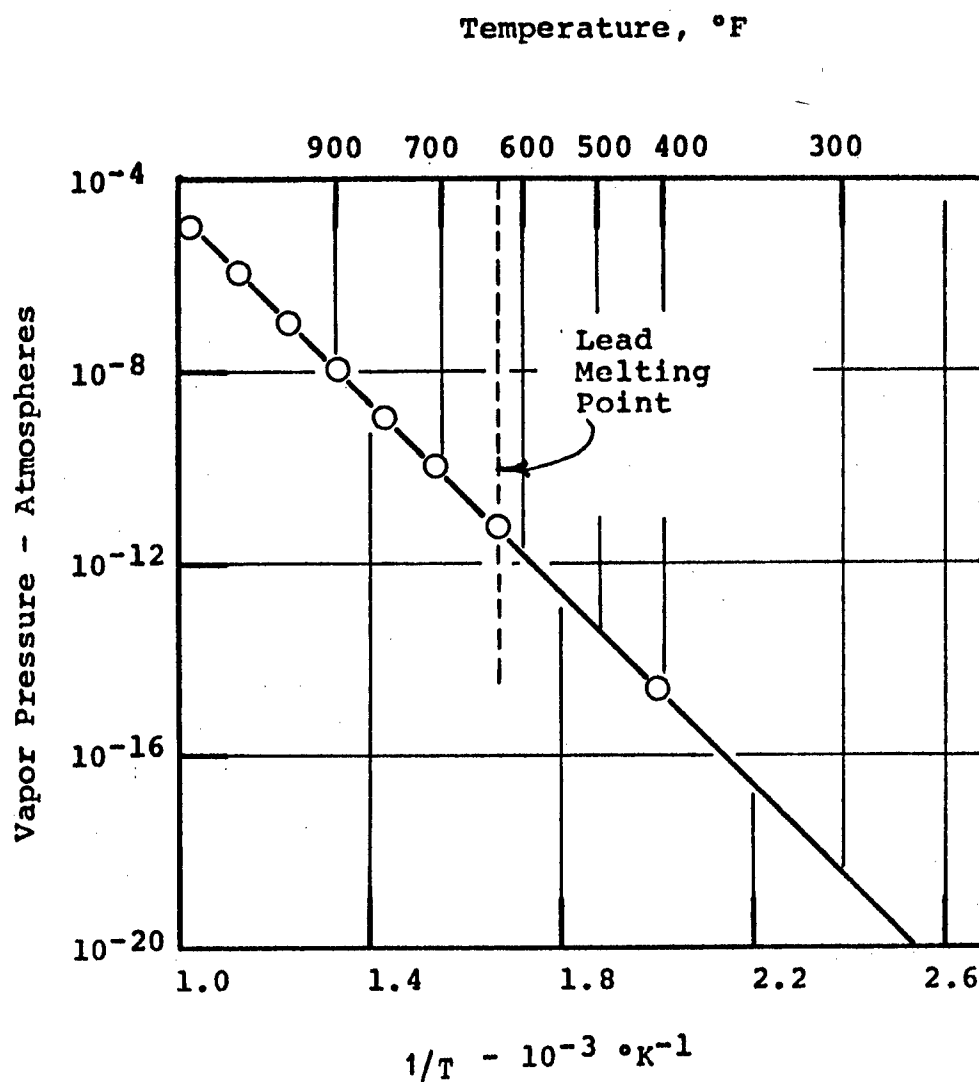


Figure 127. Vapor Pressure of Lead as a Function of the Reciprocal of Absolute Temperature. (Note Fahrenheit Scale for Reference)

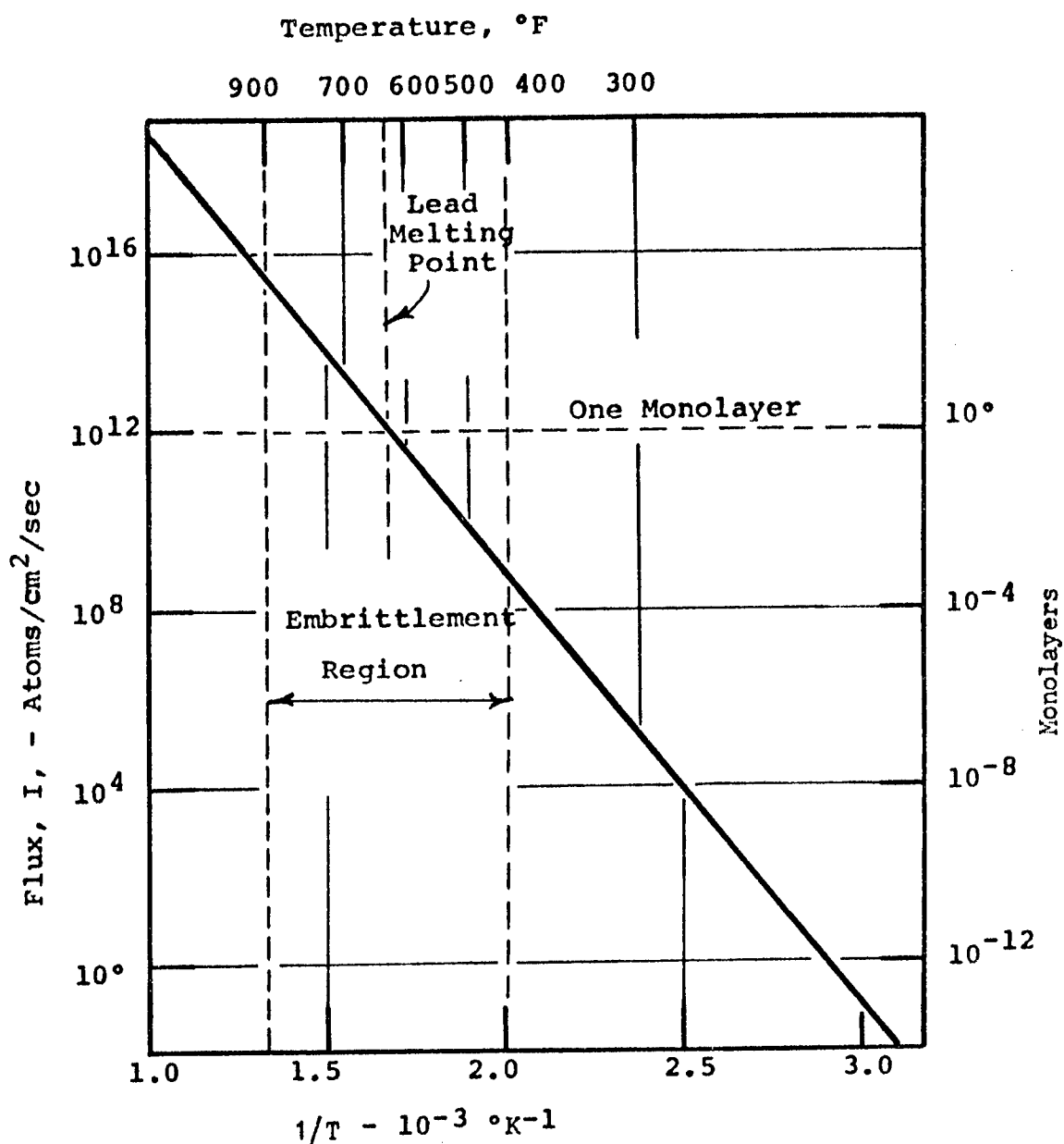


Figure 128. Atomic Flux to an Internal Surface in Equilibrium with Lead Vapor as a Function of the Reciprocal of the Absolute Temperature. (Number of Monolayers Added for Comparison Assuming $\beta = 1$, $t_m = 100$ sec., and $C_m = 100 \text{ \AA}^2$)

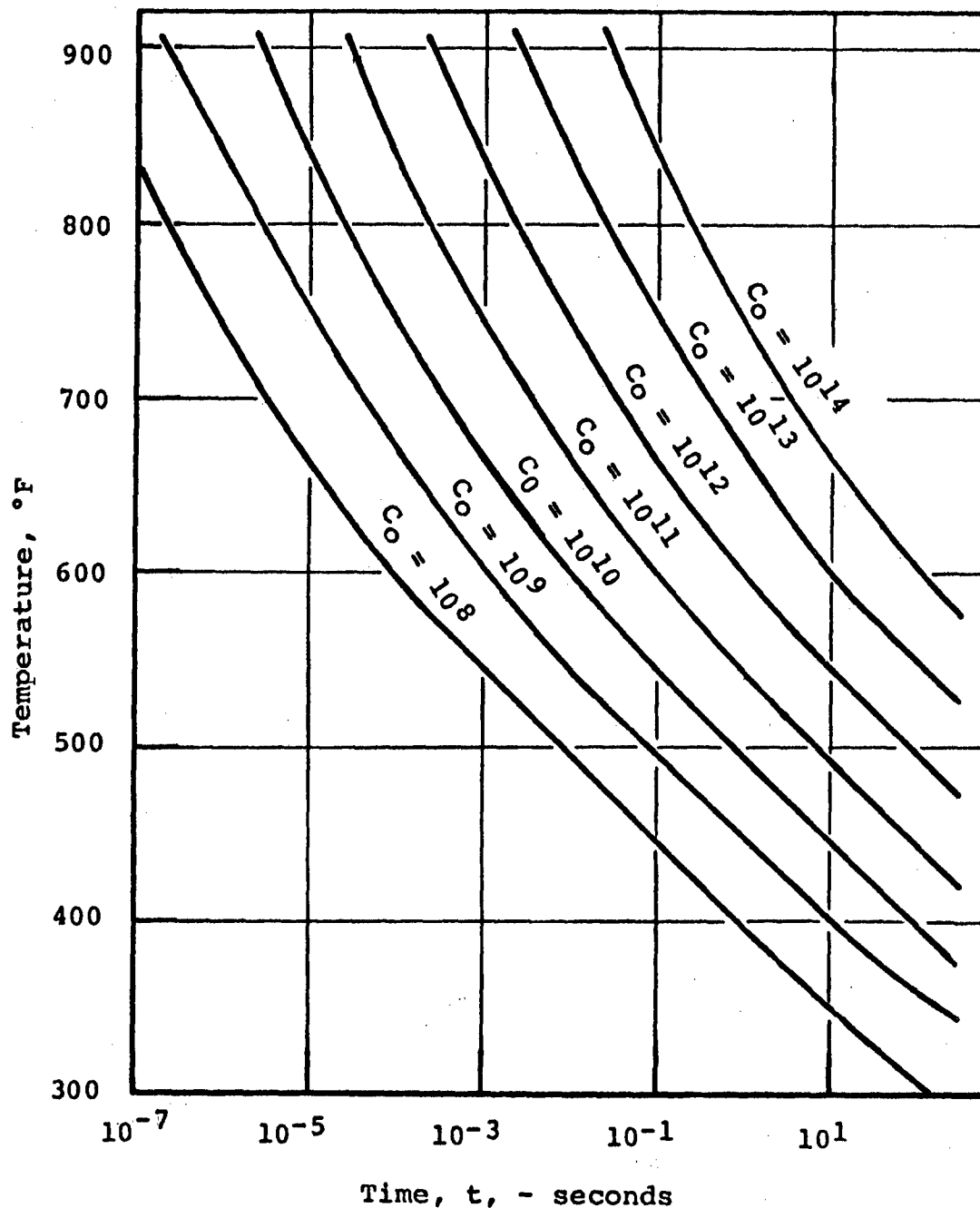


Figure 129. Parametric Plot of the Average Surface Concentration, C_O , on a Temperature-Time Plot as Obtained from the Expression: $C_O = I_t$. (Note Units of C_O are Atoms/cm²)

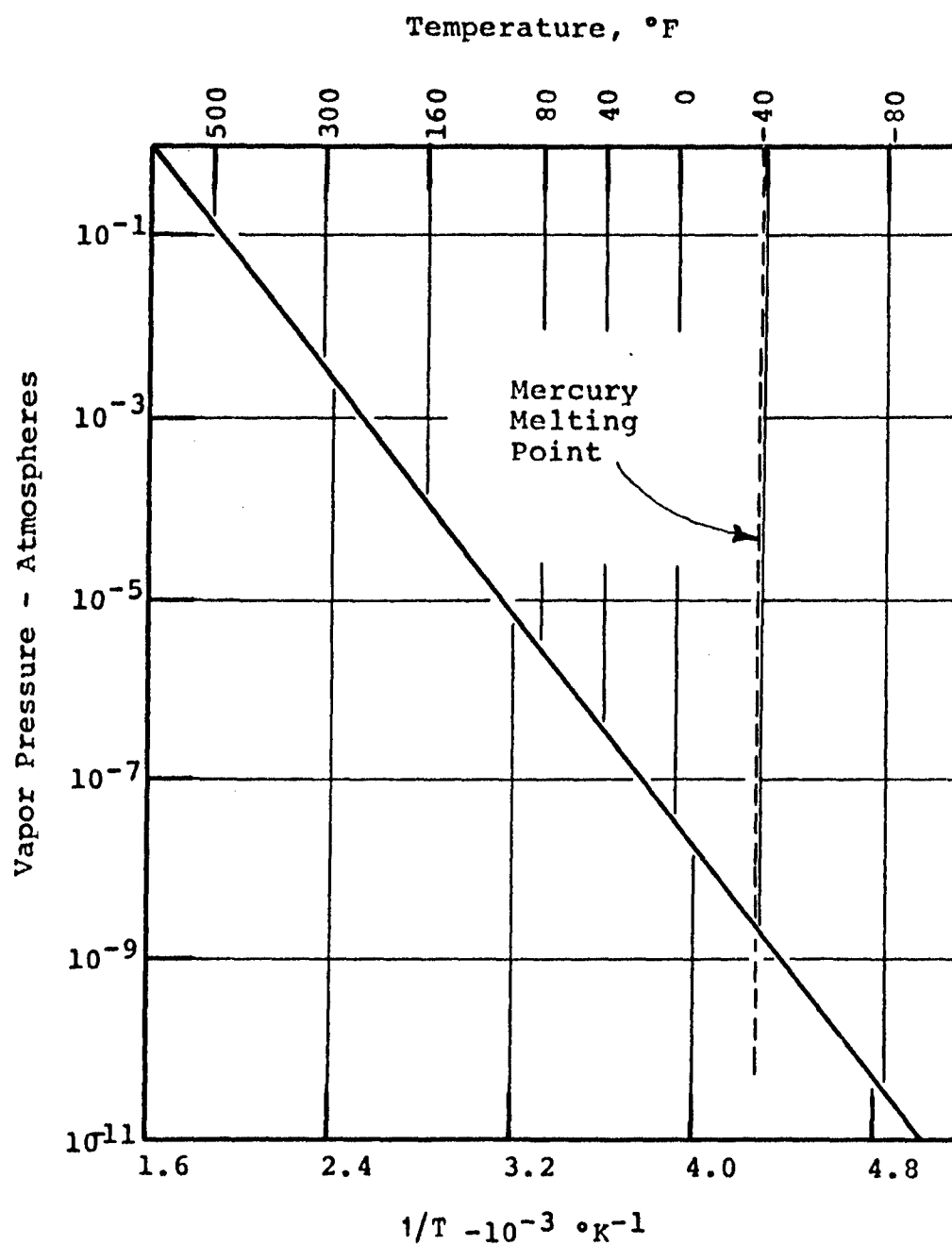


Figure 130. Vapor Pressure of Mercury as a Function of the Reciprocal of the Absolute Temperature. (Note Fahrenheit Scale for Reference)

Use revised list

28 March 1966

DISTRIBUTION LIST FOR REPORTS PREPARED FOR
CONTRACT DA-20-113-AMC-10820(T)

	<u>No. of Copies</u>
Commanding General U. S. Army Tank-Automotive Center Warren, Michigan 48090	
Attention: Director, Research and Engineering Directorate, SMOTA-R	1
Components Research and Development Labs, SMOTA-RC	3
Material Development and Engineering Div, SMOTA-RE	2
International Technical Programs Div, SMOTA-RI	1
Procurement Engineering Division, SMOTA-RS	2
Advanced Systems and Concepts Research Div, SMOTA-RR	2
Maintenance Directorate, SMOTA-M	2
Quality Assurance Directorate, SMOTA-Q	2
Plans and Commodity Office, SMOTA-W	2
Technical Data Coordination Branch, SMOTA-RTS	3
Combat Dev Comd Liaison Office, SMOTA-LCDC	2
Marine Corp Liaison Office, SMOTA-LMC	2
AF MIPR Liaison Office, SMOTA-USAF	2
Canadian Army Liaison Office, SMOTA-LCAN	2
USA EL Liaison Office, SMOTA-LEL	2
USA Weapons Comd Liaison Office, SMOTA-LWC	2
Reliability Engineering Branch, SMOTA-RTT	1
Sheridan Project Managers Office, AMCPM-SH-D	1
General Purpose Vehicles Project Managers Ofc, AMCPM-GP	1
M60, M60A1, M48A3 Project Managers Office, AMCPM-M60	1
Combat Veh Liaison Office, AMCPM-CV-D	1
US FRG MBT Detroit Office, AMCPM-MBT-D	1
XM561 Project Managers Office, AMCPM-GG	1
 Commanding General U. S. Army Material Command Washington, D.C.	
Attention: AMCRD-DM-G	2
 Commander Defense Documentation Center Cameron Station Alexandria, Virginia 22314	
	20
 Harry Diamond Laboratories Washington, D. C.	
Attention: Technical Reports Group	1

	<u>No. of Copies</u>
U. S. Naval Civil Engineer Res and Engr Lab Construction Battalion Center Port Hueneme, California 93401	1
Commanding General U. S. Army Test and Evaluation Command Aberdeen Proving Ground, Maryland 21005 Attention: AMSTE-BB	1
AMSTE-TA	1
Commanding General U. S. Army Mobility Command Warren, Michigan 48090 Attention: AMSMO-RR	1
AMSMO-RDC	1
AMSMO-RDO	1
Commanding General U. S. Army Supply and Maintenance Command Washington, D. C. 20310 Attention: AMSSM-MR	1
Commanding General 18th Airborne Corps Fort Bragg, North Carolina 28307	1
Commanding General U. S. Army Alaska APO 409 Seattle Washington 98100	1
Office, Chief of Research and Development Department of the Army Washington, D. C. 20000	2
U. S. Army Deputy Chief of Staff for Logistics Washington, D. C. 20000	2
U. S. Army Deputy Chief of Staff for Operations Washington, D. C.	2
Commander U. S. Marine Corps Washington, D. C. 20000 Attention: AO-4H	1

	<u>No. of Copies</u>
Commanding Officer U. S. Army Aviation Material Labs Fort Eustis, Virginia Attention: TCREC-SDL	1
Commanding General U. S. Army General Equipment Test Activity Fort Lee, Virginia 23801 Attention: Transportation Logistics Test Directorate	1
Commanding General U. S. Army Medical Services Combat Developments Agency Fort Sam Houston, Texas 78234	2
Commanding Officer Signal Corps Fort Mommouth, New Jersey 07703 Attention: CSRDL	2
Commanding Officer Yuma Proving Ground Yuma, Arizona 85364 Attention: STEYP-TE	1
Corps of Engineers U. S. Army Engineer Research and Development Labs Fort Belvoir, Virginia 22060	1
President U. S. Army Maintenance Board Fort Knox, Kentucky 40121	1
President U. S. Army Armor Board Fort Knox, Kentucky 40121	1
President U. S. Army Artillery Board Fort Sill, Oklahoma 73503	1
President U. S. Army Infantry Board Fort Benning, Georgia 31905	1
President U. S. Army Airborne Electronic and Special Warfare Board Fort Bragg, North Carolina 28307	1

	<u>No. of Copies</u>
President U. S. Army Arctic Test Center APO Seattle, Washington 98733	1
Director, Marine Corps Landing Forces Development Center Quantico, Virginia 22134	1
Commanding Officer Aberdeen Proving Ground Aberdeen Proving Ground, Maryland 21005 Attention: STEAP-TL	1

Unclassified

Security Classification

14.	KEY WORDS	LINK A		LINK B		LINK C	
		ROLE	WT	ROLE	WT	ROLE	WT
	Leaded Steels						
	Alloy Steels						
	High Strength Steels						
	Embrittlement						
	Liquid Metal Embrittlement						
	Cracking						
	Service Failures						
	Processing Failures						
	Static Fatigue						
	Fracture						
	Fractography						
	Impact Testing						
	Elevated Temperatures						
	Tensile Properties						
	Design Mechanical Properties						

Unclassified

Security Classification